Compact Antenna Arrays
for Efficient Direction of Arrival Estimation

Mariana Guimarães Pralon
geboren am 27.01.1983 in Rio de Janeiro, Brasilien

Abstract

In recent years, a topic that has received major attention in diverse areas of research is the miniaturization of communication devices. Society has demanded increasingly smaller and more compact equipments that allow for mobility with lower level of effort. Fields of research that have recently demanded compactness of devices include radio emitter localization, and more specifically, the localization in terms of Direction of Arrival (DoA), also referred to as direction finding. Applications for direction finding include RADAR systems, channel sounding, satellite navigation, and security applications, among others. High-resolution direction finding systems include a receiving array of antennas responsible to capture the impinging signals and feed the output to a DoA estimator. Miniaturization of such systems is accomplished by optimizing the antenna array with respect to the total volume occupied. There are two possible outcomes of array miniaturization: reduced size and lighter individual sensors or placement of elements in the array closer together. The second solution for compactness implies inter-element spacing smaller than half of the free-space wavelength, giving rise to stronger mutual coupling in the array, which causes adverse effects such as radiated far-fields pattern distortion, reduced bandwidth, and power and polarization mismatch. The contribution of this thesis is to show how the impairment that arises from strong electromagnetic interaction between neighboring elements in compact arrays affects the antenna capabilities for direction finding. We propose a solution to decouple and match compact antenna arrays, which is based on an eigenmode decomposition approach for the design of Decoupling and Matching Networks (DMN) comprised of distributed elements. We demonstrate the benefits of using the proposed DMN, to restore impairment caused by compactness, for direction finding of emitters in diverse scenarios. With the aim of evaluating and optimizing antenna arrays for direction finding based applications, we propose a workbench that connects the antenna design parameters to performance metrics for DoA estimation. Although the proposed decoupling and matching technique significantly enhances the direction finding performance of compact arrays, the frequency bandwidth may still be a limiting factor. This thesis contributes to this issue by proposing a multiband antenna array comprised of sub-arrays optimized for different frequencies. As an outlook, we evaluate wideband antenna arrays comprised of magnetic loops with respect to DoA estimation acuracy and discuss possible solutions for matching and decoupling over a wide frequency bandwidth.

Zusammenfassung

Ein wissenschaftliches Thema, welches in den letzten Jahren in den verschiedensten Bereichen der Forschung große Aufmerksamkeit erlangt hat, ist die Miniaturisierung von elektronischen Geräten insbesondere in den Anwendungsfeldern Kommunikation und Ortung. Die Gesellschaft und der zunehmende Grad der digitalen Industrialisierung fordern immer kleinere und kompaktere Geräte, die die Mobilität mit möglichst geringerem Aufwand ermöglichen. Forschungsgebiete, die eine besondere Kompaktheit von Geräten fordern, umfassen die Lokalisierung/Ortung von Radioemissionen und genauer die Bestimmung dessen Richtungsinformation (Direction of Arrival, kurz DoA). Klassische Anwendungen für die Richtungserkennung sind RADAR-Systeme, Channelsounding, Satellitennavigation oder Sicherheitsanwendungen. Hochauflösende Richtungssuchsysteme bestehen aus einem Empfangsantennenarray, welches für die Erfassung der ausgesendeten Signale und deren Weiterleitung zum DoA-Schätzer verantwortlich ist. Die Miniaturisierung derartiger Systeme erfolgt durch Optimierung der Antennenanordnung bezüglich des eingenommenen Gesamtvolumens. Es gibt zwei mögliche Ansätze zur Antennenminiaturisierung: reduzierte Größe und leichtere individuelle Sensoren oder dichtere Platzierung der Elemente innerhalb des Antennenarrays. Die zweite Lösung impliziert einen Elementabstand, der kleiner als die Hälfte der Freiraumwellenlänge ist. Dies führt zu einer stärkeren gegenseitigen Kopplung in dem Antennenarray und somit nachteilige Effekte, wie zum Beispiel eine Verzerrung der Fernfeldantenneneigenschaften, verringerte Bandbreite und Leistung- sowie Polarisationsdiskrepanz. Diese Arbeit soll zeigen, wie die Beeinträchtigung, die durch starke elektromagnetische Wechselwirkungen zwischen benachbarten Elementen in kompakten Anordnungen entsteht, die Fähigkeiten des Antennenentwurfs für die Richtungsfindung beeinflusst. Es wird eine Lösung zur Entkopplung und Anpassung kompakter Antennenarrays vorgeschlagen, die auf einem Eigenmodenzerlegungsansatz für den Entwurf von Entkopplungs- und Anpassungsnetzwerken (Decoupling and Matching Network, kurz DMN) basiert. Die Vorteile dieses Ansatzes werden in verschiedenen Szenarien für den Anwendungsfall der Richtungsfindung demonstriert. Mit dem Ziel, Antennenarrays für richtungsbezogene Anwendungen zu evaluieren und zu optimieren, wird ein Entwurfsfluss vorgeschlagen, der die Parameter der Antennenkonfiguration mit den Kenngrößer einer DoA-Schätzung verbindet. Obwohl die vorgeschlagene Entkopplungs- und Anpassungstechnik die Leistungsfähigkeit der Richtungsfindung mittels kompakter Anordnungen beträchtlich verbessert, kann die Frequenzbandbreite immer noch ein begrenzender Faktor sein. Diese Dissertation trägt zu diesem

Thema bei, indem sie ein Mehrbandantennenarray vorschlägt, dass aus Subarrays besteht, die für verschiedene Frequenzen optimiert sind. Als Ausblick wird ein Breitbandantennenarray aus magnetischen Schleifen in Bezug auf die DoA Schätzgenauigkeit untersucht und mögliche Lösungen für die Anpassung und Entkopplung über eine große Frequenzbandbreite diskutiert.

Preface

This work is a compilation of the research carried out during my four years as a Doctoral student at the Electronic Measurement Laboratory (EMT) at the Technische Universität Ilmenau, under the supervision of Univ.-Prof. Dr.-Ing. habil. Reiner Thomä and co-supervision of Univ.-Prof. Dr. rer. nat. habil. Matthias Hein. The research has been funded by the Brazilian Army, on behalf of the Brazilian Ministry of Defense, for which I am truly grateful.

My deep appreciation goes to Univ.-Prof. Dr.-Ing. habil. Reiner Thomä for valuable supervision, guidance and support, which is responsible for the successful accomplishment of this Doctoral degree. Special thanks to my co-supervisor, head of the RF and Microwave Research Laboratory (HMT) at the Technische Universität Ilmenau, Univ.-Prof. Dr. rer. nat. habil. Matthias Hein for all the support, motivation, brilliant suggestions and productive discussion. I am thankful to Univ.-Prof. Dr.-Ing. Giovanni Del Galdo, head of the DVT department for all the discussion, support, ideas and guidance. I would also like to thank Prof. Dr. Jose Ricardo Bergmann for reviewing this work.

My true appreciation to all my department colleagues, among which are Dipl.-Ing. Martin Käske, Dipl.-Ing. Christian Schneider, Dipl.-Ing. Gerd Sommerkorn, Dipl.-Ing. Stephan Häfner, Dr.-Ing. Markus Landmann, Dr.-Ing. João Paulo Carvalho Lustosa da Costa, Dipl.-Ing. Jonas König. Thanks to my colleague Dr.-Ing. Dominik Neudert-Schulz, for all the support and for co-authoring most of the publications during my Doctoral work. Special thanks go also to my two colleagues and friends Anastasia Lavrenko and Snezhana Jovanoska. I would also like to thank my colleagues at the HMT department Dr.-Ing. Safwat Irteza-Butt and Maysam Ibraheam for all the fruitful discussion. I am thankful to my colleagues at the Fraunhofer Institut, Dr.-Ing. Alexander Popugaev and Dr.-Ing. Marc Oispuu, for the cooperative work and productive discussion.

I am deeply thankful for the support of my family. My brother Leandro and his wife Barbara, thank you for always inspiring and supporting me. I am deeply grateful to my beloved boyfriend Johannes, for precious support and motivation during the last years, which have made the journey here immensely lighter. Finally, I would like to thank my dear parents, Hildebrando and Jane. I wish the completion of this work makes you proud and that I am able to one day return all the love, support, and the life you gave for me.

<div align="right">

Mariana Guimarães Pralon

Ilmenau, July 12, 2017

</div>

Contents

List of Figures

List of Tables

List of Algorithms

1. Introduction

In recent years, the estimation of parameters from electromagnetic impinging waves, such as Direction of Arrival (DoA), Time Difference of Arrival (TDoA), or Doppler frequency (for moving targets), is a field of research that has received major attention both in the academic community as well as in industry, for military and civilian operation. Several applications such as security, RADAR systems, law enforcement, among others, focus on the estimation of received signal parameters for the localization of radio emitters. More specific applications may need to estimate the polarization of impinging waves or the total number of sources radiating electromagnetic waves. The acquired waves may be, in case of non-cooperative scenario, the emission of mobile devices of criminals or from the communication device of an individual in need for rescue or, in case of cooperative scenario, may originate from the scattering of a RADAR transmission on the surface of an aerial target. In all the above mentioned scenarios, the objective is to estimate some pre-defined parameter set from the impinging waves with as high resolution and accuracy as possible.

To estimate parameters such as DoA, TDoA, polarization, or Doppler frequency of incoming waves, several techniques have been exhaustively investigated over the years. Although the techniques can be used to estimate a series of parameters, this thesis focuses on the estimation of DoA of impinging waves. A field that has received major attention over the years is DoA estimation of closely spaced sources that requires high-resolution direction finding techniques based on the array response to the impinging waves [9, 10]. We can safely divide the array-based estimation techniques into three major groups: the conventional techniques (such as multilobe amplitude comparison and phase interferometry [9]), Maximum Likelihood (ML) [11, 12, 13, 14] and subspace-based techniques [15, 16].

Among the conventional techniques is the beamforming, which consists of correlating the measured output from an antenna array to the array manifold. It linearly combines the output from each sensor by choosing weights with the aim of estimating the DoA of an incoming wave. Although easy to implement, conventional beamforming techniques are not suitable for more complex scenarios such as when, besides the Line of Sight (LoS) between transmitter and receiver, the wave propagates through multiple secondary paths arriving from different directions [17]. Inside big cities, for example, when the transmitted electromagnetic wave reflects on buildings or on other surfaces, causing multiple delayed paths from the same emission to arrive at the receiver, it is crucial that the estimator is able to distinguish between the multiple

paths, which cannot be achieved with conventional beamforming. Hence, more sophisticated high-resolution techniques such as ML or subspace-based techniques are usually employed.

Among the most popular subspace-based techniques are the so called Multiple Signal Classification (MUSIC) [15] and the Estimation of Signal Parameters via Rotation Invariance Technique (ESPRIT) [16]. These techniques are based on estimating the correlation matrix of the measured output of the antenna array and subsequently decomposing it into eigenmodes. The eigenmodes are then divided into signal and noise subspaces. The immediate drawback of such group of techniques is with respect to the requirement of a minimum number of uncoupled sensors to resolve the impinging waves. The problem is worsened if the radiators are highly coupled or if the waves are correlated, which occurs if the sources are correlated or in multipath scenarios where the relative delay between paths is shorter than the inverse of the coherency bandwidth, giving rise to what is called rank deficiency [18]. For correlated impinging waves, the performance of the estimator may be seriously degraded and additional complexity may arise from required techniques capable of decorrelating the signals, such as spatial smoothing [19]. To avoid rank deficiency for the decomposition of signal and noise subspaces, the number of sensors must be larger than the number of sources, which becomes a significant constraint, especially for applications that are based on compressed sensing [20]. In multipath or multiple emitter scenarios, when the number of source waves impinging on the receiving antenna is not known a priori, the estimation performance may be seriously degraded when arrays with insufficient number of sensors are used for reception. Although there are several researches on improved MUSIC-based techniques that are able to estimate under rank deficiency [21, 22, 23], the complexity added usually encourages the use of alternative estimation techniques.

One of the most utilized techniques for multi-source and multi-path scenarios is the Maximum Likelihood. The ML technique is based on the Log-Likelihood Function (LLF) with respect to the parameter to be estimated. For the estimation of the elevation (ϑ) of an impinging wave, for example, the LLF represents the likelihood of a certain ϑ to be the real elevation of arrival. The estimated $\hat{\vartheta}$ is the ϑ that maximizes the LLF. One possible drawback of the ML technique is with respect to the computational effort required by the search procedure for the maxima of the LLF. If the search for the maxima is exhaustive, for 2D DoA estimation when N source waves impinge on the receiving array, the LLF is computed at each point of a a $2N$-dimensional grid, what clearly results in high computational effort. Alternatively, one may use a simplified search and achieve the direction of maximum likelihood that may not be optimal in terms of global solution but is still a ML solution.

Regardless of the technique used for direction finding of targets, a bound for the corresponding estimation variance, called Cramér-Rao Lower Bound (CRLB), was published by Cramér

[24] and Rao [25] and is applicable for unbiased estimators. Although several authors, such as Friedlander [26] and Weiss [27], have made significant contributions to the use of the CRLB in various scenarios, special attention needs to be given to Stoica and his work [11, 28] to establish the CRLB as one of the most utilised metrics for direction finding accuracy. Recent publications have demonstrated the use of the CRLB for two-path scenarios. It gives results for the CRLB of a main path conditioned to the fact that an extra second path is also existent [29]. Hence, the CRLB may also be used as a metric for resolution as it gives a bound for the estimator variance of one path component, in the vicinity of the other paths. Although the CRLB may be a powerful tool for optimizing antenna arrays for direction finding, since it is strongly dependent on the array radiation characteristics, it is not able to reveal estimation errors that result from incomplete or mismatched data models or errors due to imprecise calibration (see [30] for an extensive discussion).

The CRLB as well as the cost functions for direction finding estimators are strongly dependent on the antenna array radiation pattern. As a consequence, changes in the array fundamental parameters have a definite impact on the accuracy and resolution of the estimator. Some basic parameters need to be taken into account when designing an antenna array for DoA estimation:

- Directivity: single-antennas used for direction finding are usually highly directional in order to ensure accuracy and resolution. When correlating the radiated far-fields pattern to the measured received array output, directivity guarantees that a certain direction is highlighted by higher SNR, raising the accuracy of estimation. Moreover, narrow beamwidth patterns increase the capability to resolve two sources coming from different directions. Alternatively, arrays of omnirectional elements may be employed to ensure wide angular coverage. The directivity is then achieved by increasing the number of radiators in the array, or by increasing the electrical size of the antenna array.

- Polarization: it is highly desired that receiving antennas for direction finding are dual-polarized to avoid mismatch between antenna and source signal polarization, which may degrade the accuracy of the estimation. The antenna radiation patterns (the array manifold) depend on the polarization orientation of the impinging wave. For this reason, the antenna has to be described by its full dual polarimetric response. As a consequence, ignoring polarization would end in matching the wrong data model, which is the model of the output at the array ports when waves impinge on the antenna, leading to wrong estimates. Therefore, it is inevitable to consider the polarization orientation of the impinging wave as nuisance parameter. This means that it has to be considered even

if it is not explicitly required. Exceptions are only possible if there is a clear a priori match between the polarization of the impinging wave and the preferred polarization orientation of the observation antenna [30].

- Aperture: to narrow the radiation pattern beamwidth, the overall antenna electrical size must be as wide as possible. The Rayleigh criterion establishes that the antenna angular resolution is the higher the wider the physical aperture becomes. Fortunately, High-Resolution Parameter Estimation (HRPE) can be applied to achieve accuracy and resolution performance beyond the Rayleigh limit [31]. However, physical aperture needs to be carefully investigated, since it will affect the accuracy and resolution of the estimator and may become, at the end, the most restrictive parameter for antenna design aiming DoA estimation.

- Number of radiating elements: in an array, for a fixed inter-element spacing, the antenna aperture broadens with the number of elements. Furthermore, for DoA estimation, higher number of sensors in an array inreases the degrees of freedom and SNR, leading to higher accuracy in the estimation process. If the application intended imposes constraints with respect to the antenna array physical size, e.g. direction finding on small flying copters, it may be interesting to discuss the optimization of DoA estimation performance as a compromise between number of elements and element spacing.

- Frequency bandwidth: although this thesis focuses on DoA estimation of narrowband signals propagating at a pre-defined frequency, applications such as channel sounding may require wideband receiving antennas for broadband estimation. As a consequence, the required antenna bandwidth will depend on the application intended. If the aim is to locate targets emitting at a pre-defined frequency, narrowband antennas are enough to ensure efficient direction finding. On the other hand, if the signals are propagating at non-specified frequencies over a wide range, it may become a requisite that the antenna is wideband or multiband in order to ensure proper reception. Frequency bandwidth may become a limiting parameter when using compact arrays for direction finding, since it may be drastically narrowed by mutual coupling. Moreover, solutions to decouple array ports based on the use of passive elements such as capacitors, inductors (lumped elements) or microstrip lines (distributed elements) may restrict the array frequency range of operation as suggested by Bode-Fano in [32], limiting the application.

- Arrangement: for one-dimensional direction finding, linear arrays are good candidates as arrangement, since the aperture is increased in the desired direction with number of

sensors. However, for two-dimensional DoA estimation, planar arrays need to be designed for aperture in the two directions of interest (e.g. azimuth and elevation). However, special attention needs to be paid to the data model when considering the antenna array arrangement. If, for some reason, the antenna output is modeled as one-dimensional, i.e., if we assumed that the signal is propagating co-planar to the antenna array and the estimation is carried out only with respect to one direction (e.g. azimuth), but in reality, the signal propagation with respect to the antenna array is three-dimensional, linear arrays may be prefered over circular arrangements, as reported in [30]. Model mismatch may lead to stronger degrading effects to direction finding when circular arrays are used instead of linear arrangements.

Furthermore, the increasing demand with respect to mobility of communication devices has given rise in recent years to ever more sophisticated research to optimize antenna arrays taking into account compactness. When receiving antennas are required, for example, to be hand-held or mounted on an Unmanned Aerial Vehicle (UAV) or some small flying copter for target localization, the total volume occupied by the array needs to be as reduced as possible. When optimization with respect to the size of the individual sensors is already exhausted, the solution to further reduce the overall size of the array without reducing the number of sensors is to place them together more closely, usually implying element spacing smaller than the optimal half of the free-space wavelength. Reduced inter-element spacing leads to stronger coupling between sensors and the effects to direction finding accuracy and resolution must be carefully analyzed. In this work, we parametrize antenna array compactness as the ratio between inter-element spacing d and the free-space wavelength λ. Arrays with $d/\lambda < 0.5$ usually exhibit non-neglecting degrading effects with respect to radiation performance, which arises from strong mutual coupling. We restrict the analysis to $d/\lambda < 0.5$, in order to avoid ambiguity.

There are three significant effects of mutual coupling: far field pattern distortion, impedance mismatch, and reduced degrees of freedom, rendering impaired performance [33, 34]. To overcome radiation pattern distortion, there are several publications that suggest solutions on the signal processing domain [35, 36]. The consequence of compensating for the pattern distortion in the digital domain leads to a partial mitigation but not to a total compensation of the mutual coupling effects, since the power that is lost due to impedance mismatch cannot be restored by signal processing. The power loss due to mutual coupling leads to a definite decrease of SNR, since the noise corrupts the signal before digital processing.

To completely overcome coupling, solutions need to include the analog domain for power matching, through the design of decoupling and matching networks. Passive networks may be comprised of lumped [37] or distributed [33] elements, while active networks commonly consists

of Low Noise Amplifiers (LNA) for impedance matching. The parameters for the design of networks based on distributed elements are computed from the required excitation at each antenna array port in order to ensure that the radiated array patterns are orthogonal with respect to each other. For this purpose, this thesis adapts an approach based on the modal decomposition of the array radiation matrix, rendering orthogonal fundamental patterns of radiation, for decoupling antenna arrays for direction finding.

The resulting network of antennas and Decoupling and Matching network (DMN) directly launches array radiation eigenmodes. This results from the close interaction of the passive Decoupling and Matching Network (DMN) with the physical radiating elements by exchange of energy. The DMN together with the physical antennas should then be considered a "new" antenna array. Hence, the output (eigenmodes) can be individually matched and even left unused if their contribution can be considered minor. Of course, the resulting radiation patterns have to be precisely measured (including all implementation losses) and subsequently used as reference for DoA estimation.

When using a compact array for direction finding, the coupling certainly affects the accuracy and resolution of DoA estimation. However, there is very little research on the actual effects to High Resolution Parameter Estimation (HRPE) and solutions to mitigate them. Most important, there is no conclusive study on the effects of the solutions already presented for compensating mutual coupling to the direction finding capabilities of an array.

The contribution of this work inlcudes attempts to answer some fundamental questions:

- How do the fundamental parameters of antenna arrays influence the capability for direction finding?

- What are the effects of mutual coupling on DoA estimation with respect to direction findig accuracy and resolution?

- Are the effects of mutual coupling dependent on the scenario: does it have stronger effect in coherent multi-source scenarios? How does it affect resolution of closely spaced paths or emitters?

- How is it possible to tackle degrading effects of coupling to direction finding of electromagnetic waves? Are techniques for decoupling in the digital domain as effective as techniques based on the use of analog devices to alter the interaction between array elements?

- Does the DMN help to improve the accuracy and resolution of DoA estimation when compact antenna arrays are used as receiving antennas for direction finding? Is the

improvement observed both with respect to the CRLB as well as with respect to actual parameter estimation based on techniques such as MUSIC or ML?

- What is the role of decoupling when compared to power matching for direction finding? Does it make sense to spend effort in decoupling an array when good matching is achieved?

- To overcome the drawback of passive DM networks with respect to ohmic losses and narrow bandwidth, is it suitable to use active components for wideband matching? Does wideband matching have any impact on the antenna array mutual coupling over a wide frequency bandwidth?

With the aim of evaluating antenna arrays for direction finding-based applications, we propose a multi-disciplinary workbench that connects the antenna design to the DoA estimation of the waves and allows for the computation of performance metrics for specific antenna design parameters. Owing to the fact that metrics for DoA estimation performance are not fundamental antenna parameters, it becomes imperative that a design flow is able to connect antenna design to DoA estimation techniques. Figure 1.1 depicts the workbench established in this thesis, which begins by defining the propagation scenario with the use of tools such as Winprop ProMan [38], allowing for the precise model e.g. of a multipath environment. Subsequently, the antenna array response needs to be accurately obtained by measurements in anehoic chamber or with the use of 3D electromagnetic Computer Aided Design (CAD) tools such as Ansoft HFSS 14.0 [39]. The antenna may include feeding networks that are designed either with the help of 3D simulation tools or with 2D tools such as Agilent Design System (ADS) [40]. After proper scenario definition and equipped with the antenna array response, we compute performance metrics such as accuracy and resolution, based on the CRLB or on the error of the DoA estimator, based on techniques such as MUSIC or ML, in a programming environment such as Matlab [41]. If an optimal design is to be achieved, the workbench may become a cycle in which antenna parameters are modified with the aim of achieving required DoA estimation performance metrics, as illustrated in Figure 1.2.

This work is organized as follows. Chapter 2 reviews the system model for the received output of the antenna array for parameter estimation-based applications. Direction finding techniques such as Maximum Likelihood and the subspace based technique MUSIC are detailed with the aim of further evaluation with respect to the antenna array radiation patterns. The commonly used bound to unbiased estimation variance, known as CRLB, is subsequently detailed with the aim of serving as a suitable metric of performance for the capability of antenna arrays for direction finding. We proceed to detailing the EADF used for the interpolation of the
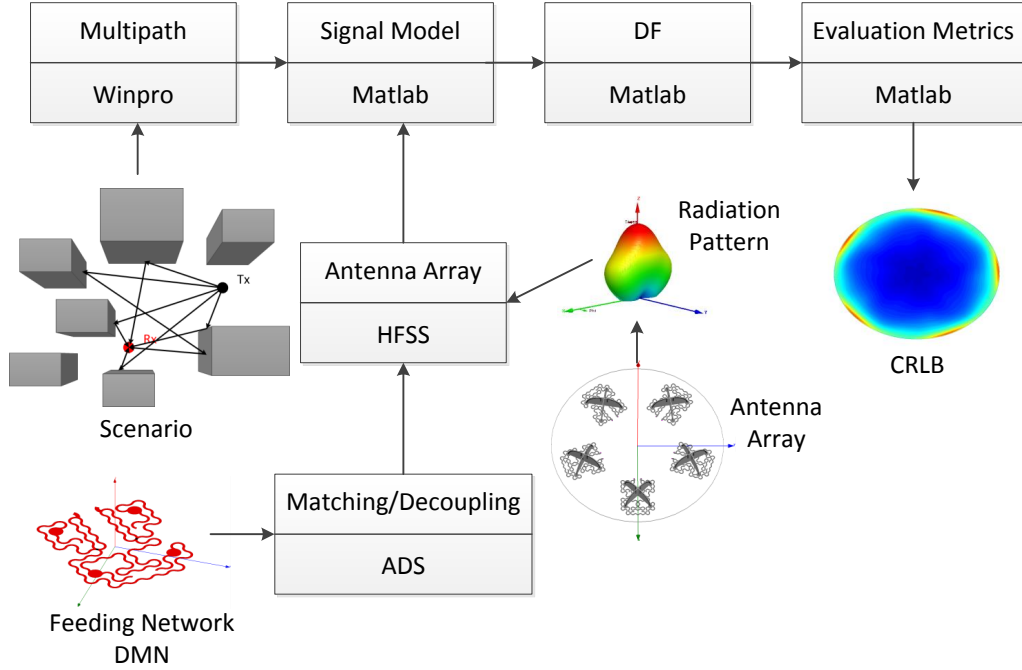
Figure 1.1.: Workbench for the evaluation of antenna arrays for direction finding.

array radiation patterns and computation of derivatives with respect to the set of parameters to be estimated, for the CRLB. Metrics related to direction finding resolution of multiple impinging waves are proposed to complement the accuracy measured by the CRLB.

Chapter 3 begins with the description of the fundamental antenna parameters and proceeds to presenting details on the electromagnetic coupling between radiators, when arrays of antennas are used for the reception of waves. Real antenna arrays such as microstrip patch antenna arrays and L-Quad arrays are detailed, and relations are established between parameters of the antenna array and metrics for direction finding performance.

Chapter 4 describes antenna arrays with respect to the fundamental modes of radiation. We propose a passive decoupling and matching network comprised of distributed elements for direction finding systems, which is based on the eigenmode approach. We derive the CRLB of a decoupled array, and compare it to the CRLB of the original array prior to decoupling. Finally, we illustrate the effects of eigenmode excitation to the radiation patterns of L-Quad and microstrip patch antenna arrays.

Chapter 5 presents results on the evaluation of real antenna arrays for direction finding, both
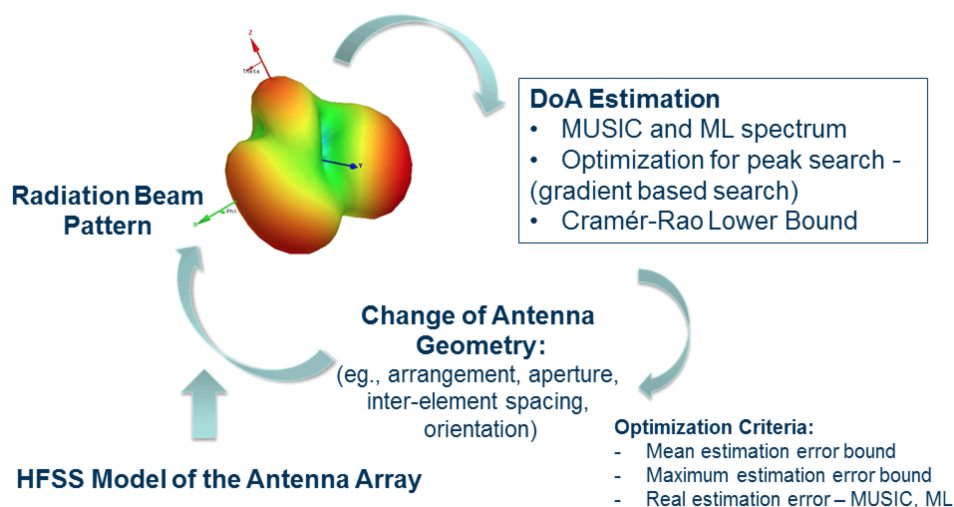
Figure 1.2.: Optimization loop.

with respect to the CRLB, as with respect to MUSIC and ML estimation errors. The evaluation of the antenna arrays is carried out with the use of the multi-disciplinary workbench proposed in this work. The performance of antenna arrays in several scenarios is investigated, focusing on compact arrays with inter-element spacing d smaller than half of the free-space wavelength λ. A comparison of performance with respect to direction finding accuracy and resolution is subsequently drawn between coupled and decoupled antenna arrays in order to evaluate the use of the proposed DMN for direction finding. An optimization is subsequently carried out for arrays used for direction finding in applications that set constraints with respect to size. Finally, a multiband L-Quad antenna array comprised of subarrays optimized for different frequency bands is proposed and investigated with respect to direction finding performance metrics.

2. Direction of Arrival Estimation

In recent years, one of the research areas that has received highest attention in the signal processing community is the estimation of parameters from incoming electromagnetic waves. Desired parameters may include Direction of Arrival (DoA), Time Difference of Arrival (TDoA), polarization, number of sources, or Doppler shift. For target localization, it is important that DoA is estimated with high accuracy and resolution and that the computational effort is optimized to avoid constraints to the application. To attain this goal, recent research investigates and proposes an extensive number of signal processing techniques with applications including RADAR systems [1, 2], navigation and sonar, among others.

For each aimed application, it is possible to encounter a wide range of adequate algorithms and data models for direction finding, and as a consequence, it becomes impractical to go in detail into all proposed techniques. However, it is safe to affirm that there are major groups into which they are divided. First, less computational effort demanding, are techniques such as amplitude comparison and phase interferometry. The former compares the amplitudes from the outputs of two directional antennas and the latter computes the phase difference between the outputs for DoA estimation. Although requiring low signal processing complexity, the two above mentioned techniques have limited application due to the low estimation accuracy and inability to resolve multiple sources or multipath.

Modern techniques are based on processing the output of one or more narrowband source signals that impinge on multiple sensors. Estimators based on techniques such as beamforming, Maximum Likelihood and MUSIC extract the desired information from the array output and exploit the spatial diversity that arises from the use of multiple array sensors for the DoA estimation of the impinging waves. Each technique has a series of advantages and drawbacks that need to be carefully investigated for each intended application.

This chapter reviews some of the most popular DoA estimation techniques, highlights the advantages, and discusses the most significant drawbacks as well as solutions to overcome specific constraints. It begins by modeling the array output and giving light to the parameters that will define the characteristics of each scenario. Following, the popular Cramér Rao Lower Bound is reviewed as a bound to the variance of unbiased estimators. The CRLB is one of the metrics that are deeply investigated throughout this thesis for direction finding accuracy and resolution. We proceed to investigating limitations imposed when multiple correlated waves are received and discuss wideband direction finding, highlighting the main characteristics that

differ from the estimation of narrowband source signals. Finally, we present some of the most commonly used search procedures for parameter estimation.

2.1. System Model

The starting point for modelling the system is the definition of the antenna array response, also referred to as array manifold, which is sampled over a grid of elevation and azimuth angles defined by ϑ and φ. This thesis uses a full-polarimetric notation that explicitly separates the two orthogonal components, vertical and horizontal, or ϑ and φ, of the antenna radiation pattern, for polarimetric two-dimensional DoA estimation.

To describe the antenna array response to a wavefront impinging from the direction (ϑ_n, φ_n), we define the following complex matrix, denoted by $\boldsymbol{A}_n \in \mathbb{C}^{M \times 2}$, comprised of the polarimetric array steering vectors.

$$\boldsymbol{A}_n := \begin{bmatrix} \boldsymbol{a}_{e_\theta}(\vartheta_n, \varphi_n) & \boldsymbol{a}_{e_\varphi}(\vartheta_n, \varphi_n) \end{bmatrix} \tag{2.1}$$

where $\boldsymbol{a}_p(\vartheta, \varphi) \in \mathbb{C}^{M \times 1}$ for $p = e_\vartheta, e_\varphi$ is the polarimetric array response of an antenna array comprised of M elements. The unitary vectors e_ϑ and e_φ define the direction of the vector of the electrical field and are defined in spherical coordinate system as depicted in Figure 2.1. The direction defined by e_ϑ characterizes vertical polarization, while e_φ characterizes horizontal polarization.

The model assumes far-field radiation, implying that the distance between the sources and the antenna array is larger than the Rayleigh distance $2D^2/\lambda$, where D is the overall size of the array and λ is the free-space wavelength [42]. As a consequence, the radiation impinging on the array is comprised of a set of planar wavefronts. The schematic in Figure 2.2 depicts a scenario where three planar waves impinge on a linear array of antennas from different directions.

To describe the polarization state of each individual impinging wave, we define the Jones vector of each of the N sources as $\boldsymbol{k}_n := \begin{bmatrix} \cos(\beta_n) & \sin(\beta_n)e^{j\phi_n} \end{bmatrix}^{\mathrm{T}} \in \mathbb{C}^{2 \times 1}$, for $n = 1...N$. It maps the arbitrary wave polarization state into each array element output.

The polarization state of an electromagnetic wave is detailed in the next chapter. However, at this point it is important to specify the values of β_n and ϕ_n for linear, circular and elliptical polarizations, as following.
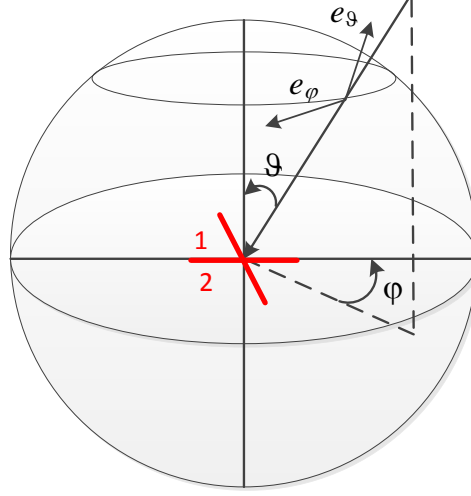
Figure 2.1.: Definition of the 3D spherical coordinate system for the polarization orientation of impinging waves and its projection to dual polar antenna ports (1/2).

$$
\begin{cases}
\phi_n = 0°, & \text{for linear polarization} \\
\beta_n = 45° \quad \text{and} \quad \phi_n = \pm\frac{\pi}{2}, & \text{for circular polarization} \\
\beta_n \neq 45° \quad \text{and} \quad \phi_n = \pm\frac{\pi}{2}, \quad \text{or} \\
\beta_n = 45° \quad \text{and} \quad \phi_n \neq \pm\frac{\pi}{2} & \text{for elliptical polarization}
\end{cases}
\tag{2.2}
$$

The measured output of the array, assuming that L snapshots are observed, can be given by:

$$
\boldsymbol{Y} = \sum_{n=1}^{N} \boldsymbol{A}_n \boldsymbol{k}_n \boldsymbol{s}_n^{\mathrm{T}} + \boldsymbol{N}
\tag{2.3}
$$

In (2.3), $\boldsymbol{Y} \in \mathbb{C}^{M \times L}$ is the array output matrix, $\boldsymbol{N} \in \mathbb{C}^{M \times L}$ is the matrix for the circular zero mean symmetric complex Gaussian noise, and $\boldsymbol{s}_n \in \mathbb{C}^{L \times 1}$ is the vector of the n-th complex source signal. The noise is assumed to be spatially uncorrelated with the source signals. Moreover, the signals are assumed to be narrowband, implying that the corresponding amplitude and phase vary very slowly with time.

Letting $\boldsymbol{n}(t) \in \mathbb{C}^{M \times 1}$ be the noise vector for each snapshot, from (2.3), the model for the
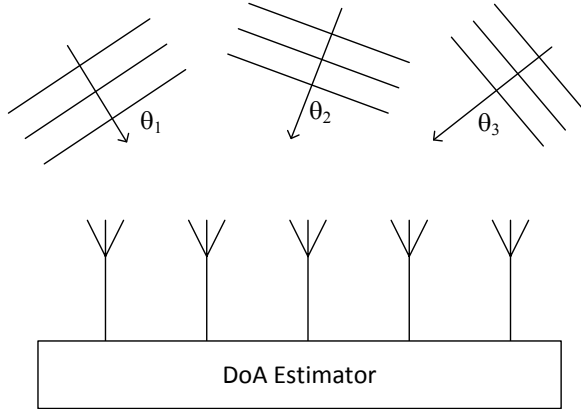
Figure 2.2.: Multiple planar wavefronts impinging on an array of antennas.

t-th snapshot observed can be given by:

$$\boldsymbol{y}(t) = \sum_{n=1}^{N} \boldsymbol{A}_n \boldsymbol{k}_n s_n(t) + \boldsymbol{n}(t) = \boldsymbol{A}\boldsymbol{K}\boldsymbol{s}(t) + \boldsymbol{n}(t) \tag{2.4}$$

where $\boldsymbol{A} = [\boldsymbol{A}_1, ..., \boldsymbol{A}_N]$ comprises the steering matrices of each source wave, $\boldsymbol{K}$ is the block diagonal matrix for the Jones vectors and $\boldsymbol{s}(t) = [s_1(t), ..., s_N(t)]^{\mathrm{T}} \in \mathbb{C}^{N \times 1}$ is the vector of source signals for each snapshot.

Omitting the dependency on the direction (ϑ, φ) for simplicity of notation, the true received data covariance given is then given by:

$$\boldsymbol{R}_{\mathrm{yy}} = \mathbb{E}[\boldsymbol{y}(t)\boldsymbol{y}(t)^H] = (\boldsymbol{A}\boldsymbol{K})^{\mathrm{H}}\boldsymbol{R}_{\mathrm{s}}(\boldsymbol{A}\boldsymbol{K}) + \boldsymbol{R}_{\mathrm{n}} \tag{2.5}$$

where $\boldsymbol{R}_{\mathrm{s}} = \mathbb{E}[\boldsymbol{s}(t)\boldsymbol{s}(t)^H]$ is the signal covariance matrix and $\boldsymbol{R}_{\mathrm{n}} = \mathbb{E}[\boldsymbol{n}(t)\boldsymbol{n}(t)^H] = \boldsymbol{I}\sigma^2$ is the noise covariance matrix. The signal covariance matrix $\boldsymbol{R}_{\mathrm{s}}$ is a positive definite matrix comprised of the correlations between pairs of impinging signals. If all signals are uncorrelated, the signal covariance matrix will be a diagonal matrix. Otherwise, the off-diagonal elements will move the further away from zero the more correlated the pairs of signals become.

At this point, it is important to highlight that in the literature, there are two commonly utilized conditions on the mean and variance of the distribution for the sample data. These conditions are most known as stochastic and deterministic or conditional and unconditional. As pointed out in [28], to name the conditions as stochastic and deterministic may be misleading since the data is anyhow assumed to be stochastic. Hence, it is more adequate to refer

to the assumptions as conditional and unconditional respectively. The Conditional Model Assumption (CMA) assumes that the signals are deterministic functions of time. This implies that the signals are frozen over all observations in time and that the estimation is conditioned on $s_n(t)$. On the other hand, the Unconditional Model Assumption (UMA) assumes that the signals are samples of a stationary stochastic process.

The model assumption have a significant impact on the definition of the Cramér-Rao Lower Bound and on estimation techniques based on the statistical properties of the measured output, such as Maximum Likelihood, since each model introduces some specific statistical properties on the data and will change the behavior of the estimator, as detailed in the next sections. On the other hand, subspace-based estimators, that are not statistically based, are not dependent on unconditional or conditional model assumptions. In this thesis, we model the incoming signals as deterministic variables, and thus, we use the CMA for the computation of the CRLB and Maximum Likelihood DoA estimation.

2.2. Maximum Likelihood

The probability density function (PDF) of the measured output in (2.3), assuming conditional model, can be written as following [11].

$$f(\boldsymbol{Y}) = \frac{1}{(2\pi)^{ML}(\sigma/2)^{ML}}\exp\{\sum_{t=1}^{L}[\,\boldsymbol{y}(t) - \boldsymbol{A}\boldsymbol{K}\boldsymbol{s}(t)\,]^{\mathrm{H}}\boldsymbol{R}_{\mathrm{n}}^{-1}[\,\boldsymbol{y}(t) - \boldsymbol{A}\boldsymbol{K}\boldsymbol{s}(t)\,]\} \tag{2.6}$$

where $\boldsymbol{R}_n = \boldsymbol{I}\sigma^2$.

As a first step for the DoA estimation of the waves, it is necessary to estimate the complex signals, including the corresponding polarization state, and the noise over time. In [11], it was suggested that the minimization of the logarithm of (2.6) with respect to the unknown $\boldsymbol{s}(t)$ and σ could be carried out as an initial step to the final DoA estimation. However, this publication ignored the signal polarization state and assumed a perfect match between signal and antenna polarizations. It was suggested in [43] that, for polarimetric DoA estimation, the polarization state of each impinging wave, characterized by the Jones vector $\boldsymbol{k}_n$, could be estimated in a similar way as suggested in [11]. Using the notation $\boldsymbol{K}\boldsymbol{s} = \boldsymbol{x}$, the estimation of the incoming signals in time, including the corresponding polarization states, and the estimation for the noise covariance are given respectively by:

$$\hat{\boldsymbol{x}}(t) = [\,\boldsymbol{A}^{\mathrm{H}}\boldsymbol{A}\,]^{-1}\boldsymbol{A}^{\mathrm{H}}\boldsymbol{y}(t) \tag{2.7}$$

$$\hat{\sigma} = \frac{1}{ML}\sum_{t=1}^{L}[\,\boldsymbol{y}(t) - \boldsymbol{A}\boldsymbol{x}(t)\,]^{\mathrm{H}}[\,\boldsymbol{y}(t) - \boldsymbol{A}\boldsymbol{x}(t)\,] \tag{2.8}$$

Taking the logarithm of (2.6) and replacing $\hat{\boldsymbol{x}}(t)$ and $\hat{\sigma}$, we get to the cost function for the ML estimator, as a function of the direction matrix defined as $\boldsymbol{\theta} \in \mathbb{C}^{N \times 2}$, comprised of each impinging wave DoA (ϑ_n, φ_n), for $n = 1...N$, when constant terms are ignored:

$$P_{\mathrm{ML}}(\boldsymbol{\theta}) = M\,L\,\mathrm{tr}\Big[(I - \boldsymbol{A}(\boldsymbol{A}^{\mathrm{H}}\boldsymbol{A})^{-1}\boldsymbol{A}^{\mathrm{H}})\hat{\boldsymbol{R}}_{\mathrm{yy}}\Big] \tag{2.9}$$

where $\hat{\boldsymbol{R}}_{\mathrm{yy}}$ denotes the estimated covariance matrix of the measured array output, and, assuming that the source signals and the noise are statistically independent, is given by:

$$\hat{\boldsymbol{R}}_{\mathrm{yy}} = \frac{1}{L}\sum_{t=1}^{L}\boldsymbol{y}(t)\boldsymbol{y}^{H}(t) \tag{2.10}$$

For the estimation of the DoA of the N impinging source waves, the problem is now to find the minimum value of (2.9). For only one impinging wave, the cost function to be minimized is two-dimensional (for every ϑ and φ on the grid for the impinging direction of the source), but for N impinging waves, the optimization needs to be carried out for a $2N$-dimensional cost function. Hence, the level of optimization complexity increases with the number of sources, and prevents from simple visual observation of the effects of the array beam pattern to the shape of the cost function.

2.3. Multiple Signal Classification – MUSIC

Multiple Signal Classification (MUSIC), one of the most popular subspace-based direction finding techniques, was first introduced in [15], and explores the eigen-structure of the output covariance matrix, $\boldsymbol{R}_{\mathrm{yy}}$. It is proposed that the eigenvalue decomposition of $\boldsymbol{R}_{\mathrm{yy}}$ is divided into a signal subspace $\boldsymbol{Q}_{\mathrm{S}} \in \mathbb{C}^{M \times N}$ and a noise subspace $\boldsymbol{Q}_{\mathrm{NN}} \in \mathbb{C}^{M \times (M-N)}$, as following.

$$\boldsymbol{R}_{\mathrm{yy}} = \boldsymbol{Q}_{\mathrm{S}}\boldsymbol{\Upsilon}\boldsymbol{Q}_{\mathrm{S}}^{H} + \boldsymbol{Q}_{\mathrm{NN}}(\sigma^2\boldsymbol{I})\boldsymbol{Q}_{\mathrm{NN}}^{H}. \tag{2.11}$$

where $\boldsymbol{\Upsilon}$ is a diagonal matrix comprising the signal eigenvalues, and $\sigma^2\boldsymbol{I}$ is a diagonal matrix comprising the noise eigenvalues. The partitioned eigenvalue decomposition then leads to the signal eigenvectors matrix $\boldsymbol{Q}_{\mathrm{S}}$ with the number of columns being equal to the number of signal

eigenvalues (N) and the noise eigenvectors matrix $\boldsymbol{Q}_{\mathrm{NN}}$ with ($M - N$) columns, the number of noise eigenvalues (the $M - N$ smallest eigenvalues). Note that it is assumed that the number of elements in the array is higher than the number of impinging sources. If this assumption is not fulfilled, it is said that the noise subspace is rank deficient. Although there are some publications such as [23, 44] that consider DoA estimation under rank deficiency, for the sake of simplicity, we assume that $M > N$.

At this point it is important to draw the reader's attention to the fact that the division of the eigenvalue decomposition of the correlation matrix relies on the assumption that the number of impinging sources N is known a priori. Otherwise, it would not be possible to get to the signal and the noise subspace before estimating N. In this work, we consider N as a known parameter and thus, the estimation of number of sources is not carried out.

Since $\boldsymbol{Q}_{\mathrm{S}}$ and $\boldsymbol{Q}_{\mathrm{NN}}$ are orthogonal subspaces, it is true that, for each impinging wave, $\boldsymbol{A}_n \boldsymbol{k}_n$ is also orthogonal to $\boldsymbol{Q}_{\mathrm{NN}}$. And this is the basis for MUSIC. The MUSIC cost function of ϑ and φ, normalized by the Frobenius norm $\| \boldsymbol{A}^{\mathrm{H}} \boldsymbol{A} \|_{\mathrm{F}}^2$, is then given by [45, 46]:

$$P_{\mathrm{MUSIC}}(\vartheta, \varphi) = \frac{\| \boldsymbol{A}^{\mathrm{H}}(\vartheta, \varphi) \boldsymbol{A}(\vartheta, \varphi) \|_{\mathrm{F}}^2}{\boldsymbol{k}^{\mathrm{H}} \boldsymbol{A}^{\mathrm{H}}(\vartheta, \varphi) \boldsymbol{Q}_{\mathrm{NN}} \boldsymbol{Q}_{\mathrm{NN}}^{\mathrm{H}} \boldsymbol{A}(\vartheta, \varphi) \boldsymbol{k}} \tag{2.12}$$

Since we are using a polarimetric system model that includes the polarization state of the impinging wave, the expression for the MUSIC spectrum will also include the signal polarization characterized by the Jones vector. However, this implies that, in (2.12), either the polarization states of the waves are known a priori, and the search in the spectrum is carried out only for the DoA ϑ and φ, or that the search in the spectrum is also carried out with respect to polarization. Although the first assumption is unrealistic, if we are not interested in estimating the polarization of the incoming waves, a solution to take the polarization out from the MUSIC spectrum is to recall the fact that since $\boldsymbol{A}_n \boldsymbol{k}_n$ is orthogonal to the noise subspace $\boldsymbol{Q}_{\mathrm{NN}}$, it follows that, in order to minimize $\boldsymbol{k}^{\mathrm{H}} \boldsymbol{A}^{\mathrm{H}} \boldsymbol{Q}_{\mathrm{NN}} \boldsymbol{Q}_{\mathrm{NN}}^{\mathrm{H}} \boldsymbol{A} \boldsymbol{k}$, it is enough to minimize the determinant $\det(\boldsymbol{A}^{\mathrm{H}} \boldsymbol{Q}_{\mathrm{NN}} \boldsymbol{Q}_{\mathrm{NN}}^{\mathrm{H}} \boldsymbol{A})$ [47, 48]. The adapted MUSIC spectrum becomes:

$$P_{\mathrm{MUSIC}}(\vartheta, \varphi) = \frac{\| \boldsymbol{A}^{\mathrm{H}}(\vartheta, \varphi) \boldsymbol{A}(\vartheta, \varphi) \|_{\mathrm{F}}^2}{\det(\boldsymbol{A}^{\mathrm{H}}(\vartheta, \varphi) \boldsymbol{Q}_{\mathrm{NN}} \boldsymbol{Q}_{\mathrm{NN}}^{\mathrm{H}} \boldsymbol{A}(\vartheta, \varphi))} \tag{2.13}$$

For the estimation of the DoA of the N impinging source waves, the problem is now to find the N maximum values of (2.13). MUSIC has become a popular technique in the recent years due to the low complexity and high performance. On the other hand, there are some

disadvantages such as with respect to the coherency of sources. Although there are some MUSIC techniques adapted for coherent sources [21, 22, 23], it is still most commonly utilized in uncoherent multisource scenarios.

2.4. Cramér-Rao Lower Bound

The goal of estimators based on the processing of incoming signals is to find a set of desired parameters, which we denote hereafter as $\boldsymbol{\theta}$, from the received data $\boldsymbol{y}(t)$, modeled as detailed in the last section. From the details presented, assuming $\boldsymbol{y}_{\mathrm{L}} = \left[y^T(1), \ldots y^T(L) \right]^T$ to be the vector of all observations of the received data over time, it is easy to observe that $\boldsymbol{y}(t)$ is characterized by the following stochastic distribution.

$$\boldsymbol{y}_{\mathrm{L}} \sim \mathcal{G}(\boldsymbol{m}(\boldsymbol{\theta}), \boldsymbol{\Gamma}(\boldsymbol{\theta})) \tag{2.14}$$

where $\mathcal{G}$ denotes the Gaussian distribution with mean $\boldsymbol{m}(\boldsymbol{\theta})$ and covariance matrix $\boldsymbol{\Gamma}(\boldsymbol{\theta})$. The set of parameters to be estimated, $\boldsymbol{\theta}$, may include DoA, TDoA, polarization, and Doppler frequency, among others. However, it may be the case that the set of parameters to be estimated is only a part from the total set of parameters that characterizes the received data. Hence, the total parameter set may be comprised not only of $\boldsymbol{\theta}$ but also of nuisance parameters that are not required to be estimated.

For unbiased parameter estimators, the CRLB establishes a lower bound on its variance, equipping us with a metric for the estimation accuracy. We may write the covariance matrix of the estimator with respect to the vector of parameters $\boldsymbol{\theta}$ as:

$$\boldsymbol{R}_{\theta\theta} = \mathrm{E}\left[(\hat{\boldsymbol{\theta}} - \boldsymbol{\theta})(\hat{\boldsymbol{\theta}} - \boldsymbol{\theta})^T \right] \tag{2.15}$$

where $\hat{\boldsymbol{\theta}}$ denotes the vector of estimated parameters. Hence, we can affirm, by definition, that the CRLB is always lower than the estimator covariance matrix $\boldsymbol{R}_{\theta\theta}$:

$$CRLB \leq \boldsymbol{R}_{\theta\theta} \tag{2.16}$$

However, it is important to highlight the fact that in order to achieve the CRLB, it is necessary that the data model detailed in the last section is reliable, implying accurate characterization. The CRLB will not reveal estimation errors that result from incomplete or mismatched data models or errors due to imprecise calibration (see [30] for an extensive discussion). Nev-

ertheless, if the object of study is the optimization of antenna arrays for DoA estimation, it is important to establish a metric that quantifies how well the array can perform in terms of direction finding accuracy. The general formula for the CRLB with respect to the parameter set $\boldsymbol{\theta}$ can be given by [28]:

$$
\begin{aligned}
(\text{CRLB})_{ij}^{-1} &= \text{tr}[\boldsymbol{\Gamma}^{-1}(\boldsymbol{\theta}) \frac{\partial \boldsymbol{\Gamma}(\boldsymbol{\theta})}{\partial \theta_i} \boldsymbol{\Gamma}^{-1}(\boldsymbol{\theta}) \frac{\partial \boldsymbol{\Gamma}(\boldsymbol{\theta})}{\partial \theta_j}] + \\
&\quad + 2\Re\mathfrak{e} \frac{\partial \boldsymbol{m}^{\text{H}}(\boldsymbol{\theta})}{\partial \theta_i} \boldsymbol{\Gamma}^{-1}(\boldsymbol{\theta}) \frac{\partial \boldsymbol{m}(\boldsymbol{\theta})}{\partial \theta_j}
\end{aligned}
\tag{2.17}
$$

where θ_i and θ_j denotes two of the parameters from the parameters vector $\boldsymbol{\theta}$.

Under conditional model assumption, the source signals are modeled as deterministic variables, i. e., frozen over all observations in time, and thus, the data vector received at the t-snapshot can be written as:

$$
\boldsymbol{y}_{\text{L}} \sim \mathcal{G}\left(\left[\boldsymbol{\mu}^T(1), \dots \boldsymbol{\mu}^T(L)\right]^T, \sigma^2 \boldsymbol{I}\right)
\tag{2.18}
$$

This implies that the covariance matrix and the mean of the distribution in Equation (2.17) are given respectively by $\boldsymbol{\Gamma}(\boldsymbol{\theta}) = \sigma^2 \boldsymbol{I}$ and $\boldsymbol{m}(\boldsymbol{\theta}) = \left[\boldsymbol{\mu}^T(1), \dots \boldsymbol{\mu}^T(L)\right]^T$, where $\boldsymbol{\mu}(t) = \boldsymbol{B}\boldsymbol{s}(t)$. Replacing $\boldsymbol{\Gamma}(\boldsymbol{\theta})$ and $\boldsymbol{m}(\boldsymbol{\theta})$ in (2.17), we get the simplified expression for the conditional CRLB:

$$
\text{CRLB} = 0.5\sigma^2 \Re\mathfrak{e}^{-1}[\boldsymbol{D}^H \boldsymbol{D}]
\tag{2.19}
$$

The matrix $\boldsymbol{D}$ comprises the derivatives of the received signal $\boldsymbol{y}$ with respect to the vector of parameters $\boldsymbol{\theta}$. For 2D DoA estimation, the parameters to be estimated are $\boldsymbol{\theta} = \begin{bmatrix} \boldsymbol{\vartheta} & \boldsymbol{\varphi} \end{bmatrix}$, in which $\boldsymbol{\vartheta} = \begin{bmatrix} \vartheta_1, \dots, \vartheta_N \end{bmatrix}$ and $\boldsymbol{\varphi} = \begin{bmatrix} \varphi_1, \dots, \varphi_N \end{bmatrix}$ are the DoAs of the impinging signals. However, other parameters may influence the direction finding process and shall be taken into account for the computation of the CRLB. Hence, we may split the vector of parameters for estimation into wanted and unwanted parameters.

The wanted parameters are the parameters that both influence the direction finding and are to be estimated. On the other hand, the unwanted parameters, although influencing the characteristics of the received data and thus the estimation itself, are assumed to be only nuisance parameters. As a consequence, the vector of parameters $\boldsymbol{\theta}$ may be written as $\boldsymbol{\theta} = \begin{bmatrix} \boldsymbol{\theta}_w^{\text{T}} & \boldsymbol{\theta}_u^{\text{T}} \end{bmatrix}^{\text{T}}$, in which $\boldsymbol{\theta}_w$ is the vector of wanted parameters, hitherto denoted by $\boldsymbol{\theta}$ and $\boldsymbol{\theta}_u$ is the vector of nuisance parameters. The derivatives matrix $\boldsymbol{D}$ can be written as

$\boldsymbol{D} = \begin{bmatrix} \boldsymbol{D}_w & \boldsymbol{D}_u \end{bmatrix}$, in which $\boldsymbol{D}_w$ is the matrix comprising the derivatives of the array output with respect to the wanted parameters and $\boldsymbol{D}_u$ the matrix of derivatives with respect to the unwanted parameters.

The polarimetric CRLB, in which the signal polarization affects the direction finding but is not to be estimated, can be computed using (2.19). The vector of wanted and unwanted parameters are denoted respectively by $\boldsymbol{\theta}_w = \begin{bmatrix} \boldsymbol{\vartheta}^{\mathrm{T}} & \boldsymbol{\varphi}^{\mathrm{T}} \end{bmatrix}^{\mathrm{T}}$ and $\boldsymbol{\theta}_u = \begin{bmatrix} \mathfrak{Re}^{T}(\mathrm{vec}(\boldsymbol{S})) & \mathfrak{Im}^{\mathrm{T}}(\mathrm{vec}(\boldsymbol{S})) \end{bmatrix}^{\mathrm{T}}$ [29]. Defining the following derivatives:

$$\boldsymbol{A}^{\vartheta} := \frac{\partial \boldsymbol{A}}{\partial \boldsymbol{\vartheta}^{\mathrm{T}}} = \begin{bmatrix} \dfrac{\partial \boldsymbol{A}}{\partial \vartheta_1} & \cdots & \dfrac{\partial \boldsymbol{A}}{\partial \vartheta_N} \end{bmatrix} \tag{2.20}$$

$$\boldsymbol{A}^{\varphi} := \frac{\partial \boldsymbol{A}}{\partial \boldsymbol{\varphi}^{\mathrm{T}}} = \begin{bmatrix} \dfrac{\partial \boldsymbol{A}}{\partial \varphi_1} & \cdots & \dfrac{\partial \boldsymbol{A}}{\partial \varphi_N} \end{bmatrix} \tag{2.21}$$

The expression for the derivatives matrices $\boldsymbol{D}_w$ and $\boldsymbol{D}_u$ is then given by:

$$\boldsymbol{D}_w = \frac{\partial \boldsymbol{Y}}{\partial \boldsymbol{\theta}_w} = \begin{bmatrix} \boldsymbol{S}^{\mathrm{T}} \diamond (\boldsymbol{A}^{\vartheta} \boldsymbol{K}) & \boldsymbol{S}^{\mathrm{T}} \diamond (\boldsymbol{A}^{\varphi} \boldsymbol{K}) \end{bmatrix} \tag{2.22}$$

$$\boldsymbol{D}_u = \frac{\partial \boldsymbol{Y}}{\partial \boldsymbol{\theta}_u} = \begin{bmatrix} \boldsymbol{I}_L & j\boldsymbol{I}_L \end{bmatrix} \otimes \boldsymbol{A} \tag{2.23}$$

in which $\otimes$ denotes the Kronecker product between two matrices and $\diamond$ denotes the Khatri-Rao product. Note that $\boldsymbol{\vartheta}$ denotes the vector comprising the N values of ϑ to be estimated, corresponding to the N impinging planar source waves and $\boldsymbol{\varphi}$, the vector of φ. The matrix $\boldsymbol{S}$ is the matrix of source signals for the L snapshots and the N sources.

To alleviate the computational effort introduced by the inverse of $\mathfrak{Re}[\boldsymbol{D}^H \boldsymbol{D}]$ in (2.19) when both wanted and unwanted parameters are taken into account, a reduced version of the CRLB may be used as in [28, 46] for 1D DoA estimation. The results for the reduced CRLB were extended in [49] to 2D estimation. The solution for the CRLB is decomposed into blocks and only the block consisting of $\boldsymbol{D}_w^H \boldsymbol{D}_w$, the derivatives with respect to the wanted parameters (ϑ, φ) is considered for matrix inversion. The full CRLB can be written as:

$$CRLB = \frac{\sigma^2}{2} \mathfrak{Re}^{-1} \begin{bmatrix} \boldsymbol{D}_u^H \boldsymbol{D}_u & \boldsymbol{D}_u^H \boldsymbol{D}_w \\ \boldsymbol{D}_w^H \boldsymbol{D}_u & \boldsymbol{D}_w^H \boldsymbol{D}_w \end{bmatrix} \tag{2.24}$$

Since we are only interested in the block $\boldsymbol{D}_w^H \boldsymbol{D}_w$, there is no need to carry out with the

inversion of the full matrix comprising all the wanted and unwanted derivatives. The solution for the reduced CRLB is the written as following.

$$\text{CRLB} = \frac{\sigma^2}{2L} \mathfrak{Re}^{-1}[\boldsymbol{H} \odot \boldsymbol{R}_{\text{s}}^{\text{T}}] \tag{2.25}$$

where $\odot$ denotes the Hadamard matrix product and:

$$\boldsymbol{H} = \boldsymbol{D}_{\vartheta,\varphi}^{H}[\boldsymbol{I} - \boldsymbol{A}\boldsymbol{K}(\boldsymbol{K}^{\text{H}}\boldsymbol{A}^{\text{H}}\boldsymbol{A}\boldsymbol{K})^{-1}\boldsymbol{K}^{\text{H}}\boldsymbol{A}^{\text{H}}]\boldsymbol{D}_{\vartheta,\varphi} \tag{2.26}$$

$$\boldsymbol{D}_{\vartheta,\varphi} = \begin{bmatrix} \boldsymbol{A}^{\vartheta}\boldsymbol{K} & \boldsymbol{A}^{\varphi}\boldsymbol{K} \end{bmatrix} \tag{2.27}$$

Figure 2.3 depicts an example surface plot of the CRLB for the estimation of elevation (ϑ) when a five-element dual-polarized L-Quad array, detailed in Chapter 3 and depicted in Figure 3.11, is used for the reception of incoming signals. It is possible to note that the CRLB gets higher at the azimuths (φ) corresponding to the direction of the dipoles in the L-Quad array, since the dipole is not capable of capturing waves coming from the same direction as its alignment. The five peaks observed in the surface plot as corresponding to the five elements in the array.

Although in this thesis we do not investigate the Unconditional Model Assumption, some overview follows, with the aim of showing the differences on the system model and how it affects the expression for the CRLB. Under UMA, the data vector received at the t-snapshot can be written as:

$$\boldsymbol{y}_{\text{L}} \sim \mathcal{G}(\boldsymbol{0}, \boldsymbol{R}_{\text{yy}}) \tag{2.28}$$

This implies that the mean and the covariance matrix of the distribution are given respectively by $\boldsymbol{\Gamma}(\boldsymbol{\theta}) = \boldsymbol{R}_{\text{yy}}$ and $\boldsymbol{m}(\boldsymbol{\theta}) = \boldsymbol{0}$. The expression for the CRLB, replacing $\Gamma(\boldsymbol{\theta})$ and $m(\boldsymbol{\theta})$ in (2.17) can be written as:

$$(\text{CRLB})_{ij}^{-1} = L \quad \text{tr}[\boldsymbol{R}_{\text{yy}}^{-1}(\boldsymbol{\theta})\frac{\boldsymbol{R}_{\text{yy}}(\boldsymbol{\theta})}{\partial\theta_i}\boldsymbol{R}_{\text{yy}}^{-1}(\boldsymbol{\theta})\frac{\boldsymbol{R}_{\text{yy}}(\boldsymbol{\theta})}{\partial\theta_j}] \tag{2.29}$$

Until beginning of the 90's, there was no expression available in the literature for the CRLB when signals were modeled as stochastics variables. Although some expressions were already derived, they were only valid for some special cases [50, 51]. Stoica [28] was the first to
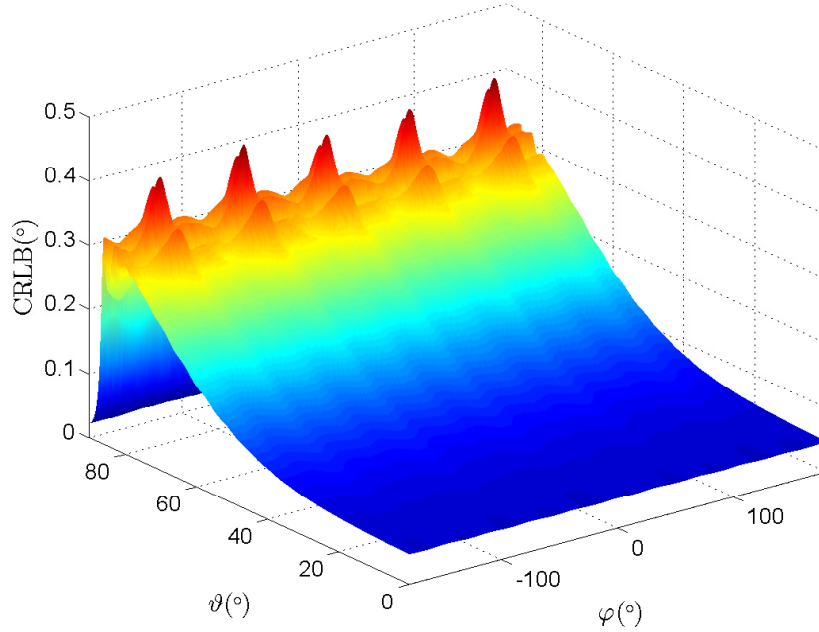
Figure 2.3.: CRLB for the estimation of ϑ when a five-element L-Quad array as in Figure 3.11 is used for reception.

explicitly derive a general formula for the unconditional CRLB.

2.5. Cramér-Rao Lower Bound as a Figure of Merit

Analysis and optimization of antenna arrays for direction finding demand an adequate figure of merit, which is capable of characterizing the corresponding capabilities for direction finding, given a set of antenna array parameters. Although the CRLB has proven to be a powerful metric that relates the direction finding accuracy of an antenna array to its far field radiation patterns, it is DoA dependent, and as presented in the last section, does not serve as a practical figure of merit for analysis and optimization.

A straightforward solution is to compute the mean CRLB for the estimation of both ϑ and φ over some specific grid in the sphere. However, appropriate weights need to be considered for the average. To this end, we compute the weights for averaging the CRLB based on the ratio of the area spanned by the CRLB for the estimation of ϑ and φ and the total area of the sphere. Let us start by defining the area of a section in a sphere spanned by the interval $[\,\vartheta_n - \Delta\vartheta,\, \vartheta_n + \Delta\vartheta\,]$ and $[\,\varphi_n - \Delta\varphi,\, \varphi_n + \Delta\varphi\,]$ is given by:

$$\text{Area}_n = \int_{\varphi_n - \Delta\varphi}^{\varphi_n + \Delta\varphi} cos\vartheta \Delta\varphi d\vartheta$$

$$= 2\Delta\varphi cos\vartheta_n \sin(\frac{\Delta\vartheta}{2})$$

(2.30)

Let $\sigma_{\text{CRLB},\vartheta}$ and $\sigma_{\text{CRLB},\varphi}$ refer to the CRLB for the estimation of ϑ and φ respectively. The area spanned by the CRLB can then be computed by replacing $\Delta\vartheta$ by $\sigma_{\text{CRLB},\vartheta}$ and $\Delta\varphi$ by $\sigma_{\text{CRLB},\varphi}$. In fact, the area spanned by $\sigma_{\text{CRLB},\vartheta}$ and $\sigma_{\text{CRLB},\varphi}$ may be useful when a single figure of merit is required for optimization, since it provides a measure of direction finding capability for both the estimation of ϑ and φ. It can be expressed as:

$$\text{Area}_{\text{CRLB}}(\vartheta, \varphi) = \sigma_\varphi(\vartheta, \varphi) \cos\vartheta \sin\sigma_\vartheta(\vartheta, \varphi)$$

(2.31)

The total area of the sphere can be computed from the contributions of each section area defined in (2.30) and is written as:

$$\text{Area} = \sum_{n=1}^{N_\varphi} \sum_{m=1}^{N_\vartheta} \text{Area}_n = 2N_\varphi \Delta\varphi \sin(\frac{\Delta\vartheta}{2}) \sum_{m=1}^{N_\vartheta} \cos\vartheta_m$$

(2.32)

where N_ϑ and N_φ denotes the number of sections over the sphere, that equals the number of points in the grid for ϑ and φ respectively. The weights denoted by w are then defined as the ratio of the area spanned and the total area of the sphere as following.

$$w(\vartheta) = \frac{\text{Area}_n}{\text{Area}} = \frac{\cos\vartheta}{N_\varphi \sum_{m=1}^{N_\vartheta} \cos\vartheta_m}$$

(2.33)

Finally, the weighted mean CRLB for the estimation of ϑ and φ, denoted by $\bar{\sigma}_{\text{CRLB},\vartheta}$ and $\bar{\sigma}_{\text{CRLB},\varphi}$ respectively, over a grid with $N_\vartheta \times N_\varphi$ points can be written as:

$$\bar{\sigma}_{\text{CRLB},\vartheta} = \sum_{n=1}^{N_\varphi} \sum_{m=1}^{N_\vartheta} w(\vartheta)\sigma_{\text{CRLB},\vartheta}(\vartheta_n, \varphi_n)$$

$$\bar{\sigma}_{\text{CRLB},\varphi} = \sum_{n=1}^{N_\varphi} \sum_{m=1}^{N_\vartheta} w(\vartheta)\sigma_{\text{CRLB},\varphi}(\vartheta_n, \varphi_n)$$

(2.34)

It is possible to observe that the CRLB for the estimation of φ gets abnormally high close to the pole. This is due to the fact that, at the pole, the azimuth is not properly defined, since all azimuths are corresponding to the same point in the solid sphere. To tackle this issue, it is possible to define a CRLB for the azimuth arc that is defined as [48]:

$$\mathrm{CRLB}_{\mathrm{arc}\varphi} = \mathrm{CRLB}_{\varphi} \left| \cos\vartheta \right| \tag{2.35}$$

2.6. Effective Aperture Distribution Function

For the computation of the derivatives of the array manifold with respect to ϑ and φ, $\partial \boldsymbol{A}/\partial\vartheta$ and $\partial \boldsymbol{A}/\partial\varphi$ as in (2.20), the Effective Aperture Distribution Function (EADF) detailed in [52, 53, 54] is a powerful tool, which allows both for the computation of the derivatives and for the interpolation of the array manifold. However, it is necessary that the sampling frequency of the original array response over φ and ϑ fulfills the Nyquist sampling condition in order to avoid non-neglecting aliasing errors.

In [54], details were presented for the interpolation and the derivatives computation of the array manifold, neglecting mutual coupling between neighboring elements, and assuming a 1D isotropic array response. Analogous procedure may be carried out for the 2D array response, in case of 2D DoA estimation. Moreover, the details presented did not consider the full-polarimetric characterization of the array manifold. However, the interpolation and computation of the derivatives of an array response orthogonal components (for spherical coordinates, $\boldsymbol{a}_{e_\theta}$ and $\boldsymbol{a}_{e_\varphi}$) may be identically carried out as presented for the total array response. Note only that each polarimetric component requires a separate EADF.

Landmann [53] described the procedure named EADF for the interpolation and derivatives computation, taking into account a real antenna array with radiation patterns measured in an anechoic chamber, although the same procedure can be carried out when the array response is sampled by simulation with full-wave electromagnetic tools such as Ansoft HFSS [39]. The measured (or simulated) response of each antenna array element is denoted by the matrix $\boldsymbol{A}_m \in \mathcal{C}^{Q_\vartheta \times Q_\varphi}$ comprised of the measurement (simulation) samples over Q_ϑ points in elevation and Q_φ in azimuth for the M array elements.

A discrete Fourier transform is then carried out over the Q_ϑ points in elevation and Q_φ in azimuth for each antenna element. It is important to note that the array response measured must be 2π-periodic with respect to both elevation and azimuth in order to avoid errors from the Fourier transform. Although measurements carried out for azimuth in $[\,0, 2\pi)$ and elevation in $[\,0, \pi]$ are enough to describe the spherical radiation pattern, they are not enough to ensure the required periodicity. A redundant extension is required by using an elevation and azimuth transformation matrix, denoted by $\boldsymbol{F}_\vartheta \in \mathcal{C}^{Q_\vartheta \times Q_\vartheta}$ and $\boldsymbol{F}_\varphi \in \mathcal{C}^{Q_\varphi \times Q_\varphi}$ respectively, defined as following.

$$\boldsymbol{F}_\vartheta = e^{-j2\pi\boldsymbol{\mu}_\vartheta\boldsymbol{\mu}_\vartheta^{\mathrm{T}}/Q_\vartheta} \tag{2.36}$$

where $\boldsymbol{\mu}_\vartheta^{\mathrm{T}} = \left[-Q_\vartheta/2 \ldots Q_\vartheta/2 - 1\right]$.

$$\boldsymbol{F}_\varphi = e^{-j2\pi\boldsymbol{\mu}_\varphi\boldsymbol{\mu}_\varphi^{\mathrm{T}}/Q_\varphi} \tag{2.37}$$

where $\boldsymbol{\mu}_\varphi^{\mathrm{T}} = \left[-Q_\varphi/2 \ldots Q_\varphi/2 - 1\right]$. The EADF of the m-th antenna element can then be written as:

$$\boldsymbol{G}_m = \frac{1}{\sqrt{Q}}\boldsymbol{F}_\vartheta \boldsymbol{A}_m \boldsymbol{F}_\varphi \tag{2.38}$$

where $Q = Q_\vartheta Q_\varphi$. The interpolated beam pattern of each antenna element, for every direction (ϑ, φ) is then given as following, assuming that a new grid comprised of $Q_{\mathrm{A}} = Q_{\mathrm{A}\vartheta}Q_{\mathrm{A}\varphi}$ points is chosen for adequate interpolation.

$$
\begin{aligned}
\boldsymbol{b}_m^{\mathrm{EADF}}(\vartheta, \varphi) &= \frac{1}{\sqrt{Q_{\mathrm{A}}}}\boldsymbol{d}_\vartheta(\vartheta)\boldsymbol{G}_m\boldsymbol{d}_\varphi(\varphi) \\
\frac{\partial}{\partial\vartheta}\boldsymbol{b}_m^{\mathrm{EADF}}(\vartheta, \varphi) &= \frac{1}{\sqrt{Q_{\mathrm{A}}}}j\boldsymbol{d}_\vartheta(\vartheta)\mathrm{diag}(\mu_{\mathrm{A}\vartheta}^{\mathrm{T}})\boldsymbol{G}_m\boldsymbol{d}_\varphi(\varphi) \\
\frac{\partial}{\partial\varphi}\boldsymbol{b}_m^{\mathrm{EADF}}(\vartheta, \varphi) &= \frac{1}{\sqrt{Q_{\mathrm{A}}}}j\boldsymbol{d}_\vartheta(\vartheta)\boldsymbol{G}_m\mathrm{diag}(\mu_{\mathrm{A}\varphi}^{\mathrm{T}})\boldsymbol{d}_\varphi(\varphi)
\end{aligned} \tag{2.39}
$$

where:

$$
\begin{aligned}
\boldsymbol{d}_\vartheta(\vartheta) &= e^{j\mu_{\mathrm{A}\vartheta}^{\mathrm{T}}\vartheta} \\
\boldsymbol{d}_\varphi(\varphi) &= e^{j\mu_{\mathrm{A}\varphi}\varphi} \\
\mu_{\mathrm{A}\vartheta}^{\mathrm{T}} &= \left[-(Q_{\mathrm{A}\vartheta} - 1)/2 \ldots (Q_\vartheta - 1)/2\right] \\
\mu_{\mathrm{A}\varphi}^{\mathrm{T}} &= \left[-(Q_{\mathrm{A}\varphi} - 1)/2 \ldots (Q_\varphi - 1)/2\right]
\end{aligned} \tag{2.40}
$$

2.7. Correlated and Coherent Signals

Traditional high-resolution array-based DoA estimation is only capable of resolving a certain number of impinging specular waves, which depends on the number of antenna elements. This capability to estimate multiple waves depends on whether the waves are partially correlated or coherent (perfect correlation). In scattering environments, where the received signals have

strong influence of multipath components, or in military scenarios attacked by smart jammers, the signals impinging on the antenna array may be highly correlated, giving rise to degraded direction finding performance [55]. The case where the signals are 100% correlated is also referred to as coherent case and occurs e.g. when the phase difference between two signals does not vary over time. If some of the signals that impinge on the array of sensors are correlated or coherent to each other, two arising issues need to be taken into account for precise DoA estimation:

1. the rank of the estimated covariance matrix of the measured output will be reduced and

2. the estimated output covariance matrix may be singular

For dense multipath scenarios, when signals arrive from the same source through different paths, delayed multipath copies from the same source appear to be correlated as long as the multipath excess delay is lower than the inverse of the coherence bandwidth. Moreover, different sources may emit signals that are correlated, what significantly degrades the direction finding performance, especially for subspace-based estimators. The MUSIC technique, for example, relies on the full-rank of the output covariance matrix to determine the signal subspace. Hence, if the rank is reduced, the desired impinging directions may not be accurately estimated. The distinction between coherent and non-coherent components has major impact on the estimation procedure and asymptotic performance of the estimator, as some kind of statistical averaging for correlation estimation may be additionally involved.

Techniques based on averaging measured ouputs from the antenna array have been reported for more than thirty years. The averaging is usually based on some scheme that may involve mechanical antenna array positioning [56] or Doppler smoothing when there is sufficient relative motion between sources [57]. To avoid mechanical rotation of the receiving antenna or the requirement of relative movement between sources, an averaging scheme based on spatial smoothing was introduced by Evans [19, 58], further investigated by Shan [59] for uniform linear arrays and subsequently extended to uniform circular arrays by Wax [60]. Pillai [55] contributed to the research on spatial smoothing techniques by proposing a forward/backward scheme for the averaging of measured outputs from linear arrays as depicted in Figure 2.4. Note that not only subarrays in the forward direction, but also subarrays in the backward direction, were considered for the averaging.

The spatial smoothing techniques consist in decorrelating the signals by averaging the outputs from spatially separated subarrays and have been exhaustively investigated and used to avoid degrading performance if correlated or coherent sources arrive at the receiver. They are based on gathering subarrays from the total number of sensors, as illustrated in Figure 2.4
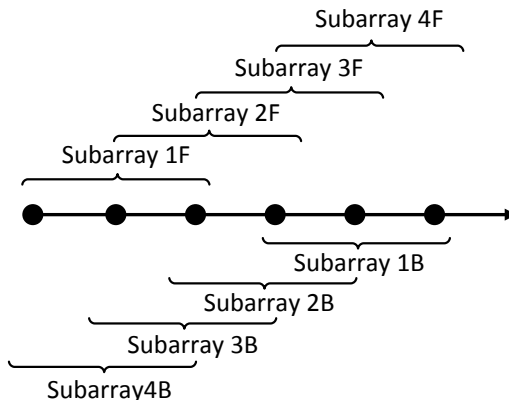
Figure 2.4.: Subarray geometry for 1D spatial smoothing in linear arrays.

for the linear array, and averaging the output covariance matrix estimated for each of the subarrays.

Although efficient to decorrelate the signals, two are the most limiting drawbacks of smoothing techniques. First, the array aperture is reduced, since the subarray only comprises a set of sensors from the complete antenna array, leading to degraded estimation accuracy and resolution. Moreover, the number of radiating elements that is necessary to resolve the multiple incoming waves may significantly increase. At this point, we remind the reader that subspace-based techniques rely on full-rank condition that allows for decomposition into signal and noise subspace. Hence, the number of signals is assumed to be lower than the number of receiving sensors. When dividing the full array into subarrays, the number of sensors in the subarray will be only a fraction from the total number of elements, which limits the number of signals that can be resolved by traditional subspace-based estimators.

2.8. Direction Finding Resolution of Multiple Signals

The CRLB has been proven to be a powerful tool for the evaluation of antenna arrays with respect to direction finding based on unbiased estimators. It allows us to draw conclusions on the bound for the DoA estimation accuracy, depending on the radiation characteristics of the antenna array, and as a consequence, equip the user with comparative results that allow for efficient design decisions. Although the CRLB measures the accuracy of DoA estimation when a single wave impinges on the antenna array, it is still possible to compute the CRLB of a main source signal conditioned to the existence of secondary sources or paths [29]. The CRLB

can then tell the user how accurate the DoA estimation of a first signal is in the vicinity of a second signal and may be used as a means of measuring the capability to resolve two or more impinging waves.

Algorithm 1 details the procedure to compute the DoA estimation resolution bound based on the CRLB in a two-path scenario.

Algorithm 1 Computation of resolution in the ϑ direction

1: Input:

       ϑ_2: true secondary path elevation of arrival

       CRLB_ϑ: main path CRLB for the estimation of ϑ

       δ: sets the range in elevation for the computation of resolution

2: $\vartheta_1 \leftarrow \vartheta_2 - \delta$

3: *loop*:

4: **for** $\vartheta_1 < \vartheta_2$ **do**

5:     **if** $\max(\text{CRLB}_\vartheta, |\vartheta_1 - \vartheta_2|) = \text{CRLB}_\vartheta$ **then**

6:        $\text{res}_{\inf,\vartheta} = \text{CRLB}_\vartheta$

7: $\vartheta_1 \leftarrow \vartheta_2$

8: *loop*:

9: **for** $\vartheta_1 < \vartheta_2 + \delta$ **do**

10:     **if** $\max(\text{CRLB}_\vartheta, |\vartheta_1 - \vartheta_2|) = |\vartheta_1 - \vartheta_2|$ **then**

11:        $\text{res}_{\sup,\vartheta} = \text{CRLB}_\vartheta$

12: $\text{res}_\vartheta = 0.5 \times (\text{res}_{\sup,\vartheta} + \text{res}_{\inf,\vartheta})$

For the computation of the resolution in ϑ, for two impinging waves, the idea is to compare the CRLB for the main path, at some ϑ_1 in the grid, to the difference between this test ϑ_1 and the true elevation of arrival of the secondary path. If the CRLB of the main path at some specific elevation angle is greater than the difference between this elevation angle and the secondary path elevation of arrival, the direction finder is not capable of estimating the elevation angle. This implies that if we set a test range in elevation angle $\vartheta_2 - \delta < \vartheta_1 < \vartheta_2$, and start comparing the CRLB to the absloute value of the difference $\vartheta_1 - \vartheta_2$, we will stop at the point where the CRLB is the smallest of the two values. From this test, we obtain what we define as inferior resolution, implying that it is the resolution we obtain if performing the comparison test for elevation angles smaller than the true secondary elevation of arrival. Analogous procedure is carried out for the computation of the superior resolution, obtained if we perform the comparison test for elevation angles larger than the true secondary elevation of arrival. The final resolution is computed as an average between the superior resolution and the inferior resolution.

Figure 2.5 depicts results for the resolution of two uncorrelated waves impinging on a five-

element dual-polarized L-Quad array [61] with different degrees of coupling (element spacing ranging from 0.35λ to 0.5λ) and compares to the resolution observed when the waves impinge on a three-element array. The resolution is computed fixing the DoA of a second signal and computing the CRLB for the first signal over a grid in elevation and azimuth. From the computed CRLB, we estimate the resolution using the procedure detailed above. The DoA of the second signal is then changed, the CRLB is once again computed for the first signal over the grid and the resolution estimated. The DoA of the second signal may be varied over a grid and the resolution may be computed as the average of the resolutions estimated for each DoA assumed for the second signal. The results presented in Figure 2.5 are based on an average of resolutions when the second wave impinges from $0°$ to $90°$ in elevation with a step of $10°$ and $0°$ to $70°$ in azimuth with a step of $10°$. The azimuth is varied only up to $70°$, due to the symmetry of the five-element array. The grid used for the computation of the CRLB for the first source is $0°$ to $90°$ in elevation with 241 points and $-180°$ to $180°$ in azimuth with 481 points.
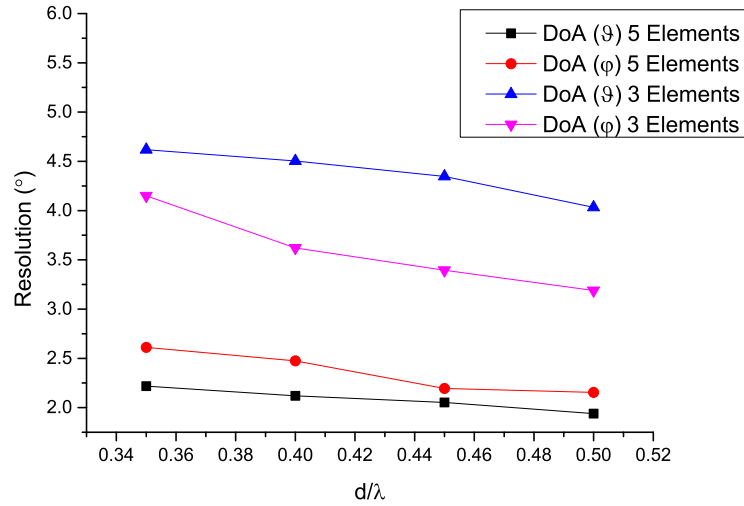
Figure 2.5.: Direction finding resolution of two uncorrelated waves impinging on a three and a five-element L-Quad array.

2.9. Model Order Estimation

For many applications, it may be important that the number of waves impinging on the array is previously estimated, before the actual DoA estimation. Subspace-based techniques strongly rely on the knowledge of the signal covariance matrix rank in order to divide the eigenvalue decomposition into signal and noise subspace. Beamforming techniques also assume that the numbers of desired and undesired source signals are known a priori for the computation of the weights to be used to steer the far field patterns. ML estimators may be able to find all the desired impinging directions without a priori knowledge of the model order, although it comes at a very high computational cost and under specific scenario assumptions. Nevertheless, it is safe to say that a previous estimation of the number of source signals leads to increased direction finding accuracy.

When the measured output estimated covariance matrix $\hat{\boldsymbol{R}}_{\mathrm{yy}}$ is decomposed into eigenvalues, if the smaller values, corresponding to the noise eigenvalues, are identical, the estimation of the number of source signals is carried out by observing the number of identical values from the decomposition, and subtracting it from the number of radiating elements. However, when the noise eigenvalues are not identical, or under rank deficiency condition (number of sensors smaller than the number of signals), more elaborate techniques may be mandatory in order to precisely estimate the order of the model.

2.10. Data Model Mismatch

High-Resolution Parameter Estimation (HRPE) is used for direction finding with the aim of achieving accuracy and resolution performance. However, it is important to note that HRPE relies on the fact that an appropriate parametric data model fits to the measured array output. As explained by Landmann in [30, 62], this data model consists both of the propagation and the device data.

In this thesis, the propagation data model assumes a superposition of narrowband planar waveforms. The device data model, on the other hand, consists of the transfer characteristics of the observer device, including the antenna frequency response and radiation characteristics. In [30], it was shown that any uncertainty error in the device data model will result in estimation artifacts as long as these modelling errors are not masked by receiver noise. For this reason, HRPE quality is limited by noise and model error. Antenna radiation patterns may be distorted by many implementation effects, e.g., the parasitic electromagnetic coupling between radiators in an array.

In the same publication, it was also shown that improper simplification of the data model

may completely destroy the estimation performance. This occurs, e.g., if the impact of polarization to radiation patterns is not taken into account, since the antenna radiation patterns depend on polarization orientation of the impinging wave. It becomes fundamental that the antenna is described by its full dual polarimetric response. As a consequence, ignoring polarization would end in matching the wrong data model, leading to wrong estimates. Therefore, the polarization orientation of the impinging wave has to be considered even if it is not explicitly required. Exceptions are only possible if there is a clear a priori match between the polarization of the impinging wave and the preferred polarization orientation of the observation antenna. In Figure 2.1 the polarization orientation was defined in terms of ϑ and φ as tangent vector to ϑ and φ latitude and longitude circles (elevation and azimuth). It can be observed that the two orthogonal components of the wave in its polar coordinate system do normally not match the preferred orientation of the sensor antennas. Hence, the antenna array architecture design (which consists of both the design of the individual radiators and their spatial arrangement) needs to consider an arrangement that is able to cover the observed space and to identify all parameters, including the desired DoA (elevation and azimuth) and the nuisance (polarization).

2.11. Search Procedure

The estimation of each impinging signal DoA is not only dependent on the direction finding technique and the related cost function, but also on the optimization method used to find the minima or maxima corresponding to the parameters to be estimated. As we have seen up to now, each two-dimensional direction finding technique, such as ML and MUSIC, renders a cost function with respect to the directions ϑ and ϑ, which needs to be either minimized or maximized for the estimation of the true signal DoA. The ML spectrum, e.g., quantifies the likelihood of each direction to be the true DoA. If a direction (ϑ_1, φ_1) exhibits a higher likelihood compared to the direction (ϑ_2, φ_2), this means that it is more likely that the former is the true signal DoA. Hence, the DoA estimation becomes an optimization problem in which we try to optimize the parameters to be estimated (in this case, azimuth and elevation).

The maximization (or minimization, depending on how we construct the direction finding spectrum) procedure is an optimization problem well reported in the literature and may be divided into two main categories: the brute-force methods and the iterative methods, such as Gauss-Newton and Levenberg-Marquardt. In this section, we detail the most commonly utilized search methods for DoA estimation.

2.11.1. Exhaustive Search Methods

The exhaustive search method, also referred to as brute-force method, is a technique to find the solution for some specific optimization problem. In case of direction finding, the method tests all the possible directions over a pre-defined grid by computing the cost function (using ML, MUSIC, or some other DoA estimation technique) for each point in the grid and subsequently deciding for the point in the grid that is most suitable to be the desired solution (maxima or minima of the cost function). It then assumes this point to be the estimated signal DoA. Although the exhaustive search method is very simple to implement and always able to find an estimation for the signal DoA, it may come at the cost of prohibitively high computational effort. If the scenario is comprised of multiple impinging waves, and the DoA estimation is two-dimensional, e.g., the dimension of the search, when testing all possible solutions over a direction grid, will definitely lead to higher processing time. Hence, for direction finding, exhaustive search is mostly utilized in scenarios with only one impinging wave.

The Space-Alternating Generalized Expectation-Maximization method, also referred to as SAGE [63] is an example of exhaustive search procedure commonly used for direction finding, and is an alternative for the classical Expectation Maximization (EM) method to tackle some undesired drawbacks such as slow convergence. Instead of updating all the parameters to be estimated simultaneously in each iteration, as the EM method, the SAGE method updates the parameters sequentially by alternating between pre-defined sub-groups, or spaces. The division of a whole space in sub-spaces is a well-known technique to speed up exhaustive search methods. However, even with the use of fancier techniques as SAGE, exhaustive search methods may still result in prohibitively high computational time and alternatively, it may be desirable to use an iterative method for direction finding of signals.

2.11.2. Iterative Methods

The search procedure for direction finding may be understood as a non-linear least squares problem, in which we try to minimize the error that arises from observations. In general, we have a function of the desired parameter vector $\boldsymbol{\theta}$, denoted by $S(\boldsymbol{\theta})$, which is the sum of the squared errors computed from each observation $\hat{y}_i$, with $i = 1, ..., L$:

$$S(\boldsymbol{\theta}) = \sum_{i=1}^{L} [\hat{y}_i - f(\boldsymbol{x}_i, \boldsymbol{\theta})]^2 \tag{2.41}$$

The goal is then to find the set of parameters $\boldsymbol{\theta}$ that minimizes the function S. Each of the following iterative methods starts with an initial guess for the parameter set denoted by $\boldsymbol{\theta}_0$

and updates the value at each iteration based on some specific rule.

2.11.2.1. Gauss-Newton

Let us define a function $r(\theta)$ of the parameter set as $r(\theta) = \hat{y}_i - f(x_i, \theta)$. The Gauss-Newton method uses the following iterations for computing the values of θ, considering the index n to be correspondent to the n-th iteration:

$$\begin{aligned} \theta_n &= \theta_{n-1} + \delta \\ r(\theta_n) &= r(\theta_{n-1} + \delta) = r(\theta_n) + J(\theta)\delta \end{aligned} \tag{2.42}$$

where J is the Jacobian of $r(\theta)$ given by:

$$J = \frac{\partial r(\theta)}{\partial \theta^{\mathrm{T}}} \tag{2.43}$$

The value of δ is then obtained by plugging $r(\theta + \delta)$ in (2.41) and differentiating S with respect to δ. It is then given by the following expression:

$$\delta(\theta) = H^{-1}(\theta)g(\theta) \tag{2.44}$$

where $H(\theta)$ is the Hessian matrix and $g(\theta)$ is the gradient vector of $S(\theta)$ with entries given by:

$$g_j(\theta) = 2 \sum i = 1^L r_i \frac{\partial r_i}{\partial \theta_j} \tag{2.45}$$

The entries of the Hessian matrix can be given by:

$$H_{jk} = 2 \sum_{i=1}^{L} \left(\frac{\partial r_i}{\partial \theta_j} \frac{\partial r_i}{\partial \theta_k} + r_i \frac{\partial^2 r_i}{\partial \theta_j \partial \theta_k} \right) \tag{2.46}$$

The Gauss-Newton method ignores the second-order derivative terms and simplify the entries of H as following:

$$H_{jk} \approx 2 \sum_{i=1}^{L} J_{ij} J_{ik} \tag{2.47}$$

The value of the function S is then updated for θ_n until θ converges to the optimum solution. The Gauss-Newton method is known as a local convergence method. This implies that if not adequately initialized (adequate initial iteration θ_0), the search procedure may not converge

to the global optimal solution.

2.11.2.2. Steepest Descendent

For the steepest descendent method, commonly referred to as gradient descendent method, the iterations for the values of $\boldsymbol{\theta}$ are based on the gradient of the function to be minimized. Hence, we can express the iterations as following:

$$\boldsymbol{\theta}_n = \boldsymbol{\theta}_{n-1} + \boldsymbol{\delta}(\boldsymbol{\theta}) = \boldsymbol{\theta}_{n-1} - \left[\gamma \boldsymbol{J}\right] \tag{2.48}$$

where γ denotes the length of the update step in the direction of the steepest descendent.

The steepest descendent is known as a global convergence method. This implies, in contrast to the Gauss-Newton method, that even if initialized far from the optimal solution, the method is guaranteed to converge to a global minima, what comes to a cost of higher computational effort [64].

2.11.2.3. Levenberg-Marquardt

The Levenberg-Marquardt method is also referred to as damped Gauss-Newton method, since it modifies the definition of δ for each iteration by adding a damping factor λ. The algorithm was first reported by Levenberg in 1944 [65] and the proposed δ is:

$$\boldsymbol{\delta}(\boldsymbol{\theta}, \lambda) = -\left[\boldsymbol{H}(\boldsymbol{\theta}) + \lambda \boldsymbol{I}\right]^{-1} \boldsymbol{g}(\boldsymbol{\theta}) \tag{2.49}$$

Later, Marquardt reported in 1963 [66] a slightly different expression for δ and the resulting method is finally known as Levenberg-Marquardt search:

$$\boldsymbol{\delta}(\boldsymbol{\theta}, \lambda) = -\left[\boldsymbol{H}(\boldsymbol{\theta}) + \lambda(\boldsymbol{I} \odot \det(\boldsymbol{H}(\boldsymbol{\theta})))\right]^{-1} \boldsymbol{g}(\boldsymbol{\theta}) \tag{2.50}$$

The set of parameters $\boldsymbol{\theta}$ is then updated as in (2.42) with the difference lying on the fact that the value of the parameter $\boldsymbol{\delta}$ is now also dependent on the damping factor λ, which is varied at each iteration, depending on the value of the function $S(\boldsymbol{\theta})$ [67]. If the current value of the function S is far from the local minima, the damp factor is increased. Otherwise, if close to the optimal solution, the damp factor is decreased, as detailed in Algorithm 2.

Note that close to the optimal solution, the damped factor is smaller and the Levenberg-Marquardt method approaches the Gauss-Newton method, converging fast to the local minima. On the other hand, far from the optimal solution, the damp factor is larger and the method approaches the steepest descendent method, with low, but guaranteed convergence.

Algorithm 2 Levenberg-Marquardt Method

1: Choose:
   - ε: indicates that the parameter converged to an optimal solution
   - $k_{\max}$: establishes the maximum number of iterations
   - κ: multiplier or divider for the damp factor λ
   - $\lambda_{\max}$: maximum value for the damp factor
2: Initial iteration $\boldsymbol{\theta}_0$
3: $k \leftarrow 0$
4: $\boldsymbol{\theta} \leftarrow \boldsymbol{\theta}_0$
5: $F_{\min} \leftarrow S(\boldsymbol{\theta})$
6: Compute the Hessian matrix $\boldsymbol{H}(\boldsymbol{\theta})$ and the gradient vector $\boldsymbol{g}(\boldsymbol{\theta})$ according to (2.47) and (2.45) respectively
7: $\lambda \leftarrow 1$
8: **while** $k < k_{\max}$ **do**
9:      $k \leftarrow k + 1$
10:      $\delta \leftarrow [\boldsymbol{H}(\boldsymbol{\theta}) + \lambda(\boldsymbol{I} \odot \det(\boldsymbol{H}(\boldsymbol{\theta})))]^{-1}\boldsymbol{g}(\boldsymbol{\theta})$
11:      $\boldsymbol{\theta}_{\mathrm{new}} \leftarrow \theta - \delta$
12:      $F \leftarrow S(\boldsymbol{\theta}_{\mathrm{new}})$
13:      **if** $F < F_{\min}$ **then**
14:          $\zeta \leftarrow \boldsymbol{\theta} - \boldsymbol{\theta}_{\mathrm{new}}$
15:          $\boldsymbol{\theta} \leftarrow \boldsymbol{\theta}_{\mathrm{new}}$
16:          **if** $| \zeta | \leq \varepsilon$ **then** Method converged
17:          $F_{\min} \leftarrow F$
18:          Compute the Hessian matrix $\boldsymbol{H}(\boldsymbol{\theta})$ and the gradient vector $\boldsymbol{g}(\boldsymbol{\theta})$ according to (2.47) and (2.45) respectively
19:          $\lambda \leftarrow \lambda/\kappa$
20:      **else**
21:          $\lambda \leftarrow \lambda\kappa$
22:          **if** $\lambda > \lambda_{\max}$ **then** Method did not converge

---

3. Receiving Antenna Design

Wireless communication relies on the existence of a receiving antenna to capture electromagnetic impinging waves, and transform them in current distribution to be fed to the electronic devices of which the system is comprised [68]. It is the "entrance" for the source signals to be further processed and from where the desired information will be extracted. Many applications also depend on the performance of a transmitting antenna, which radiates electromagnetic waves into the far field. In this case, the antenna transforms the input excitation into electromagnetic radiated fields. The transmitting and receiving properties of any antenna is well known to be reciprocal [69]. Accordingly, although this thesis focuses on DoA estimation, for which receiving antennas play a fundamental role on the overall performance, the antenna parameters reviewed in this chapter assume transmitting antennas and rely on the reciprocity to receiving antennas.

Depending on the design parameters, the response of an antenna to some incident electromagnetic wave arriving from a specific direction will be different. For direction finding, the ouput of an array of antennas is fed to the DoA estimator, and as a consquence, it becomes important to accurately characterize the array response over all possible directions of arrival to ensure precise estimation. For high-resolution array-based direction finding, one of the most significant requirements is high directivity, strongly related to the antenna beamwidth and hence, to its physical aperture size. On the other hand, for mobile direction finding systems, the overall size of the receiver is a definite constraint, making it highly desirable that the antenna is designed as compact as possible. In arrays, it may be necessary to place radiating elements together more closely, which gives rise to stronger mutual coupling. Moreover, other fundamental parameters such as gain, polarization, radiation efficiency and frequency bandwidth are reviewed in this chapter, with the aim of further investigating the effects to direction finding.

3.1. Antenna Fundamental Parameters

3.1.1. Directivity, Gain and Realized Gain

The directivity of an antenna is defined in [69] as the "ratio of the radiation intensity in a given direction from the antenna to the radiation intensity averaged over all directions". It may be interpreted as a way to describe the capability of the antenna to direct energy density

in a certain direction.

$$D(\vartheta, \varphi) = \frac{4\pi U(\vartheta, \varphi)}{P_{\text{rad}}} \tag{3.1}$$

where $U(\vartheta, \varphi)$ radiation intensity, in Watts per unit solid angle, in the direction given by (ϑ, φ) and P_{rad} is the total radiated power, in Watts. The directivity can also be expressed as:

$$D(\vartheta, \varphi) = 4\pi \frac{A(\vartheta, \varphi)}{\int_0^{2\pi} \int_0^{2\pi} A(\vartheta, \varphi) \sin(\vartheta, \varphi) d\vartheta d\varphi} \tag{3.2}$$

where $A(\vartheta, \varphi)$ is the antenna realized gain for each direction (ϑ, φ), compared to an ideal isotropic radiator, which includes the Ohmic losses and power mismatch within the array. The maximum directivity is taken at the direction of maximum radiation intensity and can be approximated and expressed with respect to the half-power beamwidth in the vertical (ϑ) and horizontal (φ) planes as following.

$$D = \frac{4\pi U_{\text{max}}}{\Theta_\vartheta \Theta_\varphi} \tag{3.3}$$

where Θ_ϑ is the beamwidth in the ϑ-plane and Θ_φ is the beamwidth in the φ-plane.

The antenna electrical aperture is directly related to the directivity. The larger the effective area of an antenna, the higher the maximum directivity becomes. It is defined in [69] as the "ratio of the available power at the terminals of a receiving antenna to the power flux density of a plane wave incident on the antenna" from the direction of maximum radiation intensity, and given by:

$$A_e = \frac{\lambda^2}{4\pi} D \tag{3.4}$$

The gain of an antenna can be defined as the ratio of the radiation intensity to the power that is actually accepted by the antenna. Thus, it is related to the directivity, but in contrast, takes into account power dissipated within the antenna, e.g. due to Ohmic losses. Part of the power that is accepted by the antenna, denoted by P_{acc}, is then dissipated and is thus not available for radiation. As a consequence, the power accepted is higher than the power radiated, implying that the gain is always lower than directivity, if Ohmic losses or other source of power dissipation cannot be neglected. It can be given by the following expression.

$$G(\vartheta, \varphi) = 4\pi \frac{U(\vartheta, \varphi)}{P_{\text{acc}}} \tag{3.5}$$

For the expression of the antenna gain as defined above, the power accepted, denoted by P_{acc} may be lower than the input power, denoted by P_{in}, if impedance mismatch at the antenna excitation port is observed. Hence, the above defined gain does not account for power lost due to mismatch at the antenna terminals. A parameter commonly used to characterize the antenna gain, taking into account impedance mismatch, is the realized gain, which refers to the ratio of the radiation intensity to the input power at the antenna terminals. If the antenna is not matched to the impedance of the power generator, part of the input power will be reflected and as a consequence does not contribute to the power accepted by the antenna. The realized gain can be written as:

$$RG(\vartheta, \varphi) = 4\pi \frac{U(\vartheta, \varphi)}{P_{\text{in}}} \tag{3.6}$$

If we define the antenna efficiency as e, we can write it as a product of the efficiency due to power mismatch (e_m) at the antenna terminals and the efficiency due to dissipation in conductor or dielectric materials (e_d), as following.

$$e = e_m e_d \tag{3.7}$$

The relation between directivity, gain and realized gain is then given by:

$$G(\vartheta, \varphi) = e_d D(\vartheta, \varphi) \qquad \text{and} \qquad RG(\vartheta, \varphi) = e_m G(\vartheta, \varphi) \tag{3.8}$$

The antenna efficiency due to power mismatch (e_m) at the terminals is also expressed as $1 - |\Gamma|^2$, where Γ is the reflection coefficient.

3.1.2. Polarization

The polarization of the antenna is of great importance for DoA estimation based applications since it defines how much power from the impinging signal the antenna will be capable of capturing. If the antenna exhibits a single orthogonal polarization relative to the polarization of the impinging wave, it will not be able to capture the wave, leading to a polarization mismatch loss [30]. Since the polarization of a transmitting antenna is defined as the polarization of the wave radiated by the antenna, let us start with the definition of the wave polarization. It can be interpreted as the curve traced by the wave's electric field vector over time. It thus describes the direction and relative magnitude of the electric field vector at every instant of time.

The electric field orthogonal components in the x and y-directions, of a wave traveling in

the negative z-direction, are given by the following expressions.

$$
\begin{aligned}
E_x(z,t) &= E_{xo}\cos(\omega t + kz + \phi_x) \\
E_y(z,t) &= E_{yo}\cos(\omega t + kz + \phi_y)
\end{aligned}
\tag{3.9}
$$

where E_{x0} and E_{yo} are the maximum electric field magnitudes in the x and y-directions and k is the propagation constant. The phase difference between the two orthogonal components $E_x(z,t)$ and $E_y(z,t)$ will define how the wave is polarized.

Linear polarized antennas radiate waves that exhibit electric field possessing either one component, or two orthogonal components with 0° or 180° of phase difference. The phase difference between ϕ_x and ϕ_y, observed at every instant of time is then:

$$
\Delta\phi = \phi_y - \phi_x = n\pi, \qquad n = 0, 1, 2, 3, \ldots
\tag{3.10}
$$

Circular polarized antennas radiate waves that exhibit electric field possessing two orthogonal components with same magnitude and 90°, or multiples, of phase difference. The phase difference between ϕ_x and ϕ_y, observed at every instant of time is:

$$
\begin{cases}
\Delta\phi = \phi_y - \phi_x = (\frac{1}{2} + n)\pi, & n = 0, 1, 2, \ldots \quad \text{for right-hand polarization} \\
\Delta\phi = \phi_y - \phi_x = -(\frac{1}{2} + n)\pi, & n = 0, 1, 2, \ldots \quad \text{for left-hand polarization}
\end{cases}
\tag{3.11}
$$

Elliptical polarized antennas radiate waves that exhibit electric field possessing two orthogonal components with equal or different magnitudes. If the magnitudes are not the same, the phase difference between the components are odd multiples of 90°. If, on the other hand, the phase difference between components is multiples of 90°, then the wave is elliptical polarized, regardless of the magnitudes. The phase difference between ϕ_x and ϕ_y, observed at every instant of time is:

$$
\begin{cases}
\Delta\phi = \phi_y - \phi_x = \pm(\frac{1}{2} + n)\pi, & n = 0, 1, 2, \ldots \quad \text{if } E_{xo} \neq E_{yo} \\
\Delta\phi = \phi_y - \phi_x = n\frac{\pi}{2}, & n = 0, 1, 2, \ldots \quad \text{otherwise}
\end{cases}
\tag{3.12}
$$

It is possible to observe that linear and circular polarizations are special cases of the elliptical polarization. Every wave that is not linearly or circularly polarized will be, as a consequence, elliptically polarized. Note that we decompose the electrical field vector into components in the x and y-directions due to the fact that we assumed a wave traveling in the z-direction – Cartesian coordinates. Since, the electric field is perpendicular to the direction of propagation, if we choose to use spherical coordinates to represent the fields, assuming that the wave travels

in the radial direction, then we would decompose the fields into ϑ and φ components. However, the phase differences between them, for each of the defined polarizations, are the same as depicted above.

Figure 3.1 illustrates the polarization of a wave traveling along the z-direction. The green curve depicts the total electrical field, the blue curve shows the component in the y-direction and the red curve, the component in the x-direction.
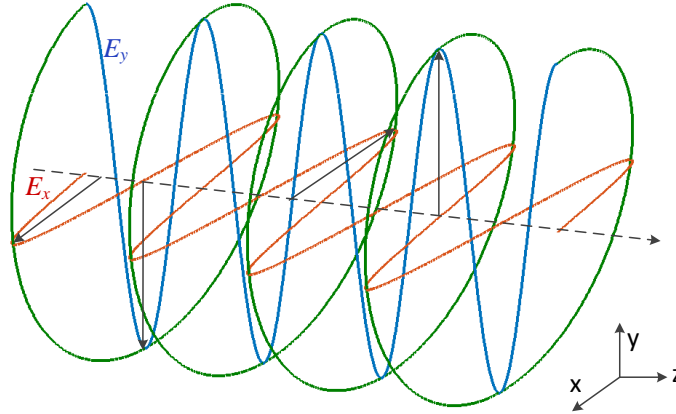
Figure 3.1.: Polarization of a wave propagating along the z-direction.

Polarization mismatch occurs if the polarization of the impinging wave is different from the receiving antenna polarization. It is defined as [69]:

$$L_{\mathrm{pol}} = \mid \hat{\boldsymbol{\rho}}_i \cdot \hat{\boldsymbol{\rho}}_r \mid^2 \tag{3.13}$$

where $\hat{\boldsymbol{\rho}}_i$ is the unit vector defining the polarization of the impinging wave and $\hat{\boldsymbol{\rho}}_r$ is the unit vector defining the polarization of the receiving antenna.

3.1.3. Frequency Bandwidth

The frequency bandwidth (BW) of an antenna is defined by the Institute of Electrical and Electronics Engineers (*IEEE*) as "the range of frequencies within which the performance of the antenna, with respect to some characteristic, conforms to a specified standard". It is the frequency range in which the antenna is assumed to behave well with respect to a specific parameter. One commonly used parameter to quantify the antenna performance and establish the corresponding frequency bandwidth is the return loss, given by the scattering parameter of

the antenna. By establishing a threshold bellow which the return loss may not fall, it is possible to define the antenna lower and highest frequency of operation. The frequency bandwidth is then calculated as the difference between the highest and the lowest frequency, divided by the central frequency, as follows, in percentage.

$$\text{BW} = 100\frac{f_h - f_l}{f_c} \tag{3.14}$$

Example of antennas that are typically narrowband are microstrip patch antennas, with frequency bandwidth ranging from as few as 1%. The narrow range of frequency is due to the fact that the patches are resonant antennas, designed to perform well near the resonance frequency. On the other hand, typical wideband antennas are e.g. horn reflectors and loop antennas. Recent research has reported ultra-wideband antennas that are capable of performing well over a frequency bandwidth of more than 20% of the central frequency [70]. Although the majority of results presented in this thesis are focused on narrowband antenna arrays, the outlook of this thesis details the design of a wideband loop antenna that may be used for direction finding of electromagnetic waves.

3.2. Antenna Arrays

For many applications, the use of one single radiating element as an antenna to capture electromagnetic waves is not enough to meet specific requirements such as radiation pattern, gain or spatial diversity. Hence, it may be necessary to arrange more than one radiating element as an array of antennas. High-resolution DoA estimation exploits the differential information from the output at each element in an array in order to achieve accurate direction finding. Moreover, as will be discussed later, the accuracy of DoA estimation increases monotonically with the number of elements in the array, as a result of increased SNR [28] and degrees of freedom, when mutual coupling is not accounted for. To achieve the desired accuracy, the elements may be arranged e.g. in linear or circular arrays, and the array manifold is calculated for each geometry, as discussed hereupon.

The total radiation pattern of an antenna array can be given as a combination of each individual radiation pattern and the array factor. The former describes the radiation pattern of each radiating element in the presence of all other elements terminated by matched loads, and may be different to each other if e.g. the array is not uniform or if the elements are rotated with respect to each other. The array factor, on the other hand, describes the array architecture, i.e., the element phase shift when positioned in the array. For an array comprised

of M elements, with element position given by the vector $\boldsymbol{p} \in \mathbb{R}^{M \times 3}$, the array factor is given by:

$$\boldsymbol{A}(\vartheta, \varphi) = e^{j\boldsymbol{k}^{\mathrm{T}}(\vartheta, \varphi)\boldsymbol{p}} \tag{3.15}$$

where $\boldsymbol{k}$ is the wave vector with $\|\boldsymbol{k}\|_2 = 2\pi/\lambda$ and (ϑ, φ) is the source DoA (elevation, azimuth). For a circular array with inter-element spacing d comprised of M elements, as in Figure 3.2, the array factor of the array manifold can be given by:
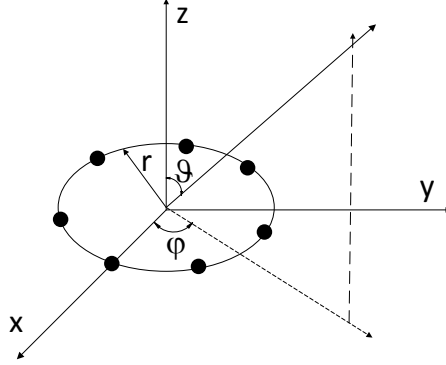
Figure 3.2.: Circular uniform array geometry with seven elements.

$$\boldsymbol{A}(\vartheta, \varphi) = \begin{bmatrix} e^{jk_0 r\sin\vartheta\cos(\varphi - 2\pi/M)} \\ e^{jk_0 r\sin\vartheta\cos(\varphi - 4\pi/M)} \\ \vdots \\ e^{jk_0 r\sin\vartheta\cos(\varphi - 2\pi)} \end{bmatrix} \tag{3.16}$$

where $k_0 = 2\pi/\lambda$ is the propagation constant, $r = (d/2)/\sin(\pi/M)$ the radius of the circular array, and (ϑ, φ) is the source impinging direction (elevation, azimuth).

It is clear that, if coupling is accounted for, extra effects arise from grouping elements in an array. Due to the fact that the coupling effects are usually very complex and depend on several factors such as the single-element design, orientation and inter-element spacing, it is important careful investigation is carried out with respect to the degrading effects to the application intended due to impairment caused by mutual coupling.

Dual-Polarized Antenna Arrays

When dealing with waves that impinge on a specific antenna array, it is of crucial importance that the array is dual-polarized in order to mitigate errors due to polarization mismatch, as detailed in [30]. Depending on the level of mismatch, considerable error may occur which can lead to a severe degradation of the direction finding performance. Diversely polarized antenna array design becomes then a key issue in order to ensure the required direction finding performance. In [71], a circular polarized direction finding antenna array for unknown polarization is presented. Although circular polarized antenna arrays render more accurate DoA estimation with respect to polarization mismatch, considerable estimation errors may still occur if the source signals impinge with polarization orthogonal to the polarization of the receiving antenna array. In [47], antenna arrays with diverse polarization are employed for direction finding based on different estimation algorithms and in [72], Maximum Likelihood Methods for DoA estimation of one source impinging with unknown polarization is investigated. Full-polarimetric arrays, with dual orthogonal polarization, are capable of considerably improving the accuracy of estimators if signals impinge from unkown polarization.

In general, there are two ways of designing full-polarimetric antennas: each radiating element may be dual-polarized, or polarization diversity may be achieved when each element is comprised by two ports, one for each polarization.

3.3. Mutual Coupling

When individual elements are arranged in an array of antennas, the electromagnetic interaction between radiators, also referred to as mutual coupling, renders altered current distribution at the terminals and as a consequence, distorted array radiated fields and modification of the antenna impedance are observed.

The feeding-point impedance of isolated radiating elements can be solely determined by the antenna geometry, the frequency of operation and the excitation. However, in the presence of neighboring elements, the spacing and arrangement of the array also strongly influence the feeding-point impedance of each element, since it affects the degree of interaction between them. The input impedance must then account both for the antenna self-impedance, which is the impedance of the isolated antenna when no interaction with other radiators or with the bounding medium occurs, and the mutual impedance, driven by the coupling effects between neighbors.

To illustrate the process of electromagnetic interaction between neighboring antenna elements, we start by describing a two-port antenna array, as illustrated in Figure 3.3. We

assume that only one antenna port is being excited while the second port is terminated by a load. We refer to the excited port as first port and the terminated port as second port. From the power excited at the first port, a fraction will be radiated, another fraction will be reflected due to impedance mismatch and a third fraction will be scattered to the second port. At the second port, part of the power coupled from the excitation at the first port will be radiated, another part will be dissipated at the terminated load and another fraction will be coupled back to the first port due to the mutual coupling and so on. The fraction of power coupled back to the first port will eventually lead to a fraction of power reflected, that is responsible to change the antenna impedance. As a consequence, besides distorting the radiated field patterns, since part of the excited power will scatter to the other radiator, mutual coupling also contributes to change the impedance of the antenna.
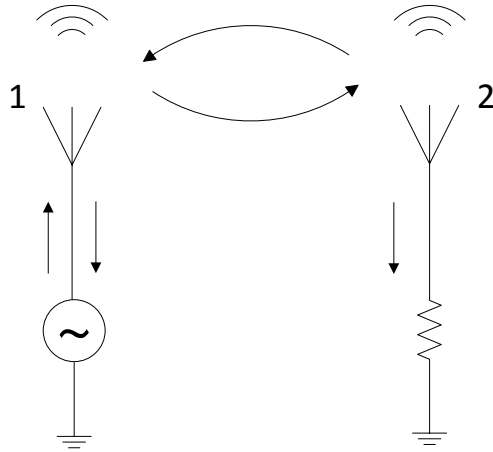
Figure 3.3.: Power scattering by mutual coupling within a two-port antenna array.

It has been extensively reported that mutual coupling is a very complex process that depends not only on the placement of elements but also on the type of radiator and on the array excitation. For simple antenna geometries, it may be viable to analytically compute the mutual coupling using the Method of Moments (MoM) as in [73], the Cavity Model (CM) or the Transmission Line Model (TLM). However, it becomes impractical to precisely predict the effects of coupling for general complex antenna geometries and in most cases, it is numerically [74] or experimentally estimated as in [75] and [76].

A first step to understand how mutual coupling affects the performance of an antenna array and further to measure or compute the required parameters for evaluation, is to accurately model the antenna with respect to coupling, which can be described by the array impedances,

the scattering parameters or by a coupling matrix that relates the far-field radiation pattern of the ideally uncoupled array to the radiation pattern of the coupled array.

3.3.1. Antenna Array Impedance Parameters

By representing the M-element antenna array as an equivalent M-port network, it is possible to compute the relation between voltages and induced current distribution at the antenna terminals and thus, to compute the desired impedances or admittances. Let us start with a simple two-port antenna array, wherein the impedance may be illustrated as in Figure 3.4.

Figure 3.4.: Two-port network equivalent for a two-element antenna array.

The voltages at each of the antenna ports terminals V_1 and V_2 can then be written as:

$$V_1 = Z_{11}I_1 + Z_{12}I_2$$
$$V_2 = Z_{21}I_1 + Z_{22}I_2$$

(3.17)

Note that the mutual impedance Z_{mn} is computed as the ratio of the voltage at the terminals of port m to the current induced in port n when all other ports but port n are open-circuited, i.e.:

$$Z_{mn} = \left. \frac{V_m}{I_n} \right|_{I_k=0}$$

(3.18)

By looking at (3.17), we observe that the voltages are thus characterized not only by the antenna self-impedances Z_{11} and Z_{22} but also by the mutual-impedances Z_{12} and Z_{21}. The driving-point impedance, also referred to as active input impedance, which corresponds to the impedance of each element in the array when all of the elements are excited, denoted by Z_{1d} and Z_{2d}, are computed as the ratio between voltage at the terminals and induced current as

following:

$$Z_{1d} = \frac{V_1}{I_1} = Z_{11} + Z_{12}\frac{I_2}{I_1}$$

$$Z_{2d} = \frac{V_2}{I_2} = Z_{22} + Z_{21}\frac{I_1}{I_2}$$

(3.19)
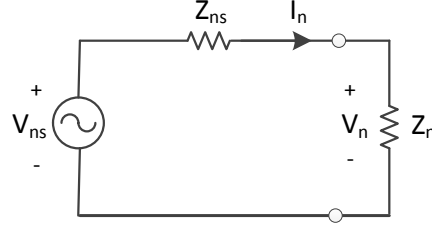
Figure 3.5.: Circuit equivalent representation of the n-th element port excited by a source with voltage V_{ns} and internal impedance Z_{ns}.

By allowing an equivalent circuit representation of each antenna element as depicted in Figure 3.5, if independent sources are exciting the radiators, it is possible to write:

$$V_{1s} = I_1 Z_{1s} + I_1 Z_{1d} = I_1(Z_{1s} + Z_{1d})$$

$$V_{2s} = I_2 Z_{2s} + I_2 Z_{2d} = I_2(Z_{2s} + Z_{2d})$$

(3.20)

where V_{ms} is the source (excitation) voltage at port m, and Z_{ms} is source internal impedance at port m, for $m = 1, 2$. Plugging (3.19) into (3.20), we get:

$$V_{1s} = I_1\left(Z_{1s} + Z_{11} + Z_{12}\frac{I_2}{I_1}\right) = Z_{1s}I_1 + Z_{11}I_1 + Z_{12}I_2$$

$$V_{2s} = I_2\left(Z_{2s} + Z_{22} + Z_{21}\frac{I_1}{I_2}\right) = Z_{2s}I_2 + Z_{21}I_1 + Z_{22}I_2$$

(3.21)

Using matrix representation and generalizing for a M-element antenna array, we get to:

$$\boldsymbol{V}_s = (\boldsymbol{Z} + \boldsymbol{Z}_s)\boldsymbol{I}$$

(3.22)

where

$$\boldsymbol{V}_s = \begin{bmatrix} V_1 s \\ \vdots \\ V_M s \end{bmatrix} \qquad \boldsymbol{Z} = \begin{bmatrix} Z_{11} & \ldots & Z_{1M} \\ \vdots & \ddots & \vdots \\ Z_{M1} & \ldots & Z_{MM} \end{bmatrix} \qquad \boldsymbol{Z}_s = \begin{bmatrix} Z_{1s} & \ldots & 0 \\ \vdots & \ddots & \vdots \\ 0 & \ldots & Z_{sM} \end{bmatrix} \qquad \boldsymbol{I} = \begin{bmatrix} I_1 \\ \vdots \\ I_M \end{bmatrix} \qquad (3.23)$$

It is easy to observe that the matrix comprising the terminal current I_m at the terminal of the each element in the array can be computed as following.

$$\boldsymbol{I} = (\boldsymbol{Z} + \boldsymbol{Z}_s)^{-1} \boldsymbol{V}_s \qquad (3.24)$$

To find the impedances at the terminals of each element port, denoted by V_m, we can make use of (3.24) and recall from (3.17) extended to an M-element array, that $\boldsymbol{V} = \boldsymbol{Z}\boldsymbol{I}$:

$$\boldsymbol{V} = \boldsymbol{Z}(\boldsymbol{Z} + \boldsymbol{Z}_s)^{-1} \boldsymbol{V}_s \qquad (3.25)$$

Equation (3.25) equips us with a relation between the source voltages, which equals the open-circuit voltages of each element port, and the voltages at the terminals of each element taking into account mismatch at the ports (characterized by the self-impedances) and mutual coupling (characterized by the mutual impedances). It allows for the computation of the uncoupled voltage, i.e., the voltage that would be observed at the terminals of each antenna, if the neighboring elements were extracted from the array.

If we assume that all sources have the same internal impedance Z_s we get to [77]:

$$\begin{bmatrix} 1 + \dfrac{Z_{11}}{Z_s} & \dfrac{Z_{12}}{Z_s} & \cdots & \dfrac{Z_{1M}}{Z_s} \\ \dfrac{Z_{21}}{Z_s} & 1 + \dfrac{Z_{22}}{Z_s} & \cdots & \dfrac{Z_{2M}}{Z_s} \\ \vdots & \vdots & \ddots & \vdots \\ \dfrac{Z_{M1}}{Z_s} & \dfrac{Z_{M2}}{Z_s} & \cdots & 1 + \dfrac{Z_{MM}}{Z_s} \end{bmatrix} \begin{bmatrix} V_1 \\ V_2 \\ \vdots \\ V_M \end{bmatrix} = \begin{bmatrix} V_1 s \\ V_2 s \\ \vdots \\ V_M s \end{bmatrix} \qquad (3.26)$$

The possibility to compute uncoupled voltages from parameters measured or computed from coupled arrays is a useful tool to compensate for mutual coupling, since it allows for a decoupled characterization of the array and may be used as a means to improve the accuracy of the source signal DoA estimation. However, the computation of impedances as in Equation (3.26) rely on the assumption that the antenna is operating in the transmitting mode, with sources exciting

the radiating elements. The method for computing impedances as in Equation (3.26) is also referred to in the literature as Conventional Mutual Impedance Method (CMIM), and allows for the computation of uncoupled voltages from the array coupled voltages and impedances (driving-point impedances). Although the method is precise when antennas are transmitting, and thus the excitation is being applied at the port terminals, this is not true when antennas are operating in the receiving mode and the ports are excited if an electromagnetic wave impinges on the array [78].

Hui [79, 78, 80, 81, 82, 83] had a major impact in researching mutual coupling and the effects on fields such as direction finding, in which the antenna array operates in the receiving mode to capture impinging electromagnetic waves, and estimate the correspondent DoAs. In [78], the authors stated the reasons why the mutual coupling process within transmitting antenna arrays differs from the process of coupling within receiving antenna arrays.

- The mutual impedances computation as in (3.26) assumes that the arrays are operating in the transmitting mode. The coupling process for an antenna array in the receiving mode differ from the process of coupling when the antenna is transmitting;

- The characterization of impedance for each array element assumes that they are open-circuited, but if operating in the receiving mode, the elements are terminated with load impedances that affects the mutual coupling; and

- The method of conventional mutual impedances assume that the array radiators do not radiate if open-circuited, which is clearly not true, since even then, current distribution is induced and radiation, as a consequence, occurs.

Hui proposed in [80] a method denoted by Receiving Mutual Impedance Method (RMIM) that allows for the computation of the voltages at the terminals of each element in an uncoupled array with respect to the voltages in the correspondent coupled array. The voltage at the terminals of each antenna element can be expressed as a sum of the voltage that would be observed if the array was uncoupled and the voltage observed as a result of mutual coupling:

$$V_m = Z_l \, I_m = U_m + W_m \tag{3.27}$$

where Z_l is the load impedance with which the antenna element is terminated, U_m is the uncoupled voltage if all neighboring elements are extracted from the array and W_m is the voltage at the terminals of the element due to mutual coupling between neighbors. We can express the voltages at the terminals of the antenna elements with respect to the voltages if the array is uncoupled as following.

$$
\begin{bmatrix}
1 & -\dfrac{Z_{12,t}}{Z_s} & \cdots & -\dfrac{Z_{1M,t}}{Z_s} \\[2mm]
-\dfrac{Z_{21}}{Z_s} & 1 & \cdots & -\dfrac{Z_{2M,t}}{Z_s} \\[2mm]
\vdots & \vdots & \ddots & \vdots \\[2mm]
-\dfrac{Z_{M1,t}}{Z_s} & -\dfrac{Z_{M2,t}}{Z_s} & \cdots & 1
\end{bmatrix}
\begin{bmatrix}
V_1 \\ V_2 \\ \vdots \\ V_M
\end{bmatrix}
=
\begin{bmatrix}
U_1 \\ U_2 \\ \vdots \\ U_M
\end{bmatrix}
\tag{3.28}
$$

Both (3.26) and (3.28) allow for accurate computation of voltages at the terminals of a coupled array with respect to the voltages that would be observed if the array was uncoupled. Equation (3.26) accurately describes the voltages when the antenna is operating in the transmitting mode and Equation (3.28) is accurate for antenna arrays operating in the receiving mode. The voltages that would be observed in the uncoupled transmitting and receiving array, $V_m s$ and U_m respectively, with $m = 1, ..., M$, are then fed to the direction finding method and renders more accurate estimation when compared to what is obtained when the voltages V_m with $m = 1, ..., M$ are used. However, since the antenna array operates as a receiver in direction finding applications, much more accurate estimation is carried out when the RMIM method is used in comparison to the conventional CIMM.

3.3.2. Antenna Array Scattering Parameters

Although useful to characterize current and voltage relations at the terminals of antenna arrays and through easy equivalent representation as T-networks, the array impedances do not render straightforward description of power flow. Let us assume that the reflected power at each port is completely dissipated at the generator internal load and is thus not available for radiation. Furthermore, let the vector $\boldsymbol{a} \in \mathbb{C}^{M \times 1}$ represent the excitation of a transmitting M-element antenna array. From the input power at each of the array ports, only a fraction will be available for radiation due to power mismatch (which includes the effect of mutual coupling as well as the effect of impedance mismatch at the terminals), characterized by the scattering matrix $\boldsymbol{S} \in \mathbb{C}^{M \times M}$. The reflected power wave, denoted by $\boldsymbol{b} \in \mathbb{C}^{M \times 1}$ can be given by:

$$
\boldsymbol{b} = \boldsymbol{S}\boldsymbol{a}
\tag{3.29}
$$

For easier comprehension, we write the reflected wave at each port as:

$$
\begin{cases}
b_1 = S_{11}a_1 + S_{12}a_2 + \cdots + S_{1M}a_M \\
b_2 = S_{21}a_1 + S_{22}a_2 + \cdots + S_{2M}a_M \\
\vdots \\
b_M = S_{11}a_1 + S_{M2}a_2 + \cdots + S_{MM}a_M
\end{cases}
\tag{3.30}
$$

It is easy to observe that the wave reflected at each port, denoted by b_m, has contributions not only from the wave excited at the port, a_m, but also from the waves excited at the neighbors, a_n with $n = 1...M$ and $n \neq m$. The amount of contribution of the power reflected at other ports to the power excited at one specific port is given by the off-diagonal elements of the scattering matrix. Due to reciprocity, the power flow for the receiving mode can be analogously described. In this case, part of the incident wave is reflected to the free-space and part is received by antenna. As a consequence, mutual coupling, together with impedance mismatch at each port (described by the diagonal elements of the scattering matrix), contributes to decrease the amount of power radiated by the transmitting antenna. Figure 3.6 depicts the transmitting mode of an antenna array comprised of two elements.
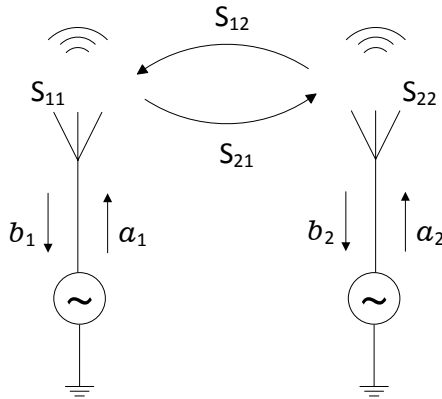
Figure 3.6.: Power flow description of a two-element antenna array through the array scattering parameters.

If we use an equivalent circuit representation as in Figure 3.5, we may characterize each antenna element as depicted in Figure 3.7, with the incident power wave a_n representing the wave that travels towards the antenna port, and the reflected power wave b_n representing the power wave reflected at the port.
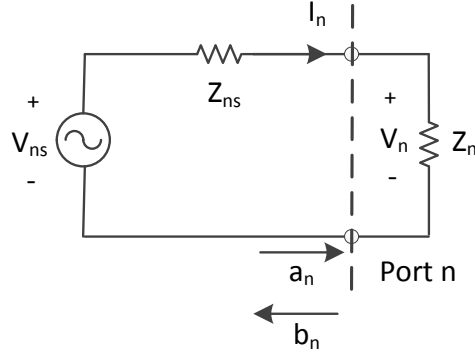
Figure 3.7.: Circuit equivalent representation of the n-th element port with respect to the incident and reflected power waves.

The power waves a_n and b_n at each port with $n = 1, ..., M$ are defined with respect to the voltage at the terminals of the antenna port V_n, the induced current I_n and the internal impedance of the source as following.

$$a_n = \frac{V_n + I_n Z_{ns}}{2\sqrt{Z_{ns}}} = \frac{V_{\text{inc},n}}{\sqrt{Z_{ns}}}$$

$$b_n = \frac{V_n - I_n Z_{ns}}{2\sqrt{Z_{ns}}} = \frac{V_{\text{refl},n}}{\sqrt{Z_{ns}}}$$

(3.31)

where $V_{\text{inc},n}$ is the voltage wave incident at the n-th port, and $V_{\text{refl},n}$ is the reflected wave voltage. We assume that the source internal impedance at each port is equal to Z_s, often referred to as the system impedance, to which it is desired to match the antenna ports to ensure minimum reflected power (maximum power transfer). The system impedance is usually assumed to be 50 Ω.

Note that, although Figure 3.7 assumes that the antenna array is excited by a source with internal impedance Z_{ns} and is thus operating in the transmitting mode, the definition of incident and reflected power waves remain unchanged. The source internal impedance would be replaced by a load impedance Z_l, but the relation between reflected and incident power using the scattering parameters is not altered, which makes the characterization of mutual coupling using scattering parameters advantageous in comparison to the characterization resulting from the use of impedance parameters. The computation of scattering parameters from impedance parameters can be easily carried out with the use of the expressions in Appendix A.

The voltage V_n at the terminals of each element port and the induced current I_n can be written as:

$$V_n = (a_n + b_n)\sqrt{Z_{ns}}$$
$$I_n = \frac{a_n - b_n}{\sqrt{Z_{ns}}} \tag{3.32}$$

The total power accepted by each antenna element, without accounting for Ohmic losses, is then given by $V_n I_n = a_n a_n^*$. For all the antenna ports, using matrix representation, the reflected power can be computed from the total incident power with the use of the following expression.

$$P_{\text{ref}} = \boldsymbol{b}^{\text{H}}\boldsymbol{b} = \boldsymbol{a}^{\text{H}}\boldsymbol{S}^{\text{H}}\boldsymbol{S}\boldsymbol{a} \tag{3.33}$$

The radiated power can then be written as:

$$P_{\text{rad}} = P_{\text{inc}} - P_{\text{ref}} = \boldsymbol{a}^{\text{H}}\boldsymbol{a} - \boldsymbol{a}^{\text{H}}\boldsymbol{S}^{\text{H}}\boldsymbol{S}\boldsymbol{a} = \boldsymbol{a}^{\text{H}}(\boldsymbol{I} - \boldsymbol{S}^{\text{H}}\boldsymbol{S})\boldsymbol{a} \tag{3.34}$$

From this point on we will refer to the matrix $\boldsymbol{I} - \boldsymbol{S}^{\text{H}}\boldsymbol{S}$ as the antenna radiation matrix $\boldsymbol{H}$, when Ohmic losses within the array can be neglected. The power radiated by the array can then be given by:

$$P_{\text{rad}} = \boldsymbol{a}^{\text{H}}\boldsymbol{H}\boldsymbol{a} \tag{3.35}$$

The antenna radiation efficiency for a specific excitation vector $\boldsymbol{a}$ can be written as the ratio of the radiated power and the total incident power as following.

$$\lambda(\boldsymbol{a}) = \frac{P_{\text{rad}}}{P_{\text{inc}}} = \frac{\boldsymbol{a}^{\text{H}}\boldsymbol{H}\boldsymbol{a}}{\boldsymbol{a}^{\text{H}}\boldsymbol{a}} \tag{3.36}$$

When, besides power mismatch at each port and coupling between neighboring ports, Ohmic losses also significantly contribute for power loss within the array, the scattering matrix does not suffice to describe the array radiation efficiency. The total radiated far-fields are then necessary to accurately characterize the power radiated by the antenna. In this case, the radiation matrix needs to be computed from the far-field patterns as following.

$$H_{ij} = \frac{1}{4\pi} \oint \boldsymbol{A}_i^{\text{H}}(\vartheta,\varphi)\boldsymbol{A}_j(\vartheta,\varphi)d\Omega \tag{3.37}$$

where $\boldsymbol{A}_i(\theta,\phi)$ is the array response of each port $i = 1...M$. It is easy to observe that if the radiation matrix equals the identity matrix, all the incident power is radiated by the

transmitting antenna, which will, as a consequence, posses 100% radiation efficiency. The diagonal elements of the radiation matrix measure the amount of power incident at one specific port that is available for radiation, and will be different from 1 due to impedance mismatch at the port and coupling to the neighboring ports (or due to power dissipation caused by Ohmic losses). The off-diagonal elements describe the amount of overlapping between the radiated far field patterns. Uncoupled arrays exhibit zero-valued off-diagonal elements in the scattering matrix and as a consequence, if Ohmic losses are not significant, possess orthogonal far-field patterns (zero-valued off-diagonal elements in the radiation matrix). However, the contrary is not necessarily true and it may be possible to encounter a scattering matrix with off-diagonal elements different from zero (coupled array) and still observe zero-valued off-diagonal elements in the array radiation matrix.

In Chapter 4, we detail a description of the antenna array mutual coupling based on the decomposition of the array radiation matrix $\boldsymbol{H}$ into fundamental modes of radiation, each with its own modal radiation efficiency. We will discuss how the modal efficiencies are useful do characterize the amount of coupling between radiators within the array.

3.3.3. Antenna Array Coupling Matrix

As discussed so far, the mutual coupling within antenna arrays may be described by the impedances or by the scattering parameters. Alternatively, an error matrix $\boldsymbol{E}$ may be used to describe mutual coupling between neighbors, since it characterizes the array patterns of radiation and accounts for the three possible sources of mismatch between ideal and real antenna array model: 1) Ohmic or dielectric losses, 2) impedance mismatch at the input ports and 3) mutual coupling between neighboring elements [84]. The distorted radiation pattern may be expressed as:

$$\tilde{\boldsymbol{A}} = \boldsymbol{E}\boldsymbol{A} = \begin{bmatrix} E_{11} & \dots & E_{1M} \\ \vdots & \ddots & \vdots \\ C_{E1} & \dots & E_{MM} \end{bmatrix} \boldsymbol{A} \tag{3.38}$$

The diagonal elements of the error matrix $\boldsymbol{E}$ are related to the impedance mismatch at the input ports and the off-diagonal elements are related to mutual coupling. The matrix $\boldsymbol{E}$ may be obtained through calibration measurements [85], analytically computed using MOM, CM or TLM, or obtained through simulations carried out by an electromagnetic full-wave simulation tool. Equation (3.38) allows for direct computation of the radiation patterns of real antenna arrays from the patterns observed in the corresponding ideal array. Going back to (2.25) and recalling that the CRLB for DoA estimation of sources strongly depends on the array radiation

patterns, it becomes easy to compute the effects to the array capability for direction finding when the error matrix $\boldsymbol{E}$ is known (either by calibration or by 3D electromagnetic simulation). On the other hand, if the computation of the CRLB is carried out by assuming ideal arrays if instead, real arrays are used, inaccurate results may be obtained due to model mismatch characterized by the error matrix.

3.4. Real Direction Finding Antenna Arrays

3.4.1. Microstrip Patch Antenna Arrays

Microstrip antennas are one of the most utilized antennas for several fields ranging from military to civilian applications. Satellite communication, RADAR systems, remote sensing, cellular communication, and biomedicine are some of the possible fields in which microstrip antennas may be employed. Among some of the most remarkable advantages of such type of antennas are the low profile, low complexity, low cost, light weight, conformability, simple manufacturing and mechanical robustness. Moreover, requirements such as dual-polarization or dual-frequency band can be achieved through design parameters.

Microstrip antennas have been reported since the early 1950s [86, 87]. However, it was only after the 1970s that the technology started to attract significant attention from academics. The companion papers by Carver and Mink [88], and Mailloux and McIlvenna [89] reported, back in 1981, the current state of development of microstrip antennas, challenges, and pointed out the direction of further development. Additionally, Pozar had major impact on the investigation of microstrip antennas with several publications such as in [90, 91], and a book [92] guiding the reader through details on the fundamentals of microstrip radiators, challenges related to the technology, and recent research.

A microstrip antenna consists of a metalized radiator printed on a grounded dielectric slab, as depicted in Figure 3.8. The size of the metallic radiator defines the resonance frequency, and due to limitations with respect to the antenna physical size, the frequency bandwidth of a microstrip antenna is usually very narrow and may in some cases, not even achieve 1% of the central resonance frequency. The properties of the dielectric layer play an important role to the radiation performance of the antenna. Thick layers are usually preferred when the objective is frequency bandwidth enhancement, although it will definitely come with the cost of higher dissipation loss within the substrate. Moreover, the shape of the metalized radiator, hereafter referred to as patch, also influences the antenna efficiency. Rectangular and circular patch antennas are the two most used configurations due to simplicity, although fancy shapes may also be considered for the antenna performance optimization.

The technique employed for the feeding of the radiators is of fundamental importance for the overall antenna performance. The antenna may be fed e.g. by a probe as depicted in Figure 3.8a, by an edge, by proximity coupling or by a microstrip line. Another feeding technique, which consists of coupling the energy fed by a microstrip line through an aperture on the antenna ground plane, was first introduced by Pozar in 1985 [93], and is proven to have many advantages over the other feeding techniques. Some advantages include the possibility to use suitable substrates for the feeding and patches support, and to use thick layer of substrate for bandwidth enhancement. The shape of the aperture may also be designed in order to ensure high coupling through the aperture and thus, to enhance the antenna radiation efficiency. The aperture coupled microstrip antenna consists of two dielectric layers separated by a slotted ground plane. The patch is placed on the top of the layers, and at the bottom, the microstrip feeding line is positioned as depicted in Figure 3.8b. The fields from the feeding line are then coupled to the patches through the slot.
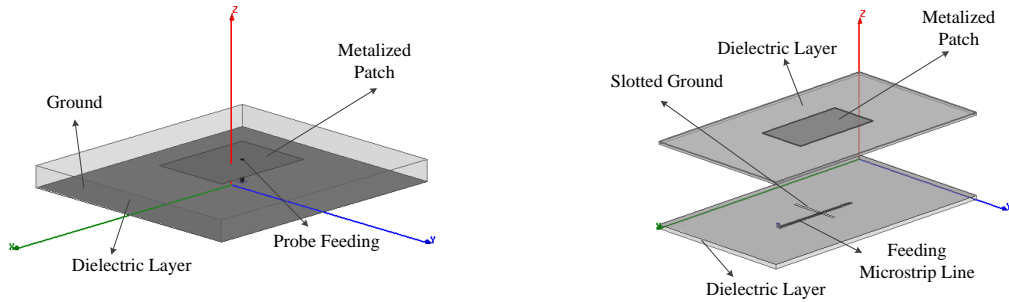
(a) Probe feeding.

(b) Aperture coupling.

Figure 3.8.: Probe-fed and aperture coupled patch antenna.

It is important to note that one possible significant disadvantage of microstrip antennas, independent of the feeding technique, or the geometry of the patch, is the loss associated to the antenna metallic components and the dielectric slab. Depending on the choice of material, non-negligible losses may give rise to degraded radiation performance. The power radiated by a microstrip antenna, considering the area of the patch to be represented by S, can be written as:

$$P_{\mathrm{r}} = \frac{1}{2} \; \mathfrak{Re}\Big[\iint\limits_{\text{aperture}} (\boldsymbol{E} \times \boldsymbol{H})\, dS \Big] \tag{3.39}$$

The loss associated with the conducting material, considering only the radiating patch as

source of loss, also referred to as Ohmic loss, is expressed with respect to the density current $\boldsymbol{J}$ within the surface of the patch:

$$P_{\text{Ohmic}} = 2\frac{R_s}{2} \iint\limits_{S} (\boldsymbol{J}\boldsymbol{J}^*)dS \tag{3.40}$$

where R_s denotes the surface resistance. Finally, we express the loss due to the dielectric slab, which occupies a volume V as:

$$P_{\text{dielectric}} = \frac{2\pi f\varepsilon}{2} = \iiint\limits_{V} \mid \boldsymbol{E} \mid^2 dV \tag{3.41}$$

where f is the antenna central frequency of operation and ε is the imaginary part of the complex substrate permittivity. It is important to accurately quantify the losses from conducting and dielectric materials, since it may significantly degrade the performance of the antenna for the intended application.

3.4.1.1. Analysis of Microstrip Antennas

There are several techniques that can be applied to analyze patch antennas, such as TL, CM and MoM. By using one of the above mentioned techniques, the designer can analytically compute parameters such as the antenna self-impedance or the mutual impedance, in case of an array of radiators. However, analytical models rely on a series of assumptions that may lead to degraded accuracy if violated, limiting the application. Moreover, analytical methods do not account for effects of mutual coupling, that may become expressive, especially in compact antenna arrays, with inter-element spacing smaller than $\lambda/2$. To overcome these issues, Maxwell's equations for full-wave analysis, Green's functions for MoM, may be used. However, the higher accuracy in comparison to analytical models comes with the cost of higher numerical effort [94].

The characterization of an antenna with respect to the impedance may be a highly complex task, especially when accounting for mutual coupling within an array. Analytical models, numerical techniques, as well as empirical curves may be used to describe the desired parameters. Empirical curves, e.g., were generated by Metzler [95] to describe the conductance of the microstrip radiator when mutual coupling cannot be neglected in the investigation of the antenna performance. The radiation conductance g was then computed from the insertion loss measurement of samples, in dB, and the number of elements M in the array as following.

$$10\log 10(1+g) = \frac{\text{Insertion loss dB}}{M} \tag{3.42}$$

Alternatively, Pozar [90] reported expressions for the input and mutual impedance of rectangular microstrip arrays based on MoM that uses the exact Green's function for the antenna substrate, thus accounting both for surface waves and for the coupling between neighboring elements in the array.

3.4.1.2. Polarization

Microstrip radiators are traditionally linearly polarized due to the fact that within single-fed antennas, mainly one mode is excited, which exhibits linear polarization in the direction of the resonant patch dimension. However, circular or dual-polarization may be achieved by a single patch with proper excitation or by an array of patches with suitable arrangement. For circular polarization, instead of the usual single mode being excited within the antenna, it is necessary that two modes with equal amplitude and ±90° of phase difference are simultaneously excited. Several patch geometries may be utilized and the feeding may be accomplished either by single or by dual-point when only one patch is used. On the other hand, linearly polarized patches may be positioned in an array aiming spatial orthogonality for circular polarization. Although easier to implement, the immediate drawback of achieving dual-polarization with array arrangement is that the array occupies larger space than single elements.

3.4.1.3. Frequency Bandwidth Enhancement

One notorious drawback of microstrip antennas comes from the fact that efficient radiation is limited to a relative narrow band of frequency, which may be prohibitive for many applications. To overcome this issue, there are several techniques [96] for broadening the bandwidth of patch antennas such as suitable choice of dielectric slab and feeding technique, multimodal techniques [68], impedance matching and resistive loading. Multimodal techniques include the use of stacked antennas comprised of two patches with different size and thus, slightly different resonance frequency. Another multimodal technique uses coplanar parasitic patch antennas with slightly different resonance frequency with the feeding line driving only one main patch.

From the above mentioned solutions to tackle narrow frequency bandwidth, the suitable choice of feeding is one of the least complex techniques. When employing e.g. aperture coupling as the feeding technique, the antenna designer can change the geometry of the slot in the ground plane and achieve an enhanced performance with respect to frequency bandwidth.

However, for applications such as DoA estimation, it is also important to analyze the influence of changing the antenna geometry with respect to direction finding capabilities.

One possible aperture coupling patch array design, reported in the literature for bandwidth enhancement, is the U-shaped slotted ground patch array [97], as in Figure 3.9. For the U-slotted ground, only the transverse portion of the slot couples to the patch and to the microstrip lines. The orthogonal portion of the slot contributes only to the reactive part of the antenna input impedance, and is used to obtain nearly uniform field distribution in the transverse portion, and thus, increase coupling without an increase in back radiation. In [3], such type of antennas was investigated with respect to the CRLB for direction finding. It was proven that optimum performance may be achieved for direction finding, while accomplishing frequency bandwidth enhancement with U-shaped slotted ground for the feeding of microstrip patches.
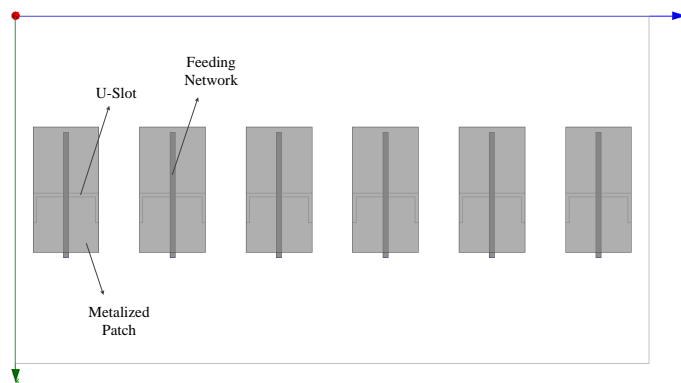
Figure 3.9.: 6 patches antenna array with U-slotted ground.

3.4.2. L-Quad Antenna Arrays

3.4.2.1. L-Quad Single Element

Modern mobile communication systems require receiving and transmitting antennas that are compact, lightweight, low cost and exhibit good mechanical stability when required to be mounted at some vehicle or flying copter. Antennas such as the crossed dipoles have proven over the years to be a good candidate for several mobile applications such as satellite systems, cellular communication and direction finding based applications. Ta et al. recently published in [98] a very useful review on the characteristics, designs and applications of crossed dipole antennas. Some of the main advantages of such type of radiators are the possibility of generating omnidirectional radiation pattern, the mechanical stability of the overall array and

the possibility of allowing for circular or dual-polarization. Moreover, depending on design parameters, crossed dipoles may operate over a wide frequency bandwidth, or over multiple narrow bands. With first development dating the 1930s [99], it is still the subject of research for many applications in mobile communication systems.

In this thesis, crossed pairs of monopoles, also referred to as L-Quads due to the L-shaped dipoles, as in Figure 3.10, are used as an example of antenna elements for direction finding and allow us to evaluate the theory presented. The crossed dipoles are good candidates for direction finding since the individual element radiation patterns cover almost half of the solid sphere and are mechanically stable, e.g., to be mounted on flying copters for DoA estimation of terrestrial targets. The L-Quad element contains four pairs of folded monopoles acting as dipoles, placed orthogonally to each other [61]. The feeding network is designed for dual linear polarization. The monopoles are folded for wider coverage over elevation. The pair of monopoles is excited at the end points instead of at the center, with 180° relative phase difference and is optimized for the frequency band 1.76 GHz–1.84 GHz. Figure 3.10 depicts the L-Quad element and the radiation patterns (ϑ and φ components) of each port. Hereafter, the term "element", when referring to the dual-polarized L-Quad, is used to describe an arrangement of two antennas (two ports) for reception of two orthogonal polarizations in some local coordinate system.
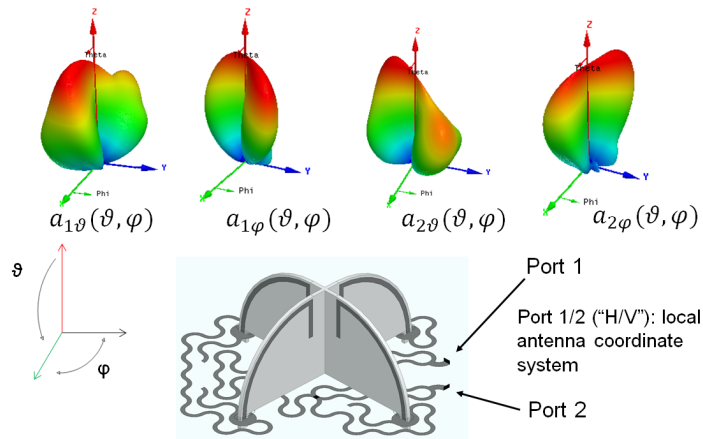
Figure 3.10.: Polarimetric radiation pattern of one L-Quad element comprised of two ports.

The L-Quad elements have many advantages over the patch antennas detailed in the last section. First of all, L-Quad elements are naturally dual-polarized, while the design of dual-polarized patch antennas demands additional effort. Second, the L-Quad elements radiate a more omnidirectional pattern if compared to patch antennas. Third, L-Quads, when placed in an array, are more stable and more compact than patch antenna arrays. Throughout this

thesis, we focused on the investigation of L-Quad elements placed in arrays, although some results are depicted at the end of Chapter 5, with the aim of illustrating the performance of patch antenna arrays for direction finding.

3.4.2.2. Practical Direction Finding L-Quad Arrays

The antenna array investigated in this thesis, hereafter referred to as L-Quad array, reported in [100, 61], is one example of an array comprised of crossed dipole radiators. The L-Quad antenna arrays are comprised of M elements, each containing four pairs of monopoles acting as crossed dipoles placed orthogonally to each other. The feeding network is designed for dual linear polarization. The full-polarimetric array allows for the mitigation of polarization mismatch that may occur when the polarization of a source signal is different from the polarization of the receiving antenna [30]. Moreover, for two-dimensional direction finding, circular arrays are required, since it allows for the estimation of both elevation and azimuth of arrival.

Figure 3.11 depicts a five-element dual-polarized circular L-Quad array. Note that the meander-shaped microstrip lines are part of the network that feeds and matches the pair of dipoles. Depending on the frequency of operation, the length of the network may get prohibitively large, encouraging research for efficient techniques for miniaturization. One possible method is to design the network microstrip lines as meandering shaped lines. This technique was investigated in [101, 102, 103] and is based on 90° meandering that renders sharp angles within the transmission lines. A practical solution to avoid sharp angles is to design the meandering lines as sets of curved segments as reported in [104]. The L-Quad antenna array investigated in this thesis includes a feeding network comprised by meander-shaped microstrip lines that feeds and matches the pair of dipoles. The meandering shape allows for the miniaturization of the network and details on the design can be found in [104, 105]. The overall diameter of the circular array, when 0.5λ inter-element spacing is considered, is approximately 22 cm. The dielectric layer on which the ground plane and the monopoles are printed has relative permittivity $\epsilon_r = 3.38$ and no Ohmic losses are assumed within the array.

It is important to note that in Figure 3.11, the elements are rotated with respect to each other for wider coverage over azimuth and for lower mutual coupling. Investigation carried out with respect to element rotation shows that it allows for a smoother CRLB over azimuth and elevation, if compared to the CRLB observed when the elements are aligned, as depicted in Figure 3.12.

Figure 3.13 depicts the far field radiation pattern of one port of the five-element L-Quad array. The results were obtained through full-wave simulation carried out with the use of Ansoft HFSS version 14.0 [39] and verified by measurements.
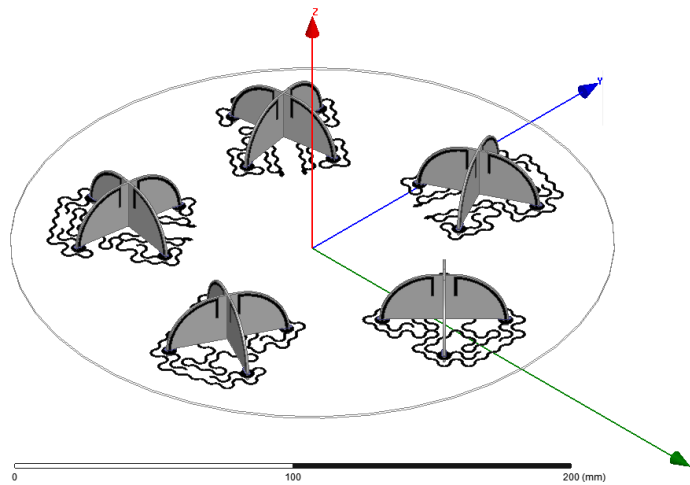
Figure 3.11.: L-Quad five-element circular array.
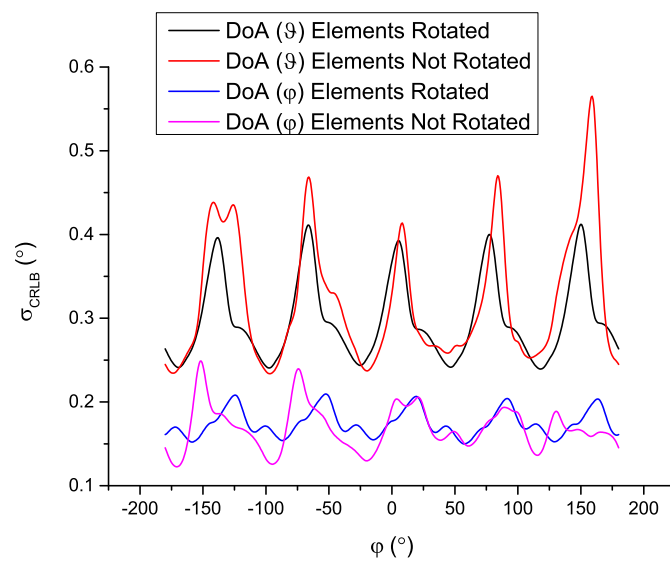
Figure 3.12.: CRLB (cut in $\vartheta = 85°$) for L-Quad circular five-element arrays with and without rotating the elements.

(a) Cut in ϑ.

(b) Cut in φ.
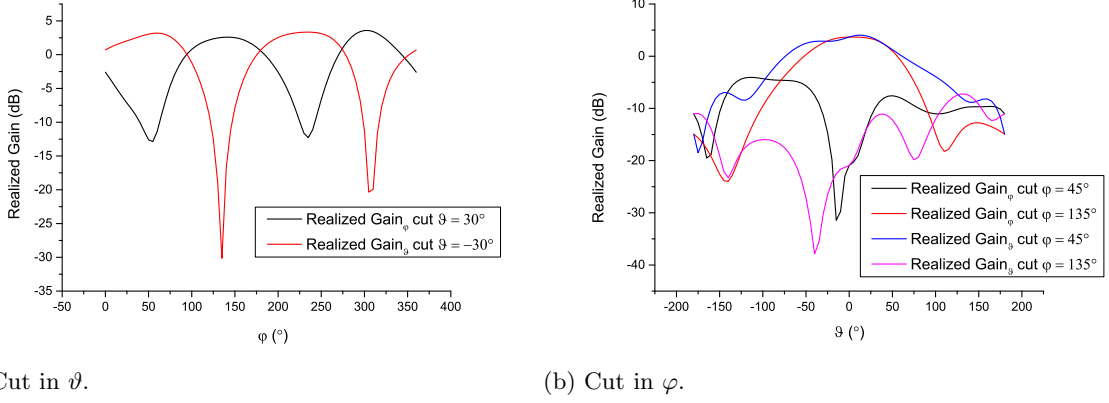
Figure 3.13.: Radiation pattern of a single element comprised of one pair of monopoles.

3.5. Relation Between Direction Finding Accuracy and Antenna Parameters

Having said that the receiving antenna fundamental parameters are the key to direction finding, it is important to investigate how each antenna parameter affects the capability for direction finding. In this section, direction finding capability is translated into the CRLB for DoA estimation. Let us begin by investigating a Uniform Linear Array (ULA) of ideally uncoupled radiators with omnidirectional radiation pattern. The array manifold denoted by $\boldsymbol{a} \in \mathcal{C}^{M \times 1}$ can be written as:

$$\boldsymbol{a} = \begin{bmatrix} 1 & e^{jkd\cos\varphi} & e^{2jkd\cos\varphi} & \dots & e^{jk(M-1)d\cos\varphi} \end{bmatrix} \tag{3.43}$$

where $k = 2\pi/\lambda$ is the propagation constant. Note that we focus at this point on the estimation of φ only. Note also that for the sake of simplicity, the full-polarimetric notation was skipped. The derivative of the array manifold with respect to φ, denoted by $\boldsymbol{d}$ is then given by:

$$\boldsymbol{d} = \begin{bmatrix} 0 & j\zeta e^{jkd\cos\varphi} & 2j\zeta e^{2jkd\cos\varphi} & \dots & (M-1)j\zeta e^{jk(M-1)d\cos\varphi} \end{bmatrix} \tag{3.44}$$

where $\zeta = -kd\sin\varphi$. We may as well write the following products:

$$\boldsymbol{a}^{\mathrm{H}}\boldsymbol{a} = 1 + 1 + \ldots + 1 = M$$

$$\boldsymbol{d}^{\mathrm{H}}\boldsymbol{d} = 0 + \zeta^2 + 2^2\zeta^2 + \ldots + (M-1)^2\zeta^2 = \zeta^2 \frac{M(M-1)(2M-1)}{6} \tag{3.45}$$

$$\boldsymbol{d}^{\mathrm{H}}\boldsymbol{a} = 0 - j\zeta - 2j\zeta - \ldots - (M-1)j\zeta = -j\zeta\frac{M(M-1)}{2}$$

From (2.25), it is easy to observe that the CRLB of the array can be directly expressed with respect to the array manifold and the corresponding derivatives as following:

$$\mathrm{CRLB}^{-1} = 2\,\mathrm{SNR}\,\{\boldsymbol{d}^{\mathrm{H}}\boldsymbol{d} - \boldsymbol{d}^{\mathrm{H}}\boldsymbol{a}(\boldsymbol{a}^{\mathrm{H}}\boldsymbol{a})^{-1}(\boldsymbol{d}^{\mathrm{H}}\boldsymbol{a})^{\mathrm{H}}\} \tag{3.46}$$

where $\mathrm{SNR} = \sigma^2 L/\sum_{t=1}^{L}\boldsymbol{s}^{\mathrm{T}}(t)(\boldsymbol{s}^{\mathrm{T}}(t))^{H}$ is the Signal-to-Noise ratio. Substituting (3.45) into (3.46), we get the following expression for the CRLB of a linear array comprised of M radiators with omnidirectional radiation pattern:

$$\mathrm{CRLB} = \frac{6}{\mathrm{SNR}}\frac{1}{k^2 d^2 \sin^2\varphi\, M(M^2-1)} \tag{3.47}$$

If we assume that the number of radiators in the array is large enough, i. e. $M \gg 1$, then we can write:

$$\mathrm{CRLB} = \frac{6}{\mathrm{SNR}}\frac{1}{k^2 d^2 \sin^2\varphi\, M^3} \tag{3.48}$$

Since the aperture of a linear array, denoted by A_l is given by $A_l = Md$ for large M, we can rewrite the CRLB with respect to the antenna array aperture:

$$\mathrm{CRLB} = \frac{6}{\mathrm{SNR}}\frac{1}{k^2\sin^2}\frac{1}{A_l^2 M} \tag{3.49}$$

It is possible to observe that for the ideal situation of uncoupled radiators, if the aperture of the array is kept fixed but the number of elements is increased, the CRLB will be reduced proportionally to M. For a Uniform Circular Array (UCA) of ideally uncoupled omnidirectional radiators, let us assume for simplicity that the signal impinging from the same plane as the antenna array so that $\vartheta = 90°$, and the DoA estimation is carried out only with respect to φ. Making use of (3.16) for circular arrays, with each port being excited with same amplitude and zero relative phase, the derivatives of the radiated pattern at each port with respect to φ, denoted by $\boldsymbol{d}$ can be written as following.

$$\boldsymbol{d} = \big[\, j\zeta_1 e^{jkd\cos(\varphi-2\pi/M)} \ j\zeta_2 e^{2jkd\cos(\varphi-4\pi/M)} \ \cdots$$
$$\cdots \ j\zeta_M e^{jk(M-1)d\cos(\varphi-2\pi)} \big] \tag{3.50}$$

where $\zeta_m = -(kd/2)\sin(\pi/M)\sin(\varphi-2m\pi/M)$. We may as well write the following products:

$$\boldsymbol{a}^{\mathrm{H}}\boldsymbol{a} = 1 + 1 + \ldots + 1 = M$$
$$\boldsymbol{d}^{\mathrm{H}}\boldsymbol{d} = \zeta_1^2 + \zeta_2^2 + \ldots + \zeta_M^2 =$$
$$= \big[(kd/2)\sin(\pi/M)\big]^2 \sum_{m=1}^{M} \big(\sin(\varphi-2m\pi/M)\big)^2 \tag{3.51}$$
$$\boldsymbol{d}^{\mathrm{H}}\boldsymbol{a} = -j\zeta_1 - j\zeta_2 - \ldots - j\zeta_M =$$
$$= j(kd/2)\sin(\pi/M) \sum_{m=1}^{M} \sin(\varphi-2m\pi/M)$$

Substituting (3.51) into (3.46), and assuming that the number of radiators in the array is large enough, i. e. $M \gg 1$, we get the following expression for the CRLB of a circular array comprised of M radiators with omnidirectional radiation pattern:

$$\mathrm{CRLB} = \frac{1}{2L\,\mathrm{SNR}}\frac{1}{k^2 r^2\,M} \tag{3.52}$$

It is possible to observe that for the ideal situation of uncoupled radiators, if the aperture of the array, given by the radius r of the circular arrangement, is kept fixed but the number of elements is increased, the CRLB will decrease proportionally to M. However, when mutual coupling is properly accounted for, the resulting power mismatch will lead to reduced SNR, and may overcome the improving effect of the increased number of elements in a fixed array aperture.

Until this point, the equations presented in this section rely on the assumption that arrays of antennas with omnidirectional pattern is used for direction finding. However, for general array manifold characterization, three relations can still be established, independent of the individual antenna element radiation pattern:

$$\mathrm{CRLB}(L) \geq \mathrm{CRLB}(L+1) \tag{3.53}$$

$$\mathrm{CRLB}(M) \geq \mathrm{CRLB}(M+1) \tag{3.54}$$

$$\begin{bmatrix} \boldsymbol{I}_N & 0 \end{bmatrix} \mathrm{CRLB}(N+1) \begin{bmatrix} \boldsymbol{I}_N \\ 0 \end{bmatrix} \geq \mathrm{CRLB}(N) \tag{3.55}$$
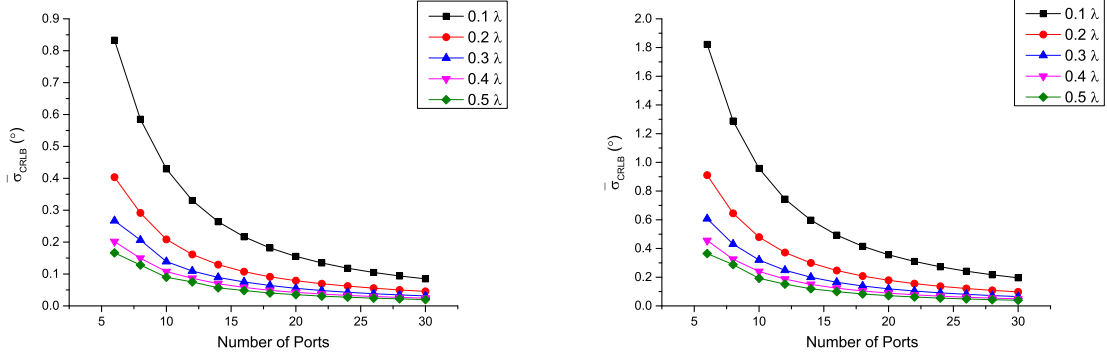
(a) Estimation of θ.

(b) Estimation of φ.

Figure 3.14.: CRLB over number of ports and different inter-element separation, for isotropic antenna elements.
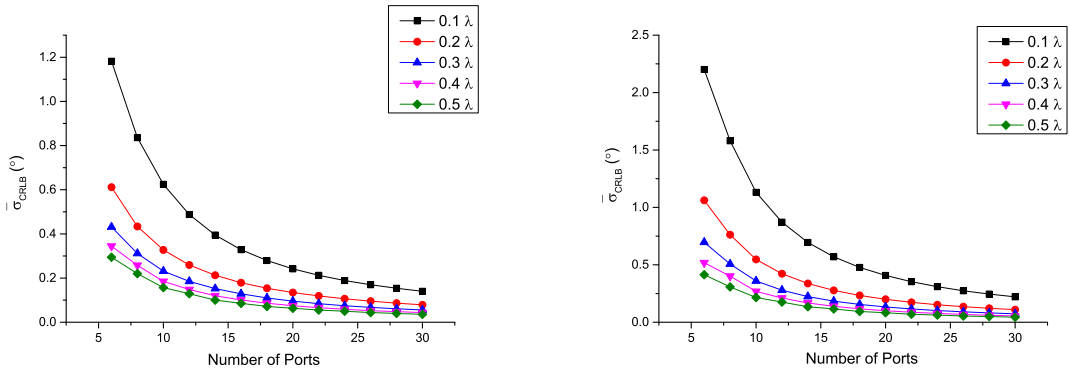
(a) Estimation of θ.

(b) Estimation of φ.

Figure 3.15.: CRLB over number of ports and different inter-element separation, for L-Quad antenna arrays.

Equations (3.53), (3.54) and (3.55) imply, respectively that the CRLB decreases monotonically with increasing number of snapshots and radiators in the antenna array, but increases monotonically with increasing number of impinging signals. For proof of Equations (3.53) and (3.54), the reader should consult Appendix A. For proof of Equation (3.55), we refer to [28].

Figures 3.14 and 3.15 show, for an ideally uncoupled array of isotropic elements and an ideally uncoupled L-Quad array, respectively, how the CRLB varies with the number of elements and the inter-element spacing in the array. It is possible to observe that, without accounting for mutual coupling, the CRLB for DoA estimation is the higher, the lower the number of elements becomes and the more closely the elements are placed with respect to each other.

3.6. A Practical Design Decision Example

In the previous section, we were able to observe how direction finding is affected by the number of elements in an array, the spacing between neighboring elements and the coupling. It is clear that for larger number of sensors, or for arrays with larger inter-element spacing, the accuracy and the resolution of the DoA estimation is improved, as expected due to the higher SNR and the enlarged aperture, respectively. However, in a situation where the aperture of the array needs to be fixed, if one increases the number of elements in the array, it becomes necessary to place them together more closely, leading to stronger mutual coupling. On the other hand, the larger number of elements leads to an improvement of resolution and accuracy of the DoA estimation, due to increased SNR and degrees of freedom. It is necessary to investigate which effect plays a stronger role to the direction finding performance: stronger coupling or increased SNR.

The following practical example investigates linear dual-polarized L-Quad arrays with fixed length of 44 cm. Results for three arrangements were compared: a five-element array with 0.5λ spacing, a six-element with 0.4λ spacing and a seven-element array with $\lambda/3$ spacing as depicted in Figure 3.16.

Figure 3.17 illustrates the total gain of the three antenna arrays investigated, for a cut at $\vartheta = 45°$ (Figure 3.17a) and a cut at $\varphi = 45°$ (Figure 3.17b). Figure 3.18 illustrates the individual gain (ϑ polarization) of one antenna port, for a cut at $\vartheta = 45°$ (Figure 3.18a) and a cut at $\varphi = 120°$ (Figure 3.18b).

From Figures 3.17 and 3.18 one can observe that for higher number of elements in the array, the coupling that arises from the closer inter-element spacing exceeds the gain that would be naturally observed in ideally uncoupled arrays, and reduces the total and individual gains.
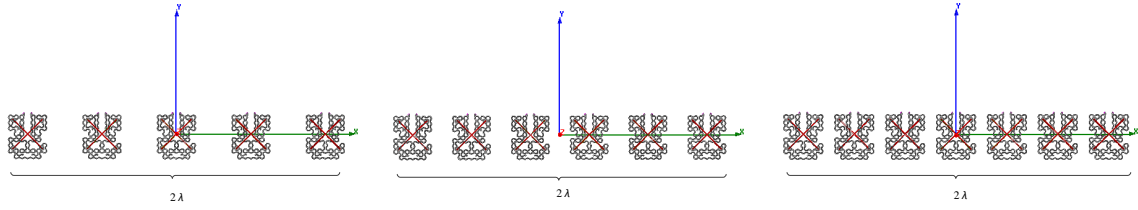
(a) Five-element L-Quad array.   (b) Six-element L-Quad array.   (c) Seven-element L-Quad array.

Figure 3.16.: Linear L-Quad antenna arrays 44 cm long.
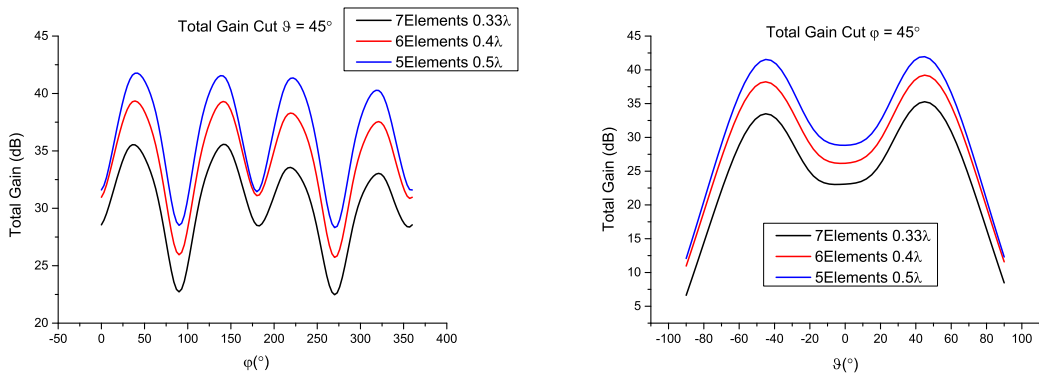
(a) Total gain in dB - cut at $\vartheta = 45°$.   (b) Total gain in dB - cut at $\varphi = 45°$.

Figure 3.17.: Total Gain – L-Quad Linear Antenna Array.
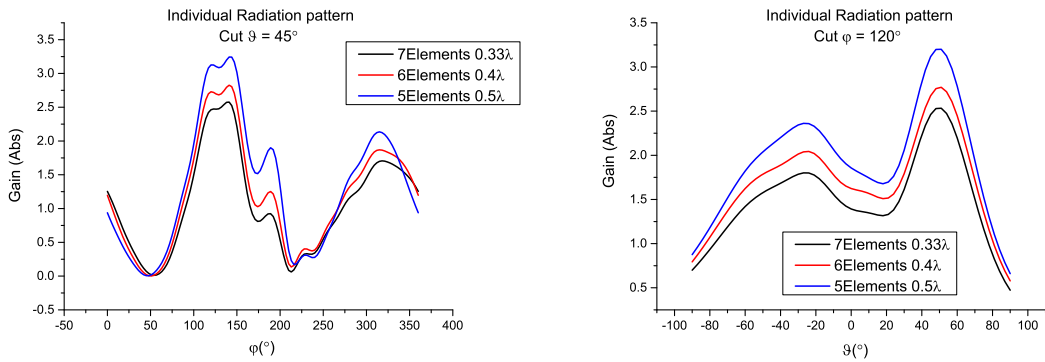
(a) Individual port gain in absolute value - cut at $\vartheta =$ (b) Individual port gain in absolute value - cut at $\varphi =$ 45°.   120°.

Figure 3.18.: Individual Port Gain – L-Quad Linear Antenna Array.

Table 3.1 depicts results for DoA accuracy (mean CRLB over all elevation and azimuth angles over the grid) for the five-element, the six-element and the seven-element dual-polarized array. Results were compared for the accuracy of the azimuth estimation (φ direction). Note that the CRLB is the higher, the larger the number of elements are placed in the array with aperture fixed.

	CRLB
Five-Element $- 0.5\lambda$	$0.0889°$
Six-Element $- 0.4\lambda$	$0.0913°$
Seven-Element $- \lambda/3$	$0.1040°$

Table 3.1.: Effects of coupling to direction finding accuracy - fixed aperture - linear array

We now proceed to investigating L-Quad arrays in circular arrangements with overall diameter of 22 cm. It is necessary to decide on whether to use five elements with 0.5λ spacing, six elements with 0.35λ spacing or seven elements with 0.35λ spacing, as depicted in Figure 3.19. Figure 3.20 illustrates the total gain of the three antenna arrays investigated, for a cut at $\vartheta = 30°$ (Figure 3.20a) and a cut at $\varphi = 0°$ (Figure 3.20b). Figure 3.21 illustrates the individual gain (ϑ polarization) of one antenna port, for a cut at $\vartheta = 15°$ (Figure 3.21a) and a cut at $\varphi = 60°$ (Figure 3.21b).


(a) Five-element L-Quad array. (b) Six-element L-Quad array. (c) Seven-element L-Quad array.
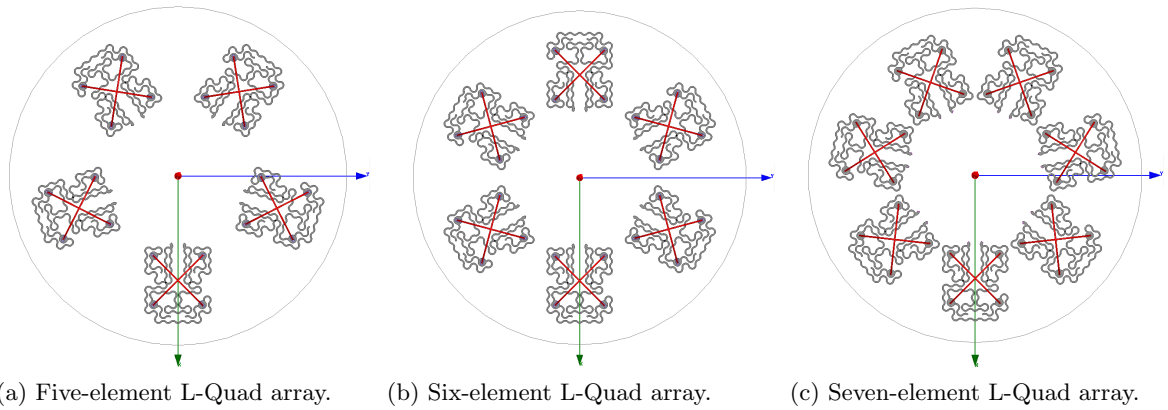
Figure 3.19.: Circular L-Quad antenna arrays with 22 cm diameter.

Table 3.2 depicts results for DoA accuracy (mean CRLB over all elevation and azimuth angles over the grid) and resolution (mean resolution assuming two sources from all elevation and azimuth angles over the grid) for the five-element, the six-element and the seven-element arrays.
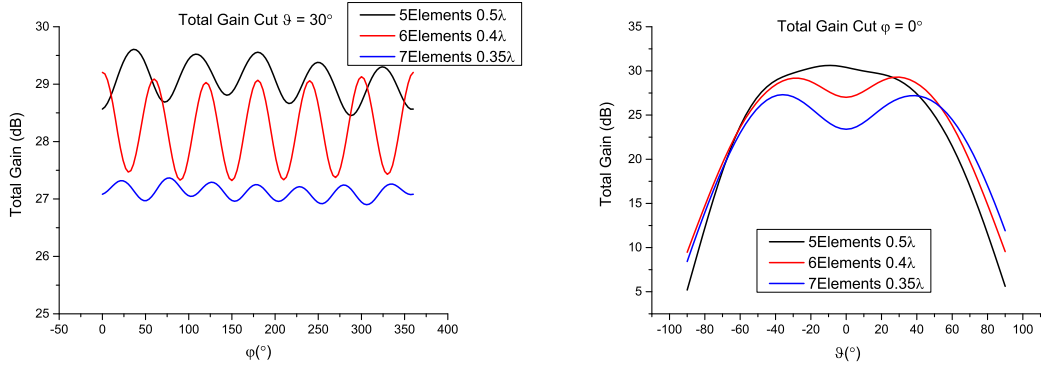
(a) Total gain in dB - cut at $\vartheta = 30°$.

(b) Total gain in dB - cut at $\varphi = 0°$.

Figure 3.20.: Total Gain – L-Quad Circular Antenna Array.
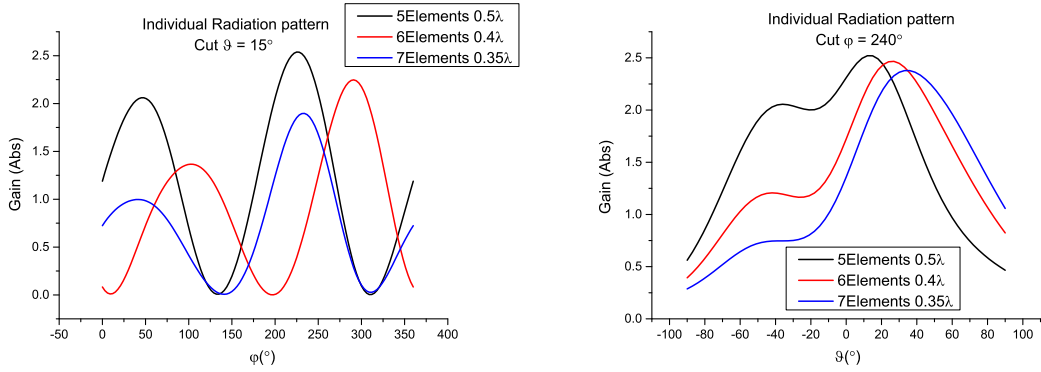
(a) Individual port gain in absolute value - cut at $\vartheta = 15°$.

(b) Individual port gain in absolute value - cut at $\varphi = 60°$.

Figure 3.21.: Individual Port Gain – L-Quad Circular Antenna Array.

	CRLB$_\vartheta$	**CRLB$_\varphi$**	**Res$_\vartheta$**	**Res$_\varphi$**
Five-Element − 0.5λ	0.1249°	0.0599°	1.9397°	2.1548°
Six-Element − 0.4λ	0.1363°	0.0626°	1.9592°	2.1693°
Seven-Element − 0.35λ	0.1480°	0.0666°	1.9823°	2.1785°

Table 3.2.: Effects of coupling to direction finding accuracy and resolution - fixed aperture - circular array

Figure 3.22 compares results for the CRLB of the estimation of ϑ for the three arrangements investigated in the circular array. It is possible to observe that the array with seven elements exhibits higher mutual coupling, and as a consequence, the bound for the variance of the DoA estimation (given by the CRLB) is higher, as expected from the analysis of the individual element gain and the total antenna gain patterns. An extended investigation on scenarios where the aperture of the array is kept fixed due to constraints imposed by the application is carried out in Chapter 5.
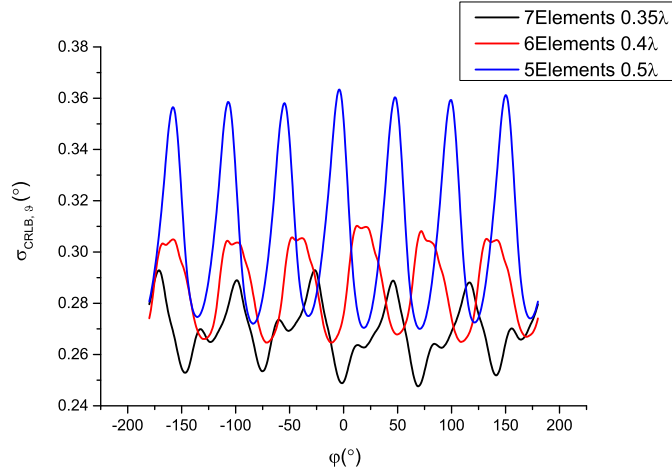
Figure 3.22.: CRLB for the estimation of ϑ, cut $\vartheta = 80°$ - Circular L-Quad Array with fixed aperture as in Figure 3.19.

3.7. Antenna Array Calibration

High Resolution Parameter Estimation (HRPE) techniques strongly rely on the precise characterization of the array manifold and three are the immediate ways of obtaining the array response to be fed to direction finding algorithms. First of all, if it is possible to analitically derive the single isolated radiator response, one can make use of the array factor presented in Section 3.2 to get to the response of each element when positioned in an array. This approach clearly does not account for the mutual coupling when the elements are placed closely to each other or for possible ohmic losses within the array. Second of all, with the use of a three-dimensional electromagnetic simulation tool, such as Ansoft HFSS [39], it is possible to get the simulated array response, which considers coupling and ohmic losses, if the properties of project materials are adequately modeled. However, after manufacturing the

antenna, deviations to the prototyped design may occur with respect to the dimensions, ohmic losses, dielectric losses, positioning, or material properties. As a consequence, there will be a mismatch between the model considered and the real antenna array, leading to degrading estimation performance. To avoid model mismatch, a more realistic array manifold may be obtained through calibration measurements carried out in an anechoic chamber.

For this thesis, results are obtained from the elecromagnetic simulation tool Ansoft HFSS 14.0 [39] and from calibration measurements carried out in an anechoic chamber. The five-element L-Quad antenna array detailed in Section 3.4.2 was calibrated in the anechoic chamber located at the Technische Universität Ilmenau. Measurements were carried out by the Electronic Measurement Research Laboratory (EMT) and compared to simulation results for far field radiation patterns over frequency. Figure 3.23 depicts the antenna array under test.

Figure 3.23.: Antenna array under test.

3.7.1. Measurement Setup

The antena array under test is aligned and positioned at a distance from the transmiting antenna that is greater than the Fraunhofer distance ensuring far field radiation patterns [69] and is defined as:

$$d_f = \frac{2D^2}{\lambda} \tag{3.56}$$

where D is the physical length of the antenna array. The antenna under test is rotated along two axis as depicted in Figure 3.24, for measurement over a set of angle points in azimuth and elevation. The transmiting antenna is comprised of two ports for verical and horizontal polarization. The measurements are then recorded for each polarization and allows for full-polarimetric array response characterization. It is important to highlight that the antenna array response measurement is carried out for each port through the use of a switch that is responsible to switch between ports without the need to connect and disconnect cables for the measurement of the individual far field patterns, avoiding mechanical errors.
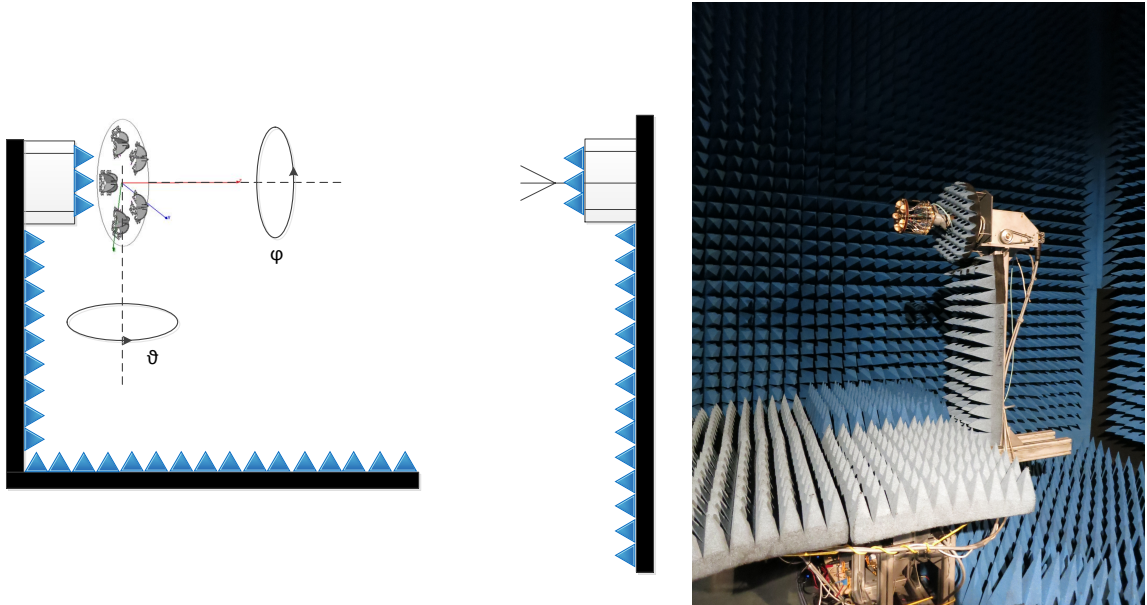
(a) Measurement setup and axis for rotation over azimuth and elevation.

(b) Antenna array and positioning system.

Figure 3.24.: Positioning system.

Figure 3.25 illustrates the calibration signal flow and details the steps that are included from the transmission of the source signal to the reception by the antenna array under test. The transmitting switch is responsible to switch between sending the signal to one of the two transmitting antennas (one for vertical polarization and the other for horizontal polarization) and sending it to the reference channel for calibration. The receiving antenna switch is responsible to switch between the eleven ports by which the array is comprised, including a probe
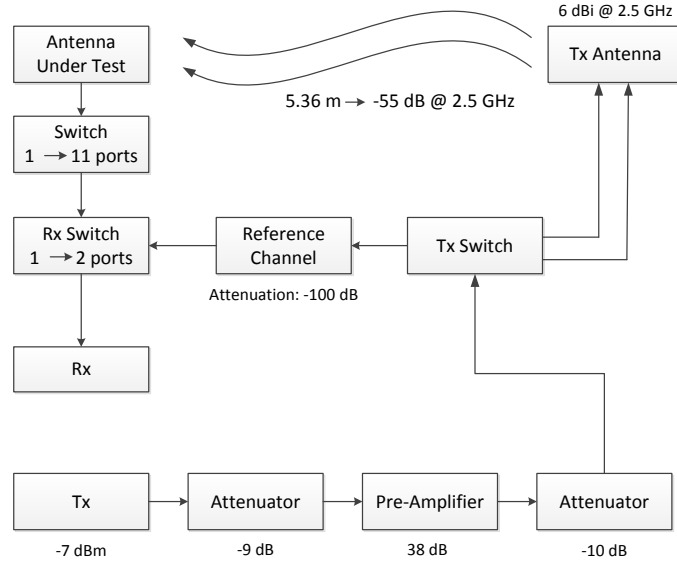
Figure 3.25.: Signal flow for the calibration measurement.

antenna. The measurement results included in this thesis were carried out for an L-Quad array comprised of five dual-polarized elements and one probe antenna, which is used to calibrate the array when operating in transmitting mode, resulting in eleven ports. Finally, the receiving switch is responsible to switch between receiving the signal from the antenna under test or from the reference channel, and sending it to the receiver for processing.

After the measurement is carried out for both polarizations, and over all azimuth and elevation angle points over the measurement grid, a calibration function needs to be applied to the measured far field radiation patterns to correct for losses in the measurement channel, losses in the cables (also referred to as back-to-back calibration) and to account for the transmiting antenna characteristics, [62]. Details on the calibration function are detailed as follows.

3.7.2. Back-to-Back Calibration of the Measurement System

The back-to-back calibration consists in correcting the measured array response with respect to the cables that are connected to the antenna under test and to the transmitting antenna. The system response over frequency is first measured without any of the receiving or transmitting antenna. The cable at the receiving antenna switch is connected to the cables at the transmitting antenna for each port, correspondent to one polarization (vertical or horizontal), giving rise to the estimated system frequency response denoted by $G_{\mathrm{sys,H}}(f)$ and $G_{\mathrm{sys,V}}(f)$, for each port of

the transmiting antenna (horizontal and vertical, respectively).

3.7.3. Calibration of the Transmiting Antenna

Two identical transmiting antennas are used for the calibration of the antenna array response. Due to the fact that the array response measured is an output from the reception of what was transmited by the reference antenna, its frequency response needs to be accounted for and the measured response needs to be corrected in order to avoid inconsistent measurement. The transmiting antenna response for each horizontal and vertical polarization can be expressed as following.

$$G_{\text{Tx,H|V}}(f) = \sqrt{\frac{G_{\text{HH|VV}}(f)4\pi\tau f}{G_{\text{sys,H|V}}(f)}} \qquad (3.57)$$

where $G_{\text{HH|VV}}(f)$ is the reference antenna response when two identical antennas are pointed to each other, aligned, one acting as the receiver, the other as the transmiter (horizontal to horizontal or vertical to vertical), and the response is measured. The measurement is carried out when the port correspondent to the vertical polarization transmits from the transmiting antenna and the port correspondent to the vertical polarization receives from the receiving antenna. Analogous procedure is carried out for the horizontal polarization. The measurement is subsequently corrected by the free-space response $4\pi\tau f$, in which τ is the time delay between the two reference antennas, and by the system response, implying that the effects of the cables are also accounted for at this point. The square root in (3.57) is due to the fact that identical reference antennas are used for transmiting and receiving for the estimation of the reference frequency response.

The final antenna array under test response over frequency can be expressed with respect to the measured response and the calibration responses as following.

$$G_{\text{H|V}}(f) = \frac{G_{\text{measured,H|V}}(f)}{4\pi\tau f G_{\text{Tx,H|V}}(f) G_{\text{sys,H|V}}(f) e^{j\alpha_{ref}(f)}} \qquad (3.58)$$

where $\alpha_r ef(f)$ is the frequency dependent correction phase due to effects of phase drift from the calibration system. Positioning of the receiving and transmitting antennas is illustrated in Figure 3.26.

It is important to consider that there may still be errors that arise from the calibration procedure. In [30], the effects of calibration errors to the accuracy of DoA estimation were investigated as a source of model mismatch. It is important that the array manifold is char-
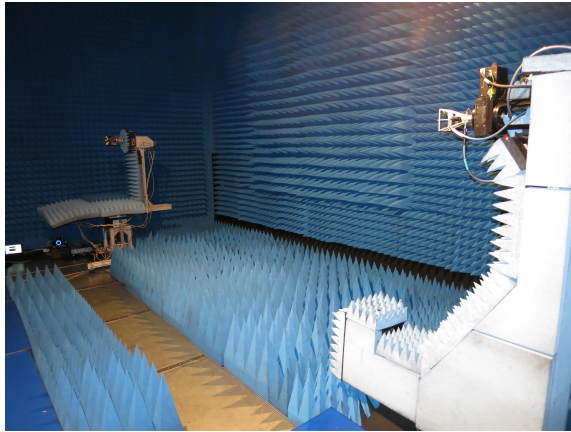
Figure 3.26.: Transmitting and receiving antenna in anechoic chamber.

acterized as precisely as posible for accurate DoA estimation.

3.7.4. Measurement Results

Figure 3.27a and 3.27b depict results for the measured gain at the two ports of which each array element is comprised, in comparison to the simulated gain, for the vertical and horizontal polarizations respectively. The results are presented for a cut at $\vartheta = 0°$. Figure 3.28a and 3.28b depict results for the measured gain at each array port in comparison to the simulated gain, for the vertical and horizontal polarizations respectively. For the vertical polarization, the results are presented for a cut at $\varphi = 45°$ for port 1 and for a cut at $\varphi = 135°$ for port 2. Since the ports are placed othogonally to each other in the azimuth (φ) direction, the radiation pattern will be shifted by 90° for a cut in φ. For the horizontal polarization, the results are presented for a cut at $\varphi = 135°$ for port 1 and for a cut at $\varphi = 45°$ for port 2.

Figure 3.29 depicts results for the total measured gain in dB of the antenna array, for a cut at $\varphi = 0°$, in comparison to the simulated total gain. The results are presented for one array port, for the two polarizations. The measurement results have proved to be in good agreement with the simulated antenna array response, allowing us to use the far field radiation patterns obtained through simulation for the evaluation of the theory presented in this thesis.
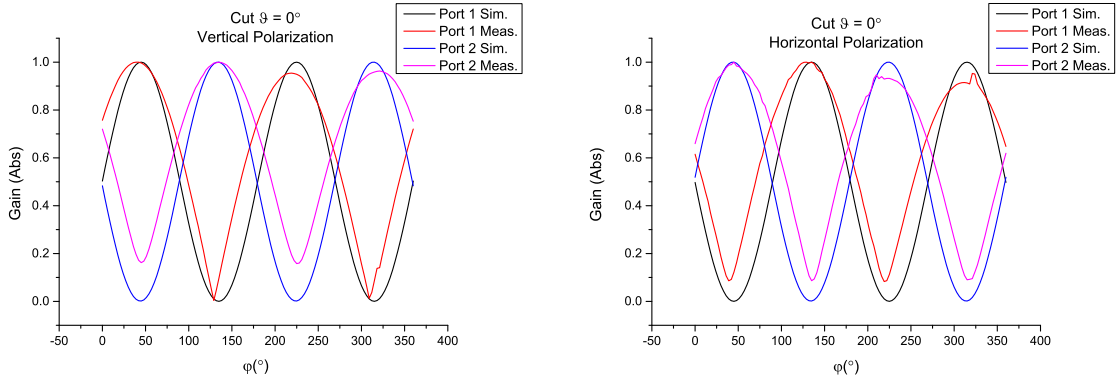
(a) Absolute value of Gain - vertical component - cut at $\vartheta = 0°$.

(b) Absolute value of Gain - horizontal component - cut at $\vartheta = 0°$.

Figure 3.27.: Comparison between calibrated and simulated results for each array element in the vertical and horizontal polarizations, cut in ϑ.
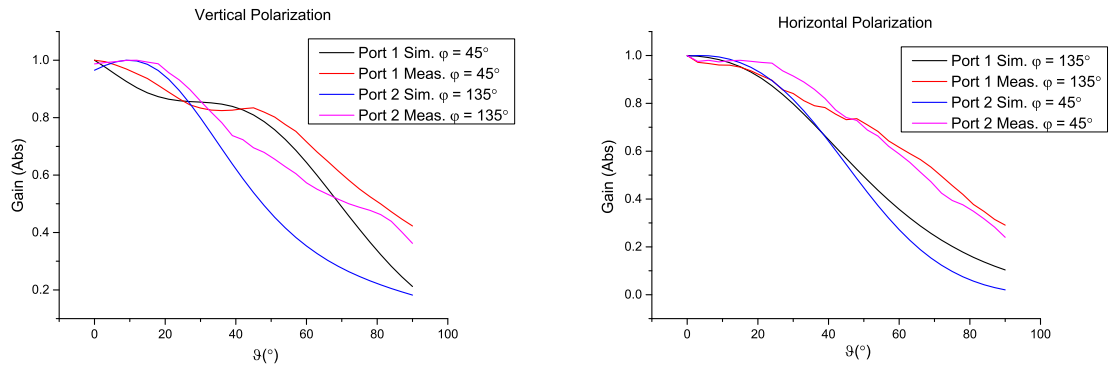
(a) Absolute value of Gain - vertical component - cut in ϕ.

(b) Absolute value of Gain - horizontal component - cut in ϕ.

Figure 3.28.: Comparison between calibrated and simulated results for each array element in the vertical and horizontal polarizations, cut in φ.
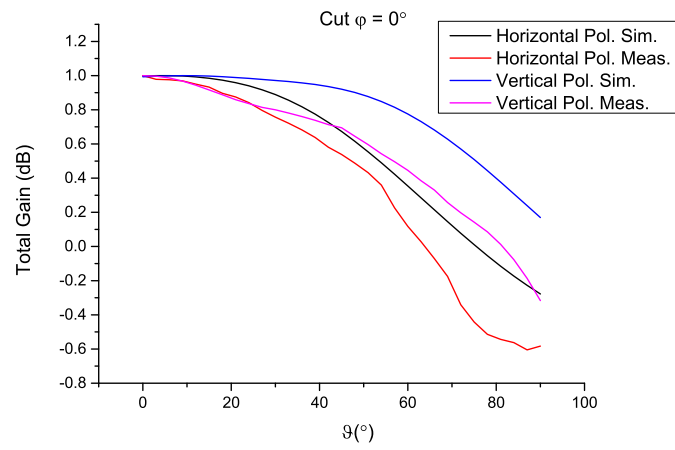
Figure 3.29.: Total array Gain in dB - cut at $\varphi = 0°$.

4. Assessment of Coupling Compensation in Compact Antenna Arrays for Direction Finding

4.1. Antenna Arrays Fundamental Modes of Radiation

In the last chapter, we detailed the mechanism of power flow within a M-port antenna array, and listed the three main sources of power loss: dissipation via Ohmic heating in conducting materials, reflection arising from impedance mismatch at the array input ports, and coupling between neighboring elements. The mutual coupling gives rise not only to power mismatch, but also to distorted individual radiation patterns [33, 34]. The radiation pattern of an isolated radiator may significantly deviate from the radiation pattern if positioned in an array under severe mutual coupling. Both power mismatch within the antenna array and distorted radiation patterns may give rise to significant degrading effects to the direction finding of impinging electromagnetic waves.

Several publications such as [30, 35, 75, 74, 106, 107, 73, 108, 109] address mutual coupling effects to direction finding and present solutions on how to mitigate them. In [30] it is stated that precise knowledge of the resulting distorted radiation pattern preserves DoA estimation quality, since only matching the correct data model would deliver correct estimation result. Normally, we would get the array manifold of the realized antenna array from calibration measurement in a well-defined reference environment, which can also be supported by some in situ reference measurements (to consider the factors of influence that change with time). In that sense, the impact of coupling to radiation patterns is correctly taken into account. But as this model is applied in the digital domain, it does not consider the loss of SNR due to power mismatch, since this happens before sampling. As a consequence, although this approach may be enough in case of weak coupling, it can be observed that the performance loss becomes severe for strong coupling. The degraded performance does not seem to be a consequence exclusively of mismatch loss at the antenna ports. The reason is that, in case of increasing coupling, the array manifold matrix will become more and more ill-conditioned. From the fundamentals of direction finding, we know that the differential information at antenna array outputs is the key as indicator of DoA. Hence, it may make sense also to decouple (meaning "compensating the coupling") by lossless circuit elements before sampling, in order to maximize the SNR for this differential information.

In [110, 37, 111, 112], techniques are investigated to increase the isolation between antenna

ports within the analog domain prior to digital conversion with the use of a lumped RF decoupling network. By Volmer, [33], decoupling and matching was achieved with the use of distributed elements, which are designed based on the analysis of the array radiation eigenmodes, which complement the S-parameters for the description of the array. It was shown in the above references that the resulting network of antennas and DMN directly launches the array radiation eigenmodes. This results from the close interaction of the passive Decoupling and Matching Network (DMN) with the physical antennas by reactive exchange of energy. So we argue that the DMN together with the physical antennas should be considered as a "new" antenna array. Hence, the output (eigenmodes) can be individually matched and even left unused if their contribution can be considered as minor. Of course, the resulting radiation patterns have to be precisely measured (including all implementation losses) and subsequently used as reference for DoA estimation.

The eigenmode decomposition approach, first introduced by Stein [113] and further detailed in [114, 115, 116], describes the antenna as an array of ideally uncoupled ports and orthogonal radiation patterns. The antenna array radiation pattern is decomposed into fundamental modes of radiation, each with an efficiency that measures the amount of power radiated to the far field, and defined as eigenefficiency. The array eigenefficiencies complement the S-parameters for the analysis of coupling within the array. Strongly coupled arrays with inter-element spacing smaller than half of the free-space wavelength often exhibit modes with very low radiation efficiency due to the high amount of incident power that is reflected as a consequence of coupling to the neighboring elements and is thus, not available for radiation. The spread between the highest and the lowest efficiencies is the larger, the stronger the mutual coupling becomes. The lowest eigenefficiency may be then a useful metric for the evaluation of mutual coupling in compact arrays, since it may become prohibitive low and inhibit the use of the antenna array for certain mobile communication applications.

The eigenefficiency will determine the SNR of each mode and it becomes important to ensure high modal efficiency, especially in low SNR environment. Low-efficiency modes may be discarded if the correspondent SNR is not high enough for HRPE [30]. In high SNR regimes, on the other hand, it may be possible to take some advantage of the low efficiency modes, assuming that the data is precisely modeled, implying that it is necessary to know a priori the radiation pattern of each eigenmode.

As detailed in the last chapter, the antenna scattering parameters, which may be used as a means to characterize mutual coupling within the array, is related to the radiation matrix of the antenna array, when Ohmic losses may be neglected, by:

$$\boldsymbol{H} = \boldsymbol{I} - \boldsymbol{S}^H \boldsymbol{S} \tag{4.1}$$

When the losses in the array cannot be neglected (which can be the case for several antennas and especially for microstrip patch arrays), the computation of the radiation matrix needs to take into account the radiation far field patterns as in Equation (3.37).

As assessed in the last chapter, ideally uncoupled arrays, with perfect impedance matching at each excitation port, neglecting Ohmic losses, will exhibit diagonal radiation matrix with diagonal elements equal to unity, implying 100% radiation efficiency. Since the matrix $\boldsymbol{H}$ is Hermitian, it is possible to diagonalize it through the following transformation.

$$\boldsymbol{\Lambda} = \boldsymbol{Q}^H \boldsymbol{H} \boldsymbol{Q} \tag{4.2}$$

where $\boldsymbol{\Lambda} \in \mathbb{R}^{M \times M}$ is a diagonal matrix with each diagonal element λ_m representing the m-th mode eigenefficiency and $\boldsymbol{Q} \in \mathbb{C}^{M \times M}$ is the matrix comprised by the M eigenvectors $\boldsymbol{q}_m$, the eigenmodes. The matrix $\boldsymbol{Q}$ characterizes the fundamental modes of radiation of an antenna array and the matrix Λ comprises the correspondent modal radiation efficiencies, the eigenefficiencies.

4.2. Multipath Rayleigh Fading

It is well known that the performance of communication systems is heavily dependent on the channel through which the waves travel. This channel is also referred to as propagation channel and characterizes the behavior of a transmitted electromagnetic wave on the way to a receiving system. The properties of the propagation channel are dependent not only on parameters such as the frequency of the propagating wave and the distance between transmitter and receiver, but also on the physical characteristics of the surrounding environment. The propagation channel needs to be accurately modeled in order to allow for the prediction of the amount of power lost by a wave propagating through it.

In communication systems, effects such as multipath significantly affect the characteristics of the signal captured by the receiving antenna, and may degrade the performance of applications based on DoA estimation. If the link between transmitter and receiver has characteristics that allow the traveling wave to reflect or diffract at obstacles, not only one single copy but multiple copies from the same signal will be captured at the receiving end. This effect is also referred to as multipath and occurs when besides the line of sight between transmitter and receiver,

there are obstacles at which the wave is scattered, giving rise to a multiplicity of possible paths through which the wave can travel.

Multipath may implicate signal coherency, since delayed multipath wave copies from the same source appear to be correlated as long as the multipath excess delay is lower than the inverse of the modulation bandwidth. The distinction between coherent and non-coherent components has major impact on parameter estimation procedure, e.g. direction finding, and asymptotic performance of the estimator, as some kind of statistical averaging for correlation estimation may be involved [55]. So, obviously, multipath can considerably complicate the DoA estimation procedure.

Figure 4.1 shows a scattering environment comprised by some buildings, the transmitting and the receiving antenna. The wave traveling through the path correspondent to the line of sight arrives at the receiver with a time delay denoted by τ_0. The waves arriving from multiple paths arrive at the receiver with different time delays, denoted by τ_1, τ_2 and τ_3.
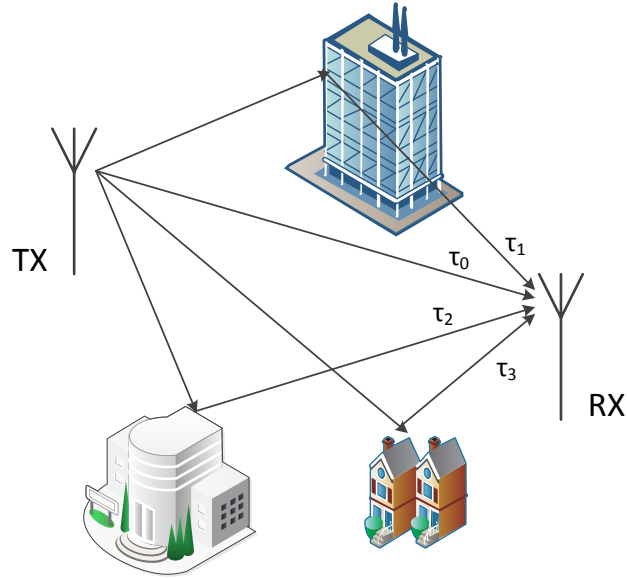
Figure 4.1.: Scattering environment.

In order to resolve the multipath components captured, a receiving antenna array needs to exhibit diversity characteristics that are related to the number of spaced radiators available for the reception of the incoming signals. From the fundamentals of direction finding, we know that the differential information at antenna array outputs is the key as indicator of DoA. The receiving system thus exploits the antenna spatial diversity and the DoA dependent phase difference between the signals captured by each radiator in the array to accurately process

the received signals. Other examples of applications that exploit spatial diversity are smart antennas and MIMO (Multiple Input Multiple Output) communication systems, which control and adapt the antenna beam pattern in order to resolve multipath components in a scattering environment.

If the array is strongly coupled, a significant fraction of the signal arriving at one radiator flows to the neighbors, and as a consequence, spatial diversity is lost due to the correlation between the outputs from the array elements. This loss is referred to as diversity loss and may substantially degrade the performance of the application intended. In DoA estimation based applications, when compact antenna arrays are used for reception, diversity loss renders lower estimation accuracy and resolution, and it becomes highly desirable that the degrading effects are properly accounted for and restored.

A commonly utilized propagating channel model, used to predict the loss due to multipath effects, is the Rayleigh model. It relies on the fact that, in a channel with high number of multipath components, the complex envelope of the correspondent impulse response may be adequately modeled as a Gaussian distribution, irrespective to the characteristics of the signal. The effect due to time delay spread, which occurs when the transmitted signal arrives at the receiver through multiple paths, is also known as fading, and is hereafter referred to as Rayleigh fading.

In scattering environments, for applications that rely on the antenna array spatial diversity for accurate performance, it is important to assess the loss that occurs due to Rayleigh fading. In [34], compact antenna arrays were investigated for diversity reception in Global Navigation Satellite Systems (GNSS). In [117], a detailed description of the effects of fading in terms of diversity loss (or gain) was reported with the aim of evaluating compact antenna arrays with focus on diversity applications. The diversity gain is established as the gain observed when multiple sensors are used to capture the receiving source signals, in comparison to a single matched radiator. It is defined as the ratio of power fading with and without diversity with an outage probability denoted by p. When the outputs at each antenna port are combined, it is possible to improve the degrading effects caused by fading. The approximate expression for the diversity gain is given by [118]:

$$G_d(\boldsymbol{H}, p) \approx \frac{q}{p}\left[1 + q\frac{\operatorname{tr}(\boldsymbol{H}^{-1})}{n(n+1)}\right] \tag{4.3}$$

where $q = \sqrt[n]{n!\det(\boldsymbol{H})p}$. The loss observed when a coupled array is used for reception, and dissipation losses cannot be neglected, when compared to an uncoupled, matched, and lossless antenna array is then given by:

$$L_d(\boldsymbol{H})\,|_{dB} \approx -\frac{10}{n}\mathrm{logdet}(\boldsymbol{H}) \tag{4.4}$$

and is reported to be independent on the outage probability p for moderate coupling [118].

Note that diversity loss and diversity gain are not dependent on the DoAs or polarization state of the receiving signals. This is due to the fact that we assume uniform scattering environment and thus, the effects of fading are equally observed irrespective of direction and polarization.

This thesis focuses on direction finding based applications, instead of diversity communication systems. However, due to the fact that direction finding accuracy and resolution are directly dependent on the differential information between the array outputs, the diversity loss can be interpreted as a loss of degrees of freedom, which will directly affect the capability of an antenna array to resolve multipath components.

4.3. Decoupling and Matching Network

Having said that the electromagnetic coupling between radiators is a limiting factor for many applications, responsible for making part of the power, originally supposed to be radiated, to flow between elements, modifying the impedance of the antenna, and resulting in power mismatch and distorted radiated far-fields pattern [33, 112, 119], it becomes important to investigate solutions to compensate for the corresponding degrading effects. Since the effect of mutual coupling varies with the excitation in the transmitting mode and reciprocally with DoA in the receiving mode, the impedance of the antenna is not kept constant. As a consequence, it becomes impractical to design a matching network that is able to match all the antenna ports for all the possible DoAs of impinging signals. It becomes fundamental that a decoupling network is connected to the receiving (or transmitting) antenna, which is able to tackle mutual coupling. This section details a design procedure based on the previously presented eigenmode decomposition, for the characterization of transmission lines that render the required excitation at each of the antenna ports. However, the decoupling network may also be designed with the use of lumped elements, as in [37].

From the decomposition of the antenna array radiation matrix into fundamental modes of radiation, as presented in the last section, it is easy to observe that the matrix of eigenvectors guides into the design of the required decoupling network. Without any decoupling or matching network, we assume that the receiving or transmitting system is comprised of a set of M generators, with impedance $Z_{\mathrm{in},i}$ with $i = 1...M$, and a set of M radiators, that can be inter-

preted as M loads Z_i with $i = 1...M$. When a decoupling and matching network is connected to the system, the excitation currents from the generators become input to the network, which will combine and feed them to the antenna array in a specific fashion, depending on the design parameters. The system is illustrated in Figure 4.2.
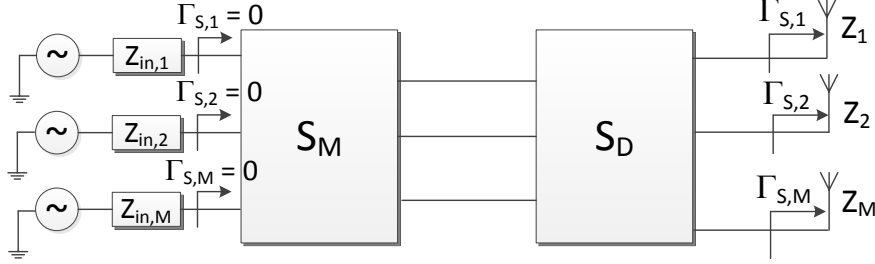

Figure 4.2.: Interconnection of decoupling and matching networks to a M-port antenna array.

In order to decouple the antenna array, the goal is to design a decoupling network that renders the excitation given by the eigenvectors. In [33], Volmer showed that a DMN can be designed as an interconnection of a matching network to a subsequent decoupling network for zero-valued reflection coefficients at the input ports of the system comprised of network and antenna array. Each network can be interpreted as a $2M$-port network connected to the M-port antenna array. The expressions for the scattering matrices of the two networks, $\boldsymbol{S}_\mathrm{M} \in \mathbb{C}^{2M \times 2M}$ and $\boldsymbol{S}_\mathrm{D} \in \mathbb{C}^{2M \times 2M}$, are then given by:

$$\boldsymbol{S}_\mathrm{M} = \begin{bmatrix} -\boldsymbol{\Gamma}_m & \sqrt{\boldsymbol{\Lambda}} \\ \sqrt{\boldsymbol{\Lambda}} & \boldsymbol{\Gamma}_m^* \end{bmatrix} \qquad \text{and} \qquad \boldsymbol{S}_\mathrm{D} = \begin{bmatrix} 0 & \boldsymbol{Q}^\mathrm{T} \\ \boldsymbol{Q} & 0 \end{bmatrix} \tag{4.5}$$

Owing to the fact that the sub-matrices that can be extracted from the scattering marix $\boldsymbol{S}_\mathrm{M}$ are diagonal, the matching network can be realized as a set of M independent matching networks, each responsible to match one of the input ports of the following decoupling network.

Let us first analyze the effects of interconnecting the decoupling network to the antenna array with scattering parameters given by $\boldsymbol{S}$. The resulting scattering matrix was derived in [33] and is given by the following expression.

$$\begin{aligned} \boldsymbol{S}_\mathrm{SD} &= \boldsymbol{S}_\mathrm{D,11} + \boldsymbol{S}_\mathrm{D,12}\boldsymbol{S}(\boldsymbol{I} - \boldsymbol{S}_\mathrm{D,22}\boldsymbol{S})^{-1}\boldsymbol{S}_\mathrm{D,21} \\ &= \boldsymbol{Q}^\mathrm{T}\boldsymbol{S}\boldsymbol{Q} = \boldsymbol{\Gamma}_m \end{aligned} \tag{4.6}$$

The resulting scattering matrix from the interconnection of the decoupling network to the

antenna ports is diagonal implying that the input ports of the network are decoupled. More-over, from the interconnection of the matching network to the decoupling network, comes the resulting scattering matrix $\boldsymbol{S}_{\text{SDM}}$, given by:

$$
\begin{aligned}
\boldsymbol{S}_{\text{SDM}} &= \boldsymbol{S}_{\text{M,11}} + \boldsymbol{S}_{\text{M,12}}\boldsymbol{S}_{\text{SD}}(\boldsymbol{I} - \boldsymbol{S}_{\text{M,22}}\boldsymbol{S}_{\text{SD}})^{-1}\boldsymbol{S}_{\text{M,21}} \\
&= -\boldsymbol{\Gamma}_m + \boldsymbol{\Lambda}^{-1/2}\boldsymbol{\Gamma}_m(\boldsymbol{I} - \boldsymbol{\Gamma}_m^*\boldsymbol{\Gamma}_m)^{-1}\boldsymbol{\Lambda}^{-1/2} \\
&= -\boldsymbol{\Gamma}_m + \boldsymbol{\Lambda}^{-1/2}\boldsymbol{\Gamma}_m\boldsymbol{\Lambda}^{-1}\boldsymbol{\Lambda}^{-1/2} \\
&= -\boldsymbol{\Gamma}_m + \boldsymbol{\Gamma}_m = \boldsymbol{0}
\end{aligned}
\tag{4.7}
$$

As expected, the resulting scattering parameters are zero-valued, implying that the input ports of the DMN are decoupled and matched. At this point it is important to highlight that the power matching of the decoupling network input ports is independent of the impinging signal DoA. For networks comprised of distributed elements, it can be easily carried out by quarter-wavelength impedance transformers, or quarter-wavelength stubs, and details on the correspondent design can be found in microwave textbooks such as [120].

Considering that the new antenna array is comprised of a decoupling network connected to the antenna array ports, the new array manifold for each mode m, denoted by $\tilde{A}_m(\vartheta, \varphi)$ is given by:

$$
\tilde{A}_m(\vartheta, \varphi) = \frac{1}{\sqrt{\lambda_m}}\boldsymbol{q}_m^{\text{T}}\boldsymbol{A}(\vartheta, \varphi)
\tag{4.8}
$$

where $\boldsymbol{q}_m, \in \mathbb{C}^{M \times 1}$ is the m-th eigenvector, corresponding to the m-th column of the matrix of eigenmodes $\boldsymbol{Q}$. The array manifold comprised by the M fundamental modes of radiation can be written as:

$$
\tilde{\boldsymbol{A}}(\vartheta, \varphi) = [\tilde{A}_1 \ldots \tilde{A}_M]^{\text{T}} = \frac{1}{\boldsymbol{\Lambda}^{-1/2}}\boldsymbol{Q}\boldsymbol{A}(\vartheta, \varphi)
\tag{4.9}
$$

where we define $\boldsymbol{\Lambda}^{-1/2}$ as a diagonal matrix comprised by the square root of each λ_m, with $m = 1...M$. The magnitude and phase of the eigenvectors thus define the magnitude and relative phase of excitation at each port, for effective decoupling. The eigenmode excitation may be thus considered as an equivalent to beamforming. Additionally, matching networks may be designed independently for each mode, to ensure optimal power transfer. However, it is important to note that there is a trade-off between matching and frequency bandwidth, as discussed in [32]. Similar to the array manifold of the non-decoupled antenna, the "new array manifold" acts now as reference for HRPE and thus has to be precisely known either by

calibration measurements or by precise simulation carried out by 3D electromagnetic tools.

4.4. Radiation Modes of a Three-Element L-Quad Antenna Array

In this section, a simple example of the radiation characteristics of a three-element single-polarized L-Quad array will be presented to illustrate the radiation patterns of the antenna array when exciting the eigenmodes. The array operates at a central frequency of 1.75 GHz and the relative permittivity ϵ_r of the substrate on which the monopoles and the feeding network are printed is 3.38. The array is comprised of single-polarimetric radiating elements consisting of a single pair of monopoles, which acts as a dipole, as detailed in Section 3.5.2. The three-element array is depicted in Figure 4.3.
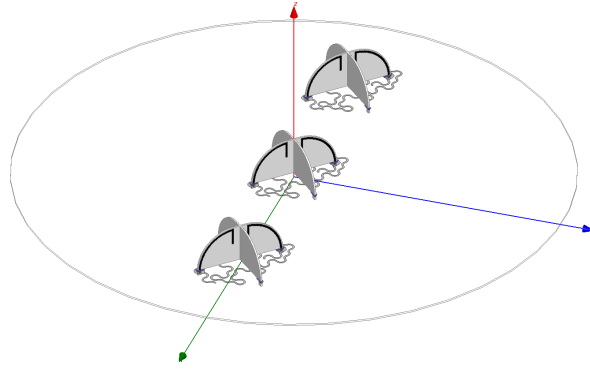
Figure 4.3.: Three-element single-polarized linear L-Quad array.

For the array in Figure 4.3 with 0.5λ inter-element spacing, at the central frequency, the diagonal elements of the radiation matrix, which correspond to the radiation efficiency of each element, computed using (4.1) and assuming that the Ohmic losses in the array can be neglected, are:

$$H_{11} = 0.9464 \qquad H_{22} = 0.9242 \qquad H_{33} = 0.9423 \tag{4.10}$$

After decomposition of the radiation matrix, the modal efficiencies, computed using (4) are:

$$\lambda_1 = 0.8309 \qquad \lambda_2 = 0.9877 \qquad \lambda_3 = 0.9942 \tag{4.11}$$

Finally, the squared magnitude and phase of the matrix of eigenvectors $\boldsymbol{Q}$ is given as following.

$$
|\,\boldsymbol{Q}\,|^2 = \begin{bmatrix} 0.2733 & 0.4949 & 0.2348 \\ 0.4287 & 0.0016 & 0.5698 \\ 0.2980 & 0.5065 & 0.1954 \end{bmatrix}
$$

$$
\angle\,\boldsymbol{Q} = \begin{bmatrix} 178.3719° & -3.7419° & 173.4413° \\ -16.7083° & -165.2908° & 160.7666° \\ -180° & 180° & 180° \end{bmatrix}
$$

The last column of the matrix $\boldsymbol{Q}$ corresponds to the mode with highest radiation efficiency, i.e., the even mode, whose eigenvector tells us that 23.48% of the power fed goes to port 1, 56.98% to port 2 and 19.54% to port 3. Additionally, port 1 is fed with relative phase shift of 173.4413°, port 2 with 160.7666° and port 3 with 180°. The first column corresponds to the pi mode, where the center element gets approximately half of the input power and the rest is equally split between the outer elements. In the pi mode, the ports are excited with 180° mutual phase difference. The second column corresponds to the odd mode, where no power goes to the central element, the power being split between the two outer ports with 180° phase difference.

It can be easily understood, that the eigenvectors guide the ports excitation for decoupled elements and based on them, the decoupling network is designed with the use of microstrip lines in order to ensure the required excitation magnitude and phase at each array feeding port. After decoupling, additional matching needs to be designed to improve the power efficiency of the least efficient modes.

Figure 4.4 depicts the radiation pattern for each feeding port at the three-element linear L-Quad array. Figure 4.5 shows the radiation pattern for each mode (even, odd and pi) when the eigenmodes are excited. Note that the higher the mode, the higher the number of nulls in the radiation pattern is observed. On the other hand, the higher the mode, the lower the gain becomes, as expected by the low eigenefficiency.

4.5. Radiation Modes of a Three-Element Probe-Fed Microstrip Patch Antenna Array

We now proceed to showing a simple example of the radiation characteristics of a three-element probe-fed microstrip patch array, as depicted in Figure 4.6. The array operates at a central

(a) Port 1   (b) Port 2   (c) Port 3

Figure 4.4.: Radiation pattern for each port of a 0.5λ three-element linear L-Quad array – cuts for $\varphi = 135°$.

(a) Even mode   (b) Odd mode   (c) Pi mode
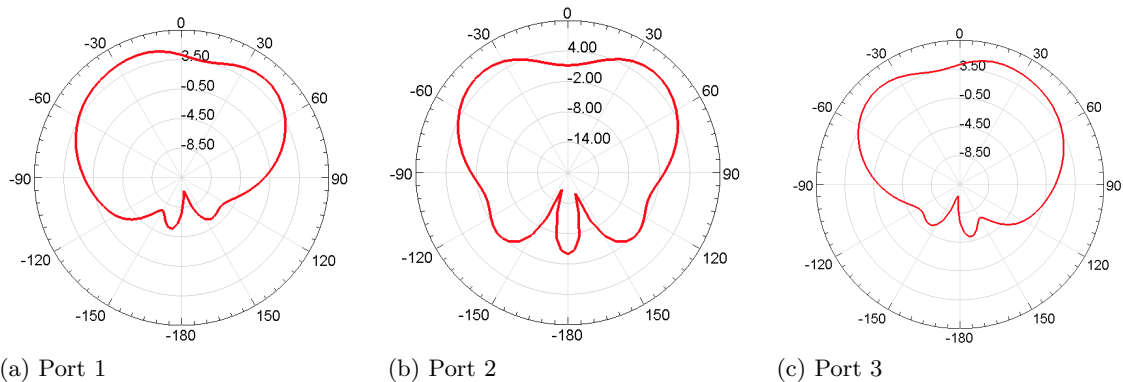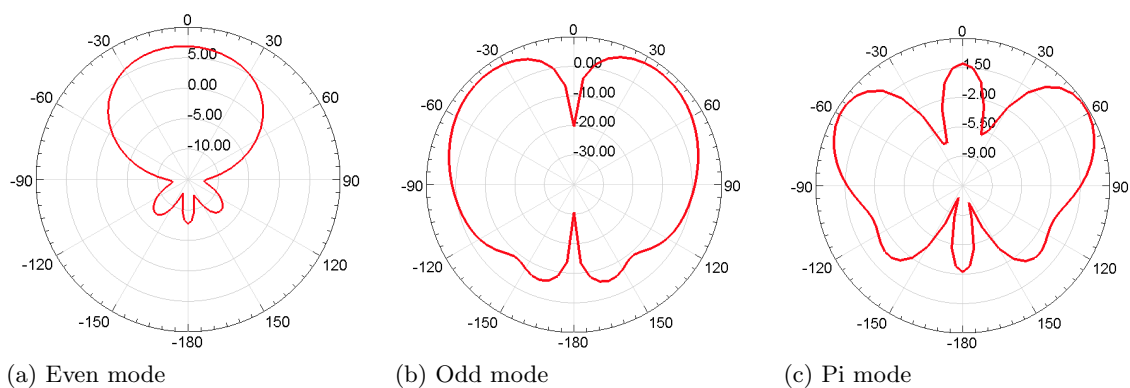
Figure 4.5.: Radiation pattern for each eigenmode of a 0.5λ three-element linear L-Quad array – cuts for $\varphi = 135°$.

frequency of 2.36 GHz and the relative permittivity ϵ_r of the substrate on which the patches are printed is 2.2. Each patch is designed with size 40 mm × 30 mm and we assume no Ohmic losses within the conducting material and no dielectric losses within the dielectric layer.
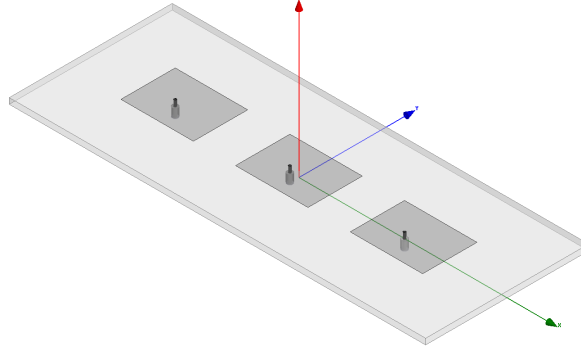

Figure 4.6.: Linear three-element single-polarized microstrip patch array.

For the array in Figure 4.6 with 0.5λ inter-element spacing, at the central frequency, the diagonal elements of the radiation matrix, that corresponds to the radiation efficiency of each element, computed using (4.1) and assuming that the Ohmic losses in the array can be neglected, are:

$$H_{11} = 0.9855 \qquad H_{22} = 0.9811 \qquad H_{33} = 0.9869 \tag{4.12}$$

After decomposition of the radiation matrix, the modal efficiencies, computed using (4) are:

$$\lambda_1 = 0.9740 \qquad \lambda_2 = 0.9861 \qquad \lambda_3 = 0.9935 \tag{4.13}$$

Finally, the squared magnitude and phase of the matrix of eigenvectors are given as following.

$$|\boldsymbol{Q}|^2 = \begin{bmatrix} 0.3404 & 0.1815 & 0.4781 \\ 0.4114 & 0.5814 & 0.0072 \\ 0.2482 & 0.2371 & 0.5148 \end{bmatrix}$$

$$\angle\boldsymbol{Q} = \begin{bmatrix} 13.7488° & -176.7817° & 9.3656° \\ -137.3964° & 132.0664° & -77.1287° \\ 0° & 180° & 180° \end{bmatrix}$$

The last column of the matrix $\boldsymbol{Q}$ corresponds to the mode with highest radiation efficiency,

in this case, the odd mode. The corresponding eigenvector tells us that 47.81% of the power fed goes to port 51.48% to port 3 and negligible power is fed to the center port. Additionally, port 1 is fed with relative phase shift of 9.3656° and port 3 with 180°, implying approximately 180° of relative phase shift between the outer ports. The first column corresponds to the pi mode, where the center element gets approximately half of the input power and the rest is equally split between the outer elements. In the pi mode, the ports are excited with 180° mutual phase difference. Finally, the second column corresponds to the even mode, where all the ports are excited with approximately the same relative phase and the center element gets approximately half of the input power, with the rest being equally split between the outer elements.

It can be easily understood, that the eigenvectors guide the ports excitation for decoupled elements and based on them, the decoupling network is designed in order to ensure the required excitation amplitude and phase. Since this example illustrates the radiation modes of an array designed with $0.5\,\lambda$ of inter-element spacing, and thus, low level of decoupling, the fundamental modes of radiation are high enough and do not require additional matching network.

Figure 4.7 depicts the radiation pattern for each feeding port at the three-element linear patch array. Figure 4.8 shows the radiation pattern for each mode (even, odd and pi) when the eigenmodes are excited. Note that, as with the L-Quad array, the higher the mode, the higher the number of nulls is observed in the fundamental radiation patterns.
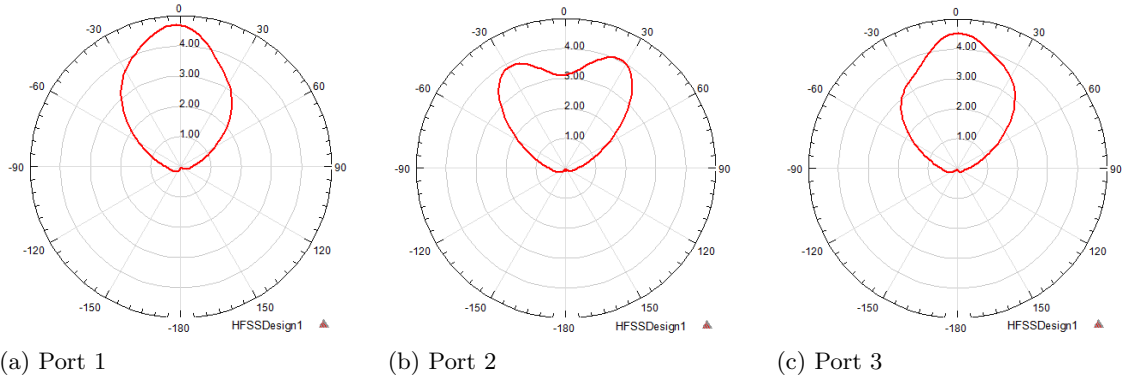

(a) Port 1   (b) Port 2   (c) Port 3

Figure 4.7.: Radiation pattern for each port of a 0.5λ three-element linear patch array – cuts for $\varphi = 0°$.
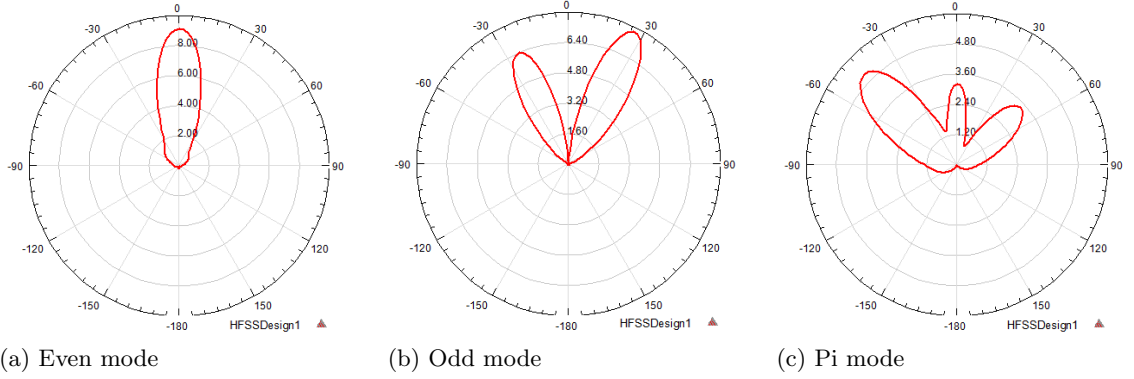
(a) Even mode   (b) Odd mode   (c) Pi mode

Figure 4.8.: Radiation pattern for each mode of a 0.5λ three-element linear patch array – cuts for $\varphi = 0°$.

4.6. Array Eigenefficiencies and the CRLB as Figures of Merit – Design Procedure

The last sections detailed the decomposition of the antenna array radiation matrix into fundamental modes of radiation, also referred to as eigenmodes, as a method for the evaluation of mutual coupling within the array and design of DMNs. We now proceed to investigating arrays in diverse arrangements and degrees of coupling with respect to the eigenefficiencies and direction finding capabilities, given by the CRLB, associated to the array far field radiation response. It is expected that the higher the coupling between elements in compact arrays, the lower the eigenefficiencies become, especially for the least efficient modes, also referred to as super-directive modes, given the fact that, as observed in the last two sections, the higher the mode, the higher the number of nulls in the radiation pattern is observed.

The super-directive modes are of major importance for direction finding, since directivity contributes to increase accuracy and resolution of DoA estimation. However, if the radiation efficiency associated to the super-directive mode, which dictates the correspondent SNR, is not high enough, the contribution will have neglecting effect on the overall performance of the array. The modes with low radiation efficiency may not significantly contribute for radiation, and may be as well neglected, lowering the signal gain. It is thus adequate to utilize the worst eigenefficiency as a figure of merit, since it allows for comparison to a pre-defined threshold below which the radiation efficiency of each mode cannot fall in order to ensure the required array performance for a certain application. This threshold may vary with the application intended.

Optimization of antenna arrays in terms of either the radiation efficiency [34], [121] or the CRLB [4], [3] has been proposed in recent publications. The goal of this section is to illustrate a design procedure aiming to find an array configuration that renders both maximum modal radiation efficiencies of the array (eigenefficiencies) and minimum CRLB for direction finding. As a consequence, both figures of merit are considered for array optimization.

Figure 4.9 depicts the four array arrangements investigated: cross, linear, circular and trapezium. The number of dual-polarized elements is kept fixed to five, resulting in ten ports.

(a) Circular Array.

(b) Cross Array.
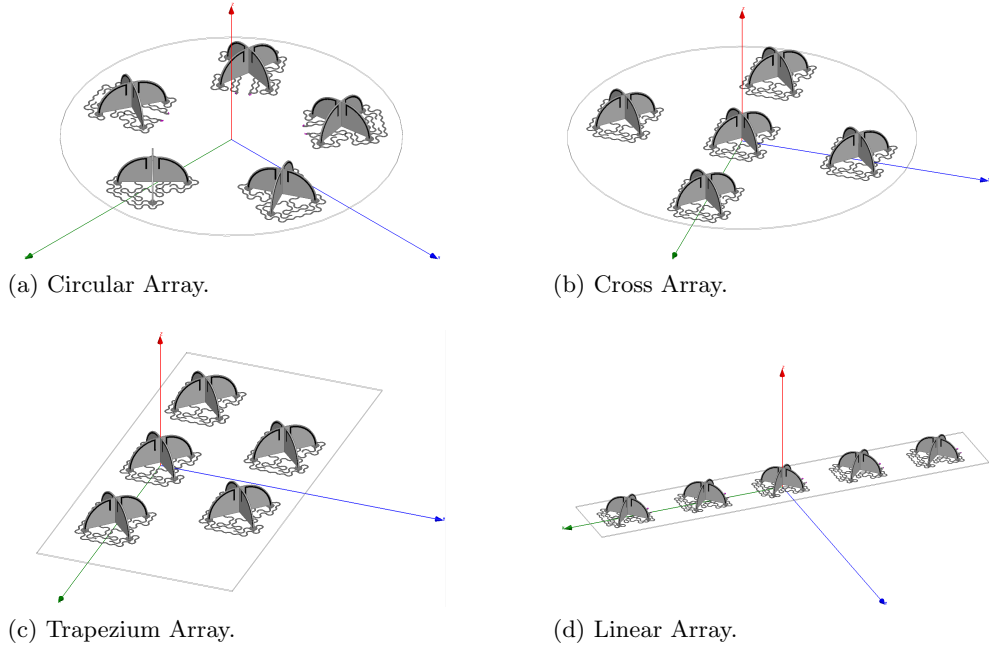
(c) Trapezium Array.

(d) Linear Array.

Figure 4.9.: The four array arrangements investigated.

We present results for the DoA estimation CRLB and the modal radiation efficiencies for the L-Quad antenna arrays. The aim is to analyze how the array arrangement affects both the coupling and the direction finding capability of the array in terms of the CRLB. The antenna 3D model is first designed in Ansoft HFSS 14.0 [39] and subsequently, outputs such as S-parameters and radiation patterns (realized gain and phase of the electrical far field) are fed to Matlab [41] for the direction finding and eigenefficiency calculation algorithm. The mean value of the CRLB over all possible elevation and azimuth angles is then obtained using EADF to interpolate and derivate the array manifold, and eigen-analysis is used to assess the coupling within the array. The goal is to minimize the CRLB and maximize the worst-case eigenefficiency ($\lambda_{\min}$) of the antenna array. Throughout the results, the SNR is assumed 20dB.

It is important to note that linear arrays may be affected in a different way by the antenna surrounding environment in comparison e.g. to circular arrays. The border effects, e.g., may be more pronounced in linear arrays than in circular arrays. However, the simulation carried out in this section considered all possible effects that may be observed in real antenna arrays with finite dimensions. Alternatively, antenna array measurements could be carried out for the precise characterization of the array far field response [122].

An analysis was drawn for the spacing between elements both with respect to the mean CRLB for direction finding and to the minimum modal radiation efficiency. The eigenefficiencies for inter-element spacing of 0.4λ and 0.5λ for the four array arrangements analyzed is shown in Figure 4.10a. Figure 4.10b depicts the CRLB for direction finding.
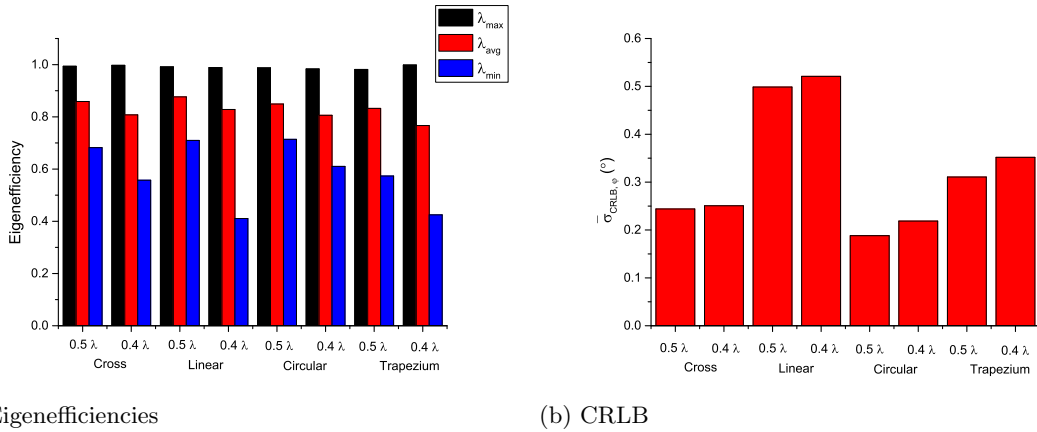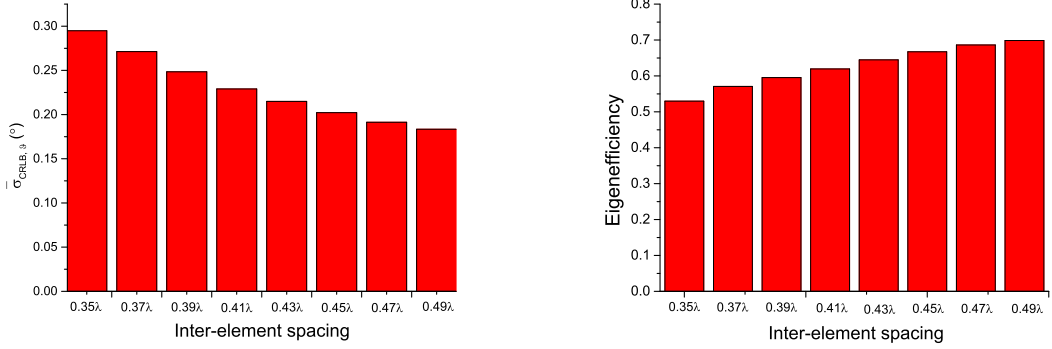

(a) Eigenefficiencies

(b) CRLB

Figure 4.10.: Eigenefficiencies and CRLB, for different array arrangements.

It is possible to conclude from Figure 4.10a and Figure 4.10b that the array arrangement that gives minimum mean CRLB and maximum worst-case eigenefficiency is the circular arrangement. Figure 4.11a depicts the plot for the mean CRLB and Figure 4.11b presents the worst-case eigenefficiency as a function of the array inter-element spacing for the circular arrangement. The calculations were carried out for a spacing range from 0.35λ to 0.5λ, with a step of 0.02λ.

For the inter-element spacing, a minimum mean CRLB and maximum worst-case eigenefficiency is obtained for the largest simulated inter-element spacing (0.5λ), as expected, since the larger the aperture, the higher the DoA estimation accuracy becomes, and the weaker the coupling between radiating elements in the array is observed. However, the analysis should be a tradeoff between the array size and direction finding accuracy. For lower values of the mean CRLB, the antenna array may become impractically large.

(a) Mean CRLB $\overline{\sigma}_{\mathrm{CRLB}}$ for different spacings.

(b) Worts-case eigenefficiencies for different spacings.

Figure 4.11.: CRLB and eigenefficiencies of circular L-Quad arrays, over inter-element spacing.

4.7. Cramér-Rao Lower Bound of Decoupled Arrays

For the computation of the CRLB to the DoA estimation of impinging waves using an array decoupled by eigenmode excitation, it is important to analyze how the derivatives of the modal eigen-patterns with respect to DoA behave. To this end, we may write the following expression for the derivative of the decoupled array manifold with respect to ϑ (analogous procedure for the derivative with respect to φ), recalling (4.9).

$$\frac{\partial}{\partial \vartheta} \tilde{A}_m(\vartheta, \varphi) = \frac{\partial}{\partial \vartheta} \left[\frac{1}{\sqrt{\lambda_m}} \boldsymbol{q}_m^{\mathrm{T}} \boldsymbol{A}(\vartheta, \varphi) \right] \tag{4.14}$$

Since the eigenvectors $\boldsymbol{q}_m$ are independent of ϑ and φ, Equation (4.14) can be expressed as:

$$\frac{\partial}{\partial \vartheta} \tilde{A}_m(\vartheta, \varphi) = \frac{1}{\sqrt{\lambda_m}} \boldsymbol{q}_m^{\mathrm{T}} \frac{\partial}{\partial \vartheta} \boldsymbol{A}(\vartheta, \varphi) \tag{4.15}$$

The derivatives of the orthogonal modes present, as a consequence, a beamforming with weights given by the eigenmodes. The matrix of the derivatives of each modal radiation pattern may be finally written with respect to the derivatives matrix of the antenna array manifold $\boldsymbol{D}$ as:

$$\tilde{\boldsymbol{D}} = \boldsymbol{\Lambda}^{-1/2} \boldsymbol{Q}^{\mathrm{T}} \boldsymbol{D} \tag{4.16}$$

where $\boldsymbol{\Lambda}^{-1/2}$ is a diagonal matrix comprised by the square root of each λ_m.

To conclude, the antenna radiation efficiency is dependent on how the array is excited and through eigenmodes excitation it is possible to ensure that the ports are decoupled. From (2.25), recalling the fact that $\boldsymbol{Q}$ is unitary, i.e. $\boldsymbol{Q}^{\mathrm{H}}\boldsymbol{Q} = 1$, and that the radiation matrix $\boldsymbol{H}$ is Hermitian, we derive the CRLB for a decoupled array using the eigenmodes approach:

$$
\begin{aligned}
\tilde{\mathrm{CRLB}}^{-1} &= 2T\,\mathrm{SNR}\,\{\tilde{\boldsymbol{D}}^{\mathrm{H}}\tilde{\boldsymbol{D}} - \tilde{\boldsymbol{D}}^{\mathrm{H}}\tilde{\boldsymbol{A}}(\tilde{\boldsymbol{A}}^{\mathrm{H}}\tilde{\boldsymbol{A}})^{-1}(\tilde{\boldsymbol{D}}^{\mathrm{H}}\tilde{\boldsymbol{A}})^{\mathrm{H}}\} \\
&= 2T\,\mathrm{SNR}\,\{\boldsymbol{D}^{\mathrm{H}}\boldsymbol{Q}^{*}\boldsymbol{\Lambda}^{-1/2}\boldsymbol{\Lambda}^{-1/2}\boldsymbol{Q}^{\mathrm{T}}\boldsymbol{D} \\
&\quad - \boldsymbol{D}^{\mathrm{H}}\boldsymbol{Q}^{*}\boldsymbol{\Lambda}^{-1/2}\boldsymbol{\Lambda}^{-1/2}\boldsymbol{Q}^{\mathrm{T}}\boldsymbol{A}(\boldsymbol{A}^{\mathrm{H}}\boldsymbol{Q}^{*}\boldsymbol{\Lambda}^{-1/2}\boldsymbol{\Lambda}^{-1/2}\boldsymbol{Q}^{\mathrm{T}}\boldsymbol{A})^{-1} \\
&\quad \times \boldsymbol{A}^{\mathrm{H}}\boldsymbol{Q}^{*}\boldsymbol{\Lambda}^{-1/2}\boldsymbol{\Lambda}^{-1/2}\boldsymbol{Q}^{\mathrm{T}}\boldsymbol{D}\}
\end{aligned}
$$

$$
\begin{aligned}
&= 2T\,\mathrm{SNR}\,\{\boldsymbol{D}^{\mathrm{H}}\boldsymbol{Q}^{*}\boldsymbol{\Lambda}^{-1}\boldsymbol{Q}^{\mathrm{T}}\boldsymbol{D} - \boldsymbol{D}^{\mathrm{H}}\boldsymbol{Q}^{*}\boldsymbol{\Lambda}^{-1}\boldsymbol{Q}^{\mathrm{T}}\boldsymbol{A} \\
&\quad \times (\boldsymbol{A}^{\mathrm{H}}\boldsymbol{Q}^{*}\boldsymbol{\Lambda}^{-1}\boldsymbol{Q}^{\mathrm{T}}\boldsymbol{A})^{-1}\boldsymbol{A}^{\mathrm{H}}\boldsymbol{Q}^{*}\boldsymbol{\Lambda}^{-1}\boldsymbol{Q}^{\mathrm{T}}\boldsymbol{D}\} \\
&= 2T\,\mathrm{SNR}\,\{\boldsymbol{D}^{\mathrm{H}}(\boldsymbol{H}^{\mathrm{T}})^{-1}\boldsymbol{D} - \boldsymbol{D}^{\mathrm{H}}(\boldsymbol{H}^{\mathrm{T}})^{-1} \\
&\quad \times \boldsymbol{A}(\boldsymbol{A}^{\mathrm{H}}(\boldsymbol{H}^{\mathrm{T}})^{-1}\boldsymbol{A})^{-1}\boldsymbol{A}^{\mathrm{H}}(\boldsymbol{H}^{\mathrm{T}})^{-1}\boldsymbol{D}\}
\end{aligned}
\tag{4.17}
$$

It is evident to see that if the fundamental modes are excited in the array, the CRLB becomes directly dependent on the array radiation efficiencies prior to decoupling and it is not straightforward to analytically relate the CRLB of the decoupled array to the CRLB prior to decoupling. Careful investigation of the CRLB for decoupled arrays is carried out in Chapter 5.

5. Evaluation of Real Antennas Arrays for Direction Finding

5.1. Effects of Antenna Polarization to Direction Finding

One of the greatest advantages of designing a dual-polarized antenna array for direction finding is the capability to tackle polarization mismatch, which may occur when waves impinge on the array with unknown polarization. As an example, if a vertical polarized antenna array is employed for direction finding of a signal impinging with horizontal polarization, the array will not be capable to detect it, and will fail to estimate the corresponding DoA. This extreme situation illustrates that, depending on the polarization of the impinging wave, significant degrading performance may be observed if a single-polarized antenna array is used for reception.

As detailed in Section 2.1, the polarization state of an impinging signal is described by the Jones vector given by:

$$\boldsymbol{k} := \begin{bmatrix} \cos(\beta) & \sin(\beta)\mathrm{e}^{j\phi} \end{bmatrix}^{\mathrm{T}} \tag{5.1}$$

where β describes the relation between the amplitudes of two orthogonal components of the electric field and ϕ describes the relative phase of the components. A vertical polarized array used to receive a signal impinging with Jones vector $k = \begin{bmatrix} \cos(45°) & \sin(45°) \end{bmatrix}^{\mathrm{T}}$ will only be able to capture half of the signal power, leading to a loss in SNR equivalent to 3dB, and as a consequence, decreased direction finding accuracy will be observed. Table 5.1 depicts results for the CRLB when a single-polarized five-element L-Quad array is used for direction finding. Each element is now comprised of a single pair of monopoles. The substrate in which the monopoles are printed is kept in the model for mechanical stability. In this case, the radiators are rotated around the z-axis for broader azimuth coverage and smoother CRLB over azimuth, as depicted in Figure 5.1 and 5.2a. Subsequently, Table 5.2 depicts results for the same single-polarized array but with all the radiators pointing to the same direction, as depicted in Figure 5.2b. Finally, Table 5.3 depicts results for the CRLB of a dual-polarized five-element L-Quad array with rotated elements.

It is possible to observe from the results depicted in Tables 5.1, 5.2 and 5.3 that the single-polarized array with radiators pointing to the same direction is the one which ren-
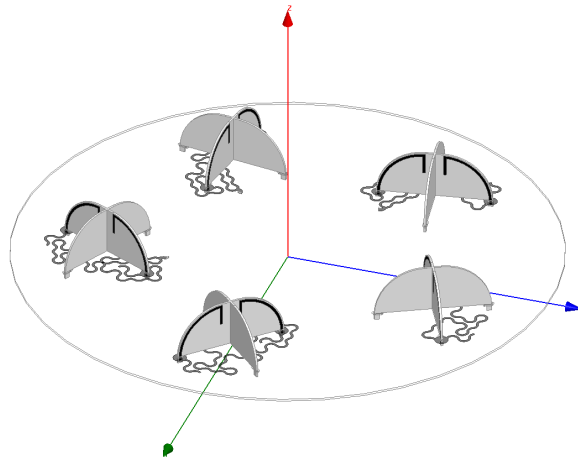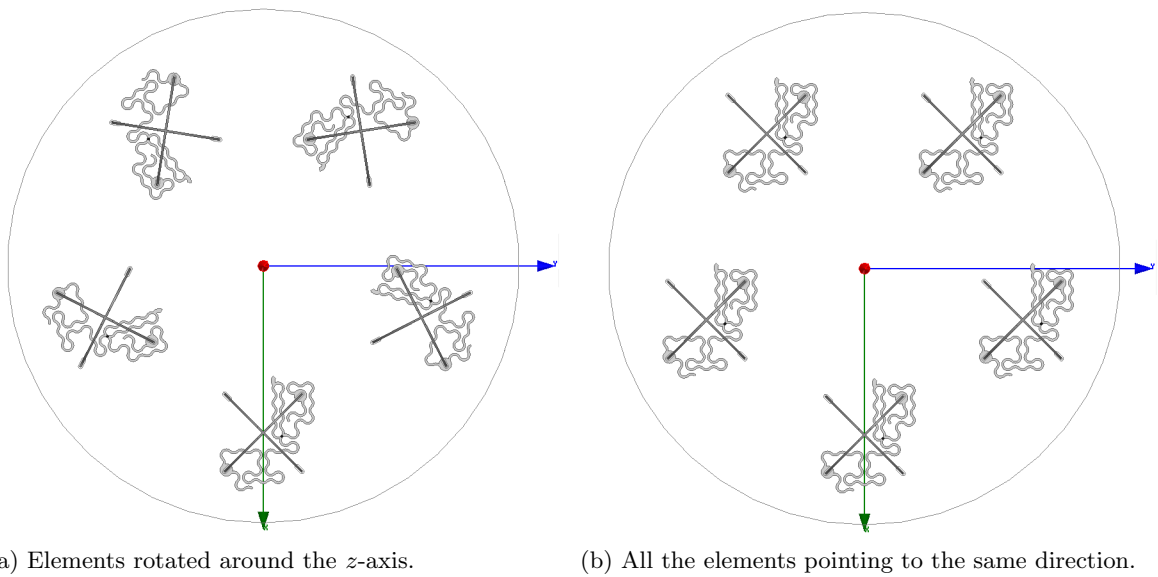
Figure 5.1.: Five-element single-polarized L-Quad array.

(a) Elements rotated around the z-axis.

(b) All the elements pointing to the same direction.

Figure 5.2.: Five-element single-polarized L-Quad array - top view.

Signal Polarization		CRLB	
β	ϕ	ϑ	φ
0°	0°	0.2232°	0.2771°
45°	0°	0.2928°	0.2857°
90°	0°	0.3933°	0.3422°
45°	90°	0.2642°	0.2888°

Table 5.1.: Effects of signal polarization to DF for a single-polarization L-Quad array - radiators rotated

Signal Polarization		CRLB	
β	ϕ	ϑ	φ
0°	0°	0.8030°	1.4113°
45°	0°	0.3305°	1.0622°
90°	0°	0.8905°	1.1342°
45°	90°	0.2980°	0.9167°

Table 5.2.: Effects of signal polarization to DF for a single-polarization L-Quad array - radiators not rotated

Signal Polarization		CRLB	
β	ϕ	ϑ	φ
0°	0°	0.1625°	0.1752°
45°	0°	0.1806°	0.1881°
90°	0°	0.2072°	0.2103°
45°	90°	0.1869°	0.2178°

Table 5.3.: Effects of signal polarization to DF for a dual-polarization L-Quad array - radiators rotated

ders highest and most variable CRLB for different impinging waves' polarization states. The single-polarized array with elements rotated in order to cover the whole half sphere has good performance in comparison to the dual-polarized array. To completely spam the whole range of 360° in azimuth, the beamwidth of each pair of dipoles should equal 360°/5 = 72°. Since the beamwidth of each pair of dipoles is approximately 60°, we can assume that rotating the radiators leads to a good coverage in azimuth. Of course, the CRLB is higher for the single-polarized array since it is comprised of half of the number of radiators in comparison to the dual-polarized array. However, effects to the CRLB when waves impinge with different polarization states is very similar to what is observed if the dual-polarized array is employed for direction finding. This is expected, since rotating the radiators around the z-axis changes the orientation of the radiated electric far field and thus, improves the robustness of the array against polarization mismatch.

5.2. Effects of Data Model Mismatch to Direction Finding

The aim of this section is to show how model mismatch, as detailed in Section 2.10, affects the accuracy of DoA estimation, measured by the CRLB. To this end, we assume that only the vertical component of the antenna array manifold is used for estimating the DoA of an impinging signal with polarization state given by the Jones vector with $\phi = 0°$ and $\beta = 45°$. In this case, the full-polarimetric response of the antenna array is not used for direction finding and we neglect the response of the array to horizontal polarization excitation.

Figure 5.3 depicts results for the DoA (ϑ and φ) estimation CRLB of a five-element dual-polarized circular L-Quad array. It is possible to observe that the estimation of the elevation of arrival of the impinging signal is strongly degraded while the estimation of azimuth does not seem to be significantly affected. This may be explained, since the elements are rotated in azimuth and are more robust to polarization mismatch for azimuth estimation.

5.3. Impact of Mutual Coupling to the Direction Finding

Since the direction finding performance of an application heavily depends on the antenna array far field radiation patterns, it becomes of primary importance to characterize, account for and investigate the effects of mutual coupling with respect to pattern distortion and power mismatch to the direction finding capabilities of compact antenna arrays. Let us first compare the radiation pattern of one element, in the presence of neighboring radiators for different inter-element spacings. Figure 5.4 depicts results for the gain of one element placed in an
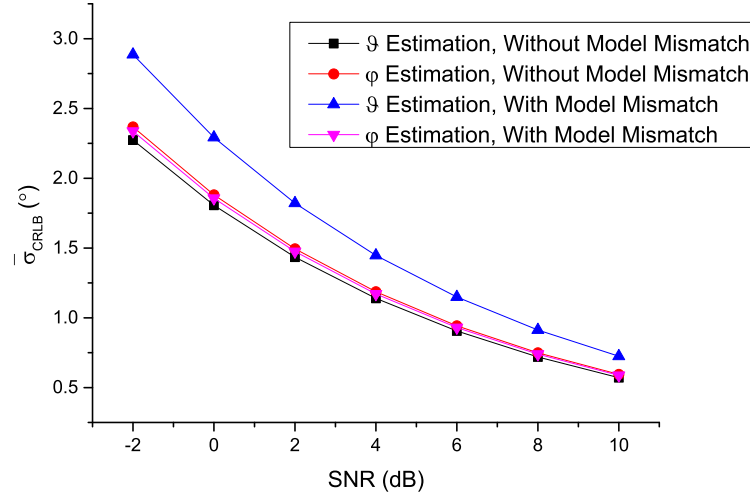
Figure 5.3.: CRLB of a five-element circular L-Quad array when model mismatch is assumed for the DoA estimation of one impinging wave.

array with five dual-polarized L-Quad elements. In this case, one element corresponds to one port from the ten total ports, since each dual-polarized element is comprised of two ports. It is possible to observe that the stronger the coupling, the more distorted the radiation patterns and the lower the realized gain.
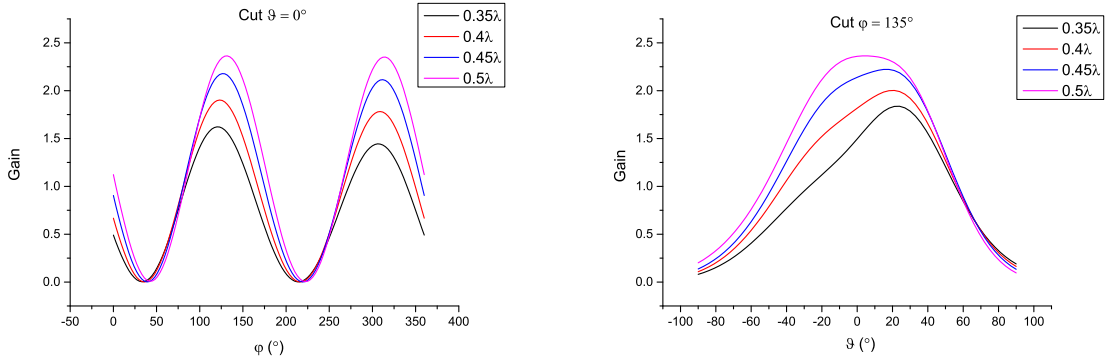
(a) Cut in $\vartheta = 0°$.

(b) Cut in $\varphi = 135°$.

Figure 5.4.: Radiation pattern of one element for different inter-element spacings, in a dual-plarized five-element L-Quad array.

We now proceed to showing the effects of mutual coupling to the accuracy of DoA estimation. Figure 5.5 depicts results for the CRLB of an ideally uncoupled five-element dual-polarized L-Quad array in comparison to the coupled array. The inter-element spacing is varied from 0.35λ to 0.5λ. We observe that the stronger the coupling, the larger the difference between the ideally uncoupled array becomes, when compared to the coupled array, with respect to the CRLB, both for the estimation of ϑ and φ.
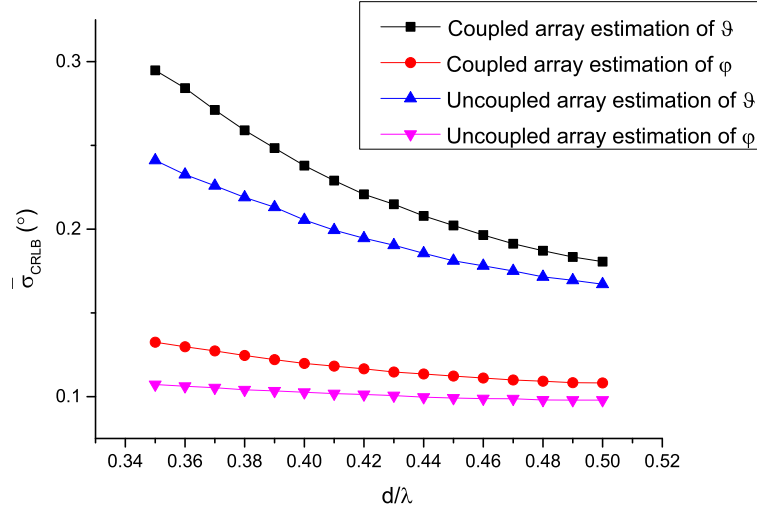

Figure 5.5.: Comparison between the CRLB for an ideally uncoupled five-element dual-polarized L-Quad array and the CRLB for a coupled array.

Figure 5.6 compares results between the CRLB of the estimation of elevation (ϑ) and azimuth (φ), when a wave front is impinging on a five-element coupled L-Quad array, and when the signal impinges on an ideally uncoupled array, for different SNR regimes, and inter-element spacing of 0.5λ and 0.35λ. Note that the lower the SNR, the stronger the effects of coupling to the direction finding capability of the array becomes.
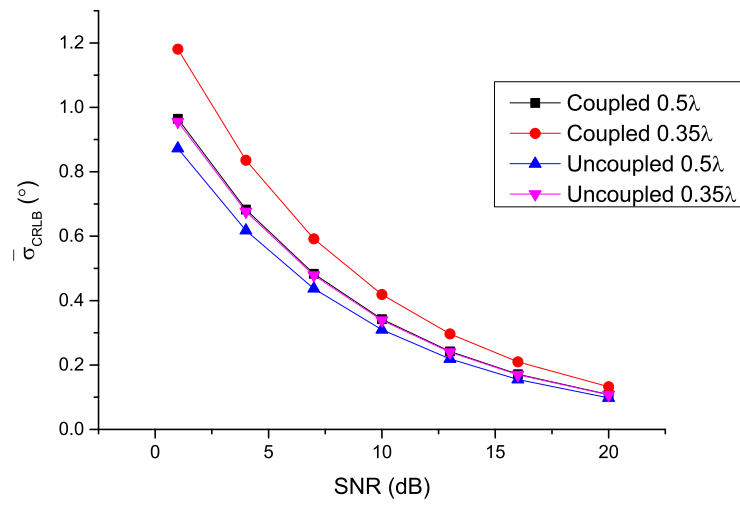
Figure 5.7 compares results for the Maximum Likelihood (CML) spectrum of a signal impinging from $(\vartheta, \varphi) = (18°, 40°)$ with SNR of 20 dB on a five-element L-Quad array with elements rotated in azimuth. The inter-element spacing is varied from 0.35λ to 0.5λ. For high SNR (20 dB), although the level of the peak is not significantly affected by mutual coupling, the lobe gets the wider the lower the inter-element spacing becomes, leading to degraded ML DoA estimation performance.

Finally, Figure 5.8 compares results for the MUSIC spectrum of a signal impinging from
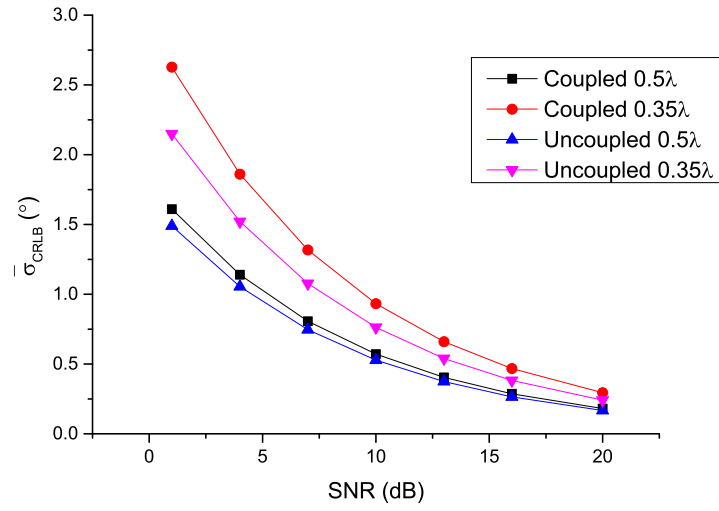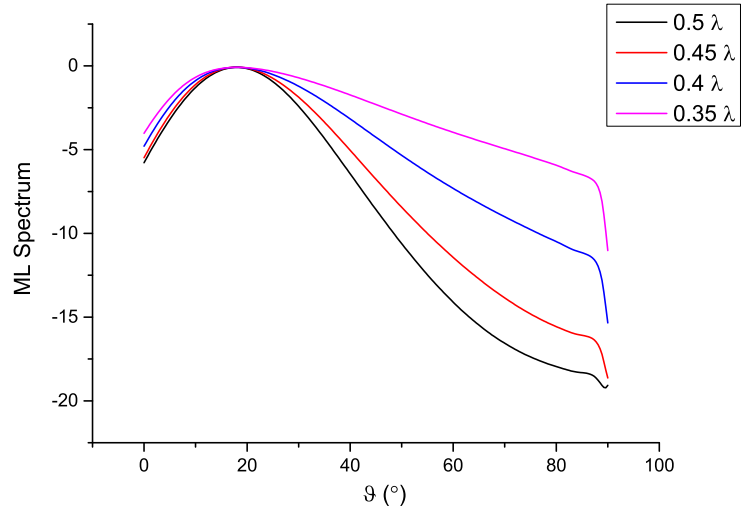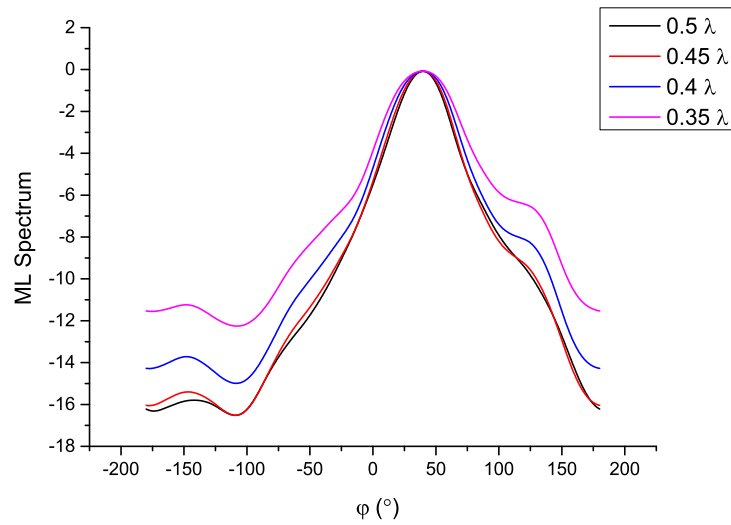
(a) Estimation of ϑ.

(b) Estimation of φ.

Figure 5.6.: Effects of coupling on the CRLB for different SNR and array inter-element spacings.

(a) Cut at $\varphi = 40°$.

(b) Cut at $\vartheta = 18°$.

Figure 5.7.: Effects of mutual coupling to the Maximum Likelihood spectrum of a signal impinging on a five-element L-Quad array with SNR 20 dB.

$(\vartheta, \varphi) = (18°, 40°)$ with SNR of -5 dB on a five-element L-Quad array with elements rotated in azimuth. The results are presented for a cut at the real signal azimuth of arrival. The inter-element spacing is varied from 0.35λ to 0.5λ.
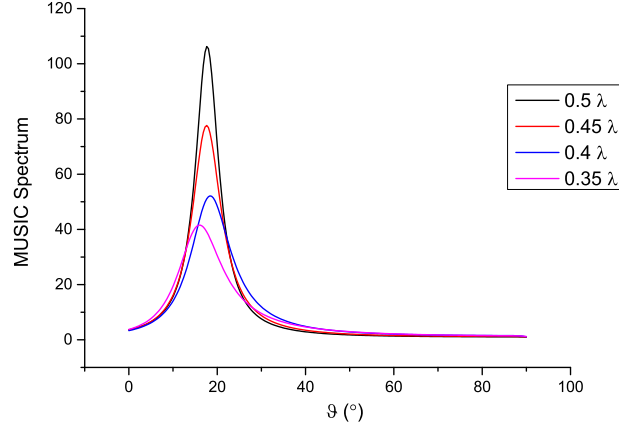

Figure 5.8.: Effects of mutual coupling to the MUSIC spectrum, cut $\varphi = 40°$ of a signal impinging on a five-element L-Quad array with SNR -5 dB.

From Figure 5.8 we observe that the coupling between neighboring elements in an array significantly affects the peak correspondent to the DoA of an impinging signal. The stronger the coupling, the lower the peak becomes, leading to degrading estimation accuracy. As a conclusion, it is safe to say that mutual coupling strongly affects the performance with respect to direction finding, and depending on the SNR level (as well as on other parameters, as detailed further in this chapter), can lead to prohibitive erroneous target localization.

5.4. Effects of Antenna Power Mismatch to Direction Finding

An important issue when designing antenna arrays is related to the impedance match at the excitation ports. In the transmitting mode, the antenna array ports are assumed to be connected to generators with some specific internal impedance, usually assumed to be 50Ω. In order to ensure maximum power transfer, the antenna impedance at the ports must be matched to the generators' impedance (assuming that the generators are directly connected to the antenna ports). For the receiving mode, the antenna ports may be connected to some feeding network or some coaxial cable that will drive the signal to the receiver. The coaxial cable and the feeding network also have certain impedances that need to match the antenna

impedance for optimal power transfer.

The L-Quad antenna array investigated throughout this thesis consists of pairs of monopoles, each connected to a feeding network responsible to combine the power received by the two monopoles with a 180° relative phase difference. Additionally, the feeding network includes stubs that transform the impedance of the antenna elements and ensure matching to the 50Ω transmission lines. Figure 5.9 depicts a dual-polarized L-Quad element comprised of four monopoles. The impedance matching stubs are highlighted in red.
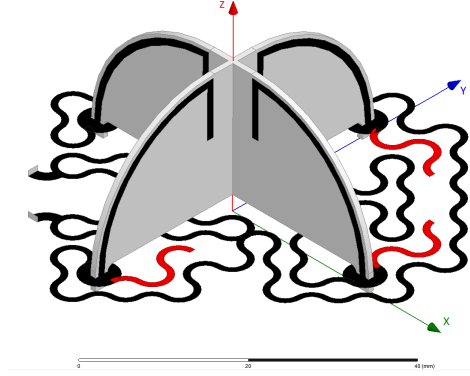

Figure 5.9.: Dual-polarized L-Quad element - highlighted: four impedance matching stubs, one for each monopole.

Ideally, the stubs are capable to perfectly match the impedance of the antenna monopoles to the 50Ω transmission lines. However, impairment may occur, leading to non-optimal power transfer at the antenna array ports, which reduces the SNR, and consequently leads to increased CRLB for direction finding. Figure 5.10 compares the CRLB for the estimation of ϑ and φ when we consider stubs optimized for impedance matching with the CRLB of ideally matched radiating elements. Although an optimization is carried out for the stubs, in order to ensure maximum power transfer, it is still not possible to observe perfect matching to the 50Ω transmission lines and some mismatch will occur. The realized gain, defined in Chapter 3 is used for the computation of the CRLB when mismatch losses are included in the model. If the array is assumed to be ideally matched, the gain is used instead of the realized gain, and by definition, losses due to power mismatch at the array ports are not taken into account, rendering higher SNR, and as a consequence, lower CRLB.

Note from Figure 5.10 that the stronger the mutual coupling within the array (that occurs for narrower element spacing), the larger the difference is observed if we compare the ideally matched array to the real array. This occurs due to the fact that mutual coupling alters the impedance at the array ports, and the impairments are the more significant, the stronger the

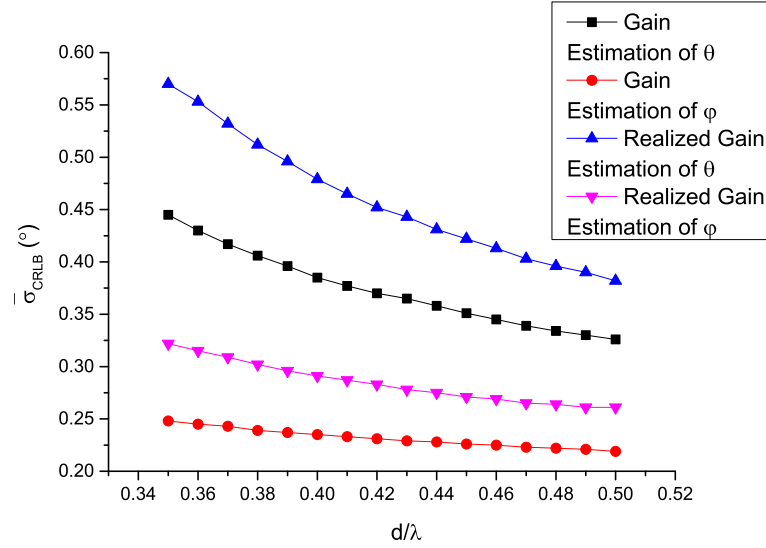interaction between neighboring radiating elements becomes.

Figure 5.10.: CRLB computed using gain and realized gain for a five-element L-Quad array – effects of power matching.
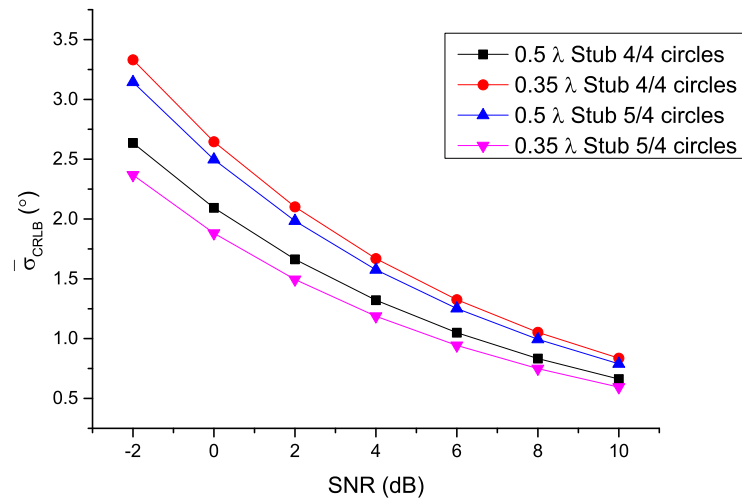
Optimal impedance matching is observed if we use stubs designed with 5/4 of a circle for meandering shaped transmission line. Table 5.4 presents the return loss observed at the resonance frequency at one of the ports, for stubs with different lengths, assuming 0.5λ inter-element spacing. Note that the stubs with length equivalent to 5/4 of a circle render lower power loss when compared to shorter stubs. Figure 5.11 compares the CRLB computed for 5/4 circles stubs to the CRLB computed for 4/4 circles stubs. Note that if we design the stubs shorter than the optimal length, the reduced power transfer, which results from non-optimal impedance matching, leads to increased direction finding CRLB.

Stub Length	Return Loss (dB)
5/4 of a circle	-17.13
4/4 of a circle	-10.29
2/4 of a circle	-5.63

Table 5.4.: Impedance matching - return loss at one port
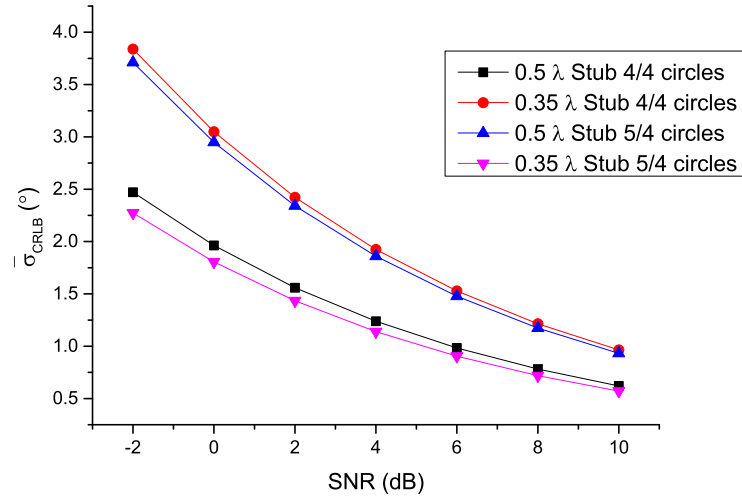
(a) Estimation of ϑ.

(b) Estimation of φ.

Figure 5.11.: CRLB computed for stubs which are not optimized for power transfer in comparison to the CRLB observed with optimal impedance matching stubs.

5.5. Evaluation of Decoupling and Matching for Direction Finding

To draw conclusions on the effect of exciting arrays with eigenmodes for effective decoupling, we start with results obtained for a five-element dual-polarized L-Quad array with several degrees of coupling. If a decoupling network is designed based on the eigenmode decomposition approach, in order to excite the original antenna array ports in a way that they radiate the fundamental modes, the radiation patterns of the original antenna connected to the decoupling network will be orthogonal, implying effective decoupling. The eigenmode excitation is equivalent to a beamforming with magnitude and phase given by the eigenvectors.

Figure 5.12 depicts the individual radiated far field patterns (ϑ component) of the five-element dual-polarized L-Quad array for 0.35λ spacing. In Figure 5.13, it is possible to observe the effects of exciting the eigenmodes to the resulting radiation patterns. Depending on the mode excited, the radiation exhibits a different pattern that ranges from highly directional (lower eigenefficiency), with multiple nulls, to almost omnidirectional patterns (higher eigenefficiency).
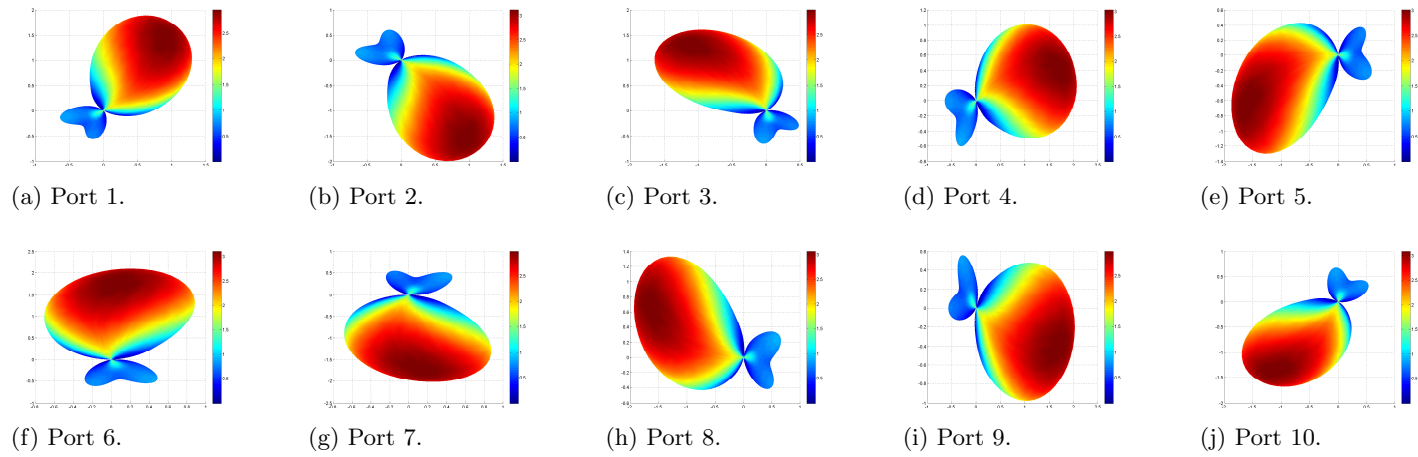
(a) Port 1.   (b) Port 2.   (c) Port 3.   (d) Port 4.   (e) Port 5.

(f) Port 6.   (g) Port 7.   (h) Port 8.   (i) Port 9.   (j) Port 10.

Figure 5.12.: Individual radiation patterns of a five-element L-Quad antenna array.

(a) Mode 1.   (b) Mode 2.   (c) Mode 3.   (d) Mode 4.   (e) Mode 5.

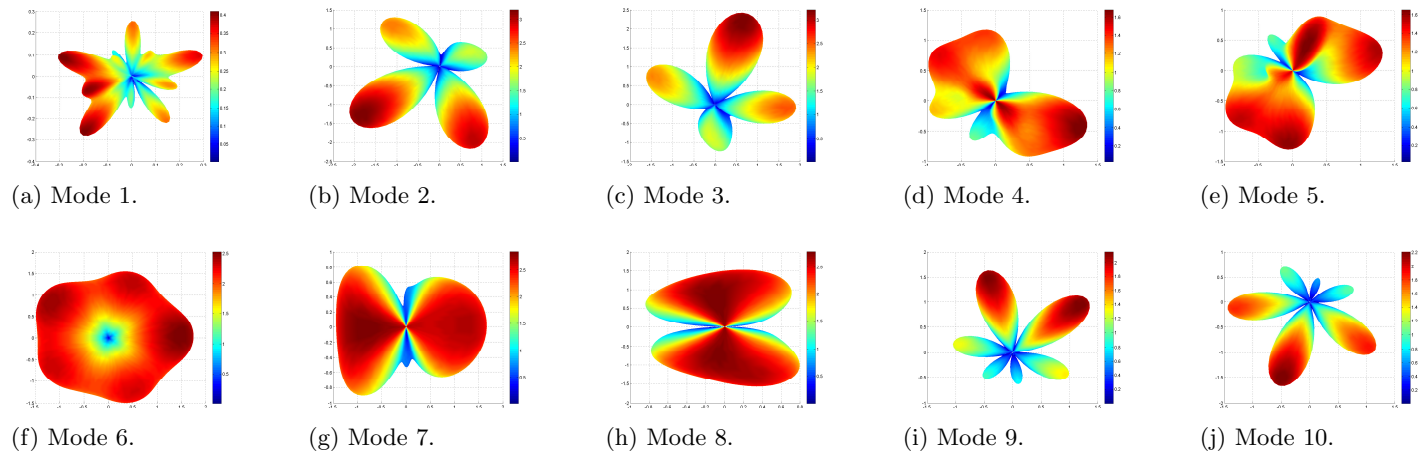(f) Mode 6.   (g) Mode 7.   (h) Mode 8.   (i) Mode 9.   (j) Mode 10.

Figure 5.13.: Eigen-patterns of a five-element L-Quad antenna array.

Figure 5.14 compares the CRLB of coupled arrays with three and five elements to the CRLB of decoupled arrays. It is easy to observe an improvement for smaller inter-element spacing (higher coupling). Exciting the array with the correspondent eigenmodes decouples the radiating elements, and the diversity loss caused by reduced effective number of elements is restored. The impact of this restoration is the stronger the more coupled the array is.

If power matching is added as a step subsequent to decoupling, aiming to improve the radiation efficiency of the least efficient modes, the SNR is increased, and as a consequence, the CRLB for DoA estimation is lowered. Figure 5.15 compares results between the CRLB of a coupled and unmatched array, the CRLB of a coupled and matched array, the CRLB of a decoupled and unmatched array, and finally, the CRLB of a decoupled and matched array. It is clear that the CRLB for the matched array is lower than the CRLB for the unmatched array. Moreover, decoupling the array via eigenmode excitation renders higher direction finding accuracy in comparison to the accuracy observed when a coupled array is employed. Finally, it is possible to observe that if a matched, but coupled array is used for signal reception, instead of a decoupled, but unmatched array, the CRLB is lower, implying higher direction finding accuracy. The highest challenge of designing efficient DMNs lies in the matching of the least efficient modes, since it may become a very complex task to design a matching network that is able to ensure high radiation efficiency over all directions.

Figure 5.16 compares the results for the CRLB when a wave impinges on a five-element L-Quad array with different SNRs and inter-element spacing of 0.35λ and 0.5λ. In addition to the effects already observed, we note that the lower the SNR, the higher the improvement is observed from decoupling the array. In low SNR regimes, one can obtain significantly higher direction finding accuracy, if decoupled compact arrays are used for reception.

Figure 5.17a and 5.17b compare the results for the resolution if two uncorrelated source waves impinge on an array with five and three elements respectively, for inter-element spacing ranging from 0.35λ to 0.5λ. The resolution is computed for the arrays with and without decoupling by eigenmode excitation. The resolution is computed as in Algorithm 1. We conclude that after decoupling the array ports, a significant improvement of direction finding with respect to resolution is observed.

Influence of Ohmic Losses in Microstrip Lines

The results presented so far, comparing coupled to decoupled and matched arrays, conclude that significant improvement of direction finding performance with respect to the CRLB (accuracy and resolution for multiple signals) is accomplished if the array is decoupled using the eigenmode approach. However, the Ohmic losses due to the use of distributed elements in
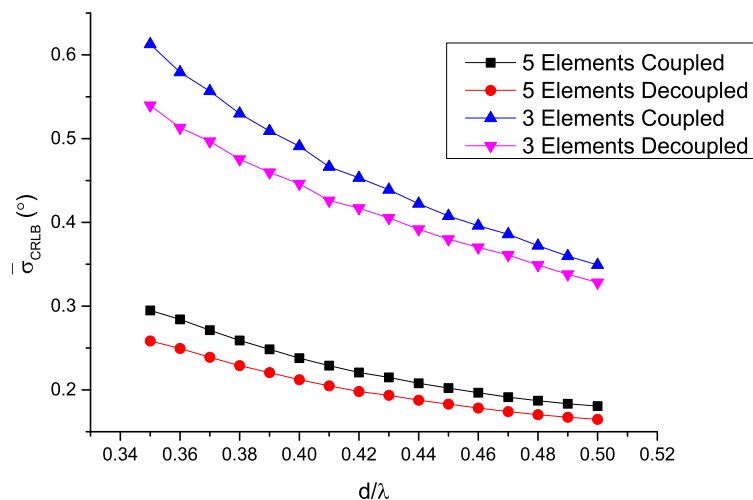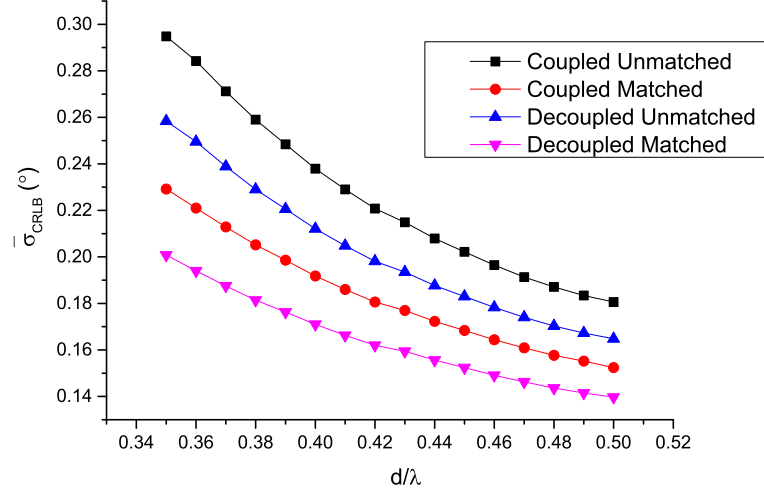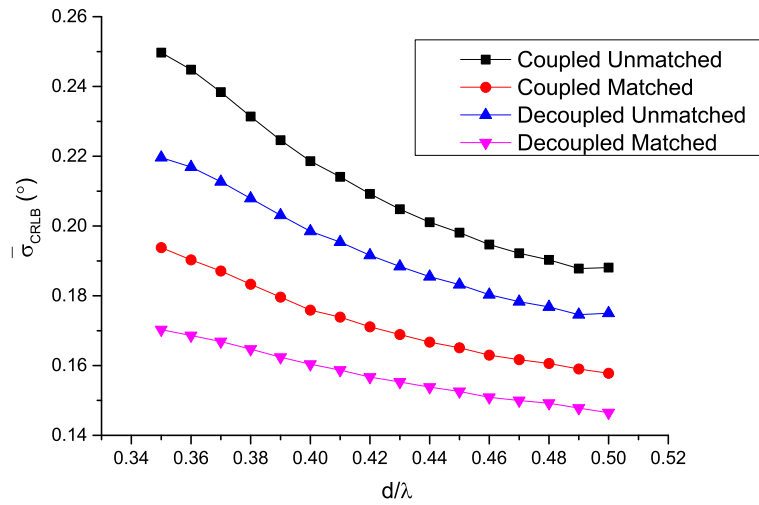
(a) Estimation of ϑ.
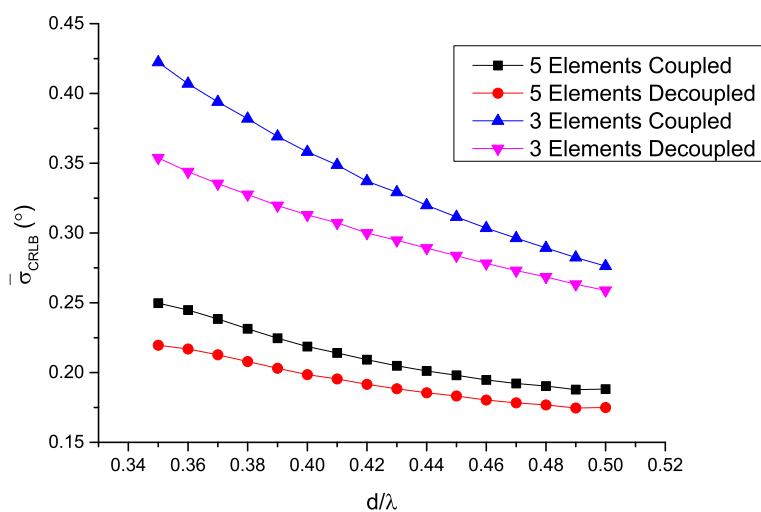
(b) Estimation of φ.

Figure 5.14.: Mean CRLB for a three and five-element dual-polarized L-Quad array with different spacings, in comparison to eigenmodes excitation.

(a) Estimation of ϑ.

(b) Estimation of φ.

Figure 5.15.: Mean CRLB for a five-element dual-polarized L-Quad array with different spacings, in comparison to eigenmodes excitation.

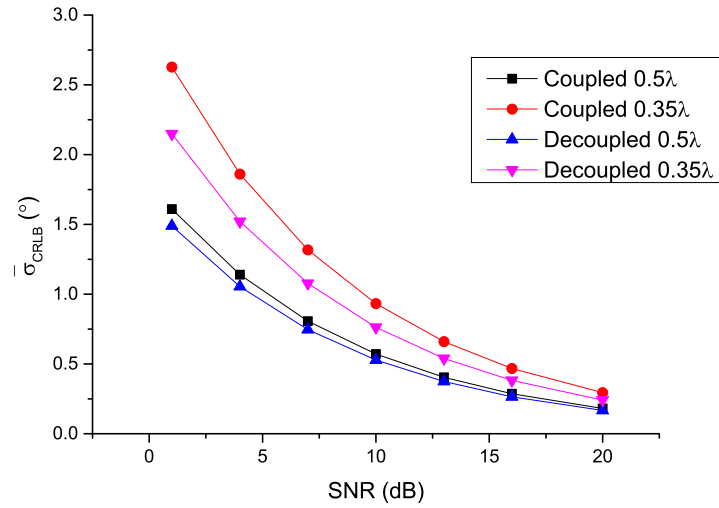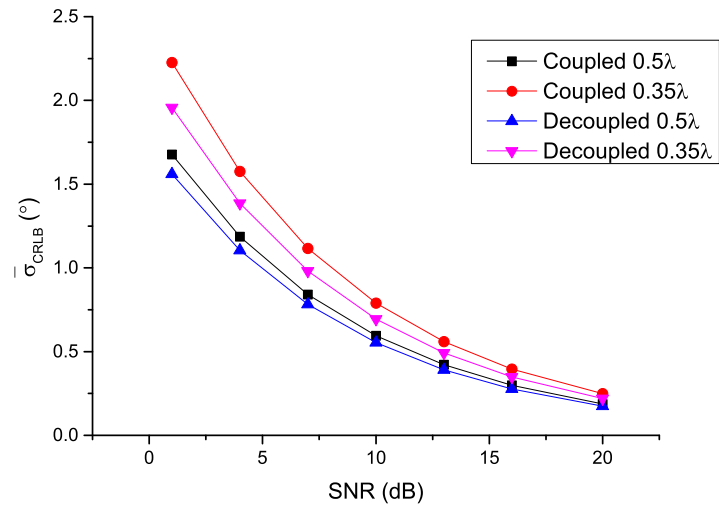(a) Estimation of ϑ.

(b) Estimation of φ.

Figure 5.16.: Influence of decoupling to the DoA estimation CRLB when a signal impinges on a five-element L-Quad array with different SNR and inter-element spacing.
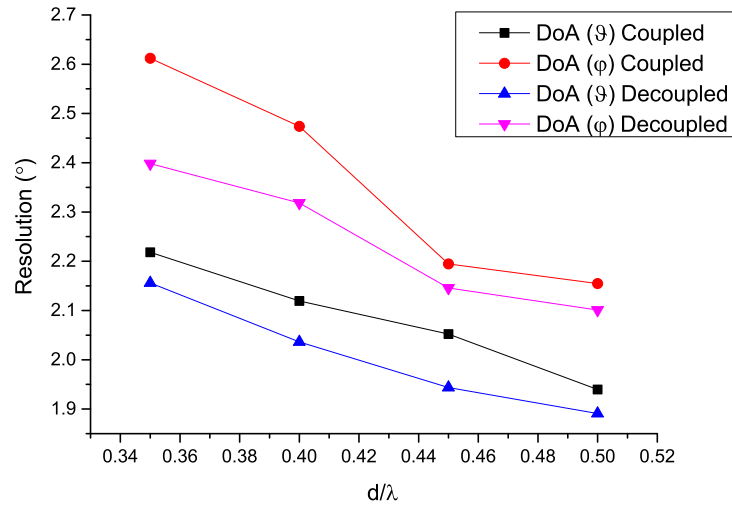
(a) Five-element array.

(b) Three-element array.

Figure 5.17.: Direction finding resolution of dual-polarized L-Quad arrays with different spacings in comparison to eigenmodes excitation for decoupling - two uncorrelated impinging waves.
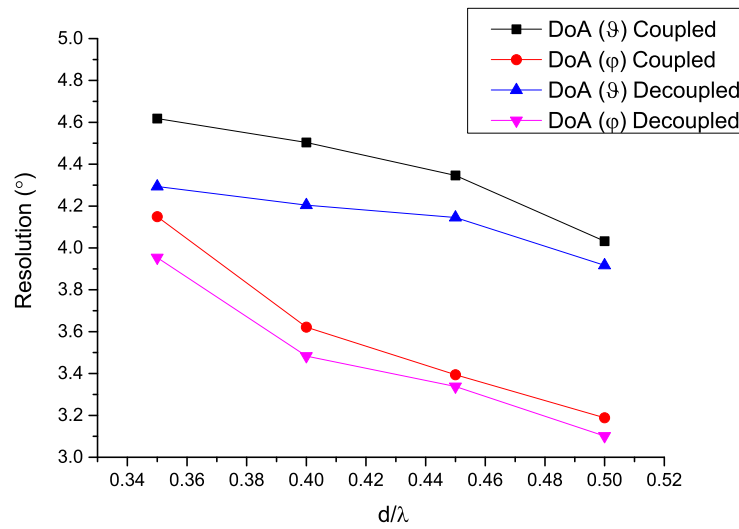
the design of DMNs were neglected up to this point. In the literature, one can easily find expressions for the attenuation due to microstrip lines, depending on design parameters such as frequency, substrate dielectric properties, and height and width of the strip line [123]. The attenuation in microstrip lines may be divided into Ohmic losses in conducting materials, dielectric losses, and radiation losses. Assuming that the DMN fits in the volume already occupied by the antenna array, and that the ground plane and the dielectric layer do not need to be extended, we may neglect dielectric losses and losses due to the ground plane. Moreover, we assume that radiation loss is much less significant than Ohmic loss for the antenna array investigated in this thesis and skip it at this point. This implies that losses due to dissipation within the microstrip lines, used for the manufacturing of networks based on distributed elements, are the most significant, and will be investigated hereupon.

Let us first start with the expression for the surface resistance of microstrip lines:

$$R_s = \sqrt{\frac{\pi f \mu}{\sigma}} \tag{5.2}$$

where f is the frequency, μ is the permeability and σ is the line electrical conductivity, which for copper e.g. can be given by $\sigma = 41 \times 10^4$ S/cm.

Hammerstad published in [124] an expression for the attenuation denoted by α_c, in dB/m, in case of thick ($w/h \leq 1$) and thin ($w/h \geq 1$) microstrip lines, where w is the strip line width and h is the thickness.

$$\alpha_c = \begin{cases} \dfrac{10}{h\,\pi\ln 10}\dfrac{R_s}{Z_c}\dfrac{32 - (w/h)^2}{32 + (w/h)^2}\left[1 + \dfrac{h}{w}\left(1 + \dfrac{\partial w}{\partial t}\right)\right] & \text{for} \quad w/h \leq 1 \\[2em] \dfrac{20}{h\ln 10}\dfrac{R_s\,Z_c\,\epsilon_{eff}}{\eta_0^2}\left\{\dfrac{w}{h} + \dfrac{6h}{w}\left[\left(1 - \dfrac{h}{w}\right)^5 + 0.08\right]\right\}\left[1 + \dfrac{h}{w}\left(1 + \dfrac{\partial w}{\partial t}\right)\right] & \text{for} \quad w/h \geq 1 \end{cases} \tag{5.3}$$

where Z_c is the line characteristic impedance, η_0 is the intrinsic impedance of free space and ϵ_{eff} is the effective dielectric permittivity, computed from the relative permittivity as in [125]. The derivative $\partial w/\partial t$ can be calculated from Wheeler's relation [126] for finite strip thickness [123]:

$$\frac{\partial w}{\partial t} = \frac{1}{\pi} \begin{cases} \ln\left(\dfrac{2h}{t}\right) & \text{for} \quad w/h \geq 1/2\pi \\[3ex] \ln\left(\dfrac{4\pi w}{t}\right) & \text{for} \quad w/h \leq 1/2\pi \end{cases} \tag{5.4}$$

The Ohmic losses are usually given in dB per unit of length and thus, the total length of the network needs to be taken into account for the computation of total attenuation. Volmer investigated in [33] antenna arrays with symmetry planes and the design of networks comprised of delay lines and directional couplers to decouple and match the elements. A network designed for a circular array with two symmetry planes comprised of five radiators, as the dual-polarized five-element L-Quad array, requires five directional couplers in order to decouple all elements. Considering that the directional couplers are $3\lambda/4$ long, it is easy to find an approximate value for the overall network length, and thus compute the total Ohmic losses within DMNs.

Figures 5.18a and 5.18b present results for direction finding performance with respect to the CRLB to the estimation of ϑ and φ, respectively, when a dual-polarized five-element L-Quad array with 0.5λ spacing is used for reception. They compare the performance of the coupled array with the decoupled and matched array when Ohmic losses within the DMN are accounted for. The Ohmic losses for a five-element array are computed and assumed to be approximately 2 dB. Figures 5.19a and 5.19b depicts the same results but for an array with 0.35λ spacing. Note that decoupling and matching a five-element dual-polarized L-Quad array leads to higher direction finding accuracy even when Ohmic losses are taken into account, proving the benefits of such an approach for applications based on DoA estimation.

5.6. Evaluation of Decoupling with Polarization Optimization

In Chapter 4, we discussed the procedures for the design of a decoupling network comprised of distributed elements using eigenmode approach. Equations (4.1) and (3.37) compute the antenna array radiation matrix $\boldsymbol{H}$, which is to be decomposed into eigenvectors and corresponding eigenefficiencies, guiding the design of the decoupling network. Equation (4.1) is used when Ohmic losses can be neglected, and as a consequence, the antenna array radiation efficiencies can be fully described by the scattering parameters. Equation (3.37), on the other hand, compute the array radiation matrix using the radiation beam patterns and thus, includes Ohmic losses within the array.

Note that in (3.37), the elements of the radiation matrix $\boldsymbol{H}$ are computed as an integral over
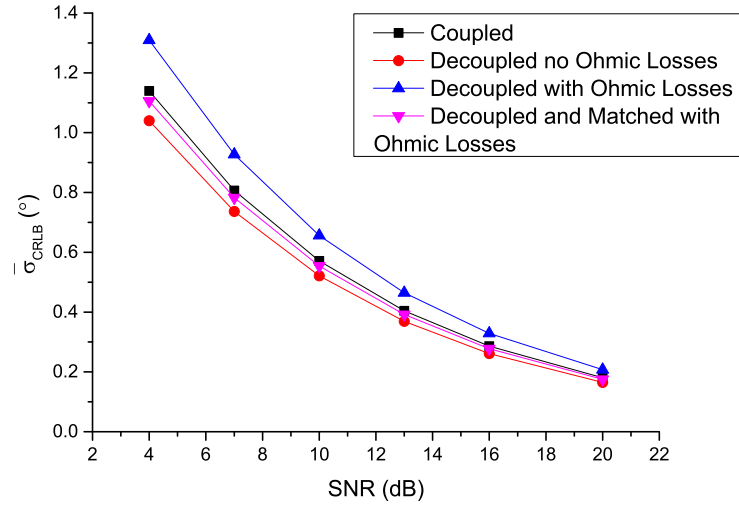
(a) Estimation of ϑ.
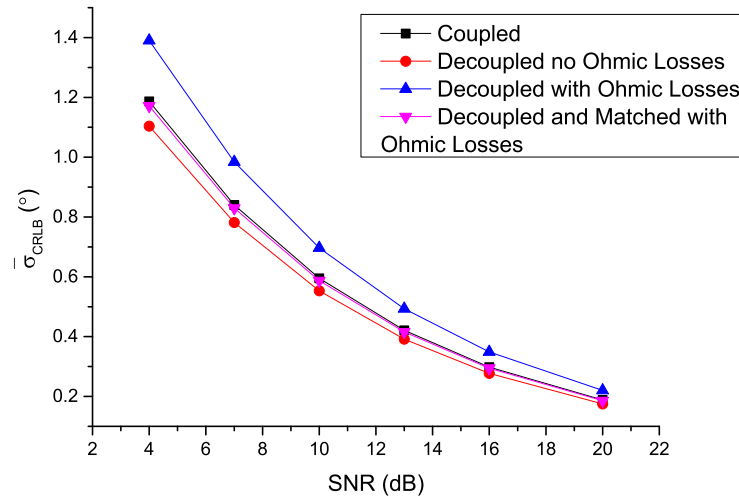
(b) Estimation of φ.

Figure 5.18.: DoA estimation CRLB for a five-element L-Quad array with 0.5λ spacing with and without DMN, accounting for Ohmic losses within the network.
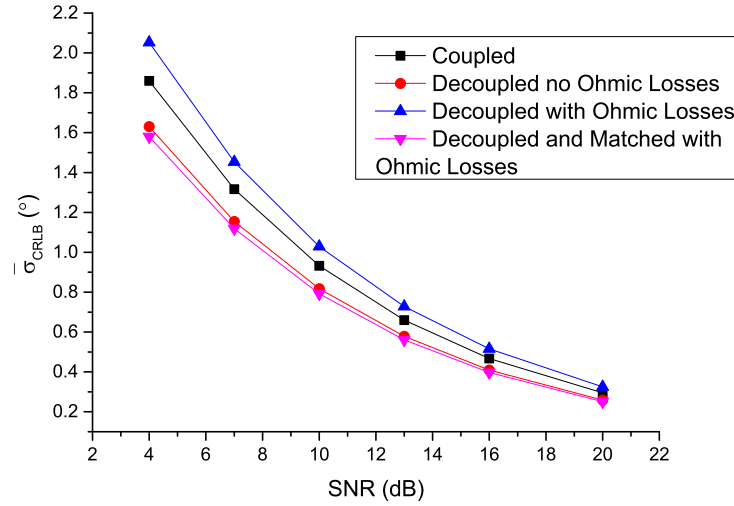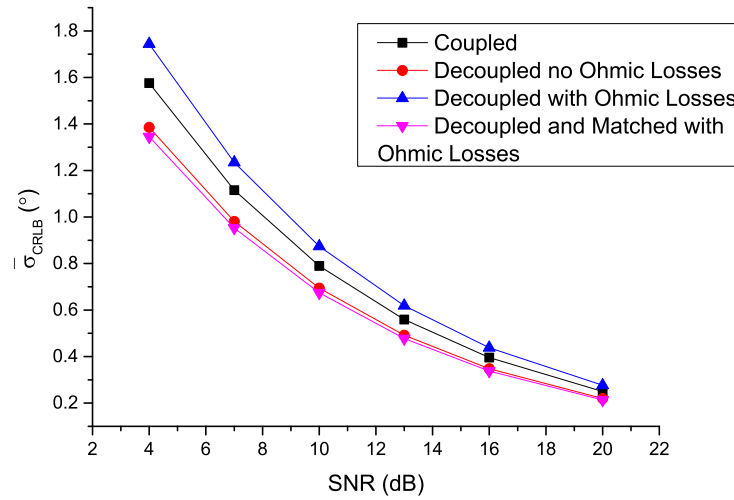
(a) Estimation of ϑ.

(b) Estimation of φ.

Figure 5.19.: DoA estimation CRLB for a five-element L-Quad array with 0.35λ spacing with and without DMN, accounting for Ohmic losses within the network.

all possible elevation and azimuth angles. Since the decoupling network is designed from the eigenvectors resulting from the decomposition of $\boldsymbol{H}$, it follows that it is optimized for all possible azimuth and elevation angles. Moreover, note that in (3.37), the product $\boldsymbol{A}_i^{\mathrm{H}}(\vartheta, \varphi)\boldsymbol{A}_j(\vartheta, \varphi)$ considers both polarization components with same weight for the computation of each element H_{ij} in the radiation matrix. However, if it is known a priori that waves are only impinging on the array e.g. with vertical polarization, the decoupling network could be optimized by assuming only the vertical component of the radiation patterns in (3.37).

Figures 5.20 – 5.22 show results for the CRLB when one wave impinges on the five-element dual-polarized L-Quad array with three possible polarization states and the decoupling network is designed taking into account the signal's Jones vector. The figures compare the results obtained when the design of the decoupling network consider the signal polarization state to the results obtained when the signal polarization is not taken into account for the computation of $\boldsymbol{H}$.
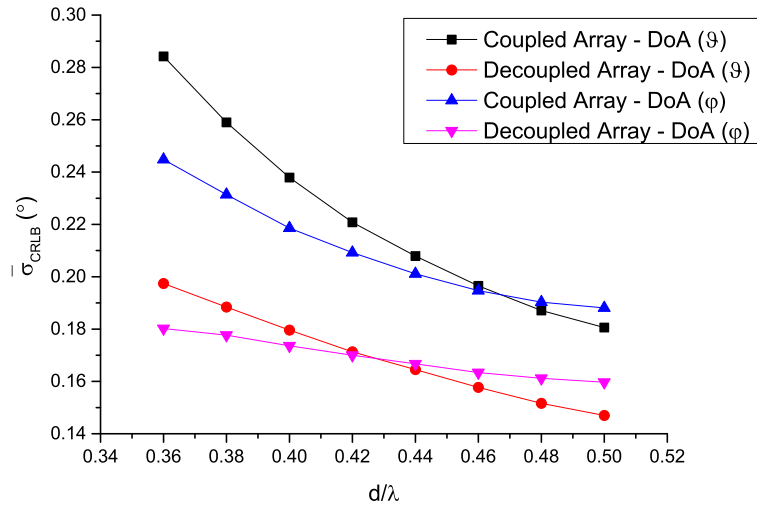
Figure 5.20.: CRLB for one impinging wave and Jones vector defined by $\beta = 45°$ and $\phi = 0°$ – linear polarization with same weighting in the vertical and horizontal directions.

It is clear to observe that the performance of the decoupling network is optimized for direction finding if the signal polarization is accounted for when computing the array radiation matrix. However, situations when the impinging wave's polarization is known a priori are unrealistic. Moreover, when multiple waves are being received by the array, each with a different polarization, it is clear that an optimal design must consider all possible polarization states,
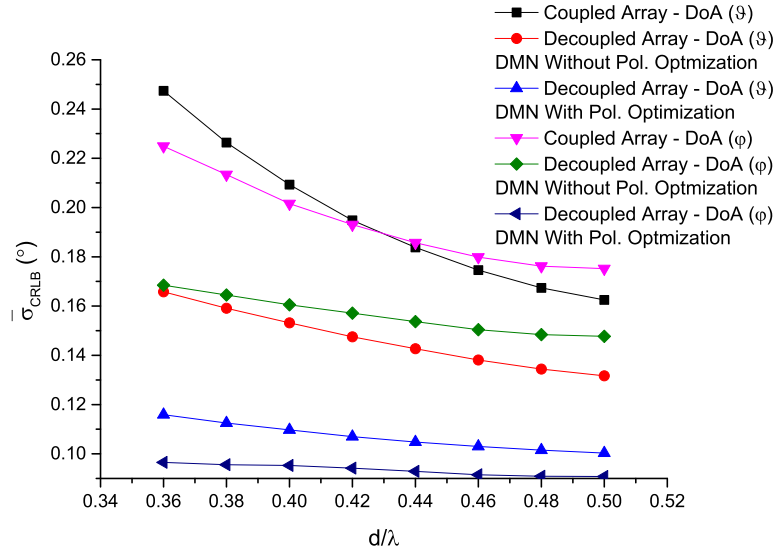
Figure 5.21.: CRLB for one impinging wave and Jones vector defined by $\beta = 0°$ and $\phi = 0°$, vertical polarization.

and hence, the computation of $\boldsymbol{H}$ must be carried out as in (3.37).

5.7. Evaluation of Performance for Direction Finding of Correlated Signals

The aim of this section is to evaluate the L-Quad arrays investigated throughout this thesis for direction finding of correlated impinging waves. Since the CRLB is strongly dependent on how the signals are modeled, it becomes clear that the correlation between them will affect the accuracy of the DoA estimation. It is expected that the more correlated the signals are, the lower the accuracy and resolution for direction finding become. Let us write the signal covariance matrix in case each two signals are correlated with each other with correlation factor given by $\rho_{ij} = \rho_{ji}$, with the index i and j referring to each signal.

$$\boldsymbol{R}_{\mathrm{s}} = \mathrm{E}\big[s^{\mathrm{H}}(t)s(t)\big] = \begin{bmatrix} 1 & \rho_{12} & \dots & \rho_{1N} \\ \rho_{21} & 1 & \dots & \rho_{N1} \\ \vdots & \vdots & \ddots & \vdots \\ \rho_{N1} & \rho_{N2} & \dots & 1 \end{bmatrix} \tag{5.5}$$

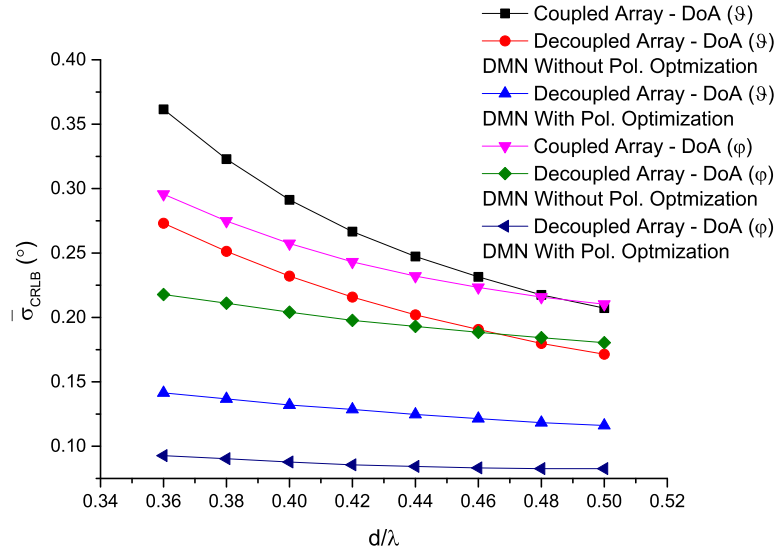In case $\rho_{ij} \neq 0$, the rank of the signal covariance matrix, defined as p, will be lower than the

Figure 5.22.: CRLB for one impinging wave and Jones vector defined by $\beta = 90°$ and $\phi = 0°$, horizontal polarization.

number of impinging signals N, and will depend on how correlated the signals are.

$$p := \operatorname{rank}(\boldsymbol{R}_\mathrm{s}) \leq N \tag{5.6}$$

In [127], the authors presented results comparing the performance of MUSIC and ML estimators to the CRLB when signal sources are correlated to each other. In [128], the performance of the ML estimator was exhaustively evaluated and discussed for the case of coherent signals. The largest contribution of [128] was to show that, for large number of observation samples, the previous knowledge of the model order is not a requisite for ML estimator, and reduced rank will, as a consequence, not imply additional complexity of order estimation under rank deficiency.

As discussed in [127], the effects of signal correlation are reinforced when the sources are closely spaced, which may lead to significant accuracy degradation. Under severe correlation conditions, the performance of MUSIC-based estimators is considerably degraded when compared to ML estimators and to the CRLB, as already mentioned in Section 2.7. Although increased SNR and larger number of radiators in antenna arrays generally increase the accuracy of DoA estimation, the performance of MUSIC is still kept far from the lower bound established by the CRLB.

We divide this section into two parts. The first part evaluates arrays with impairment caused

by mutual coupling between radiators, leading to lower SNR and distorted radiation patterns, when DoA is to be estimated from correlated waves. The second part evaluates the effects of adding a DMN to the antenna array, if we consider correlated waves.

5.7.1. Coupled Arrays

Figure 5.23 depicts results for the mean CRLB of a main source over all possible elevation and azimuth angles, assuming that a second source wave impinges from a DoA defined by $(\vartheta, \varphi) = (45°, 45°)$. The receiver SNR is considered to be 20 dB and the CRLB is computed for different degrees of correlation in order to evaluate the performance of a five-element dual-polarized circular L-Quad array with 0.5λ inter-element spacing.
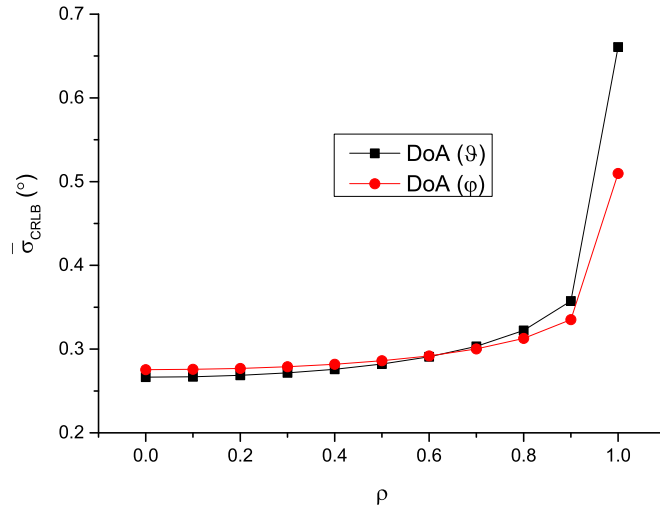
Figure 5.23.: Mean CRLB for the estimation of ϑ and φ.

It is clear to observe that, as expected, the accuracy of DoA estimation in terms of the CRLB decreases with increasing signal correlation. The CRLB increases significantly when perfectly correlated signals, i.e. coherent signals, are considered. Figures 5.24 and 5.25 compare the CRLB for the scenario of two fully correlated waves and the CRLB for two uncorrelated waves. Note that, as observed from the mean CRLB in Figure 5.23, the CRLB over azimuth and elevation gets the higher the more correlated the waves become.

Figure 5.26 depicts results for the CRLB of a five-element dual-polarized antenna array over inter-element spacing, and assuming different degrees of correlation between signals. We assume two impinging waves and compute the CRLB for the main source over all possible

(a) Estimation of θ.

(b) Estimation of ϕ.

Figure 5.24.: CRLB of a main source assuming a secondary source impinging from $(45°, 45°)$ fully correlated to the main source.
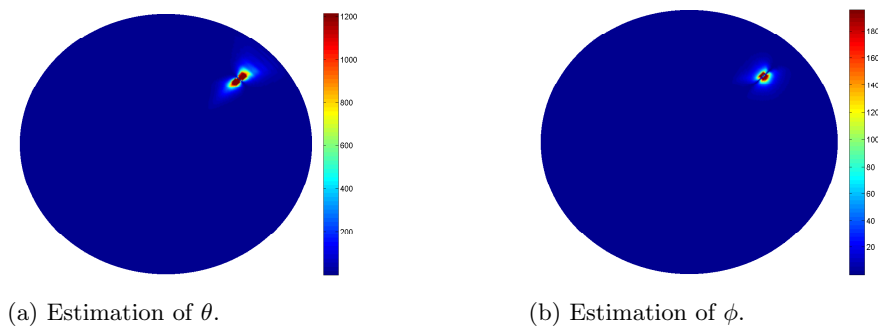

(a) Estimation of θ.

(b) Estimation of ϕ.
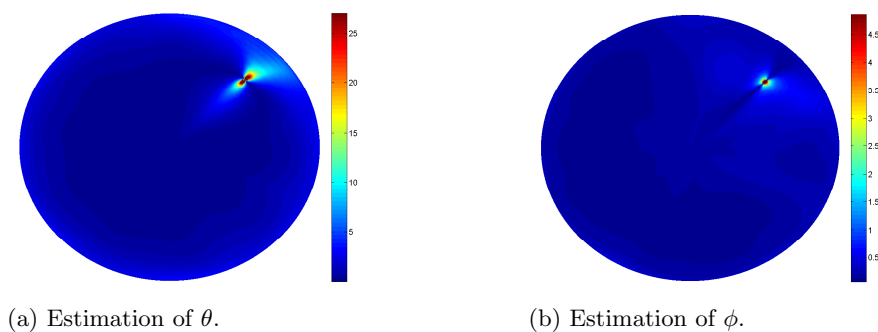
Figure 5.25.: CRLB of a main source assuming a secondary source impinging from $(45°, 45°)$ uncorrelated to the main source.

azimuth and elevation angles, and fix the second source at $(45°, 45°)$. The SNR is considered to be 20 dB. Note that, as observed in Figure 5.23, the scenario of perfectly correlated source waves renders the highest CRLB. However, the behavior of decreasing CRLB with larger spacing between neighboring elements is kept. The effect of high correlation between signals is the weaker, the lower the mutual coupling within the array becomes.

Finally, we assume perfectly correlated (coherent) signals, i.e., $\rho = 1$. The complex signal vector $\boldsymbol{s}(t) = [s_1(t), ..., s_N(t)]^T$ is modeled as following:

$$\boldsymbol{s}(t) = \begin{bmatrix} e^{j\phi_1} & e^{j\phi_2} \end{bmatrix}^T \tag{5.7}$$

The signals s_1 and s_2 are fixed over time, with same magnitude, and relative phase difference of $\Delta\phi = |\phi_1 - \phi_2|$. Note that, if we compute the signal covariance matrix, we obtain:

$$\boldsymbol{R}_s = \mathrm{E}[s^H(t)s(t)] = \begin{bmatrix} 1 & e^{-j(\phi_1-\phi_2)} \\ e^{j(\phi_1-\phi_2)} & 1 \end{bmatrix} \tag{5.8}$$

Figure 5.27 depicts results for the CRLB of a five-element dual-polarized antenna array over SNR, for array spacing of 0.5λ and assuming different phase differences between the two complex signals with same magnitude. We compute the CRLB for the main source over all possible azimuth and elevation angles and fix the second source at $(45°, 45°)$. It is clear to observe that the higher the phase difference between the complex signals, the higher the DoA estimation accuracy, given by the CRLB, becomes. Figure 5.28 presents results for the CRLB assuming the same scenario, but array spacing of 0.35λ. Note that, as observed from previous results, the direction finding performance of the antenna arrays gets the more degraded the more coupled the array becomes.

5.7.2. Decoupled Arrays

In the last section, the performance of decoupled arrays is compared to the performance of coupled arrays with respect to accuracy and resolution. We now extend the analysis in order to draw conclusions on how DoA estimation accuracy and resolution can be improved in a scenario with two received correlated signals, when arrays are decoupled using the approach of eigenmode excitation.

Figure 5.29 depicts results for the CRLB of a main signal when a second signal impinges from the direction $(\vartheta, varphi) = (45°, 45°)$ on a five-element L-Quad array. The signals are assumed to be correlated with correlation given by the parameter ρ_{ij}, as in (5.5).

It is possible to observe that exciting the array with the correspondent eigenmodes leads to
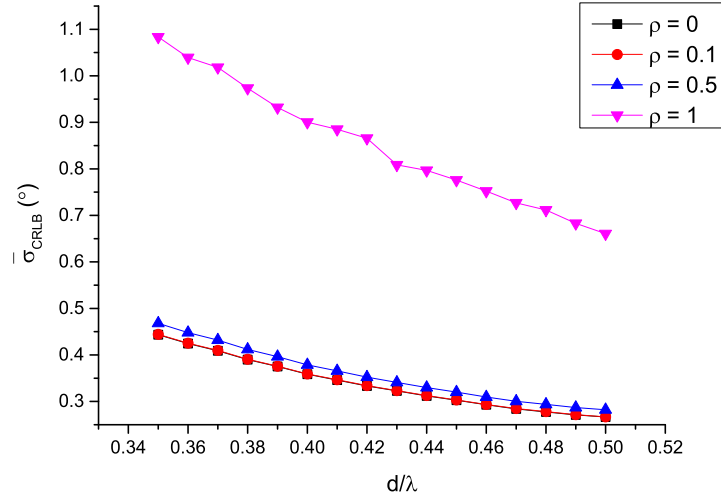
(a) Estimation of θ.
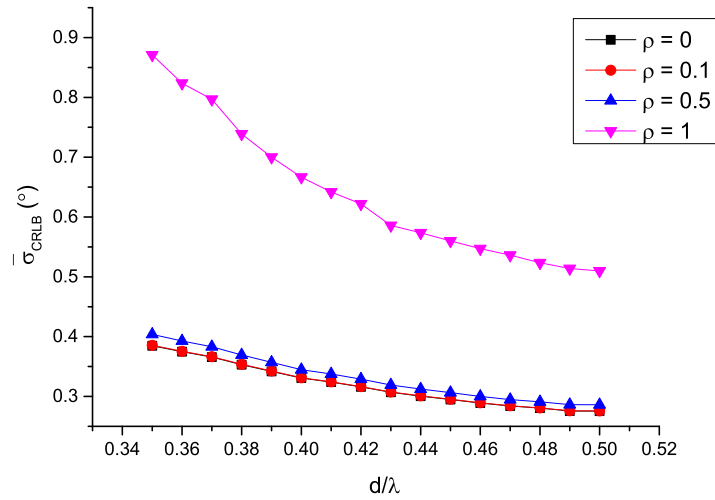
(b) Estimation of ϕ.

Figure 5.26.: CRLB for a five-element antenna array over different degrees of coupling and signal correlation.
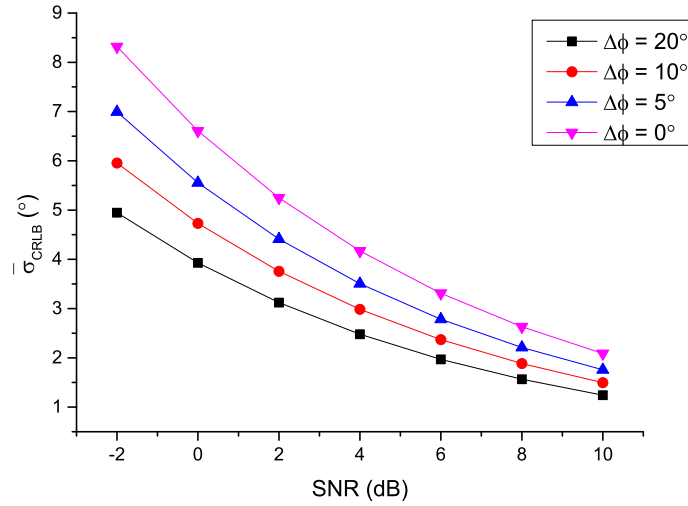
(a) Estimation of ϑ.
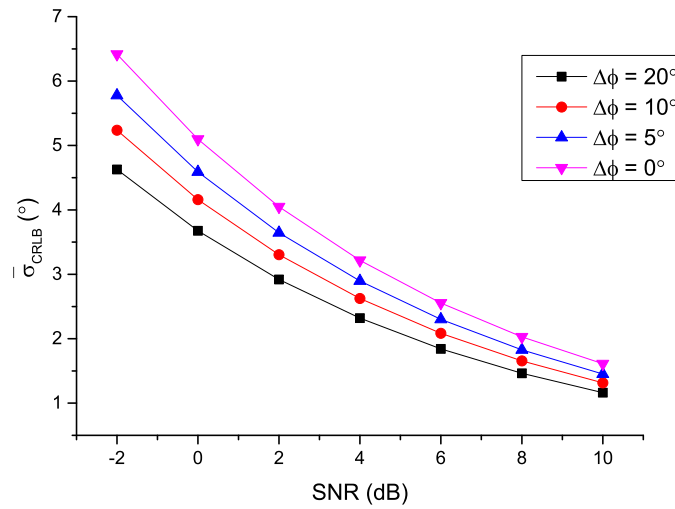
(b) Estimation of φ.

Figure 5.27.: CRLB when two coherent complex signals with different relative phase difference are received by a five-element L-Quad array with 0.5λ spacing.
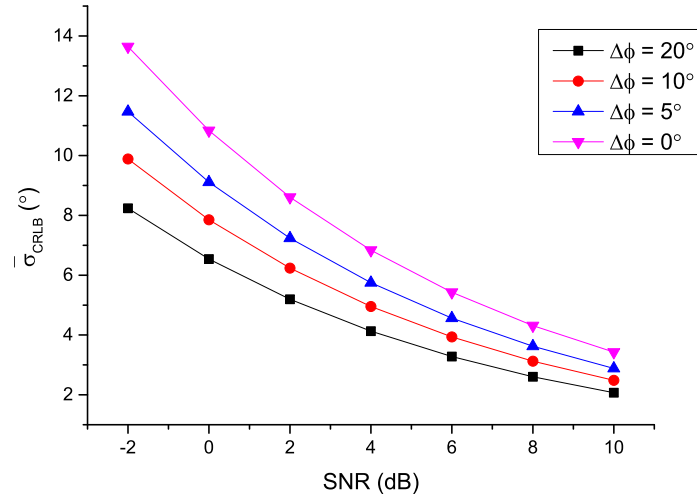
(a) Estimation of ϑ.
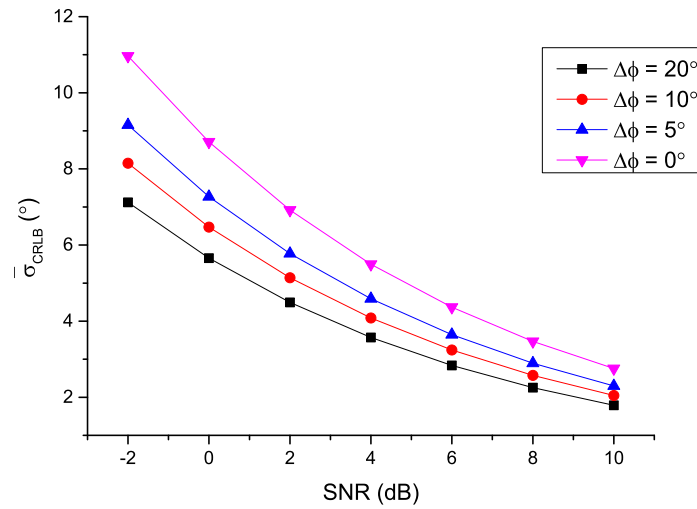
(b) Estimation of φ.

Figure 5.28.: CRLB when two coherent complex signals with different relative phase difference are received by a five-element L-Quad array with 0.35λ spacing.
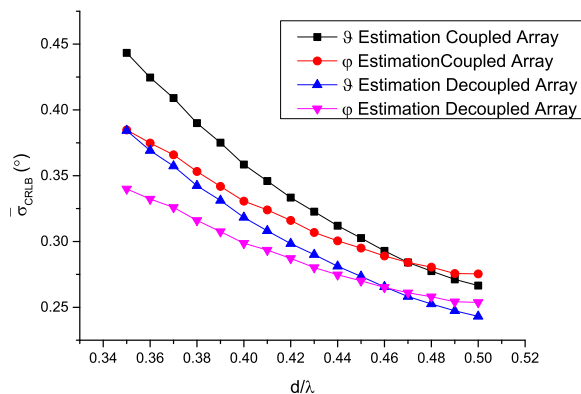
(a) Two correlated signals with $\rho = 0$.
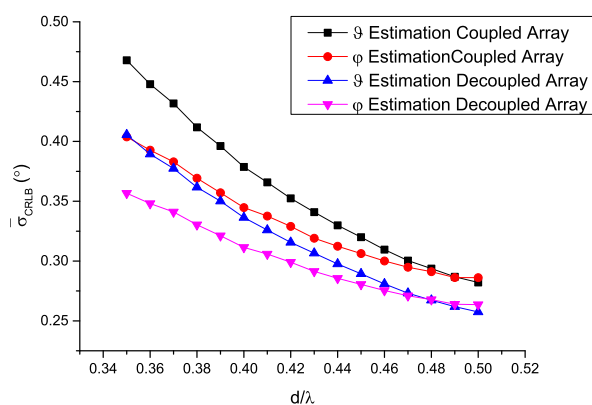
(b) Two correlated signals with $\rho = 0.5$.
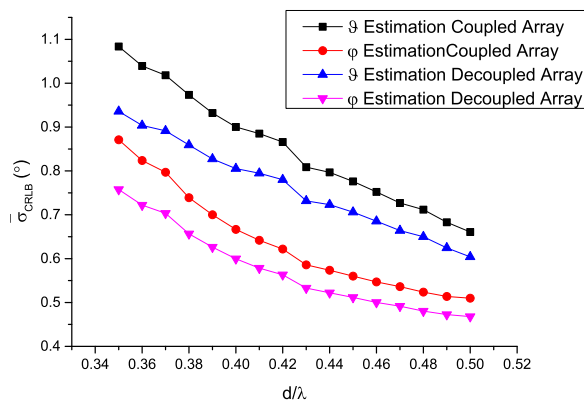
(c) Two correlated signals with $\rho = 1$.

Figure 5.29.: CRLB when two correlated signals are received by a five-element L-Quad array - comparison between coupled and decoupled array.

a significant improvement of direction finding performance, with respect to the CRLB. The effect is the more expressive the more coupled the array is and the more correlated the two impinging signals are. Figure 5.30 presents the results for the CRLB in the same scenario as described above, but when the two waves impinge on a three-element dual-polarized L-Quad array.

Figure 5.31 and 5.32 present the results for the resolution, computed with the use of Algorithm 1, when two waves impinge on a three and five-element dual-polarized L-Quad array, respectively. As already discussed, mutual coupling within antenna arrays decreases the effective number of elements that contributes to radiation. On the other hand, correlated signals require more elements in the array in order to allow for accurate direction finding. It is thus expected (and observed) that through decoupling, and as a consequence, by restoring the effective number of elements in the array, the accuracy and resolution of the DoA estimation of correlated signals is improved.

## 5.8. Performance Optimization of Fixed Physical Aperture Arrays

In Section 3.6, we compared three antenna array arrangements with fixed aperture and different number of elements, implying thus, different inter-element spacing. We presented results for a single SNR of 20 dB, with respect to the CRLB of a single impinging wave. Without accounting for coupling, the CRLB decreases monotonically with the number of elements in the array due to increased SNR and degrees of freedom. However, the degrading effects of stronger mutual coupling, which arises when the elements are placed together more closely, overtakes the improvement observed with higher number of elements, leading to increased CRLB (lower direction finding accuracy). We concluded that, for direction finding of a single signal, it is more adequate to use an array with lower number of elements, but larger inter-element spacing, and thus, weaker mutual coupling.

In this section, we go further and investigate the performance of the same three arrangements considered in Section 3.6, for different SNR, and considering the use of DMN to decouple and match the array, accounting for Ohmic losses due to the attenuation in microstrip lines [5]. Moreover, results are presented for multiple impinging waves, uncorrelated and correlated, with respect to accuracy and resolution for the arrangements investigated.

5.8.1. Single Impinging Wave

Figures 5.33a and 5.33b depict results for the CRLB of a single impinging wave when the three following arrangements are used for reception:
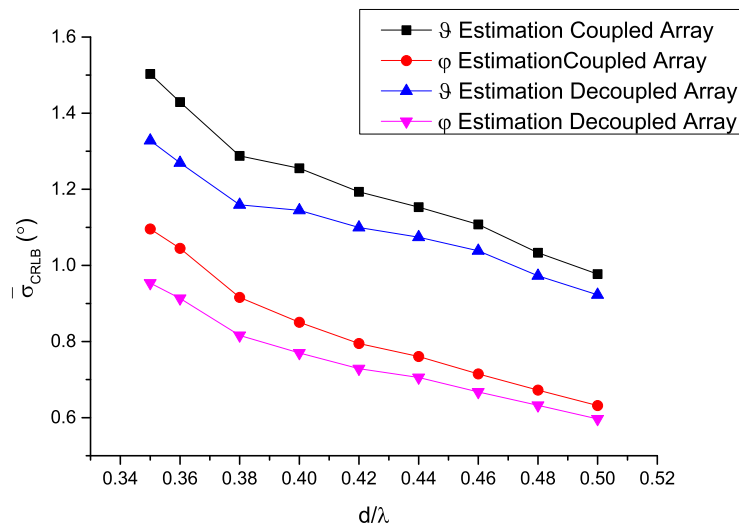
(a) Two correlated signals with $\rho = 0$.
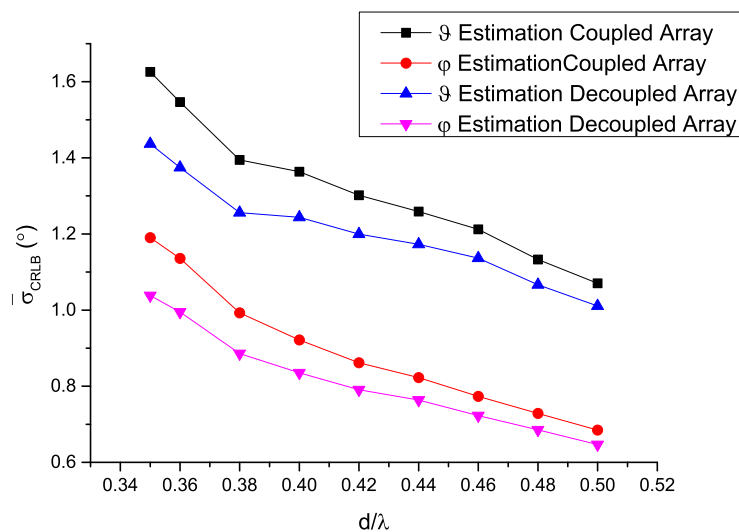
(b) Two correlated signals with $\rho = 0.5$.

Figure 5.30.: CRLB when two correlated signals are received by a three-element L-Quad array - comparison between coupled and decoupled array.
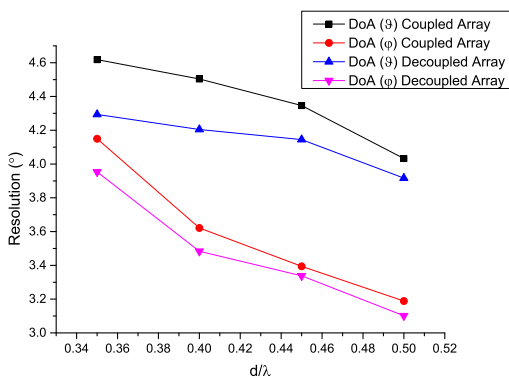
(a) Two correlated signals with $\rho = 0$.
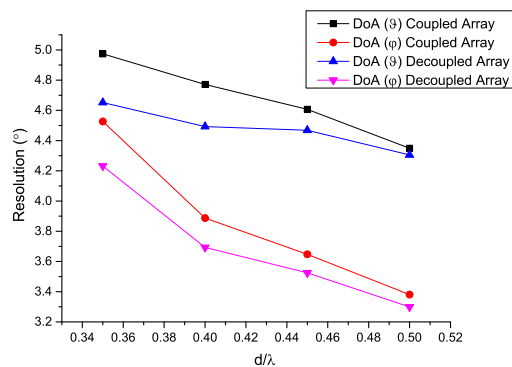
(b) Two correlated signals with $\rho = 0.5$.

Figure 5.31.: Direction finding resolution for two correlated signals received by a three-element L-Quad array - comparison between coupled and decoupled array.
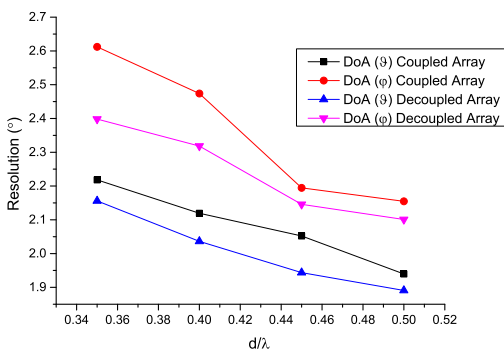
(a) Two correlated signals with $\rho = 0$.
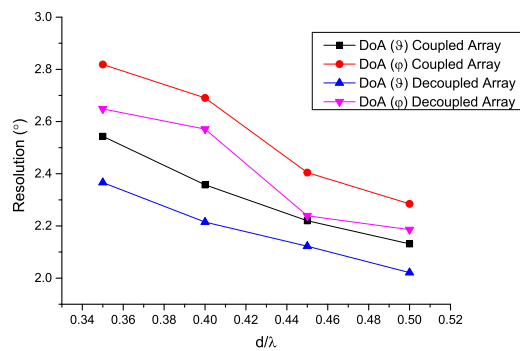
(b) Two correlated signals with $\rho = 0.5$.

Figure 5.32.: Direction finding resolution for two correlated signals received by a five-element L-Quad array - comparison between coupled and decoupled array.

- Five-element dual-polarized L-Quad array with 0.5λ inter-element spacing

- Six-element dual-polarized L-Quad array with 0.4λ inter-element spacing

- Seven-element dual-polarized L-Quad array with 0.35λ inter-element spacing

It is possible to conclude that, as expected, the effects of coupling on the CRLB are stronger than the effects of number of elements, when the aperture of the array is kept fixed. The lower the SNR, the more degraded the performance due to mutual coupling becomes. If mutual coupling between radiators could be neglected, one would decide to place as many elements in the fixed aperture as possible, to increase DoA estimation resolution and accuracy. The natural decision in our example scenario would be to decide for the seven-element array, instead of the five and six-element array. However, when coupling is properly accounted for, the degrading effects that arise from power mismatch, loss of degrees of freedom, and pattern distortion overtake the advantages of increased directivity when seven elements are placed in the array, in comparison to the five and six-element array.

In a subsequent step, we consider the use of DMNs to decouple and match the antenna arrays with six and seven elements, still assuming fixed aperture, in order to tackle the degrading effects of mutual coupling, which arise from placing elements together more closely. Figures 5.34a and 5.34b depict results for the CRLB to the estimation of ϑ and φ, respectively, of a single impinging wave when the three following arrangements are used for reception:

- Five-element dual-polarized L-Quad array with 0.5λ inter-element spacing, without DMN

- Six-element dual-polarized L-Quad array with 0.4λ inter-element spacing, with the use of a DMN, considering Ohmic losses of 2.5 dB

- Seven-element dual-polarized L-Quad array with 0.35λ inter-element spacing, with the use of a DMN, considering Ohmic losses of 3 dB

If we compare Figure 5.34a with Figure 5.33a, we observe that adding a DMN to the six and seven-element array lowered the CRLB for DoA estimation of a single impinging wave, even if taking into account Ohmic losses within the transmission lines. The same is observed from Figure 5.34b. However, for high SNR, the performance of the three arrangements considered is very similar. For low SNR, the performance of the seven-element array is slightly worse than if compared to the performance of the five and six-element for the estimation of ϑ, while it is difficult to distinguish between the performance of the five and six-element array. For the estimation of φ in low SNR regimes, the six and seven-element array exhibit better performance
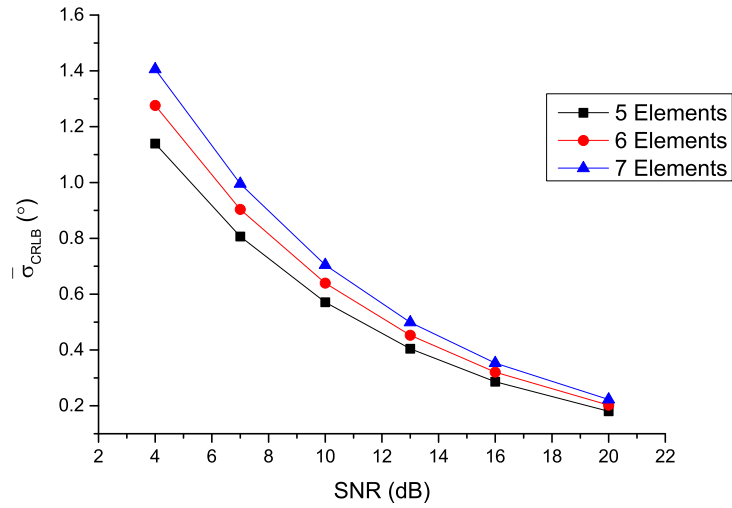
(a) Estimation of ϑ.
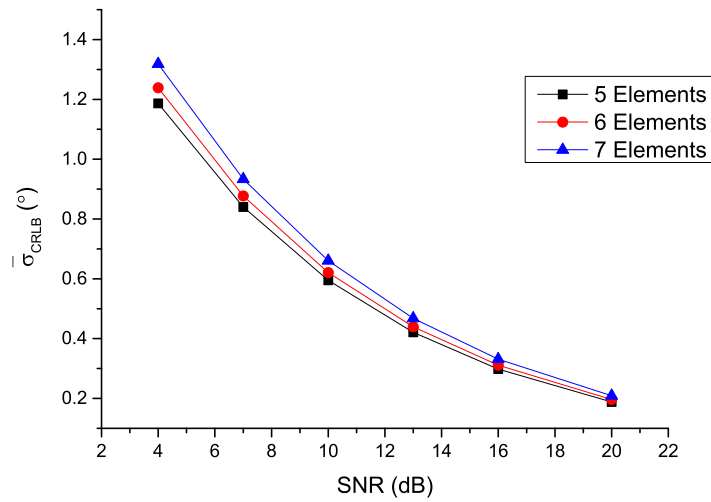
(b) Estimation of φ.

Figure 5.33.: DoA estimation CRLB of a single impinging wave on coupled arrays with same array aperture of 22 cm diameter.
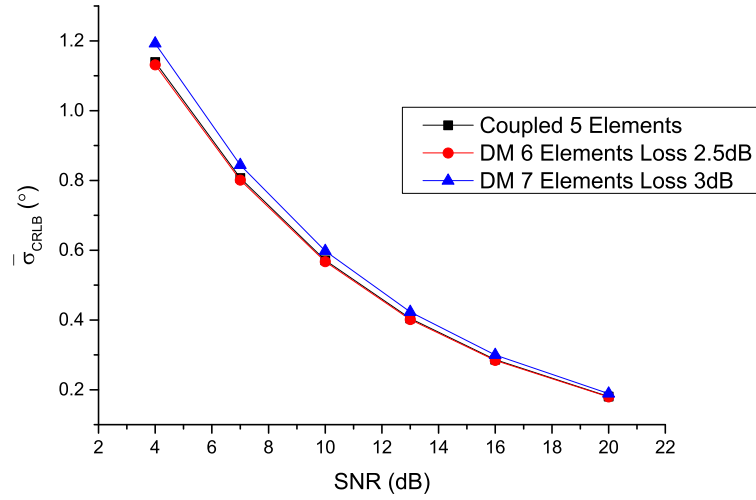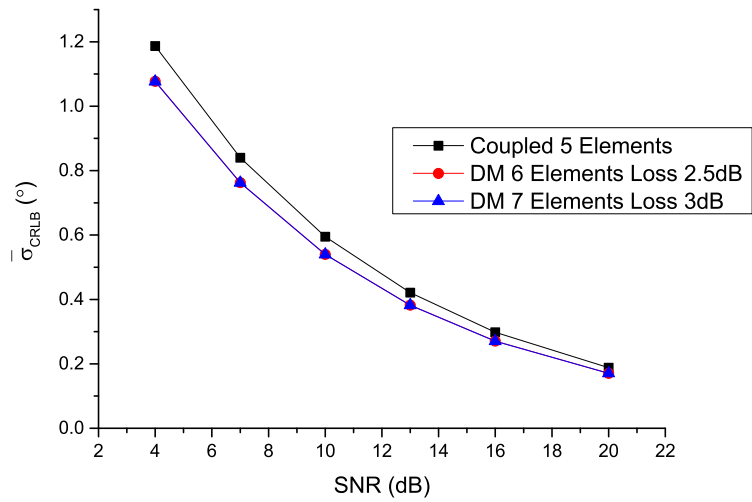
(a) Estimation of ϑ.

(b) Estimation of φ.

Figure 5.34.: Effects to the CRLB when adding a DMN to the array in case of using a six or a seven-element array, including Ohmic losses, in comparison to the coupled five-element array, same array aperture of 22 cm diameter.

when compared to the five-element array, but very similar when compared to each other. The slightly different performance between the estimation of the two directions ϑ and φ is obviously dependent on the type of antenna used for the intended application.

5.8.2. Multiple Uncorrelated Impinging Waves

Although results with respect to CRLB show that, for coupled arrays, the five-element array with 0.5λ spacing outperforms the six and seven-element array with 0.4λ and 0.35λ respectively, and that with the use of DMNs, the performance gain is not outstanding when we compare the six and seven-element arrangement to the five-element arrangement, it is important to highlight that for the computation of the CRLB, only a single impinging wave was considered. It is relevant, however, to evaluate the performance of the arrangements when multiple waves impinge on the array, when it becomes necessary to resolve them. In multipath or multiple emitter scenarios, not only accuracy, but also resolution plays an important role in the overall antenna array direction finding performance. It is important to note that the results presented in this section rely on the assumption of perfect data model, implying that the number of impinging waves is known a priori.

Figures 5.35a and 5.35b depict results for the CRLB for the estimation of ϑ and φ, respectively, when four uncorrelated waves are impinging on the antenna array. We assume that from the four impinging waves, one is the main, with DoA over a grid in elevation from $0°$ to $90°$, and in azimuth from $-180°$ to $180°$. The secondary waves are assumed to be impinging from $(\vartheta_2, \varphi_2) = (45°, 45°)$, $(\vartheta_3, \varphi_3) = (30°, 60°)$ and $(\vartheta_4, \varphi_4) = (60°, 30°)$. We compute the CRLB for the main wave as an average over the grid considered, assuming that three secondary waves are also impinging on the array, and that all waves are impinging with polarization described by the Jones vector with $\beta = 45°$ and $\alpha = 0°$.

From Figures 5.35a and 5.35b, it is possible to observe that when four waves are impinging on the arrays, all three arrangements considered are capable to resolve the signals. However, the lower the number of elements in the array, the higher the CRLB becomes. This result helps us to conclude that if multiple signals are received by an array, even if no DMN is used to decouple and match the elements, the seven-element array with 0.35λ spacing outperforms the five-element array with 0.5λ. The effects of mutual coupling to the direction finding performance of antenna arrays is thus less significant than the effects of number of elements, when it becomes necessary to resolve multiple received signals.

Additionally, simulation was carried out for five and six source waves. However, when five or six waves are impinging on a five-element array, the estimation fails and the resulting CRLB assumes inconsistent values and, as a consequence, cannot be used as a metric for

direction finding performance. The same occurs for the six-element array when six waves are received. We limit to show the consistent results for the CRLB that allows us to compare the performance of the arrangements for direction finding of multiple sources. In the worst-case scenario with six impinging waves, only the seven-element arrangement is able to resolve the sources. Figures 5.36a and 5.36b compares results for CRLB to the estimation of ϑ and φ, respectively, for the five and six signals scenario, when the array is able to resolve the multiple waves.

We now proceed to investigating the effects of using a DMN for the direction finding of four impinging wave fronts, with respect to the CRLB. Figures 5.37a and 5.37b depict results for the CRLB for the estimation of ϑ and φ, respectively, when four uncorrelated waves are impinging on a decoupled antenna array. It is important to note that the results take into account Ohmic losses within the DMN.

It is clear that when multiple waves are received by an array comprised of seven elements, enhanced performance is observed if compared to the five-element array. Additional improvement may be achieved if a DMN is used to compensate for the degrading effects of mutual coupling, which arise due to the narrow inter-element spacing in case seven elements with $d/\lambda = 0.35$ are placed in the same fixed aperture as the five-element array with $d/\lambda = 0.5$. The improvement is observed even if we consider the dissipation loss that occurs within the network.

5.8.3. Multiple Correlated Impinging Waves

Let us now investigate the scenario with multiple correlated waves impinging on the antenna array with fixed aperture of 22 cm. Figures 5.38a and 5.38b present results for the CRLB to the estimation of ϑ and φ, respectively, when four, five, and six waves are impinging on a coupled antenna array, assuming that the main signal is fully correlated to one of the secondary signals. Note that since one of the signals is fully correlated with another signal, the five-element array is not capable of estimating the DoAs when four waves impinge. Because two of the signals are fully correlated, the number of radiating elements required for proper estimation increases. Only the six and the seven-element arrays are thus capable of estimating the DoA of four signals, under strong correlation.

We now proceed to investigating the effects, with respect to the CRLB, of using a DMN for direction finding of four source waves, two of which are fully correlated with respect to each other. Figures 5.39a and 5.39b depict results for the CRLB to the estimation of ϑ and φ, respectively, when four waves are impinging on a decoupled antenna array, and assuming that the main signal is fully correlated to one of the secondary signals. It is important to note that
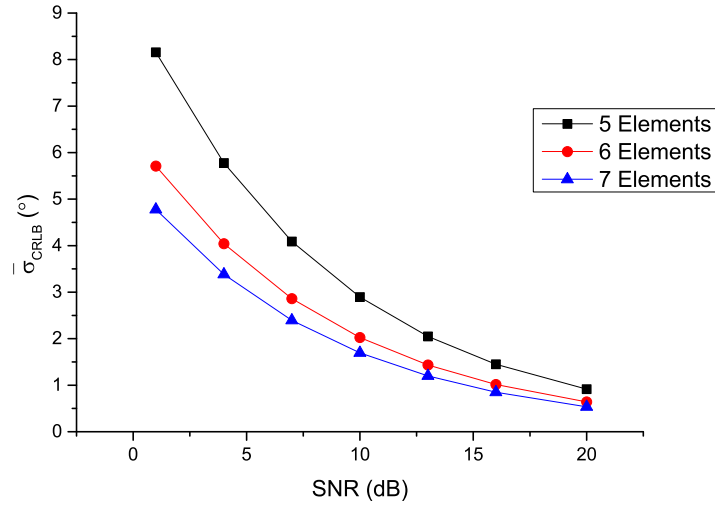
(a) Estimation of ϑ.
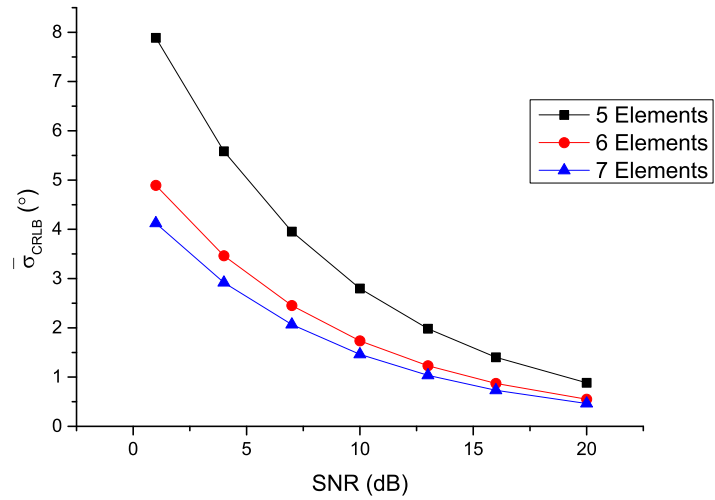
(b) Estimation of φ.

Figure 5.35.: Comparison between the CRLB for the estimation of a main signal DoA, when four uncorrelated waves are impinging on a five, six and seven-element array.
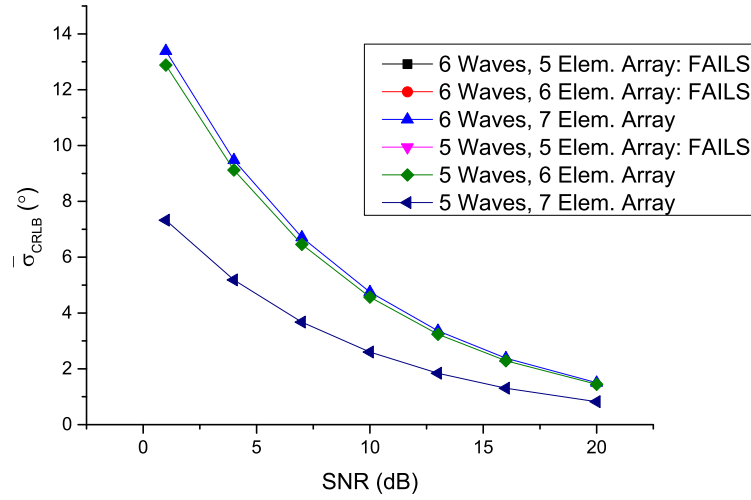
(a) Estimation of ϑ.
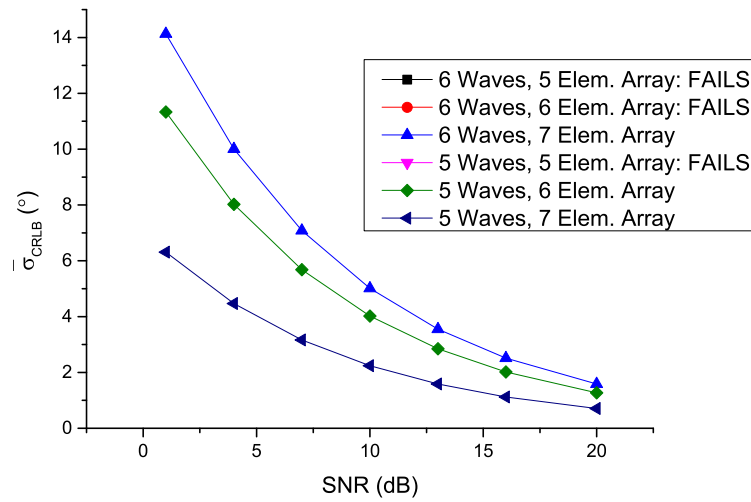
(b) Estimation of φ.

Figure 5.36.: Comparison between the CRLB for the estimation of a main signal DoA, when five and six uncorrelated waves are impinging on a five, six and seven-element array with same array aperture of 22 cm diameter.
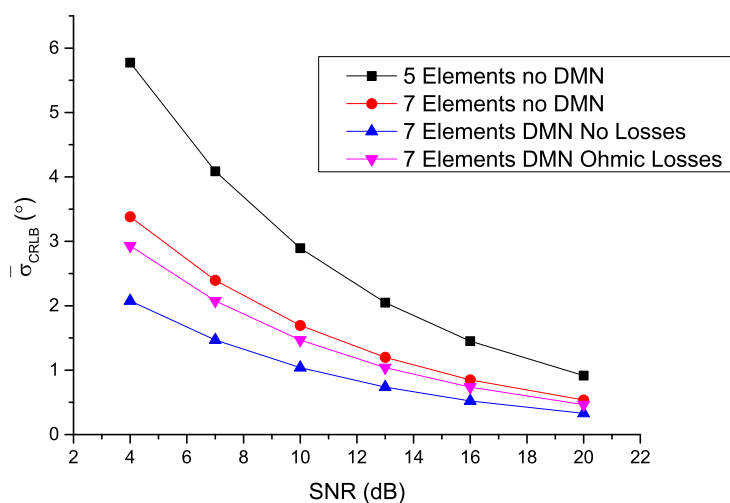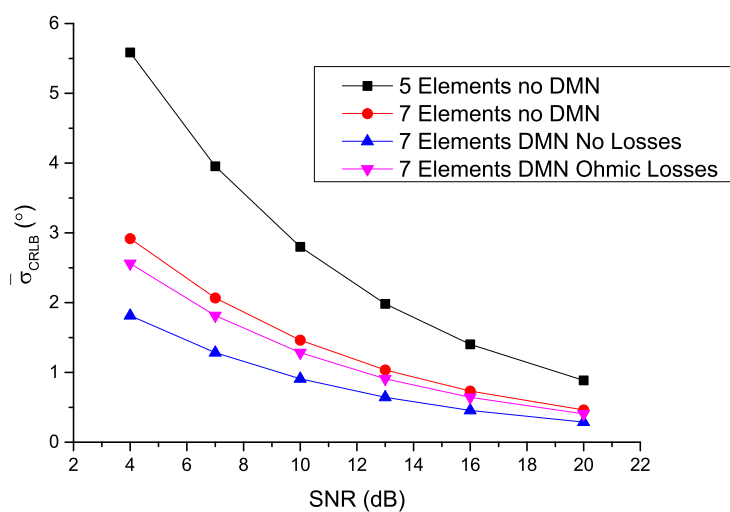
(a) Estimation of ϑ.

(b) Estimation of φ.

Figure 5.37.: Comparison between the CRLB of a five-element array for the estimation of a main signal DoA (ϑ), when four uncorrelated waves are impinging, to the CRLB of a seven-element array without DMN, with DMN with and without accounting for Ohmic losses, same array aperture of 22 cm diameter.
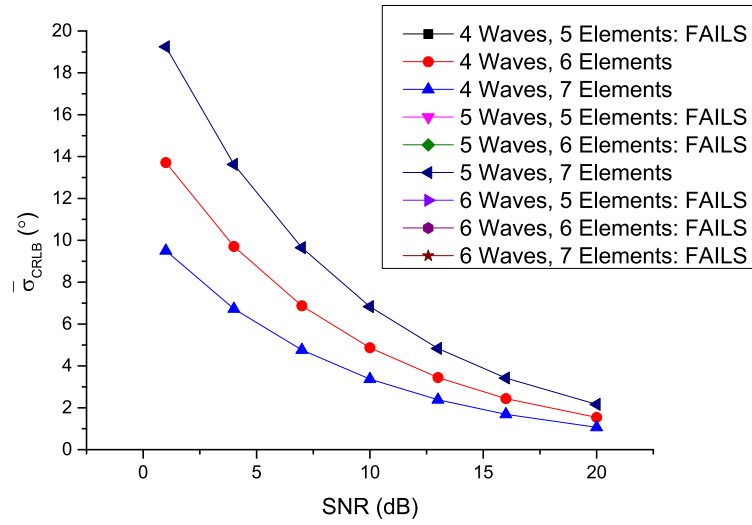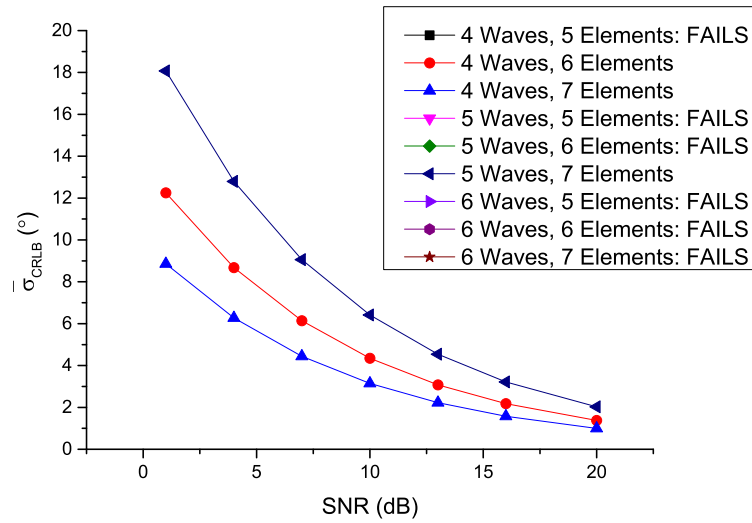
(a) Estimation of ϑ.

(b) Estimation of φ.

Figure 5.38.: Comparison between the CRLB for the estimation of a main signal DoA, when four, five and six waves, two of which are fully correlated with respect to each other, are impinging on a five, six and seven-element array with same array aperture of 22 cm diameter.

the results take into account Ohmic losses within the DMN.
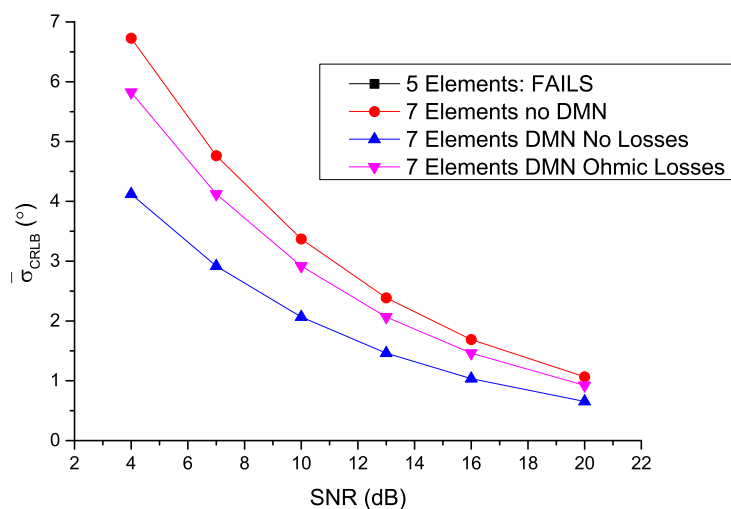
(a) Estimation of ϑ.
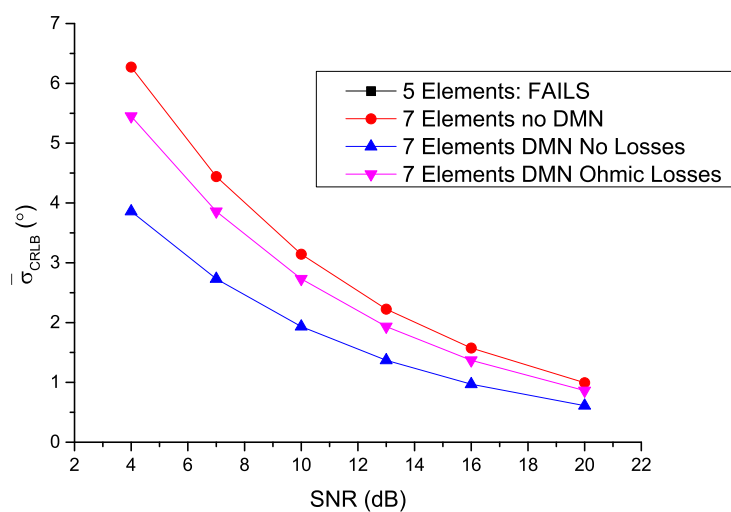
(b) Estimation of φ.

Figure 5.39.: Comparison between the CRLB of a five-element array for the estimation of a main signal DoA (ϑ), when four waves (main wave fully correlated with one secondary wave) are impinging, to the CRLB of a seven-element array without DMN, with DMN with and without accounting for Ohmic losses, same array aperture of 22 cm diameter.

It is clear that when multiple waves are received by an array comprised of seven elements, enhanced performance is observed if compared to the five-element array. As with direction finding of uncorrelated signals, additional improvement may be observed if a DMN is used, even when we consider the dissipation loss that occurs within the network.

## 5.9. Evaluation of Antenna Arrays with Respect to MUSIC and Maximum Likelihood Estimation

This section evaluates arrays comprised of dual-polarized L-Quad radiators for two-dimensional direction finding based on the MUSIC and Maximum Likelihood techniques. Circular and linear arrangements comprising five and three dual-polarized L-Quad antennas for the 1710 – 1785 MHz frequency band are investigated with respect to direction finding performance using the Root Mean Squared Error (RMSE) of the estimation as a figure of merit. The source signals are modeled as deterministic, i.e. frozen in time. Results for the error of the DoA estimation are presented both for elevation and azimuth directions for different array arrangements and inter-element spacings, with the aim of allowing the reader to draw conclusions on the effects of the array geometry and mutual coupling to MUSIC and ML DoA estimation. Previous work considered the CRLB as a figure of merit to characterize inherent direction finding capabilities of antenna arrays [6]. In this section, we go further and analyze the performance of arrays in the actual direction finding process. For this thesis, we use the exhaustive search procedure to find the maxima (or minima) of the direction finding cost functions. However, depending on the scenario, e.g., for dense multipath components arriving at the receiver, exhaustive search procedure may require restrictive high computational time. Alternatively, iterative search procedures such as the Levenberg-Marquardt can be used to reduce processing effort.

The results for the computed RMSE for DoA estimation of an impinging wave front is given for both linear and circular array arrangements. The aim is to show how the antenna array arrangement affects the direction finding performance for some specific Signal to Noise Ratio (SNR) regime. Throughout the results, the SNR is a parameter that will be varied and it is known a priori the number of waves that impinge on the array. The signal polarization is assumed to be known a priori, characterized by the Jones vector $\boldsymbol{k}$ with $\beta = 45°$ and $\alpha = 0°$ (linear polarization).

Let us start by comparing the variance of the MUSIC and the Maximum Likelihood estimation with the CRLB, by using the expressions derived in [127]. The asymptotic covariance matrix for the Maximum Likelihood estimator, assuming that the signal is modeled as deterministic, leaving the dependency of the array response with respect to DoA (ϑ, φ) out of the

expression for simplicity, can be given by:

$$C_{\mathrm{CML}}(\vartheta, \varphi) = \frac{\sigma}{2L}[\mathfrak{Re}(\boldsymbol{H} \odot \boldsymbol{R}_{\mathrm{s}}^{\mathrm{T}})]^{-1}\{\mathfrak{Re}[\boldsymbol{H} \odot (\boldsymbol{R}_{\mathrm{s}}\boldsymbol{W}\boldsymbol{R}_{\mathrm{s}})^{\mathrm{T}}]\}[\mathfrak{Re}(\boldsymbol{H} \odot \boldsymbol{R}_{\mathrm{s}}^{\mathrm{T}})]^{-1} \qquad (5.9)$$

where:

$$\begin{aligned} \boldsymbol{W} &= \boldsymbol{R}_{\mathrm{s}}^{-1} + \sigma\boldsymbol{R}_{\mathrm{s}}^{-1}(\boldsymbol{k}^{\mathrm{H}}\boldsymbol{A}^{\mathrm{H}}\boldsymbol{A}\boldsymbol{k}\boldsymbol{R}_{\mathrm{s}}^{-1}) \\ \boldsymbol{H} &= \boldsymbol{D}^{\mathrm{H}}[\boldsymbol{I} - \boldsymbol{A}\boldsymbol{k}(\boldsymbol{k}^{\mathrm{H}}\boldsymbol{A}^{\mathrm{H}}\boldsymbol{A}\boldsymbol{k})^{-1}\boldsymbol{k}^{\mathrm{H}}\boldsymbol{A}^{\mathrm{H}}]\boldsymbol{D} \end{aligned} \qquad (5.10)$$

For MUSIC, the covariance matrix is given by:

$$C_{\mathrm{MUSIC}} = \frac{\sigma}{2L}(\boldsymbol{H} \odot \boldsymbol{I})^{-1}[\mathfrak{Re}(\boldsymbol{H} \odot \boldsymbol{W}^{\mathrm{T}})](\boldsymbol{H} \odot \boldsymbol{I})^{-1} \qquad (5.11)$$

Figure 5.40a and 5.40b compare results for the deviation (square root of the variance as defined in (5.9) and (5.11)) of the MUSIC and Maximum Likelihood DoA estimation of ϑ and φ, respectively, to the bound given by the CRLB for the L-Quad antenna array with 0.5λ and 0.35λ inter-element spacing. As expected, the error in the estimation approaches the lower bound as the SNR increases. The error of both MUSIC and Maximum Likelihood, and the CRLB were computed as a weighted mean over a grid in elevation ranging from $0°$ to $90°$, and in azimuth from $-180°$ to $180°$. The weights are computed as the cosine of the elevation angle. It is possible to observe that the variance of the MUSIC and Maximum Likelihood estimation asymptotically approaches the CRLB for large SNR.
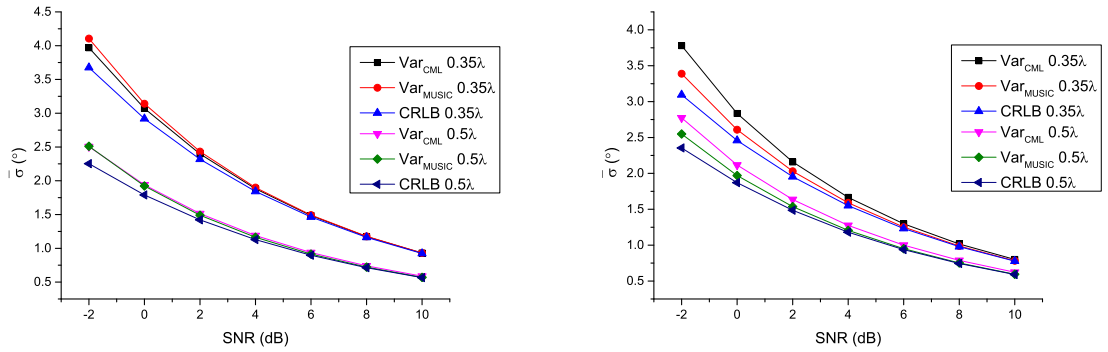
(a) Estimation of ϑ.   (b) Estimation of φ.

Figure 5.40.: Comparison between the CRLB and the asymptotic variance of MUSIC and Maximum Likelihood DoA estimation.

Figure 5.41a and Figure 5.41b depict the RMSE for the estimation of the signal DoA, in ϑ (elevation) and φ (azimuth) directions respectively, using the MUSIC spectrum and five-element L-Quad antenna arrays in circular arrangement for different degrees of coupling. The grid considered for the search over azimuth is -180° to 180° with 481 points, and over elevation 0° to 90° with 241 points. For the average of estimation error, the signal was assumed to be impinging from an azimuth grid ranging from 10° to 70° with step of 5°, and an elevation grid ranging from 10° to 80° with step of 5°.

Figure 5.42 depicts the RMSE for the estimation of the signal DoA, in ϑ (elevation) and φ (azimuth) directions, using the MUSIC spectrum and five-element L-Quad antenna arrays in linear arrangement for different degrees of coupling. The grid considered for the search and the directions of the impinging signal for the computation of the average estimation error is the same as in Figure 5.41. Since a linear array in the azimuth plane is not able to estimate elevation, we skip results for the RMSE of the estimation of ϑ.

Note that, as expected from the results of the CRLB, the stronger the electromagnetic interaction between elements in an array, the higher the DoA estimation error for both circular and linear arrangements becomes. In order to compare the performance of circular and linear arrays with respect to the error of MUSIC DoA estimation, we present in Figure 5.43 results for 0.35λ and 0.5λ inter-element spacing for both arrangements, for the estimation of the signal azimuth of arrival.

It is possible to observe that the linear arrangement suffers more from mutual coupling than circular arrangements. The estimation of DoA when using a linear array for reception becomes much less accurate if compared to what is obtained with a circular arrangement, if the mutual coupling is strong (0.35λ). However, the performance of the arrangements is very similar for 0.5λ spacing. This can be explained, since the linear array has a slightly wider aperture in the direction of the array but no aperture in the orthogonal direction. Hence, the average performance over all possible impinging directions (over the grid considered) is, at the end, similar, if we compare linear and circular arrays.

Figure 5.44 depicts the RMSE for the estimation of the signal DoA, in ϑ (elevation) and φ (azimuth) directions, using the Maximum Likelihood spectrum and five-element dual-polarized L-Quad antenna arrays in circular arrangement for different degrees of coupling. We assume that the impinging signal is nonrandom over observation and as a consequence, we use the CML for estimating the DoA. The grid considered for the search and the directions of the impinging signal for the computation of the average estimation error is the same as in Figure 5.41 and 5.42.

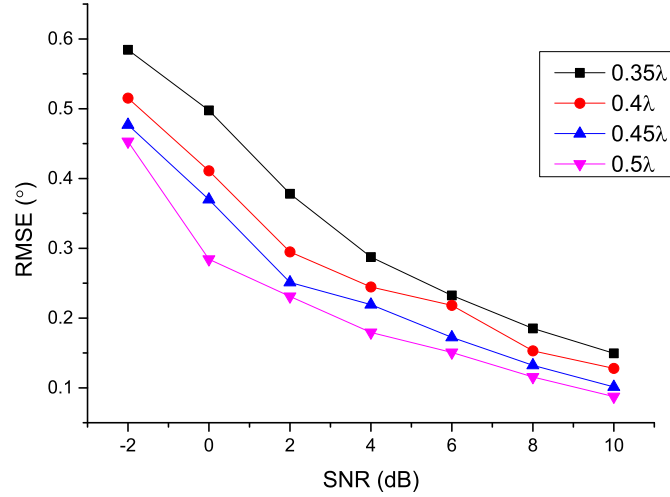Figure 5.45 depicts the RMSE for the estimation of the signal DoA, in ϑ (elevation) and φ (azimuth) directions, using the Maximum Likelihood spectrum and five-element dual-polarized

(a) Estimation of ϑ.
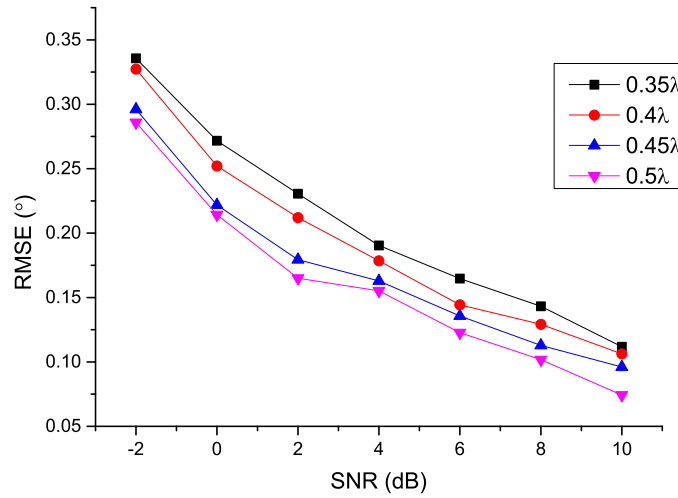
(b) Estimation of φ.

Figure 5.41.: Effects of coupling to the RMSE of the MUSIC two-dimensional DoA estimation, when a five-element circular array is used to receive the signals.

Figure 5.42.: Effects of coupling to the RMSE of the MUSIC DoA (φ) estimation, when a five-element linear array is used to receive the signals.

L-Quad antenna arrays in linear arrangement for different degrees of coupling. The grid considered for the search and the directions of the impinging signal for the computation of the average estimation error is the same as considered in the last plots. Since a linear array in the azimuth plane is not capable of estimating elevation, we skip results for the RMSE of the estimation of ϑ. Both for the linear and for the circular arrangements, the estimation error gets the higher, the stronger the coupling within the array becomes, as already observed from the CRLB and from the MUSIC DoA estimation error.

In Figure 5.46, results are presented for 0.35λ and 0.5λ inter-element spacing for both arrangements, for the Maximum Likelihood estimation of the signal azimuth of arrival. As observed with MUSIC, the difference between the performances of linear and circular arrangements is much more significant when mutual coupling within the array is stronger.

In [6], the CRLB was investigated for several array configurations. It concluded that the linear arrangement leads to higher CRLB for DoA estimation if compared to the circular array. To the same conclusion we get in this section, after observing the results for the estimation RMSE using both MUSIC and ML techniques for several SNR and different inter-element spacings. It is also possible to note that the higher the mutual coupling, the bigger the difference of performance between linear and circular arrays becomes, with respect to the estimation RMSE. The results presented in this section are in accordance with conclusions

Figure 5.43.: Comparison between the MUSIC RMSE for a circular and a linear five-element L-Quad array, for the estimation of azimuth.

drawn in [6] and [7], which argue that the higher the mutual coupling, the lower the accuracy of the DoA estimation becomes, both with respect to the CRLB as with respect to the estimation RMSE.

Decoupled Arrays

We now present results for MUSIC and ML DoA estimation using decoupled L-Quad arrays. We start with the evaluation of decoupled arrays for MUSIC DoA estimation. Although for symmetric antenna arrays, DMNs can be easily designed with the use of hybrids and directional couplers, the number of couplers required increases with the number of ports to be decoupled, leading to a serious size constraint. The results presented in this section for the ten-port L-Quad array, rely on the perfect circuit implementation of the DMN, and as a consequence, the decoupled array manifold can be assessed through Equation (4.9).

By observing Figures 5.47 one can easily conclude that decoupling the array leads to significant improvement in the performance with respect to the actual estimation error, especially for lower SNR. Moreover, the effects of decoupling the array are more expressive for decreased inter-element spacing.

Finally, we present results for CML DoA estimation, and compare the performance between coupled and decoupled arrays. From Figure 5.48, we observe the performance improvement
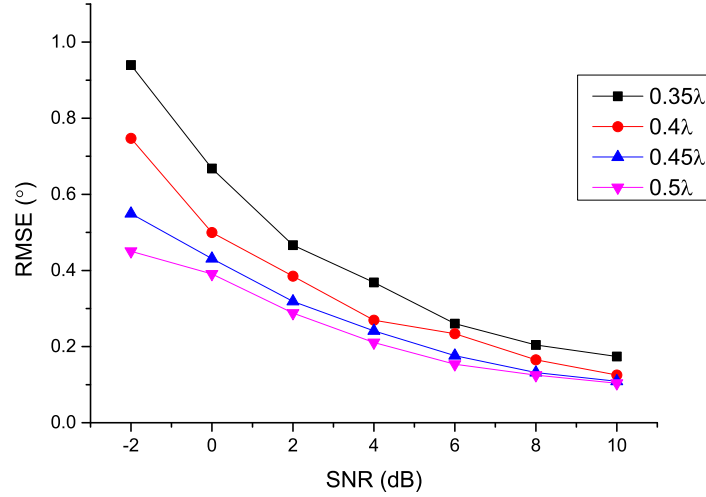
(a) Estimation of ϑ.
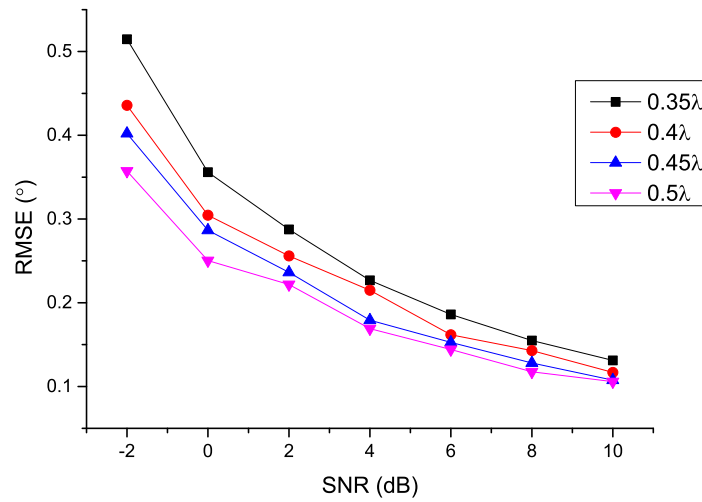
(b) Estimation of φ.

Figure 5.44.: Effects of coupling to the RMSE of the Maximum Likelihood two-dimensional DoA estimation when a five-element circular array is used to receive the signals.
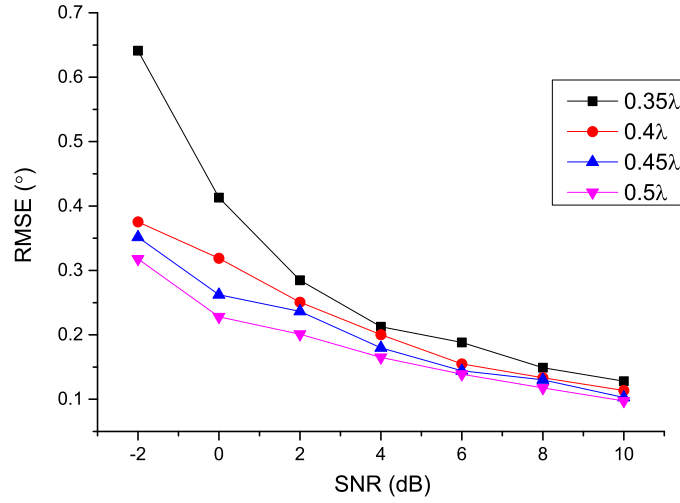
Figure 5.45.: Effects of coupling to the RMSE of the CML DoA (φ) estimation, when a five-element linear array is used to receive the signals.

achieved from decoupling the array, with respect to the actual ML estimation error, especially for lower SNR regimes. The results observed in this section are in good accordance with the results previously presented with respect to the DoA estimation CRLB, and thus, reinforce the advantages of decoupling arrays for direction finding.

Multiple Impinging Waves

We now proceed to presenting results for the MUSIC DoA estimation of two impinging wavefronts. We ran simulation for waves impinging from different directions with same power and (linear) polarization given by the Jones vector $\boldsymbol{k}$, with $\beta = 45°$ and $\alpha = 0°$. The MUSIC estimation performance is measured by the RMSE over a grid in elevation and azimuth angles ranging from $10°$ to $55°$. We compute the total RMSE as an average of the error for the DoA estimation of the first wave and the error for the DoA estimation of the second wave. The second impinging wave is assumed, for simplification, to be impinging from an elevation and azimuth separation of $25°$ with respect to the first wave. We use exhaustive search for this example, although iterative search could be employed aiming reduced processing time.

Figure 5.49 compares results for the RMSE of the DoA estimation if two waves impinge on a dual-polarized five-element L-Quad array with no DMN for decoupling and matching to the results obtained if a DMN is used.
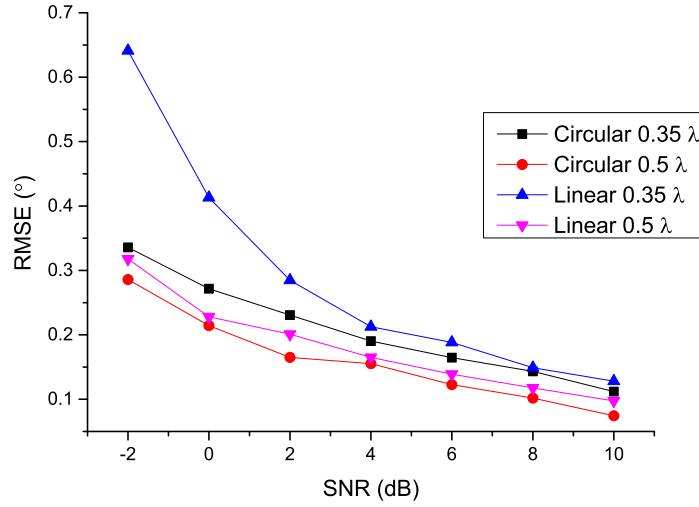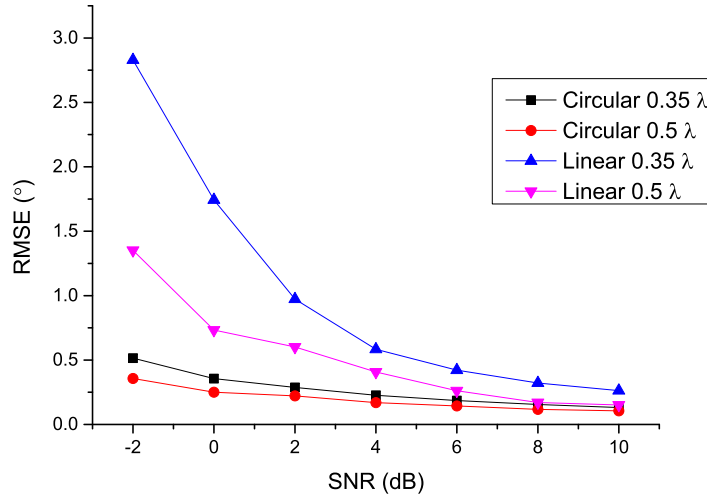
Figure 5.46.: Comparison between the CML RMSE for a circular and a linear five-element L-Quad array, for the estimation of azimuth.

It is clear to note from Figure 5.49 that, if two waves impinge on the array, the estimation error is the higher the more compact (and as a consequence, coupled) the array becomes. If we compare the error for DoA estimation using DMNs to decouple and match the arrays to the error observed if we use the originally coupled arrays, it is possible to observe that a significant performance improvement is accomplished, proving once more the benefits of using DMN for DoA estimation.

5.10. Evaluation of Microstrip Patch Arrays for Direction Finding

Until this point, we were able to present to the reader results for the performance of L-Quad arrays in several arrangements with respect to the CRLB for direction finding and the error of MUSIC and ML estimation. Exhaustive investigation on the influence of coupling and on the use of DMN and correspondent effects to the performance of the antenna array for direction finding was carried out throughout the thesis. We now proceed to investigating microstrip patch antenna arrays and the suitability for direction finding, as an alternative to L-Quad arrays, when strong coupling degrades the radiation efficiency of the array. Although we believe that L-Quad arrays are more suitable for direction finding if compared to patch arrays, we still argue that for the evaluation of the theory proposed in this thesis, it is important to
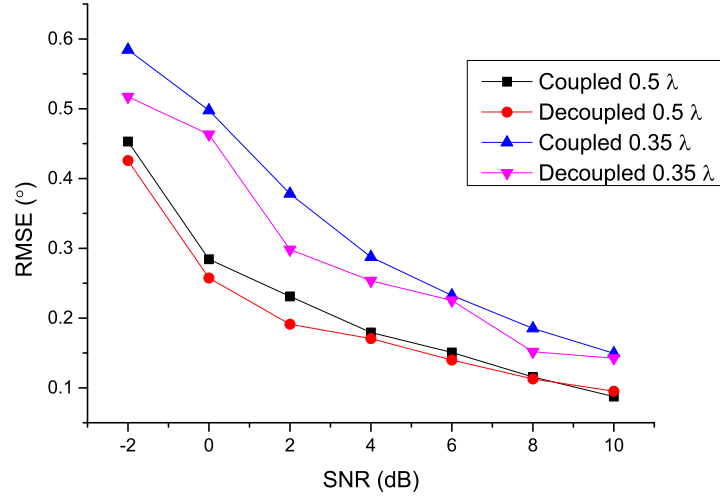
(a) Estimation of ϑ.
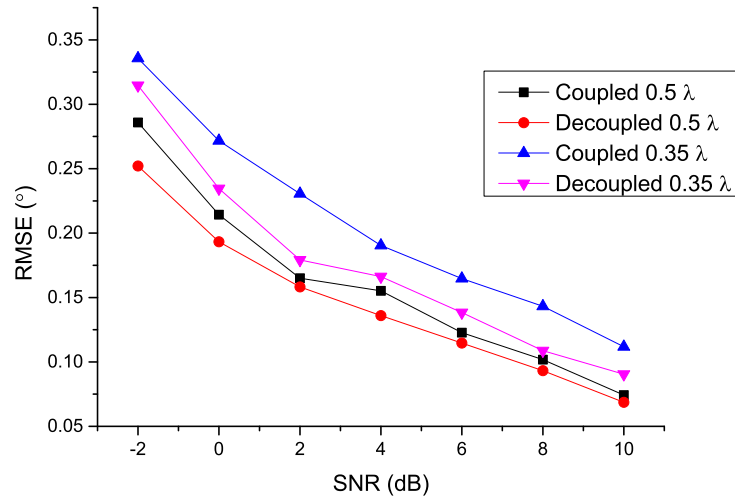
(b) Estimation of φ.

Figure 5.47.: Effects of decoupling to the RMSE of MUSIC DoA estimation, when a five-element circular array is used to receive the signals.
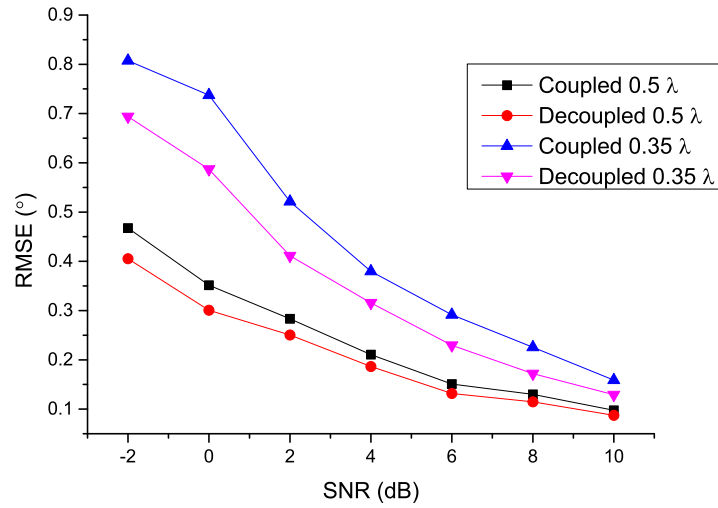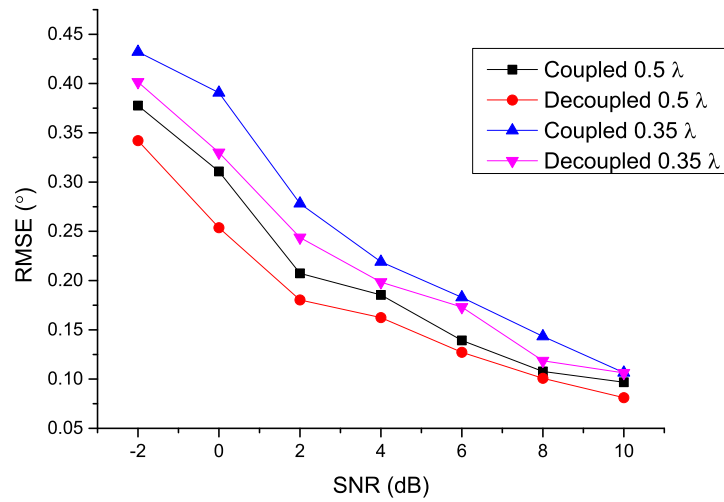
(a) Estimation of ϑ.

(b) Estimation of φ.
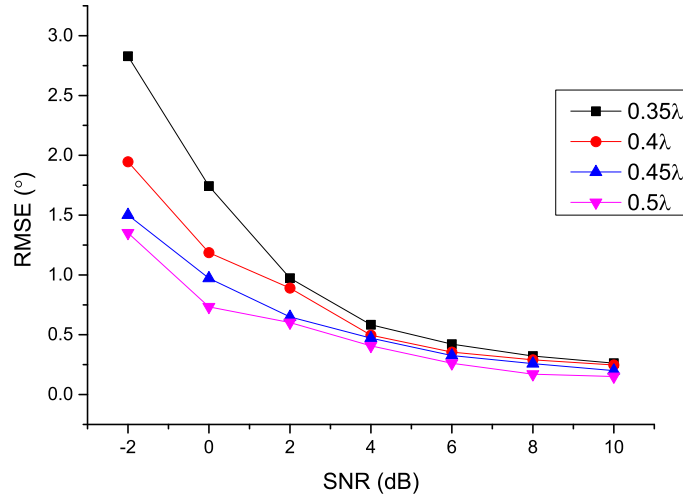
Figure 5.48.: Effects of decoupling to the RMSE of CML DoA estimation, when a five-element circular array is used to receive the signals.
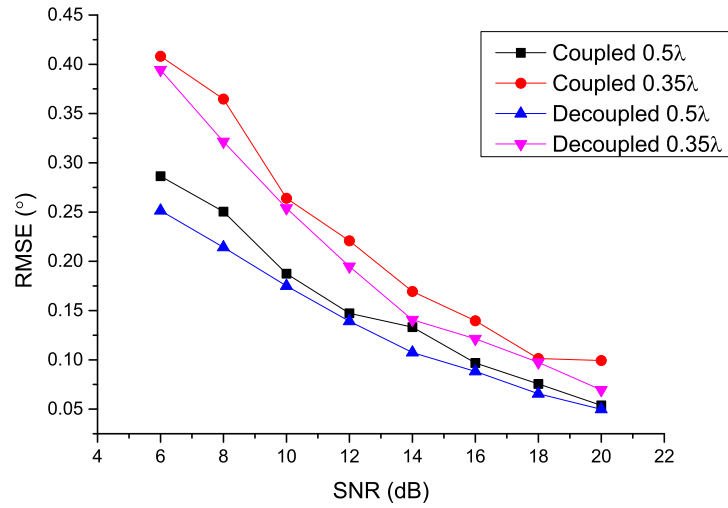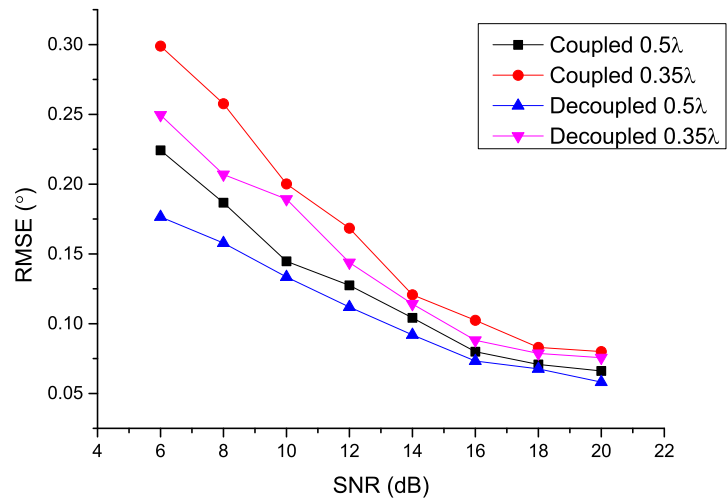
(a) Estimation of ϑ.

(b) Estimation of φ.

Figure 5.49.: Effects of decoupling to the RMSE of MUSIC DoA estimation, if two waves impinge on L-Quad dual-polarized five-element arrays.

show results for different antenna topologies.

5.10.1. Evaluation of Decoupling Patch Arrays

Let us first start with a six-element patch array as depicted in Figure 5.50. The array is comprised of six microstrip patches, in planar arrangement for 2D DoA estimation. The patches of width 40 mm and length 30 mm are printed on a dielectric layer of relative permittivity $\epsilon_r = 2.2$ and 3.2 mm height. The patches are fed by probes located at $(x_f, y_f) = (5\,\text{mm}, 0)$. The patches dimensions are optimized for the frequency of 2.35 GHz, and the probe location is varied for impedance matching.
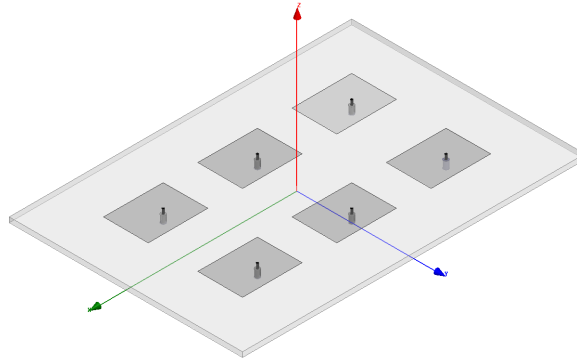
Figure 5.50.: Six-element planar probe fed microstrip patch array.

Figure 5.51 compares, with respect to the CRLB for direction finding, the coupled patch array for different inter-element spacings to the decoupled array through the eigenmode excitation approach. Note that close to 0.5λ spacing, coupling does not significantly degrade the radiation performance of the array, and as a consequence, the CRLB for the coupled array is similar to the CRLB for the decoupled array, for the estimation of both directions ϑ and φ.

5.10.2. Evaluation of Fixed Aperture Patch Arrays

Let us now proceed to investigating a scenario of fixed aperture and two possible arrangements: six-element planar array 2×3, and eight-element planar array 2×4. Figures 5.52a and 5.52b compares results for the CRLB to the estimation of ϑ and φ, respectively, for the six and eight-element planar patch array. They illustrate the fact that, if coupled patch arrays of fixed physical size are considered for direction finding of a single wave, as already observed with L-Quad arrays, the arrangement that offers higher accuracy for DoA estimation is the one with lower number of elements, in which mutual coupling is weaker. The degrading effects
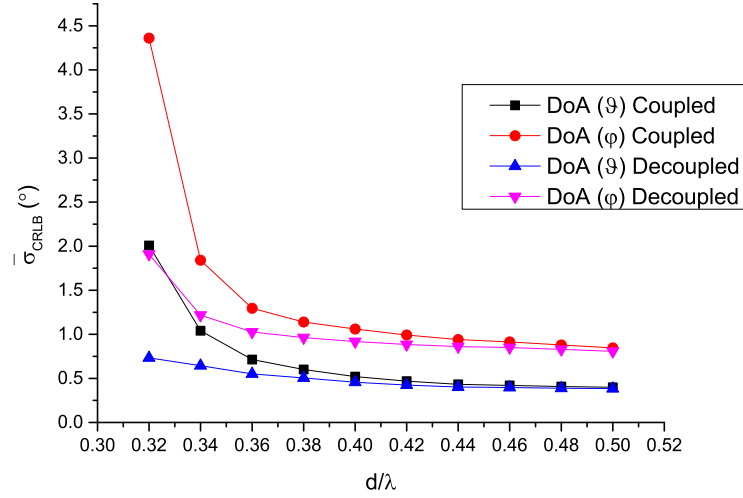
Figure 5.51.: Effects of decoupling to the CRLB of a six-element probe fed patch array in comparison to the coupled array, for different inter-element spacings.

of the interaction between radiating elements, if the antenna array is designed with element spacing smaller than 0.5λ, overcome the improvement that would be observed due to increased SNR, if more elements were placed in the same aperture, and no coupling is accounted for.

However, when a DMN is designed to compensate for the impaired performance due to mutual coupling, significant accuracy improvement is observed. The first step is to observe that the CRLB of the eight-element array, if the ports are decoupled by eigenmode excitation, approaches the CRLB of the six-element array. Although the ports are decoupled, they are still not matched, and the higher performance that would be expected from the eight-element array is overcome by the mismatch at the feeding ports. If a matching network is integrated to the decoupled array to maximize the power transfer, the resulting CRLB is significantly reduced, even when Ohmic losses that arise from the design of DMNs with microstrip lines are considered, proving the benefits of DMNs for the arrangements investigated.

5.11. Evaluation of Multiband L-Quad Antenna Arrays

In recent years, there has been considerable advance in wireless communications and the available frequency spectrum is becoming more occupied over time. The concept of applications such as cognitive radio and software defined radio, for example, which are based on spectrum
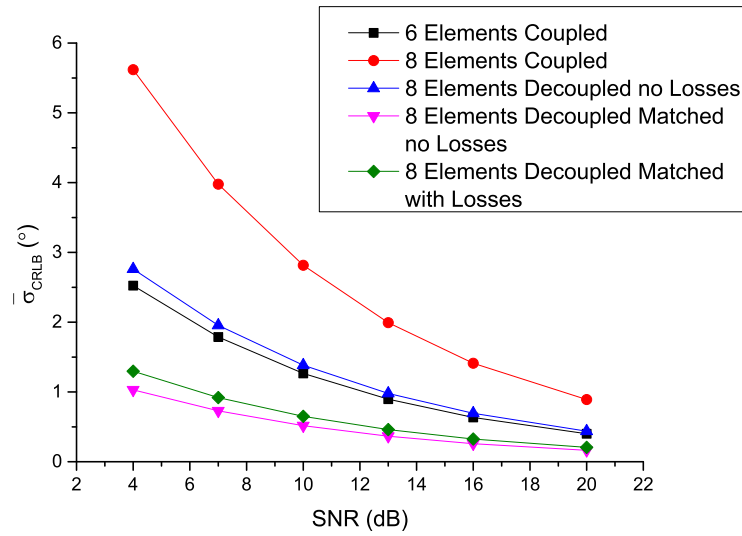
(a) Estimation of ϑ.
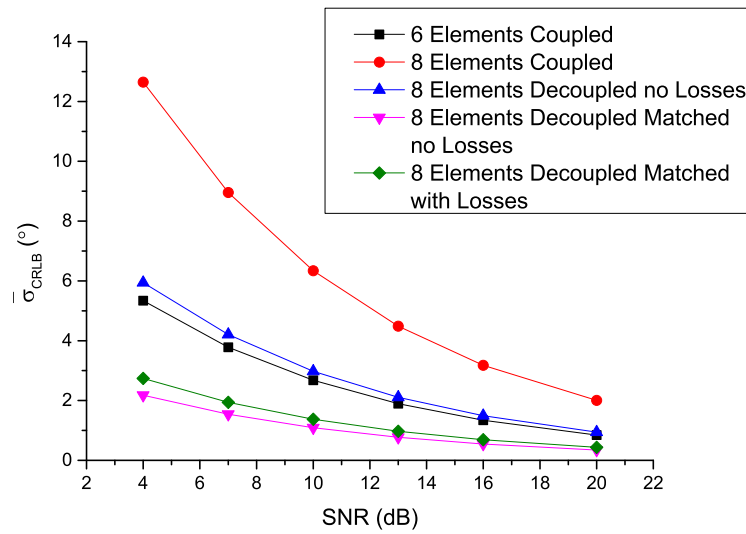
(b) Estimation of φ.

Figure 5.52.: CRLB for the DoA estimation of a single impinging signal on planar microstrip patch arrays with same aperture of 120×100 cm.

sensing and on searching for an optimal band of frequency for enhanced operation performance, has attracted ever increasing attention in the research community. Moreover, for radio emitter localization in disaster scenarios, e.g., it is highly desirable that the user can switch between different narrow bands to avoid weak performance over some specific frequency range.

To accomplish the desirable feature of operating in the widest frequency band the possible, which is the basis for Ultra-Wideband (UWB) technology, aiming to tackle the limited frequency bandwidth of existing narrowband systems, the antenna design is of crucial importance. For mobile communication which requires a wide bandwidth from as low as some MHz up to some GHz, it is of great advantage not to work with a single wide band, which would restrict the mobility because of the large required antenna size, but instead, with several narrow bands [129]. Thus, one can choose the approach of designing a multiband antenna with some switchable feeding network. Alternatively, an antenna array can be designed to have its radiating elements reconfigurable in terms of frequency.

In [129], three main ways of achieving reconfigurability are listed: selectively switching specific parts of the antenna; changing the antenna geometry by mechanical movement or adjusting the loading; or matching of the antenna externally. According to [130], the three most commonly used antennas types when dealing with frequency reconfigurability are patch antennas, planar inverted folded antennas (PIFA), and wire antennas. For each type of antenna, a different mechanism is used to address agility. Slots, switches [131] or PIN diodes are examples of mechanisms employed.

When designing compact antenna arrays, however, the coupling between elements in the array shall be taken into account to avoid poor performance. In [34], optimal arrangements with respect to the highest possible value of modal radiation efficiency are discussed. In [6], the eigen-analysis detailed in the last chapter was used to evaluate the effects that designing a compact (inter-element spacing less than half of the free-space wavelength) array can have on the antenna direction finding capabilities for several inter-element spacing and taking into account different arrangements, such as circular and linear. We proceed to investigating the performance of a dual-band antenna, which includes two single-band subarrays with half-wave spacing, designed for operation in two frequency bands. Coupling, as well as direction finding capabilities, are analyzed and compared to that of a single-band antenna with the same number of elements.

When working with dual-band arrays in an arrangement such as the one proposed in this section, one can benefit from the reduced size of the antenna, since the elements can be interleaved. Therewith, the antenna array occupies less space than it would, if the elements were arranged in a circle for single-band [8]. It is a first step for designing a universal antenna

for mobile communications, in which one does not need to design an antenna for wide band, but instead, designs an array to operate in some specifics narrower bands. Hence, it is possible to use one single antenna array for all frequency bands.

Figure 5.53 depicts the antenna array investigated. The antenna includes two single-band subarrays with half-wave spacing designed for operation in the frequency bands 1710 – 1785 MHz (outer triangle arrangement) and 2400 – 2480 MHz (three inner elements). The meander shaped structures in Figure 5.53 are the feeding network for dual-linear polarization optimized for the lower and higher frequency bands. Each full-polarimetric element is represented by four L-shaped monopoles (L-Quad). The monopoles, detailed in Chapter 3, are fed at their outer ends with nearly equal amplitudes and a phase shift of 180°, like two dipoles arranged orthogonally to each other [61]. The antenna array design and its electromagnetic simulations were performed using ANSYS HFSS 14.0 [39].
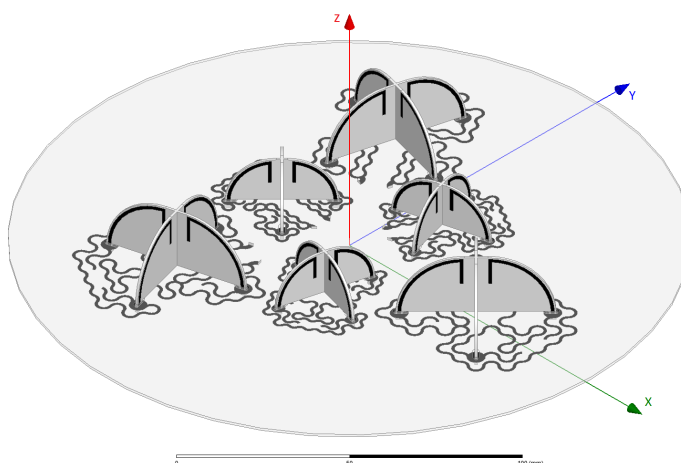
Figure 5.53.: Dual-band L-Quad antenna array investigated (semitransparent view, red and orange: metallization of the 1.8 GHz and 2.4 GHz elements respectively).

As the object for comparison, a six-element array with half-wave spacing for the frequency band 1710 – 1785 MHz will be considered – see Figure 5.54. As it can be seen, the dual-band configuration is more compact due to the interleaving of the elements. The criteria for comparison are that the antennas have the same diameter, height and number of outputs as compared to the dual-band array. This allows us to compare the performance of both antennas in terms of direction finding resolution and coupling.

The results of computed CRLB and eigen-efficiencies are given for both frequency bands. The aim of this section is to show how the antenna array arrangement affects its performance in each of the two frequency bands, and for this, a comparison is drawn between the proposed
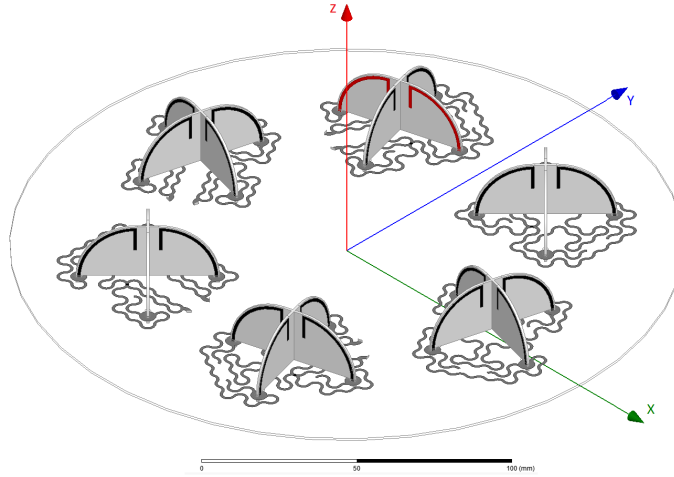
Figure 5.54.: Single-band L-Quad antenna array in circular arrangement (highlighted: a monopole pair).

antenna and a six-element single-band array in a circular arrangement.

The simulated radiation patterns and scattering matrices of the arrays are used for feeding an algorithm that addresses the antenna direction-finding capabilities and allows for direct calculation of the modal radiation efficiencies. The mean value of the CRLB over all possible elevation and azimuth angles is subsequently computed and the eigenvalues are depicted to assess coupling within the array. Throughout the results, the SNR is assumed 20 dB for the computation of the CRLB and it is known a priori that only a single wave impinges. For the Jones vector $\boldsymbol{k}$, we assume $\beta = 45°$ and $\alpha = 0°$ (linear polarized wave), and the signal is considered unmodulated and thus, $s(t) = 1$.

Due to the proximity between the two frequency ranges considered, it is to expect that the two sets of the antenna elements in the dual-band array (Figure 5.53) are coupled. Figure 5.55a shows the mean CRLB obtained for both the dual-band and the single-band array configuration. A 0.45λ inter-element spacing was considered for the inner triangle (higher frequency, 2.4 GHz) instead of 0.5λ, to avoid overlapping between the two sets of three elements. For the outer triangle (lower frequency, 1.8 GHz), 0.5λ was considered as inter-element spacing. Figure 5.55b depicts the plot for the worst-case, the average and the best-case eigenefficiencies compared to the result obtained for the single-band array.

From Figures 5.55a and 5.55b, if we compare the single-band array to the dual-band array at 1.8 GHz, we observe that the CRLB of the single-band array is lower, and the eigenefficiencies are higher. This is expected since the aperture of the dual-band array is narrower than the aperture of the single-band array, and the coupling is stronger, due to the fact that in the
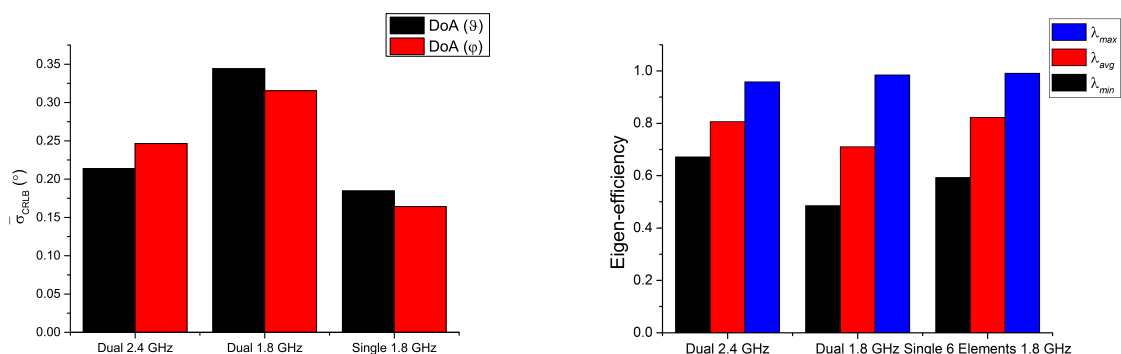
(a) Mean CRLB.

(b) Best-case, average and worst-case eigen-efficiencies.

Figure 5.55.: Mean CRLB and eigenvalues of the antenna arrays investigated.

dual-band arrangement, the inner triangle and the outer triangle, although interleaved, are positioned very close to each other. However, the dual-band arrangement at 2.4 GHz exhibits similar performance with respect to direction finding CRLB and eigenefficiencies, if compared to the single-band arrangement. Since the single-band array is optimized for the central frequency of 1.8 GHz with 80 MHz of bandwidth, at 2.4 GHz the array fails to estimate the waves' DoA. We thus conclude that one can easily benefit from the use of a dual-band array with same number of elements and reduced size if compared to a single-band array, while still enjoying good direction finding capability in two different frequency bands.

6. Conclusions and Outlook

6.1. Conclusions

Direction finding based applications have received notorious attention from the academic community and industry in the last decades, as pointed out in the Introduction of this work. To ensure high resolution and accuracy performance, attention has to be given not only to the Direction of Arrival (DoA) estimation technique employed, but also to the design of the receiving antenna array, and precise system modeling. In Chapter 2, we detailed the fundamentals of the system model and the two direction finding techniques investigated in this thesis: the Maximum Likelihood (ML) and the Multiple Signal Classification (MUSIC). Additionally, the main figure of merit investigated throughout this thesis, the Cramér-Rao Lower Bound (CRLB) was presented. Finally, optimization procedures for the estimation of the received signals' DoA were reviewed.

High-Resolution Parameter Estimation (HRPE) relies on accurate propagation data model as well as on precise modeling of the receiver. Uncertainty with respect to the receiving antenna array model may lead to significant direction finding degraded performance. The receiving antenna array response may be obtained through calibration measurements or by simulation with the use of 3D electromagnetic simulation tools. However, errors arising from calibration or simulation need to be properly accounted for. In Chapter 3, we presented some of the fundamental parameters of antenna arrays that have major impact on the corresponding radiation response, and as a consequence, dictate the capabilities of the receiving antenna for direction finding.

Irrespective of accurate device modeling, impaired antenna performance may be observed if the array designed is compact, implying inter-element spacing narrower than $\lambda/2$. Since miniaturization of devices used in communication systems is a trend topic with high demand in both military and civilian applications, it is often the case that the aperture of the receiving antenna array is somehow limited. As we place the elements together more closely, power mismatch, distorted radiation patters and loss of degrees of freedom lead to lower direction finding accuracy and resolution, as observed from the antenna array evaluation in Section 5.3.

To tackle the impairments that arise due to the electromagnetic coupling between neighboring elements in an array, focusing on the direction finding of received waves, previous work proposed compensation techniques in the digital domain. However, we argue that the miti-

gation of mutual coupling can only be achieved in the analog domain, since power mismatch leads to a definite loss of SNR, which cannot be restored in the digital domain. In Chapter 4, we proposed the design of a Decoupling and Matching Network (DMN) based on distributed elements, for DoA estimation based applications. The CRLB for arrays decoupled with the proposed technique was derived, and we illustrated the radiation patterns of decoupled three-port L-Quad and patch arrays, as examples of receiving antenna array.

In Chapter 5, we evaluated several antenna arrays, in different arrangements and scenarios, with the aim of validating the proposed DMN technique for direction finding based applications. With this aim, we introduced a multidisciplinary workbench for the evaluation and optimization of antenna arrays to be used as part of a DoA estimation system. We introduced the evaluation with results on the effects of polarization mismatch, aiming to highlight the importance of employing dual-polarized arrays for DoA estimation. We proceeded to showing the effects, with respect to DoA estimation CRLB, of mutual coupling in compact antenna arrays, where the inter-element spacing is narrower than $\lambda/2$. Following, we validated the proposed DMN design technique, by showing that improvement is observed for several array arrangements and various scenarios, including the case of correlated impinging waves, with respect to the CRLB.

We investigated the case of fixed aperture arrays and were able to draw conclusions on the effects of adding elements to the array, while keeping fixed the total occupied volume. We concluded that, for a single impinging wave, without the use of additional DMN to tackle the effects of mutual coupling, the array direction finding performance gets the more degraded, the higher the number of elements positioned in the array becomes. However, if it becomes necessary to resolve multiple received waves, higher number of elements leads to increased direction finding accuracy, even under strong mutual coupling, as observed by placing in an array seven elements instead of five, using the same available aperture. Significant DoA estimation improvement is still achieved if we consider the use of DMNs, designed with the eigenmode approach to decouple and match the more compact arrays.

Finally, we investigated the effects of mutual coupling, and validated the proposed DMN for actual direction finding using MUSIC and ML estimators, and exhaustive search procedure. It was possible to observe the degrading effects caused by mutual coupling, as well as the improved performance, with respect to the estimation error, with the use of the proposed DMN, in accordance to the results obtained from the investigation of the CRLB. To conclude, this work validated the proposed technique for decoupling and matching compact antenna arrays, which are able to fully restore the degrading effects caused by strong mutual coupling to the corresponding DoA estimation performance.

6.2. Outlook

For direction finding of narrowband electromagnetic waves, both multiband and wideband antenna arrays may be used as part of the receiving system. In Section 5.11, we proposed a multiband antenna array and validated the performance with respect to the CRLB for DoA estimation of narrowband waves. However, to capture and process signals that are spread over a wide frequency bandwidth, an antenna array that is capable of exhibiting adequate performance with respect to some performance metric, e.g. return loss or radiation pattern, over a wide range of frequencies is highly desirable. Although typical direction finding antennas traditionally include dipoles, monopoles and patches, if operating at a wide frequency bandwidth, different designs need to be taken into account [70], such as log-periodic, Yagi or magnetic loop antennas.

Several publications have recently reported results and details on the design of wideband antennas to be used for direction finding. In [132, 133], an array of conformal butterfly antennas is proposed for wideband direction finding, covering a band from 250 MHz to 3.3 GHz. Alternatively, bow-tie antennas are proposed in [134, 135] and log-periodic antennas are proposed both in [136] and [137] as design solution for direction finding systems. Bailey has recently reported in [138] the use of a compact cavity-backed spiral antenna operating at the frequency band $100 - 3000$MHz for direction finding and based on conventional beamforming.

For direction finding based applications, it is highly desirable that the radiating elements in an array exhibit radiation pattern as omnidirectional as possible. As a consequence, monopole or dipoles arrays, as well as loop antenna arrays are strong candidates to be used as receiving antennas for DoA estimation. The loop antennas offer a significant advantage over dipole (or monopole) arrays due to the capability of wideband performance. If adequate matching is connected to an array of loops, it is possible to benefit from good performance for direction finding, both with respect to low return loss as well as suitable radiation pattern, over a wide range of frequency. The loop antennas are compact, with light weight and simple manufacturing, presenting themselves as good candidates when compared to other types of wideband antennas for direction finding.

Loop antennas are usually divided into two groups: small and large or resonant loop antennas. Due to the small size in comparison to the wavelength, the current in small loop antennas exhibits same phase and amplitude along the loop. They respond to the magnetic field component of the electromagnetic radio wave and are also referred to as magnetic loops [139]. The use of small loop antennas may be useful, e.g., for low profile amateur radio. Since the directional response of small loop antennas includes a sharp null in the direction normal to the

plane of the loop [140], the procedure is to rotate the loop antenna to find the direction where the signal vanishes – the "null" direction. The large or resonant loop antenna, on the other hand, can be seen as a folded dipole which has been reformed into a circle (or square, etc.). In order to be resonant (having a purely resistive driving point impedance) the loop requires a circumference approximately equal to one wavelength (however it will also be resonant at odd multiples of a wavelength).

Small loop antennas offer the advantage of being compact and light weight. On the other hand, special attention must be paid to the antenna impedance. Small loop antennas generally exhibit very small resistance in comparison to the reactance. This gives rise to challenges with respect to impedance matching to ensure adequate radiation efficiency at the desired frequency bandwidth. One possible solution is to use active elements such as Low Noise Amplifiers (LNA) for wideband matching [141].

As an outlook, we present results from the simulation of circular arrays comprised of crossed magnetic loops, dsigned by Fraunhofer Institut für Integrierte Schaltungen (IIS), and compare them to the performance of crossed dipoles (L-Quads), as depicted in Figure 6.1, for direction finding, based on the CRLB. We compare arrays with same physical aperture of 25 cm, for the diameter of the array, comprised of six dual-polarized elements. As with the crossed dipoles (L-Quads), we refer to each element as being comprised of two ports for dual polarization. It is possible to observe that the elements are physically very similar to each other. The crossed loops are designed with half circles printed on a supporting dielectric layer, while the crossed dipoles are designed with pairs of monopoles printed on the dielectric layer.

(a) Six-element crossed dipoles.   (b) Six-element crossed loops.
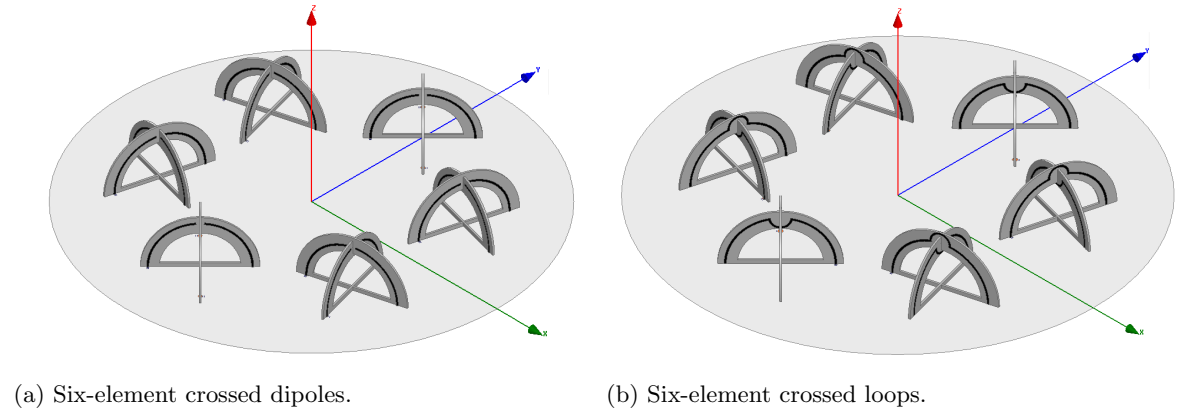
Figure 6.1.: 3D model of six-element crossed dipoles and loops.

Let us start with the results obtained from simulation of the two arrays under investigation,

at the frequency 1500 MHz. In order to analyze the performance of the array with respect to power mismatch, lumped elements were used to match the array to generators with internal impedance of 50Ω at 1500 MHz. Figure 6.2 depicts results for the CRLB of the L-Quad array in comparison to the crossed loops, assuming 0.5λ element spacing. We use the realized gain obtained from HFSS 14.0 [39], which takes into account losses from power mismatch at the antenna array ports. Figure 6.3 depicts the results that are obtained if the gain is used instead of the realized gain, also obtained from HFSS 14.0 [39], which assumes that all ports are perfectly matched.

Figures 6.4 and 6.5 depict the same results as in Figures 6.2 and 6.3, but assuming inter-element spacing of 0.4λ. Figure 6.6 depicts results for the CRLB when the arrays are assumed to be perfectly matched at the frequency of 200 MHz.

Figure 6.2.: CRLB of crossed loops array, in comparison to crossed dipoles, for 0.5 λ inter-element spacing, at 1500 MHz, assuming power mismatch at the antenna ports.

It is possible to observe that when we compare the results obtained for the 0.5λ and 0.4λ arrays, the CRLB gets higher with decreased inter-element spacing in a similar fashion both for the crossed loop array as for the L-Quad array. When using lumped elements to match the ports and assuming that some mismatch exists and needs to be taken into account in the device model, we observe that the performance of L-Quad arrays is higher when compared to crossed loops. However, if ideally matched ports are assumed, the CRLB for the crossed loop array approach the CRLB for the L-Quad array. We argue that, in order to observe similar

Figure 6.3.: CRLB of crossed loops array, in comparison to crossed dipoles, for 0.5 λ inter-element spacing, at 1500 MHz, assuming ideally matched antenna ports.

performance between the two arrays investigated, adequate matching needs to be designed for both arrays. However, when we analyze the arrays performance at 200 MHz it becomes clear that crossed dipoles are not suitable for this frequency. This is due to the fact that the crossed dipoles are optimized for 1500 MHz and do not exhibit good performance over a wide frequency bandwidth. Although the CRLB for the crossed loop array get higher at 200 MHz when compared to the CRLB at 1500 MHz, it is still possible to use the array for direction finding, especially at high SNR regimes. The crossed dipoles, on the other hand, fail to estimate DoA, resulting in inconsistently high values of CRLB.

We argue that if adequate matching is designed for the crossed loop arrays at a wide frequency bandwidth, it may be possible to benefit from the use of such type of arrays when aiming for wideband applications. However, exclusively matching the array ports may not suffice to ensure that they are decoupled, if we place the elements together more closely, and it may be necessary to design additional decoupling networks that are able to perform well over a wide range of frequencies. As future work, we propose that investigation is carried out with respect to active matching designed for wideband crossed loop arrays. It is important to draw conclusions on the effects of active matching to the array direction finding capabilities. Moreover, if the array inter-element spacing is narrower than $\lambda/2$, it becomes necessary to investigate the consequences of matching the array with active components, and how the

impairments that arise from strong mutual coupling can be restored at a wide frequency bandwidth.
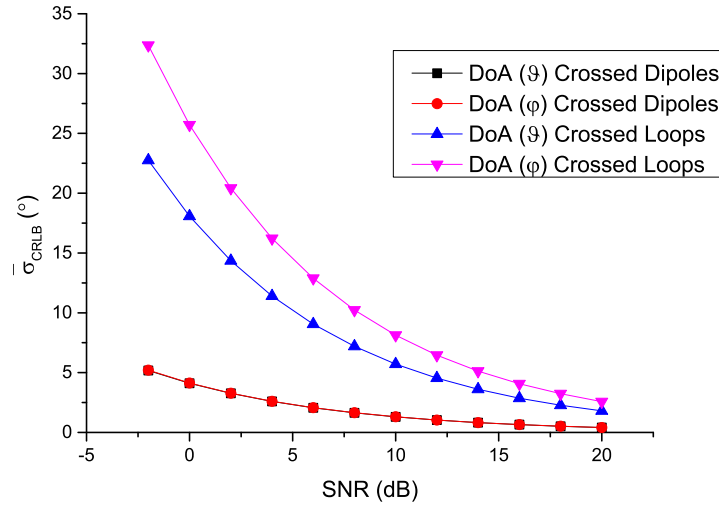
Figure 6.4.: CRLB of crossed loops array, in comparison to crossed dipoles, for $0.4\ \lambda$ interelement spacing, at 1500 MHz, assuming power mismatch at the antenna ports.
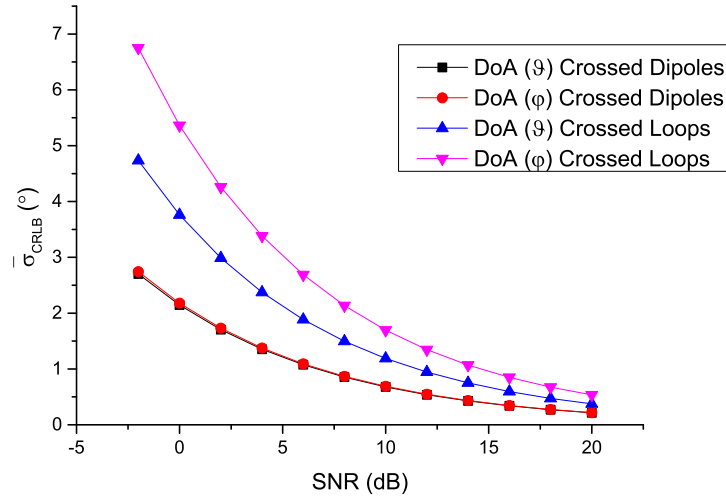
Figure 6.5.: CRLB of crossed loops array, in comparison to crossed dipoles, for 0.4 λ inter-element spacing, at 1500 MHz, assuming ideally matched antenna ports.
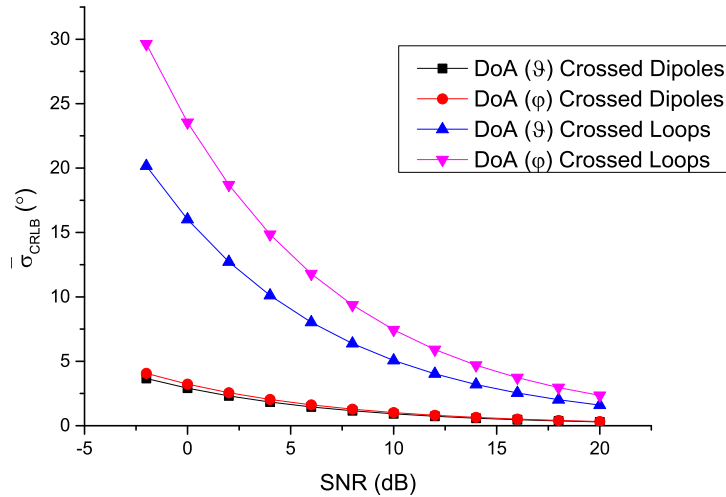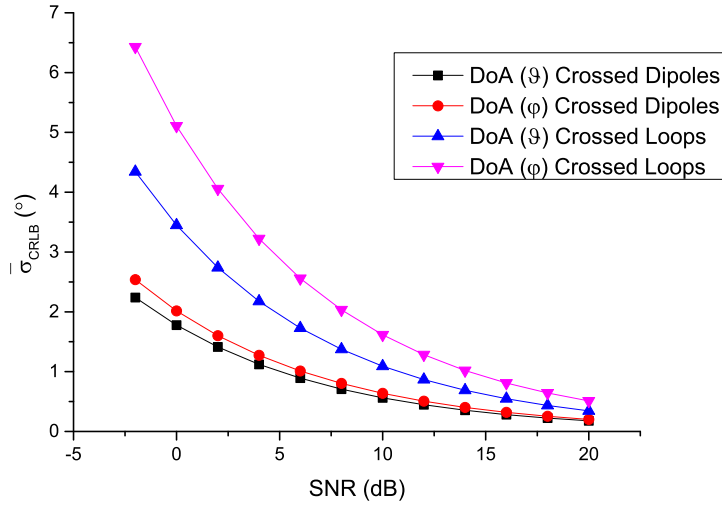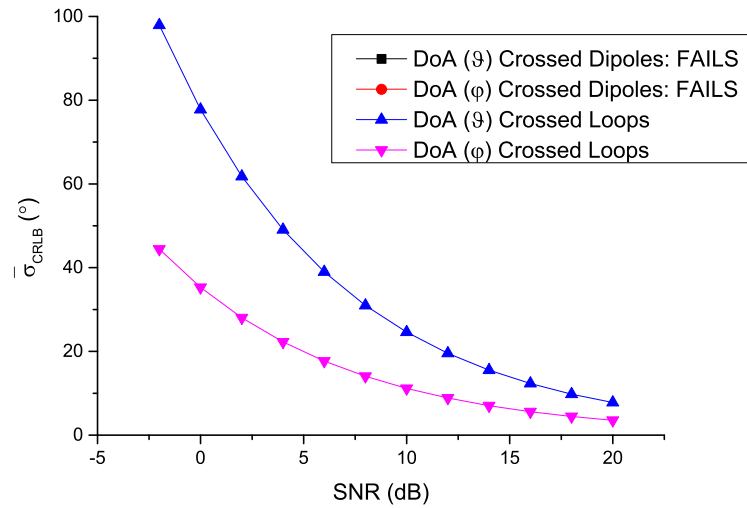

Figure 6.6.: CRLB of crossed loops array, in comparison to crossed dipoles, for 0.5 λ inter-element spacing, at 200 MHz, assuming ideally matched antenna ports.

Appendix A.

Proofs and derivations

A.1. Proof of Equation (3.45)

From (2.25), we have:

$$\mathrm{CRLB}^{-1}(L+1) = \mathrm{CRLB}^{-1}(L) + \frac{2}{\sigma^2}\mathfrak{Re}\{\boldsymbol{S}^{\mathrm{H}}(L+1)\boldsymbol{D}^{\mathrm{H}}[\boldsymbol{I} - \boldsymbol{A}(\boldsymbol{A}^{\mathrm{H}}\boldsymbol{A})^{-1}\boldsymbol{A}^{\mathrm{H}}]\boldsymbol{D}\boldsymbol{S}(L+1)\} \quad (\mathrm{A.1})$$

where $\boldsymbol{S}(t)$ is a $N \times N$ diagonal matrix comprised by the signals $s_n(t)$ with $n = 1, ..., N$:

$$\boldsymbol{S}(t) = \begin{bmatrix} s_1(t) & & 0 \\ & \ddots & \\ 0 & & s_N(t) \end{bmatrix} \quad (\mathrm{A.2})$$

Since $\boldsymbol{I} - \boldsymbol{A}(\boldsymbol{A}^{\mathrm{H}}\boldsymbol{A})^{-1}\boldsymbol{A}^{\mathrm{H}}$ is positive definite, it is proven that $\mathrm{CRLB}^{-1}(L+1) > \mathrm{CRLB}^{-1}(L)$, what proves 3.45, [11].

A.2. Proof of Equation (3.46)

Let us start by introducing a matrix structure in which a matrix $\boldsymbol{A}$ and $\boldsymbol{D}$ with $M + 1$ rows, denoted by $\boldsymbol{A}_{M+1}$ and $\boldsymbol{D}_{M+1}$ respectively, equals a matrix comprised by two submatrices ad follows.

$$\boldsymbol{A}_{M+1} = \begin{bmatrix} \boldsymbol{A}_M \\ \boldsymbol{a} \end{bmatrix} \qquad \boldsymbol{D}_{M+1} = \begin{bmatrix} \boldsymbol{D}_M \\ \boldsymbol{d} \end{bmatrix}$$

where $\boldsymbol{a}$ is the last row of matrix $\boldsymbol{A}_{M+1}$ and $\boldsymbol{d}$ is the last row of matrix $\boldsymbol{D}_{M+1}$. By using this nested structure, Stoica proved in [11] that:

$$\boldsymbol{D}_{M+1}^{\mathrm{H}}[\boldsymbol{I} - \boldsymbol{A}_{M+1}(\boldsymbol{A}_{M+1}^{\mathrm{H}}\boldsymbol{A}_{M+1})^{-1}\boldsymbol{A}_{M+1}^{\mathrm{H}}]\boldsymbol{D}_{M+1}$$

$$= \boldsymbol{D}_M^{\mathrm{H}}\boldsymbol{D}_M + \boldsymbol{d}^{\mathrm{H}}\boldsymbol{d} - (\boldsymbol{D}_M^{\mathrm{H}}\boldsymbol{A}_M + \boldsymbol{d}^{\mathrm{H}}\boldsymbol{a})(\boldsymbol{A}_M^{\mathrm{H}}\boldsymbol{A}_M + \boldsymbol{a}^{\mathrm{H}}\boldsymbol{a})^{-1}(\boldsymbol{A}_M^{\mathrm{H}}\boldsymbol{D}_M + \boldsymbol{a}^{\mathrm{H}}\boldsymbol{d}) \quad \text{(A.3)}$$

$$= \boldsymbol{D}_M^{\mathrm{H}}[\boldsymbol{I} - \boldsymbol{A}_M(\boldsymbol{A}_M^{\mathrm{H}}\boldsymbol{A}_M)^{-1}\boldsymbol{A}_M^{\mathrm{H}}]\boldsymbol{D}_M + \boldsymbol{Q}$$

where Q is a positive semidefinite matrix, what makes the left part of (A.3) larger than the right part and thus, by plugging it into the expression for the CRLB as in (2.25), proves Equation 3.46.

A.3. Conversion of Scattering Parameters into Impedance Parameters

From (3.31) we have that:

$$a_n = \frac{V_n + I_n Z_{ns}}{2\sqrt{Z_{ns}}} = \frac{V_{\mathrm{inc},n}}{\sqrt{Z_{ns}}}$$
$$b_n = \frac{V_n - I_n Z_{ns}}{2\sqrt{Z_{ns}}} = \frac{V_{\mathrm{refl},n}}{\sqrt{Z_{ns}}} \quad \text{(A.4)}$$

Assuming $\boldsymbol{a}$ and $\boldsymbol{b}$ to be respectively the vector of incident and reflected power waves for the array ports, $\boldsymbol{V}$ to be the vector of voltages at the ports terminals and $\boldsymbol{I}$ to be the vector of induced currents, we can write the following expression:

$$\boldsymbol{a} = \frac{1}{2\sqrt{Z_{ns}}}(\boldsymbol{V} + Z_{ns}\boldsymbol{I}) = \frac{1}{2Z_{ns}}(\boldsymbol{Z} + Z_{ns}\boldsymbol{I}_M)\boldsymbol{I}$$
$$\boldsymbol{b} = \frac{1}{2\sqrt{Z_{ns}}}(\boldsymbol{V} - Z_{ns}\boldsymbol{I}) = \frac{1}{2Z_{ns}}(\boldsymbol{Z} - Z_{ns}\boldsymbol{I}_M)\boldsymbol{I} \quad \text{(A.5)}$$

where $\boldsymbol{I}_M$ is the identity matrix with size $M \times M$. We can rewrite the expressions for $\boldsymbol{a}$ and $\boldsymbol{b}$ as following.

$$\frac{1}{2\sqrt{Z_{ns}}}\boldsymbol{I} = (\boldsymbol{Z} + Z_{ns}\boldsymbol{I}_M)^{-1}\boldsymbol{a}$$
$$\boldsymbol{b} = \frac{1}{2\sqrt{Z_{ns}}}(\boldsymbol{Z} - Z_{ns}\boldsymbol{I}_M)\boldsymbol{I} = (\boldsymbol{Z} - Z_{ns}\boldsymbol{I}_M)(\boldsymbol{Z} + Z_{ns}\boldsymbol{I}_M)^{-1}\boldsymbol{a} \quad \text{(A.6)}$$

Since $\boldsymbol{b} = \boldsymbol{S}\boldsymbol{a}$, we get to the scattering parameters from the impedance parameters, and vice

versa, as follows.

$$\begin{aligned}
\boldsymbol{S} &= (\boldsymbol{Z} - Z_{ns}\boldsymbol{I}_M)(\boldsymbol{Z} + Z_{ns}\boldsymbol{I}_M)^{-1} \\
\boldsymbol{Z} &= (\boldsymbol{I}_M - \boldsymbol{S})^{-1}(\boldsymbol{I}_M + \boldsymbol{S})Z_{ns}
\end{aligned} \tag{A.7}$$

For a two-element antenna array, the relation between scattering parameters and impedance parameters then becomes:

$$\begin{aligned}
Z_{11} &= Z_{ns}\frac{(1 + S_{11})(1 - S_{22}) + S_{12}S_{21}}{(1 - S_{11})(1 - S_{22}) + S_{12}S_{21}} \\[1em]
Z_{12} &= Z_{ns}\frac{2S_{12}}{(1 - S_{11})(1 - S_{22}) + S_{12}S_{21}} \\[1em]
Z_{21} &= Z_{ns}\frac{2S_{21}}{(1 - S_{11})(1 - S_{22}) + S_{12}S_{21}} \\[1em]
Z_{22} &= Z_{ns}\frac{(1 - S_{11})(1 - S_{22}) + S_{12}S_{21}}{(1 - S_{11})(1 - S_{22}) - S_{12}S_{21}}
\end{aligned} \tag{A.8}$$

Bibliography

Own Publications

[1] L. Pralon, M. Pralon, B. Pompeo, and G. Vasile, "On a probabilistic approach to detect noise radar random transmit waveforms based on a simple circularity test," in *Proceedings of the 2016 IEEE Radar Conference*, pp. 1–4, May 2016.

[2] B. Pompeo, L. Pralon, M. Pralon, and R. Mendes, "Phase-only pattern synthesis using a modified least squares method for phased arrays," in *Proceedings of the 2013 European Microwave Conference*, pp. 1755–1758, Oct. 2013.

[3] M. Pralon, D. Schulz, and R. S. Thomä, "Optimization of aperture coupled patch antenna arrays with u-slotted ground for bandwidth enhancement in DoA estimation using EADF," in *Proceedings of the 10th International Symposium on Wireless Communication Systems*, pp. 1–4, Aug. 2013.

[4] M. Pralon, D. Schulz, and R. S. Thomä, "Optimization of antenna arrays for 2D DoA estimation using EADF for Cramér-Rao lower bounds computation," in *Proc. of the International Conference on Electromagnetics in Advanced Applications*, pp. –, 2013.

[5] M. Pralon, G. D. Galdo, M. Landmann, M. A. Hein, and R. S. Thomä, "Suitability of compact antenna arrays for direction finding," *Sumbitted to IEEE Transactions on Antennas and Propagation*.

[6] M. Pralon, D. Schulz, and R. S. Thomä, "An eigen-analysis of a compact L-Quad antenna array for direction finding," in *Proc. IEEE-APS Topical Conference on Antennas and Propagation in Wireless Communications (APWC)*, pp. 369–372, 2014.

[7] M. Pralon, L. Pralon, D. Schulz, and R. S. Thomä, "On the performance of real dual-polarized antenna arrays for 2D unconditional direction of arrival estimation," in *Proceedings of the 10th European Conference on Antennas and Propagation*, pp. 1–5, Apr. 2016.

[8] M. Pralon, A. Popugaev, D. Schulz, M. A. Hein, and R. S. Thomä, "A dual-band compact l-quad antenna array for radio localization," in *Proceedings of the 9th European Conference on Antennas and Propagation*, pp. 1–4, Apr. 2015.

References by Other Authors

[9]   S. V. Schell and W. A. Gardner, *High-Resolution Direction Finding.* Handbook of Statistics, Vol. 10, N. K. Bose and C. R. Rao (Eds.), Elsevier.

[10]   S. V. Schell and W. A. Gardner, "Signal-selective high-resolution direction finding in multipath," in *Proceedings of International Conference on Acoustics, Speech, and Signal Processing*, pp. 2667–2670, Apr. 1990.

[11]   P. Stoica and A. Nehorai, "MUSIC, maximum likelihood, and Cramér-Rao bound," *IEEE Transactions on Acoustics, Speech, and Signal Processing*, vol. 37, pp. 720–741, May 1989.

[12]   M. Wax, *Detection and estimation of superimposed signals.* PhD thesis, Stanford University, Stanford, CA, Mar. 1985.

[13]   A. G. Jaffer, "Maximum likelihood direction finding of stochastic sources: A separable solution," in *Proceedings of the International Conference on Acoustics, Speech, and Signal Processing*, pp. 2893–2896, Apr. 1988.

[14]   Y. Bresler, "Maximum likelihood estimation of a linearly structured covariance with application to antenna array processing," in *Proceedings of the 4th ASSP Workshop Spectrum Estimation, Modeling*, pp. 172–175, Aug. 1988.

[15]   R. O. Schmidt, "Multiple emitter location and signal parameter estimation," *IEEE Transactions on Antennas and Propagation*, vol. AP-34, pp. 243–258, Mar. 1986.

[16]   R. Roy and T. Kailath, "ESPRIT – estimation of signal parameters via rotational invariance techniques," *IEEE Transactions on Acoustics, Speech, and Signal Processing*, vol. 37, pp. 984–995, July 1989.

[17]   L. Wang, *Array Signal Processing Algorithms for Beamforming and Direction Finding.* PhD thesis, University of York, 2009.

[18]   B. Friedlander and A. J. Weiss, "Direction finding using spatial smoothing with interpolated arrays," *IEEE Trans. Aerosp. Electron. Syst.*, vol. 28, pp. 574–587, Apr. 1992.

[19]   J. Evans, J. Johnson, and D. Sun, "High resolution angular spectrum estimation techniques for terrain scattering analysis and angle of arrival estimation," in *Proc. 1st ASSP Workshop Spectral Estimation*, (Hamilton, Canada), pp. 134–139, 1981.

[20]   S. Fortunati, R. Grasso, F. Gini, M. S. Greco, and K. LePage, "Single-snapshot DOA estimation by using compressed sensing," in *2014 IEEE International Conference on Acoustics, Speech and Signal Processing*, May 2014.

[21] K. Lee, "Subspace-augmented MUSIC for joint sparse recovery with any rank," in *Proceedings of the 2010 IEEE Sensor Array and Multichannel Signal Processing Workshop (SAM)*, (Jerusalem, Israel), pp. 205–208, Oct. 2010.

[22] J. M. Kim, O. K. Lee, and J. C. Ye, "Compressive MUSIC: Revisiting the link between compressive sensing and array signal processing," *IEEE Transactions on Information Theory*, vol. 58, pp. 278–301, Jan. 2012.

[23] F. Yan, Z. Chen, M. Sun, Y. Shen, and M. Jin, "Two-dimensional direction-of-arrivals estimation based on one-dimensional search using rank deficiency principle," *International Journal of Antennas and Propagation*, vol. 2015, pp. 1–8, 2015.

[24] H. Cramér, *Mathematical Methods of Statistics*. Princeton, NJ: Princeton Univ. Press.

[25] C. R. Rao and C. Radakrishna, "Information and the accuracy attainable in the estimation of statistical parameters," tech. rep., 1945.

[26] B. Friedlander, "Accuracy of source localization using multipath delays," *IEEE Transactions on Aerospace and Electronic Systems*, vol. 24, no. 4, pp. 346–359, 1988.

[27] A. Weiss and B. Friedlander, "Performance analysis of diversely polarized antenna arrays," *IEEE Transactions on Signal Processing*, vol. 39, pp. 1589–1603, July 1991.

[28] P. Stoica and A. Nehorai, "Performance study of conditional and unconditional direction-of-arrival estimation," *IEEE Transactions on Acoustics, Speech, and Signal Processing*, vol. 38, pp. 1783–1795, Oct. 1990.

[29] D. Schulz and R. S. Thomä, "Cramér-Rao lower bounds for polarimetric 2D direction of arrival estimation," in *Proceedings of the th Workshop on Smart Antennas*, (Ilmenau, Germany), pp. 1–8, Mar. 2015.

[30] M. Landmann, M. Kaske, and R. S. Thoma, "Impact of incomplete and inaccurate data models on high resolution parameter estimation in multidimensional channel sounding," *IEEE Transactions on Antennas and Propagation*, vol. 60, pp. 557–573, Feb. 2012.

[31] L. Rayleigh, "Investigation in optics, with special reference to the spectroscope," *The London, Edinburgh, and Dublin Phylosophical Magazine and Journal of Science*, vol. 8, Oct. 1879.

[32] R. M. Fano, "Theoretical limitations on the broadband matching of arbitrary impedances," Tech. Rep. 41, Massachusetts Institute of Technology, Jan. 1948.

[33] C. Volmer, J. Weber, R. Stephan, K. Blau, and M. A. Hein, "An eigen-analysis of compact antenna arrays and its application to port decoupling," *IEEE Transactions on Antennas and Propagation*, vol. 56, pp. 360–370, Feb. 2008.

[34] S. Irteza, N. Murtaza, S. Caizzone, R. Stephan, and M. A. Hein, "Compact planar l-band antenna arrays with optimal diversity performance," in *Proc. IEEE-APS Topical Conference on Antennas and Propagation in Wireless Communications (APWC)*, pp. 512–515, 2011.

[35] Q. Huang, F. Wei, L. Yuan, H. Zhou, and X. Shi, "A new wideband mutual coupling compensation method for adaptive arrays based on element pattern reconstruction," *International Journal of Antennas and Propagation*, vol. 2014, pp. 1–9, 2014.

[36] Q. Huang, H. Zhou, J. Bao, and X. Shi, "Accurate DOA estimations using microstrip adaptive arrays in the presence of mutual coupling effect," *International Journal of Antennas and Propagation*, vol. 2013, pp. 1–8, 2013.

[37] J. Weber, C. Volmer, K. Blau, R. Stephan, and M. A. Hein, "Miniaturized antenna arrays using decoupling networks with realistic elements," *IEEE transactions on microwave theory and techniques*, vol. 54, pp. 2733–2740, June 2006.

[38] AWE Communications GmbH, "Winprop ProMan." www.awe-communications.com.

[39] ANSYS, Inc., "Ansys HFSS." [Online]. Available: www.ansys.com.

[40] Keysight Technologies, Inc., "Advanced design system (ADS)." www.keysight.com.

[41] The Mathworks, Inc., "Matlab." www.mathworks.com.

[42] J. E. Hansen, *Spherical Near-Field Antenna Measurements*. London, UK: Peter Peregrinus Ltd.

[43] A. Richter, *Estimation of Radio Channel Parameters: Models and Algorithms*. PhD thesis, Technische Universität Ilmenau, Ilmenau, 2005.

[44] L. Wang, R. C. de Lamare, and M. Haardt, "Reduced-rank DOA estimation based on joint iterative subspace recursive optimization and grid search," in *Proc. EEE International Conference on Acoustics, Speech, and Signal Processing*, pp. 2626–2629, Mar. 2010.

[45] S. Haykin, *Adaptive Filter Theory*. Upper Saddle River, NJ: Prentice-Hall.

[46] H. L. Van Trees, *Optimum Array Processing: Detection, Estimation, and Modulation Theory, Part IV*. New York, NY: Wiley, 2002.

[47] E. Ferrara and T. Parks, "Direction finding with an array of antennas having diverse polarizations," *IEEE Transactions on Antennas and Propagation*, vol. 31, no. 2, pp. 231–236, 1983.

[48] D. Schulz and R. S. Thomä, "Search-based MUSIC techniques for 2D DoA estimation using EADF and real antenna arrays," in *Proceedings of the 17th Workshop on Smart Antennas*, (Stuttgart, Germany), Mar. 2013.

[49] F. Roemer and M. Haardt, "Deterministic Cramér-Rao bounds for strict sense non-circular sources," in *Proc. ITG/IEEE Workshop on Smart Antennas (WSA'07)*, (Vienna, Austria), Feb. 2007.

[50] R. O. Schmidt, *A signal subspace approach to multiple emitter localization and spectral estimation*. PhD thesis, Stanford University, Stanford, CA, Nov. 1981.

[51] B. Porat and B. Friedlander, "Computation of the exact information matrix of gaussian time series with stationary random components," *IEEE Transactions on Acoustics, Speech, and Signal Processing*, vol. ASSP-34, pp. 118–130, Feb. 1986.

[52] R. S. Thomä, M. Landmann, A. Richter, and U. Trautwein, "Multidimensional high-resolution channel sounding," *Smart Antennas in Europe State of the Art, EURASIP Book Series*, vol. 3, 2005.

[53] M. Landmann, A. Richter, and R. S. Thomä, "DoA resolution limits in MIMO channel sounding," in *Proc. Int. Symp. on Antennas Propag. and USNC/URSI National Radio Science Meeting*, (Monterey, CA), June 2004.

[54] F. Belloni, A. Richter, and V. Koivunen, "DOA estimation via manifold separation for arbitrary array structures," *IEEE Transactions on Signal Processing*, vol. 55, pp. 4800–4810, Oct. 2007.

[55] S. U. Pillai and B. H. Kwon, "Forward / backward spatial smoothing techniques for coherent signal identification," *IEEE Transactions on Acoustics, Speech, and Signal Processing*, vol. AASP-37, pp. 8–15, Jan. 1989.

[56] B. Widrow, K. M. Duvall, R. P. Gooch, and W. C. Newman, "Signal cancellation phenomena in adaptive antennas: causes and cures," *IEEE Transactions on Antennas and Propagation*, vol. AP-30, pp. 469–478, 1982.

[57] W. F. Gabriel, "Spectral analysis and adaptive array superresolution techniques," *Proceedings of the IEEE*, vol. 68, pp. 806–811, June 1980.

[58] J. Evans, J. Johnson, and D. Sun, "Application of advanced signal processing techniques to angle of arrival estimation in ATC navigation and surveillance systems," tech. rep., Tech. Rep. 582, M.I.T. Lincoln Laboratory, Cambridge, MA, June 1982.

[59] T. J. Shan, M. Way, and T. Kailath, "On spatial smoothing for direction-of-arrival estimation of coherent signals," *IEEE Transactions on Acoustics, Speech, and Signal Processing*, vol. AASP-33, pp. 806–811, Aug. 1985.

[60] M. Wax and J. Sheinvald, "Direction finding of coherent signals via spatial smoothing for uniform circular arrays," *IEEE Transactions on Antennas and Propagation*, vol. 42, pp. 613–620, May 1994.

[61] C. Dominguéz, F. Tiezzi, J. Padilla, R. Wansch, R. Rummel, and A. Popugaev, "Low-cost S-band antennas for mobile satellite systems,"

[62] M. Landmann, *Limitations of Experimental Channel Characterization*. PhD thesis, Technische Universität Ilmenau, Ilmenau, 2008.

[63] J. A. Fessler and A. O. Hero, "Space-alternating generalized expectation maximization algorithm," *IEEE Trans. on Signal Processing*, vol. 42, no. 10, 1994.

[64] C. T. Kelley, *Iterative Methods for Optimization*, vol. 18. Society for Industrial and Applied Mathematics, 1999.

[65] K. Levenberg, "A method for the solution of certain non-linear problems in least squares," *Quarterly of Applied Mathematics*, vol. 5, 1944.

[66] D. Marquardt, "An algorithm for least-squares estimation of nonlinear parameters," *Journal of the Society for Industrial and Applied Mathematics*, vol. 11, no. 2, 1963.

[67] W. H. Press, S. A. Teukolsky, W. T. Vetterling, and B. P. Flannery, *Numerical Recipes in C: The Art of Scientific Computing*. New York, NY: Cambridge University Press.

[68] Z. Chen, G. Gokeda, and Y. Yu, *Introduction to Direction-of-Arrival Estimation*. Norwood, MA: Artech House.

[69] A. Balanis, *Antenna Theory and Design*. New York, NY: John Wiley and Sons.

[70] E. G. Lim, Z. Wang, C. U. Lei, Y. Wang, and K. L. Man, "Ultra wideband antennas – past and present," *IAENG International Journal of Computer Science*, vol. 37, Aug. 2010.

[71] R. Mueller, S. Lutz, and R. Lorch, "A novel circular direction finding antenna array a novel circular direction finding antenna array for unknown polarizations," in *Proceedings of the European Conference on Antennas and Propagation*, pp. 1514–1518, 2013.

[72] H. Lee and R. Stovall, "Maximum likelihood methods for determining the direction of arrival for a single electromagnetic source with unknown polarization," *IEEE Transactions on Signal Processing*, vol. 42, Feb. 1994.

[73] S. Henault, Y. M. M. Antar, S. Rajan, R. Inkol, S. Wang, and C. Wilson, "Mutual coupling analysis of coplanar adcock direction finding arrays," in *Proceedings of the 24th Biennial Symposium on Communications*, (Kingston, ON), pp. 27–30, June 2008.

[74] A. J. Weiss and B. Friedlander, "Direction finding in the presence of mutual coupling," *IEEE Transactions on Antennas and Propagation*, vol. 39, no. 3, pp. 273–284, 1991.

[75] Q. Bao, C. C. Ko, and W. Zhi, "DoA estimation under unknown mutual coupling and multipath," *IEEE Transactions on Aerospace and Electronic Systems*, vol. 41, pp. 565–573, Apr. 2005.

[76] H. Lui and H. T. Hui, "Direction-of-arrival estimation of closely spaced emitters using compact arrays," *International Journal of Antennas and Propagation*, vol. 2013, pp. 1–9, 2013.

[77] I. J. Gupta and A. A. Ksienski, "Effect of mutual coupling on the performance of adaptive arrays," *IEEE Transactions on Antennas and Propagation*, Sept. 1983.

[78] H. Lui, H. T. Hui, and M. S. Leong, "A note on the mutual-coupling problems in transmitting and receiving antenna arrays," *IEEE Antennas and Propagation Magazine*, vol. 51, Oct. 2009.

[79] Y. Yu, H. Lui, C. H. Niow, and H. T. Hui, "Improved DoA estimations using the receiving mutual impedances for mutual coupling compensation: An experimental study," *IEEE Transactions on Wireless Communications*, vol. 10, July 2011.

[80] H. T. Hui, "Improved compensation for the mutual coupling effect in a dipole array for direction finding," *IEEE Transactions on Antennas and Propagation*, Sept. 2003.

[81] H. T. Hui, "A new definition of mutual impedance for application in dipole receiving antenna arrays," *IEEE Antennas and Wireless Propagation Letters*, vol. 3, 2004.

[82] H. T. Hui, "A practical approach to compensate for the mutual coupling effect in an adaptive dipole array," *IEEE Transactions on Antennas and Propagation*, vol. 52, May 2004.

[83] H. T. Hui, "Antenna designer's notebook - receiving mutual impedance between two normal-mode helical antennas (NMHAs)," *IEEE Antennas and Propagation Magazine*, vol. 48, Aug. 2006.

[84] G. Sommerkorn, D. Hampicke, R. Klukas, A. Richter, A. Schneider, and R. Thomä, "Uniform rectangular antenna array design and calibration issues for 2-D ESPRIT application," (Vienna, Austria), pp. –, Feb. 2001.

[85] H. Steyskal and J. S. Herd, "Mutual coupling compensation in small array antennas," *IEEE Transactions on Antennas and Propagation*, vol. 38, no. 12, pp. 1971–1975, 1990.

[86] G. A. Deschamps, "Microstrip microwave antennas," in *3rd USAF Symp. on Antennas*, 1953.

[87] H. Gutton and G. Baissinot, "Flat aerial for ultra high frequencies," in *French Patent No 703113*, 1955.

[88] K. Carver and J. W. Mink, "Microstrip antenna technology," *IEEE Transactions on Antennas and Propagation*, Jan. 1981.

[89] R. Mailloux and J. F. McIlvenna, "Microstrip array technology," *IEEE Transactions on Antennas and Propagation*, Jan. 1981.

[90] D. M. Pozar, "Input impedance and mutual coupling of rectangular microstrip antennas," *IEEE Transactions on Antennas and Propagation*, pp. 1191–1196, Nov. 1982.

[91] D. M. Pozar and B. Kavrman, "Design considerations for low sidelobe microstrip arrays antenna," *IEEE Transactions on Antennas and Propagation*, pp. 1176–1185, Aug. 1990.

[92] D. M. Pozar and D. H. Schaubert, *Microstrip Antennas: The Analysis and Design of Microstrip Antennas and Arrays.* New York, NY: Wiley-IEEE Press.

[93] D. M. Pozar, "A microstrip antenna aperture-coupled to a microstrip line," *Electronic Letters*, vol. 21, 1985.

[94] R. Garg, P. Bhartia, I. Bahl, and I. A, *Microstrip Antenna Design Handbook.* Norwood, MA: Artech House.

[95] T. Metzler, "Microstrip series arrays," *IEEE Transactions on Antennas and Propagation*, pp. 174–178, 1981.

[96] D. M. Pozar, "A review of bandwidth enhancement techniques for microstrip antennas," *Microstrip Antennas, The Analysis and Design of Microstrip Antennas and Arrays, D. M. Pozar and D. H. Schaubert (Eds.).*

[97] H. M. Yazidi, M. El, and J. Daniel, "Transmission line analysis of nonlinear slot coupled microstrip antenna," *Electronic Letters*, vol. 28, 1992.

[98] S. X. Ta, I. Park, and R. W. Ziolkowski, "Crossed dipole antennas: A review," *IEEE Antennas and Propagation Magazine*, vol. 57, pp. 107–122, Oct. 2015.

[99] G. Brown, "The turnstile antenna," *Electron.*, vol. 9, pp. 14–17, Apr. 1936.

[100] A. Popugaev and R. Wansch, "Low profile automotive antennas for digital broadcasting,"

[101] H. Ghali and T. A. Moselhy, "Miniaturized fractal rat-race, branchline and coupled-line hybrids," *IEEE Transactions on Microwave Theory and Techniques*, vol. 52, pp. 2513–2520, Nov. 2004.

[102] F. Sadeghi-Kia and M. Khalaj-Amirhosseini, "Three reduced-size ratrace couplers," in *ICMMT2008 Proceedings.*

[103] R. K. Settaluri, G. Sundberg, A. Weisshaar, and V. K. Tripathi, "Miniaturized fractal rat-race, branchline and coupled-line hybrids," *IEEE Transactions on Microwave and Guided Wave Letters*, vol. 10, pp. 61–63, Feb. 2000.

[104] A. Popugaev and R. Wansch, "A novel miniaturization technique in microstrip feed network design," in *Proceedings of the 3rd European Conference on Antennas and Propagation*, pp. 2309–2313, Mar. 2009.

[105] A. E. Popugaev, *Miniaturisierte Mikrostreifenleitungs-Schaltungen bestehend aus zusammengesetzten Viertelkreisringen.* PhD thesis, Technische Universität Ilmenau, Ilmenau, Germany, 2013.

[106] A. J. Weiss and B. Friedlander, "Mutual coupling effects on phase-only direction finding," *IEEE Transactions on Antennas and Propagation*, vol. 40, pp. 535–541, May 1992.

[107] Z. Ye and C. Liu, "On the resiliency of MUSIC direction finding against antenna sensor coupling," *IEEE Transactions on Antennas and Propagation*, vol. 56, pp. 371–380, Feb. 2008.

[108] H. Lui, Y. Yu, H. T. Hui, and M. S. Leong, "Experimental study of mutual coupling compensation in direction finding using a compact antenna array," in *Proceedings of the 2010 Asia-Pacific International Symposium on Electromagnetic Compability*, (Beijing, China), pp. 830–833, Apr. 2010.

[109] H. Lui and H. T. Hui, "Mutual coupling compensation for direction finding using receiving mutual impedance," in *Proceedings of the 2010 International Symposium on Antennas and Propagation*, (Kaohsiung, Taiwan), pp. 61–62, Dec. 2014.

[110] S. Chen, Y. Wang, and S. Chung, "A decoupling technique for increasing the port isolation between two strongly coupled antennas," *IEEE Transactions on Antennas and Propagation*, vol. 56, pp. 3650–3657, Dec. 2008.

[111] J. Weber, C. Volmer, R. Stephan, and M. A. Hein, "Eigenmode decoupling of miniaturised diversity antennas using compact quasi-lumped networks," in *Proc. Loughborough Antennas Propag. Conf. (LAPC)*, (Loughborough, UK), Mar. 2008.

[112] J. Weber, C. Volmer, K. Blau, R. Stephan, and M. A. Hein, "Miniaturization of antenna arrays for mobile communications," in *Proc. 35th Eur. Microwave Conf. (EuMC)*, (Paris, France), pp. 1173–1176, Oct. 2005.

[113] S. Stein, "On cross coupling in multiple-beam antennas," *IRE Trans. Antennas Propagation*, vol. 10, pp. 548–557, Sept. 1962.

[114] C. Volmer, *Compact Antenna Arrays in Mobile Communications: a Quantitative Analysis of Radiator Coupling*. PhD thesis, Technische Universität Ilmenau.

[115] H. J. Chaloupka and X. Wang, "Novel approach for diversity and MIMO antennas at small mobile platforms," in *Proc. 15th IEEE Int. Symp. Personal, Indoor Mobile Radio Commun. (PIMRC)*, (Barcelona, Spain), pp. 637–642, Sept. 2004.

[116] H. J. Chaloupka, X. Wang, and J. C. Coetzee, "Performance enhancement of smart antennas with reduced element spacing," in *Proc. IEEE Wireless Commun. Netw. Conf. (WCNC)*, (New Orleans, Louisiana), pp. 425–430, Mar. 2003.

[117] C. Volmer, R. Stephan, and M. A. Hein, "Evaluation of compact antenna arrays for mobile communications applications," in *Proceedings of the 2010 International Workshop on Antenna Technology*, (Lisbon, Portugal), pp. 1–4, Mar. 2010.

[118] C. Volmer, J. Weber, R. Stephan, and M. A. Hein, "A descriptive model for analyzing the diversity performance of compact antenna arrays," *IEEE Transactions on Antennas and Propagation*, vol. 57, pp. 395–405, Feb. 2009.

[119] S. Irteza, E. Schäfer, M. Sgammini, R. Stephan, and M. A. Hein, "Four-element compact planar antenna array for robust satellite navigation systems," in *Proc. of the 7th European Conference on Antennas and Propagation (EuCAP)*, pp. 21–25, Apr.

[120] R. E. Collin, *Foundations for Microwave Engineering*. New York, NY: Wiley-IEEE Press.

[121] M. Ibraheam, S. Irteza, and M. A. Hein, "Enhancing the radiation efficiency of compact antenna arrays using spatial tilting," in *Proceedings of the 8th European Conference on Antennas and Propagation*.

[122] M. Landmann and G. D. Galdo, "Efficient antenna description for MIMO channel modelling and estimation," in *Proceedings of the 7th European Conference on Wireless Technology*, (Amsterdam, The Netherlands), pp. 217–220, Oct. 2004.

[123] G. Kompa, *Practical Microstrip Design and Applications*. Norwood, MA: Artech House.

[124] E. O. Hammerstad and F. Bekkadal, "Microstrip handbook ELAB report," tech. rep., STF 44 A74169, University of Trondheim, Norway, 1975.

[125] K. C. Gupta and I. J. Bahl, *Microstrip Lines and Slotlines*. Norwood, MA: Artech House.

[126] H. A. Wheeler, "Transmission-line properties of parallel strips separated by a dielectric sheet," *IEEE Trans.*, vol. MTF 13, 1965.

[127] P. Stoica and A. Nehorai, "MUSIC, Maximum Likelihood, and Cramér-Rao bound: further results and comparisons," *IEEE Transactions on Acoustics, Speech, and Signal Processing*, vol. 38, pp. 2140–2150, Dec. 1990.

[128] P. Stoica, B. Ottersten, M. Viberg, and R. L. Moses, "Maximum likelihood array processing for stochastic coherent sources," *IEEE Transactions on Signal Processing*, vol. 44, pp. 96–105, Jan. 1996.

[129] P. Gardner, M. R. Hamid, P. S. Hall, J. Kelly, F. Ghanem, and E. Ebrahimi, "Reconfigurable antennas for cognitive radio: Requirements and potential design approaches," in *Proc. Institution of Engineering and Technology Seminar on Wideband, Multiband Antennas and Arrays for Defence or Civil Applications*, pp. 89–94, 2008.

[130] S. Yang, C. Zhang, H. Pan, A. Fathy, and V. Nair, "Frequency-reconfigurable antennas for multiradio wireless applications," *IEEE Microwave Magazine*.

[131] C. Ko, I. Tarn, and S. Chung, "A compact dual-band pattern diversity antenna by dual-band reconfigurable frequency-selective reflectors with a minimum number of switches," *IEEE Transactions on Antennas and Propagation*, vol. 61, pp. 646–654, Feb. 2013.

[132] I. Liberal, D. Caratelli, A. Yarovoy, R. Cicchetti, and M. Russo, "Conformal butterfly antennas for ultra-wideband radio direction finding applications," in *Proceedings of the 40th European Microwave Conference*, (Paris, France), pp. 846–849, Sept. 2010.

[133] D. Caratelli, I. Liberal, and A. Yarovoy, "Design and full-wave analysis of conformal ultra-wideband radio direction finders," *IET Microwaves, Antennas and Propagation*, vol. 5, no. 10, 2011.

[134] M. E. Ozturk, E. Korkmaz, and M. Kebeli, "Rounded-edge bow-tie antenna for wideband mobile direction finding system," *IET Microwaves, Antennas and Propagation*, vol. 9, no. 15, 2015.

[135] S. K. Sharma, J. Rayno, S. Fernandez, R. Bortolin, A. Berezin, and J. Kudva, "Wideband vertically polarized omnidirectional antennas for direction finding (DF) systems," in *Proceedings of the 2014 Antennas and Propagation Symposium*.

[136] C. Viswanadham, "A practical approach for controlling the shape of the radiation pattern of a microwave log-periodic antenna for wideband applications," *IEEE Antennas and Propagation Magazine*, vol. 56, no. 5, 2014.

[137] X. Liang and Y. W. M. Chia, "New precision wideband direction finding antenna," *IEE Proceedings Microwaves, Antennas and Propagation*, vol. 148, no. 6, 2001.

[138] M. C. Bailey, T. G. Campbell, C. J. Reddy, R. L. Kellogg, and P. Nguyen, "Compact wideband direction-finding antenna," *IEEE Antennas and Propagation Magazine*, vol. 54, pp. 44–68, Dec. 2012.

[139] J. J. Carr, *Practical Antenna Handbook*. New York, NY: McGraw-Hill.

[140] A. W. Rudge, K. Milne, A. D. Olver, and P. Knight, *Handbook of Antenna Design Vol 2*. London, UK: Peter Peregrinus Ltd.

[141] C. T. Nzwy, "Wideband loop antenna matching networks," 2008.

Abbreviations, Symbols and Notation

Abbreviations

AWGN Additive White Gaussian Noise
BF BeamForming
BP Beam Pattern
BS Base Station
BW Bandwidth
CDF Cumulative Density Function
CIR Channel Impulse Response
CM Cavity Method
CMA Conditional Maximum Assumption
CMIM Conventional Mutual Impedance Method
CML Conditional Maximum Likelihood
CRLB Cramér-Rao Lower Bound
DFT Discrete Fourier Transform
DMC Diffuse Multi-path Component
DMN Decoupling and Matching Network
DoA Direction Of Arrival
DoD Direction Of Departure
EADF Effective Aperture Distribution Function
EM ElectroMagnetic
EMT Electronic Measurement Laboratory
ESPRIT Estimation of Signal Parameters via Rotational Invariance Techniques
EVD EigenValue Decomposition
FFT Fast Fourier Transform
FIM Fisher Information Matrix
FN Feeding Network
FS Fourier Series
GNSS Global Navigation Satellite System
GPS Global Positioning System
GTD Geometrical Theory of Diffraction
HRPE High Resolution Parameter Estimation
IDFT Inverse Discrete Fourier Transform
LLF Log-Likelihood Function
LNA Low Noise Amplifier
LOS Line Of Sight
LS Least Squares
LTE Long Term Evolution
DL Diversity Loss
DL Diversity Gain

MIMO Multiple Input Multiple Output
ML Maximum Likelihood
MODE Method of Direction of Arrival Estimation
MoM Method of Moments
MUSIC Multiple Signal Classification
MPC Multi-Path Component
MRC Maximum Ratio Combining
MS Mobile Station
MSE Mean Squared Error
NLOS Non Line Of Sight
NMSE Normalized Mean Squared Error
NSE Normalized Squared Error
PDF Probability Density Function
ULPA Uniform Linear Patch Array
PCRLB Polarimetric Cramér-Rao Lower Bound
RARE Rank-Reduction Estimator
RF Radio Frequency
RLC Resistor, Inductor, Capacitor
RMIM Receiving Mutual Impedance Method
RMS Root Mean Square
RMSE Root Mean Squared Error
RX Receiver
SM Scattering Matrix
SNR Signal to Noise Ratio
SV Singular Value
SVD Singular Value Decomposition
TDoA Time Delay Of Arrival
TLM Transmission Line Method
TUI Technische Universität Ilmenau
TX Transmitter
UCA Uniform Circular Array
ULA Uniform Linear Array
UMA Unconditional Maximum Assumption
UML Unconditional Maximum Likelihood
URA Uniform Rectangular Array
URPA Uniform Rectangular Patch Array
XPD Cross-Polarization Discrimination
XPR Cross-Polarization Ratio
WLAN Wireless Local Area Network
1D One-dimensional
2D Two-dimensional
3D Three-dimensional

Symbols and Notation

$\mathcal{R}$ Set of real numbers

$\mathcal{C}$ Set of complex numbers

$\boldsymbol{A}$ Matrix $\boldsymbol{A}$

$\boldsymbol{a}$ Vector $\boldsymbol{a}$

$\boldsymbol{A}^{\mathrm{H}}$ Hermitian operation of matrix $\boldsymbol{A}$

$\boldsymbol{A}^{\mathrm{T}}$ Transpose operation of matrix $\boldsymbol{A}$

$mathrmdet\{\boldsymbol{A}\}$ Determinant of the square matrix $\boldsymbol{A}$

$|\boldsymbol{A}|$ Absolute values of matrix $\boldsymbol{A}$

$\angle\boldsymbol{Q}$ Phases of matrix $\boldsymbol{A}$

$\mathrm{tr}\{\boldsymbol{A}\}$ Trace of the matrix $\boldsymbol{A}$

$\boldsymbol{A}^{-1}$ Inverse of the matrix $\boldsymbol{A}$

$\boldsymbol{I}$ Identity matrix

$\log$ base-10 logarithm

λ Free-space wavelength

$\sum$ Sum

$\epsilon_0 = 8.8542 \times 10^{-12} \mathrm{F/m}$ Free-space permittivity

$\mu_0 = 4\pi \times 10^{-7} \mathrm{N/A}^2$ Free-space permeability

$\eta_0 = \sqrt{\dfrac{\mu_0}{\epsilon_0}} = 120\pi\,\Omega$ Intrinsic impedance

$k_0 = \dfrac{2\pi}{\lambda} = \omega\sqrt{\mu_0\epsilon_0}$ Free-space wavenumber

ϑ Elevation angle in degrees

φ Azimuth angle in degrees

$\mathbb{E}\{x\}$ Expected value of the random variable x

Erklärung

Ich versichere, dass ich die vorliegende Arbeit ohne unzulässige Hilfe Dritter und ohne Benutzung anderer als der angegebenen Hilfsmittel angefertigt habe. Die aus anderen Quellen direkt oder indirekt übernommenen Daten und Konzepte sind unter Angabe der Quelle gekennzeichnet.

Weitere Personen waren an der inhaltlich-materiellen Erstellung der vorliegenden Arbeit nicht beteiligt. Insbesondere habe ich hierfür nicht die entgeltliche Hilfe von Vermittlungs - bzw. Beratungsdiensten (Promotionsberater oder anderer Personen) in Anspruch genommen. Niemand hat von mir unmittelbar oder mittelbar geldwerte Leistungen für Arbeiten erhalten, die im Zusammenhang mit dem Inhalt der vorgelegten Dissertation stehen.

Die Arbeit wurde bisher weder im In- noch im Ausland in gleicher oder ähnlicher Form einer Prüfungsbehörde vorgelegt.

Ich bin darauf hingewiesen worden, dass die Unrichtigkeit der vorstehenden Erklärung als Täuschungsversuch bewertet wird und gemäß §7 Abs. 10 der Promotionsordnung den Abbruch des Promotionsverfahrens zur Folge hat.

Ilmenau, July 12, 2017